Millimeter-Wave MMICs and Applications

Thesis by

Matthew Alexander Morgan

In Partial Fulfillment of the Requirements for the Degree of

Doctor of Philosophy

California Institute of Technology
Pasadena, California

(Defended March 24, 2003)

© 2003

Matthew A. Morgan

All Rights Reserved

Where the telescope ends, the microscope begins. Which of the two has the grander view?

- Victor Hugo

Acknowledgements

The work detailed in this thesis would not have been possible without the generous contributions of many organizations and individuals.

For financial support of myself and the projects I have participated in, I thank the California Institute of Technology, the Jet Propulsion Laboratory, the IEEE Microwave Theory and Techniques Society, the Lee Center for Advanced Networking, Millivision, the National Radio Astronomy Observatory, TREX Enterprises, and the SETI Institute.

For fabrication of the various custom chips and components designed as part of this work, I would like to thank the staff of Aerojet, American Technical Ceramics, Applied Thin Film Products, the Caltech Physics Shop, Fineline Circuits, GGB Industries, HRL Laboratory, Precision PhotoFab, Proto Engineering, Quinstar, Raytheon, TRW, UltraSource, United Monolithic Semiconductors, and the University of California at Santa Barbara.

For technical support, invaluable advice, discussion, and essential criticism, I am deeply grateful to Ichiro Aoki, Durgadas Bagri, Patrick Cesarano, Lawrence Cheung, April Collins, Douglas Dawson, Todd Gaier, Ali Hajimiri, Scott Kee, Robert McEliece, Ricardo Paniagua, Alex Peralta, Ronald Pogorzelski, David Rutledge, Lorene Samoska, Niklas Wadefalk, Mary Wells, and Jonas Zmuidzinas.

Finally, I offer my sincerest thanks to Dr. Sandy Weinreb, who has been far more than an advisor to me in the years we have known each other, to my brother, who repeatedly sets the standards that keep me on my toes, and to my parents — my best friends — whose aggressive support of my every endeavor has never faltered for an instant since the day I was born.

Abstract

As device technology improves, interest in the millimeter-wave band grows. Wireless communication systems migrate to higher frequencies, millimeter-wave radars and passive sensors find new solid-state implementations that promise improved performance, and entirely new applications in the millimeter-wave band become feasible. The circuit or system designer is faced with a new and unique set of challenges and constraints to deal with in order to use this portion of the spectrum successfully. In particular, the advantages of monolithic integration become increasingly important.

This thesis presents many new developments in Monolithic Millimeter-Wave Integrated Circuits (MMICs), both the chips themselves and systems that use them. It begins with an overview of the various applications of millimeter waves, including a discussion of specific projects that the author is involved in and why many of them demand a MMIC implementation. In the subsequent chapters, new MMIC chips are described in detail, as is the role they play in real-world projects. Multi-chip modules are also presented with specific attention given to the practical details of MMIC packaging and multi-chip integration. The thesis concludes with a summary of the works presented thus far and their overall impact on the field of millimeter-wave engineering.

Contents

ACKNOWLEDGEMENTS **iv**

ABSTRACT **v**

CONTENTS **vi**

TABLE OF ILLUSTRATIONS **viii**

CHAPTER 1 Applications of Millimeter-Wave MMICs **1**
1.1 Introduction 1
1.2 Earth-Observing Radiometers 5
1.3 Passive Millimeter-Wave Imaging 8
1.4 Radio Telescope Arrays 13
1.5 Deep Space Communications 16
1.6 Overview of Thesis Work 19

CHAPTER 2 Broadband Frequency Multipliers **22**
2.1 A Full Waveguide-Band MMIC Tripler for 75-110 GHz 22
2.2 LO Source Multipliers for ALMA and EVLA 30

CHAPTER 3 Monolithic Millimeter-Wave Mixers **36**
3.1 Broadband Balanced Mixers 36
3.2 A 170-210 GHz Second Harmonic Mixer 48
3.3 I/Q Mixers 51
3.4 A Second-Harmonic I/Q Mixer for the DSN Array 54
3.5 Doubly Balanced Mixers 58

CHAPTER 4 Millimeter-Wave Low-Noise Amplifiers **63**
4.1 W-Band Low-Noise Amplifiers for Millimeter-Wave Imaging 63
4.2 Ka- and Q-Band Low-Noise Amplifiers for Radiometric Applications 66
4.3 A Ka-Band Low-Noise Amplifier for the DSN Array 72

CHAPTER 5 Millimeter-Wave Power Amplifiers **76**
5.1 A W-Band Monolithic Medium Power Amplifier 77
5.2 More W-Band Power Amplifiers 84

CHAPTER 6 Custom Millimeter-Wave Control Circuits **88**
6.1 Ka-Band Switched Attenuators 89
6.2 Ka-Band SP3T Switches 92

CHAPTER 7 Multi-Chip Module Design **94**
7.1 Multi-chip Integration 94
7.2 A Millimeter-Wave Perpendicular Coax-to-Microstrip Transition 98
7.3 Waveguide-to-Printed-Circuit Transitions 106
7.4 Passives in Multi-Chip Modules 110
7.5 A MMIC-Based 75-110 GHz Signal Source 119
7.6 A Ka-Band Low-Noise Amplifier Module 126
7.7 A Ka-Band Cryogenic Front End 129
7.8 A Q-Band Filtered Post-Amplifier Module for the EVLA 132

7.9 A Ka-Band Downconverter for the EVLA 134
7.10 A Ka-Band Dual-Polarization Downconverter for the DSN 137

CHAPTER 8 Conclusions 144

REFERENCES 146

Table of Illustrations

figure		*page*
1.1	Absorption spectrum in Earth's atmosphere	2
1.2	Weighting functions for atmospheric sounding	6
1.3	Prototype MMIC-based receivers for AMLS	7
1.4	Mechanical diagram of PMC2	9
1.5	Band diagram of Sb-heterostructure tunnel diode	10
1.6	Diode impedance transformers for PMC2	12
1.7	DSN capability versus time	17
1.8	Block diagram of the Ka-band receiver for the DSN Array	19
2.1	Photograph of the 75-110 GHz tripler	23
2.2	Schematic of the 75-110 GHz tripler	24
2.3	Test setup for the 75-110 GHz tripler	25
2.4	Output power vs. frequency for the 75-110 GHz tripler	26
2.5	Model vs. measurement for the 75-110 GHz tripler	26
2.6	Output power vs. input power for the 75 -110 GHz tripler	27
2.7	Flatest output power vs. frequency for the 75 -110 GHz tripler	27
2.8	Output spectrum for the 75-110 GHz tripler	28
2.9	Photograph of the 183 GHz radiometer	29
2.10	Layout of the 183 GHz radiometer	29
2.11	Layout of the 36-50 GHz tripler	32
2.12	Output power vs. frequency for the 36-50 GHz tripler	32
2.13	Layout of the 70-92 GHz tripler	34
2.14	Output power vs. frequency for the 70-92 GHz tripler	34
2.15	Layout of the 90-124 GHz tripler	35
2.16	Output power vs. frequency for the 90-124 GHz tripler	35
3.1	Photograph of the 100-140 GHz balanced mixer	37
3.2	Schematic of the 100-140 GHz balanced mixer	37
3.3	180° hybrid for the 100-140 GHz balanced mixer	38
3.4	Test setup for the 100-140 GHz balanced mixer	39
3.5	Conversion loss versus RF for the 100-140 GHz balanced mixer	41
3.6	Conversion loss versus IF for the 100-140 GHz balanced mixer	41
3.7	Conversion loss versus bias for the 100-140 GHz balanced mixer	42
3.8	Conversion loss versus LO power for the 100-140 GHz balanced mixer	42
3.9	Photograph of the revised 100-140 GHz balanced mixer	43
3.10	Photograph of the 75-110 GHz balanced mixer	44
3.11	Conversion loss versus RF for the 75-110 GHz balanced mixer	44
3.12	Layout of the 36-50 GHz balanced mixer	46
3.13	Conversion loss versus RF for the 36-50 GHz balanced mixer	46
3.14	Layout of the 40-50 GHz balanced mixer	47
3.15	Conversion loss versus RF for the 40-50 GHz balanced mixer	47
3.16	Photograph of the 170-210 GHz second-harmonic mixer	49
3.17	Schematic of the 170-210 GHz second-harmonic mixer	49
3.18	Conversion loss versus RF for the 170-210 GHz second-harmonic mixer	50
3.19	Photograph of the 49-57 GHz I/Q mixer	51
3.20	Conceptual diagram of an I/Q mixer	52
3.21	Layout of the 31-38 GHs second-harmonic I/Q mixer	55

3.22 Schematic of the 31-38 GHz second-harmonic I/Q mixer 55
3.23 Conversion loss versus RF for the 31-38 GHz second-harmonic I/Q mixer 57
3.24 Conversion loss versus IF for the 31-38 GHz second-harmonic I/Q mixer 57
3.25 Ring- and star-configurations of doubly balanced mixers 59
3.26 Layout of the 70-92 GHz doubly balanced mixer 60
3.27 Conversion loss versus RF for the 70-92 GHz doubly balanced mixer 60
3.28 Layout of the 120-144 GHz doubly balanced mixer 61
3.29 Conversion loss versus RF for the 120-144 GHz doubly balanced mixer 61

4.1 Photograph of the 47-96 GHz LNA 64
4.2 Schematic of the 47-96 GHz LNA 64
4.3 S-parameters for the 47-96 GHz LNA 65
4.4 Photograph of the 26-40 GHz LNA 67
4.5 Photograph of the 33-50 GHz LNA 67
4.6 Schematic of the 26-40 GHz and 33-50 GHz LNA 67
4.7 S-parameters for the 26-40 GHz LNA 68
4.8 S-parameters versus gate 1 bias for the 33-50 GHz LNA 69
4.9 S-parameters versus gate 2 and 3 bias for the 33-50 GHz LNA 69
4.10 S-parameters versus gate 1, 2, and 3 bias for the 33-50 GHz LNA 70
4.11 P_{1dB} versus gain for the 33-50 GHz amplifier 70
4.12 Layout of the 30-40 GHz LNA 73
4.13 Schematic of the 30-40 GHz LNA 73
4.14 S-parameters and noise temperature for the 30-40 GHz LNA 74

5.1 Photograph of the 75-95 GHz PA 78
5.2 Schematic of the 75-95 GHz PA 78
5.3 S-parameters for the 75-95 GHz PA 81
5.4 Large-signal test setup for the 75-95 GHz PA 82
5.5 Output power versus frequency for the 75-95 GHz PA 82
5.6 Output power versus bias for the 75-95 GHz PA 83
5.7 Output power versus input power for the 75-95 GHz PA 83
5.8 Layout of the 77-95 GHz PA 84
5.9 Layout of the 87-108 GHz PA 85
5.10 Layout of the 100-120 GHz PA 85
5.11 Schematic of the 100-120 GHz PA 86
5.12 Output power versus frequency for the 77-95 GHz PA 86
5.13 Output power versus frequency for the 87-108 GHz PA 87
5.14 Output power versus frequency for the 100-120 GHz PA 87

6.1 Layout of the 10 dB, 31-38 GHz switched attenuator 90
6.2 Layout of the 20 dB, 31-38 GHz switched attenuator 90
6.3 Schematic of the 31-38 GHz switched attenuators 90
6.4 S-parameters for the 10 dB, 31-38 GHz switched attenuator 91
6.5 S-parameters for the 20 dB, 31-38 GHz switched attenuator 91
6.6 Layout of the 31-38 GHz SP3T switch 93
6.7 S-parameters for the 31-38 GHz SP3T switch 93

7.1 Comparison of modules with end-launch and perpendicular coax transitions 95
7.2 Example of CPW pads on a microstrip circuit 97
7.3 Illustration of zero-current boundary in TE_{10} mode 97
7.4 Diagram of the perpendicular coax-to-microstrip transition 99
7.5 Photographs of the perpendicular transition adapter 100
7.6 Comparison of field distribution with concentric and offset ground apertures 101
7.7 Photograph of the back-to-back transition test block 103

7.8 Interior photograph of the back-to-back transition test block 103
7.9 Raw s-parameters for back-to-back transitions 104
7.10 Corrected s-parameters for a single transition 104
7.11 Photograph of the longitudinal E-field probe 107
7.12 Return loss for the 26-40 GHz longitudinal probe 107
7.13 Comparison of waveguide probe geometries 109
7.14 Layout of the differential loop probe 109
7.15 S-parameters for the 35 GHz differential loop probe 110
7.16 Photograph of a microstrip bandpass filter 112
7.17 Drawing of a multi-chip module utilizing fully-integrated waveguide filters 112
7.18 Evolution of the arc-coupler geometry 114
7.19 Photograph of the 50-110 GHz directional coupler 115
7.20 Diagram of the broadband dot-termination 117
7.21 Photograph of the forward-coupling test substrate for the 50-110 GHz coupler 117
7.22 Photograph of the isolation test substrate for the 50-110 GHz coupler 117
7.23 Photograph of the insertion loss test substrate for the 50-110 GHz coupler 117
7.24 Return loss of the 800 μm dot termination 118
7.25 S-parameters for the 50-110 GHz directional coupler 118
7.26 Photograph of the W-band signal source 120
7.27 Schematic for the W-band signal source 121
7.28 Interior photograph of the W-band signal source 121
7.29 Photograph of the PC-Board for the W-band signal source 123
7.30 Test setup for the W-band signal source 123
7.31 Output power versus frequency for the W-band signal source 124
7.32 Output power versus control voltage for the W-band signal source 124
7.33 Output power versus input power for the W-band signal source 125
7.34 Drawing of the Ka-band LNA package 128
7.35 Detail view of the chips in the Ka-band LNA package 128
7.36 Drawing of the Ka-band cryogenic front end 130
7.37 Interior view of the Ka-band cryogenic front end 130
7.38 Schematic of the EVLA Q-band receiver 133
7.39 Layout of the EVLA Q-band post-amplifier module 133
7.40 Schematic of the EVLA Ka-band downconverter 135
7.41 Layout of the EVLA Ka-band downconverter 136
7.42 Block diagram of the Ka-band downconverter for the DSN Array 138
7.43 Photograph of the test blocks for WR-22 and WR-28 septum filters 140
7.44 Open WR-22 test block and metal shim for the 37.5 GHz filter 140
7.45 Insertion loss for the two septum filters 141
7.46 Drawing of the Ka-band downconverter for the DSN Array 142
7.47 Interior layout of the Ka-band downconverter for the DSN Array 142

1 Applications of Millimeter-Wave MMICs

1.1 Introduction

The work described in this thesis is strictly millimeter-wave. That is, every circuit, component, or system described herein has the most significant of its operating frequencies between 30 and 300 GHz, where the corresponding free-space waves are millimeters in length. While many of the physical principles and techniques employed in this work will be familiar to specialists in the RF and microwave areas, the underlying system priorities and practical constraints may be quite different. Differences in economic factors, manufacturability, and even the currently available test equipment may force the millimeter-wave designer toward a completely different solution than would be appropriate for a similar microwave engineering project. It is therefore useful to begin by discussing exactly what millimeter waves are used for and what implications that has for the way systems are designed.

Probably the most significant influence on the current applications of millimeter waves is the natural absorption spectrum in Earth's atmosphere. A plot of the nominal absorption features is shown Figure 1.1. The relative transparency of the atmosphere in the RF and Microwave regions below about 15 GHz has made them an easy choice for wireless communication. Historically, the early radio systems occupied the lowest frequency bands with sufficient bandwidth for simple voice communication and for which the necessary antennas had reasonable dimensions. As technology improved and the wireless communication market increased in size as well as sophistication, system designers sought out more bandwidth at higher frequencies. The first exploration of the microwave spectrum, however, was done by the military in the development of radar, where higher frequency meant increased angular resolution for a given antenna.

As engineers pushed higher in frequency, they encountered steadily increasing absorption, initially due to electron conduction and non-resonant magnetic and electric multipolar effects. The first significant

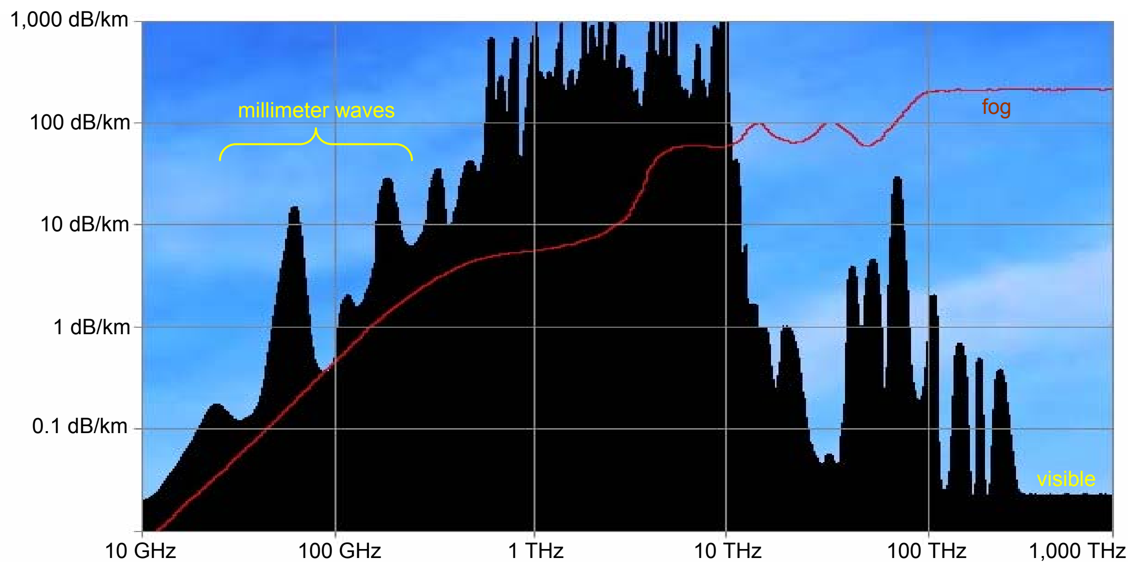

Fig. 1.1. Absorption features in Earth's atmosphere.

resonant feature appears at 22.235 GHz, associated with a rotational energy level of water vapor. A number of other rotational bands associated with molecular constituents in the atmosphere follow. These features render the atmosphere nearly opaque to most of the submillimeter and far-infrared wavelengths. Continuing even higher in frequency, the absorption characteristics become dominated by molecular vibration and electron transition energy levels, eventually clearing again in the visible spectrum [1].

Concentrating now on the lower-frequency portion of Figure 1.1, the most prominent features in the high-microwave and millimeter-wave range are the four rotational lines associated with oxygen and water vapor, in addition to the steady increase in continuum absorption in the "windows" between those lines. The water vapor lines occur at 22.235 GHz and 183.3 GHz, and the oxygen lines are at 60 GHz and 118.75 GHz (actually, the 60 GHz feature is not a single line, but an entire band of energy levels that are merged in our atmosphere by pressure broadening) [1].

The relatively high absorption in much of the millimeter-wave band hinders long-distance wireless communication on the surface, but also provides an interference-free channel in space. For example, satellites can use a 60 GHz cross-link frequency, relying on atmospheric oxygen to filter out any made-made interference from the ground [2]. Even on the surface, however, it is realized that high-absorption bands have some hidden advantages. The FCC has allocated between 57.05 and 64 GHz for unlicensed

use. About 98% of the energy from a 60 GHz signal is absorbed by molecular oxygen over a 1 km distance at ground level. This allows a large number of groups in a relatively small area to independently use the 60 GHz channel without interfering with one another. The large RF data bandwidth available there makes it ideal for short range, "last mile" segments from an optical fiber to a nearby building for much less cost than it would take to lay down additional fiber.

Some of the windows in this spectrum are occupied by millimeter-wave radars, which are currently in use by military aircraft and by the atmospheric research community for cloud detection. They are also being studied for remote characterization of foliage and snow cover, to monitor ship traffic in coastal regions, and for automotive collision avoidance. These systems are still adversely affected by absorption, but take advantage of the increased resolution for small antennas afforded by high frequency, as well as the relative lack of man-made interference.

More significant to this thesis, however, is not how these absorption features hinder signal transmission, but the information they contain about atmospheric chemistry. A consequence of thermodynamics is that frequencies of absorption for a particular molecule also correspond to the frequencies of emission of thermal radiation from that molecule. Thus, the resonant spectral lines in the millimeter-wave range provide a means of studying Earth's climate and the effects of pollution on a global scale. A large part of the research at JPL discussed in this work involves the development of millimeter-wave radiometers for remote sensing of Earth's atmosphere from an orbiting spacecraft. A more detailed description of the scientific principles and techniques employed will be given in Section 1.2.

Looking beyond Earth's atmosphere (literally), there are numerous applications for millimeter waves in radio astronomy. Some of the same chemical species that dominate the electromagnetic characteristics of our atmosphere are present in other parts of the galaxy for our observation. In addition, astronomical phenomena produce radiation in all parts of the spectrum and provide one the best methods available to us for studying them. Shorter wavelength emissions from more distant objects in our universe are red-shifted into the millimeter-wave or microwave bands by their relative velocity away from us. Most distant of all, in terms of both space and time, is the cosmic microwave background, sometimes described as an after-image of the Big-Bang. Measurements of the anisotropy in the microwave and millimeter-wave

background radiation provide information regarding the geometry of the Universe and the nature of the matter and energy within it.

Perhaps the most fundamental difference between microwave engineering and millimeter-wave engineering relates to the fact that circuit elements must scale down in size proportionally to the wavelength. This "small matter" often has enormous implications for the design approach that stem from manufacturability and relative performance of the circuit elements. Lumped element inductors are no longer physically realizable, substrates must be thinned to just a couple of mils or even removed entirely in some extreme cases, and traditional assembly techniques are often too imprecise to be practical. This last point is one of the main reasons for a monolithic approach in millimeter-wave electronics. In a Monolithic Millimeter-wave Integrated Circuit (MMIC), passive elements and interconnects are fabricated on the same semiconductor substrate as the active devices. All the critical, microscopic circuit elements are defined on-chip through photolithography from a scaled-up mask. This eliminates the parasitics associated with component packages, leads, and solder pads.

Other advantages of the MMIC approach are reduced mass and volume with respect to conventional circuit assemblies, highly repeatable performance, and low-cost fabrication in large-quantities. As will be seen in the following sections, the miniaturization and ease of mass production of MMICs make array-architectures most interesting for many millimeter-wave systems. The MMIC approach does have its disadvantages, however. Passive elements on a MMIC chip will typically have lower Q than is available in discrete packages or on other substrates. Power handling capacity will also be limited. Post-fabrication tuning of circuit elements is almost non-existent, requiring the more challenging circuit designs to go through multiple iterations before acceptable performance is achieved. Further, the complexity of MMIC fabrication leads to extremely long iteration times. A MMIC designer must often wait six months, or even a year, before making revisions. Finally, MMIC test and development requires somewhat specialized laboratory equipment such as wafer probes, probe stations, and wire bonders. The lack of some common laboratory instruments at millimeter-wave frequencies, such as synthesized signal sources or spectrum analyzers, further complicates circuit measurements.

In the following sections, some of the specific projects and JPL missions that motivated this research will be described in more detail. Particular attention will be paid to the scientific principles that call for millimeter-wave operation, the practical constraints imposed by the nature of the project, and the unique challenges that had to be overcome in order to meet the prescribed goals.

1.2 Earth Observing Radiometers

As was noted earlier, the spectral absorption/emission behavior of molecules in the microwave, millimeter-wave, and submillimeter-wave bands contains a wealth of information about the atmosphere. A variety of observation techniques has been used, including occultation experiments, detection of scattering phenomena, and measurement of thermal emission. Pioneered in many cases by JPL programs, these approaches can be used to map variations in atmospheric properties in both space and time, such as temperature, humidity, molecular concentration, pressure, wind, and density [1].

To understand how these systems work, it is important to realize that spectral lines are not infinitely narrow. Absorption/emission lines are broadened by a number of phenomena. A molecule in an excited state emits energy not as a continuous wave, but as a pulse with a certain characteristic "lifetime," or duration. The Fourier Transform of such a pulse will have a bandwidth inversely proportional to the excited state lifetime. In addition, thermal motion of molecules will result in a Doppler shift as seen by a remote observer. The statistical distribution of velocities in a gas, and thus the broadening of a spectral feature from Doppler effects, is related to the temperature. Furthermore, pressure-induced collisions result in radically changing Doppler shifts for each molecule and even more spectral broadening related to the mean time between collisions, which in turn is inversely proportional to atmospheric pressure. This so-called *Lorentz* broadening dominates at lower altitudes where the pressure is greatest, whereas simple Doppler broadening is more significant in the upper atmosphere [1].

The broadened shape of a spectral line can be used to our advantage. Consider an orbiting spacecraft monitoring emissions from our atmosphere at the peak absorption frequency in the center of a

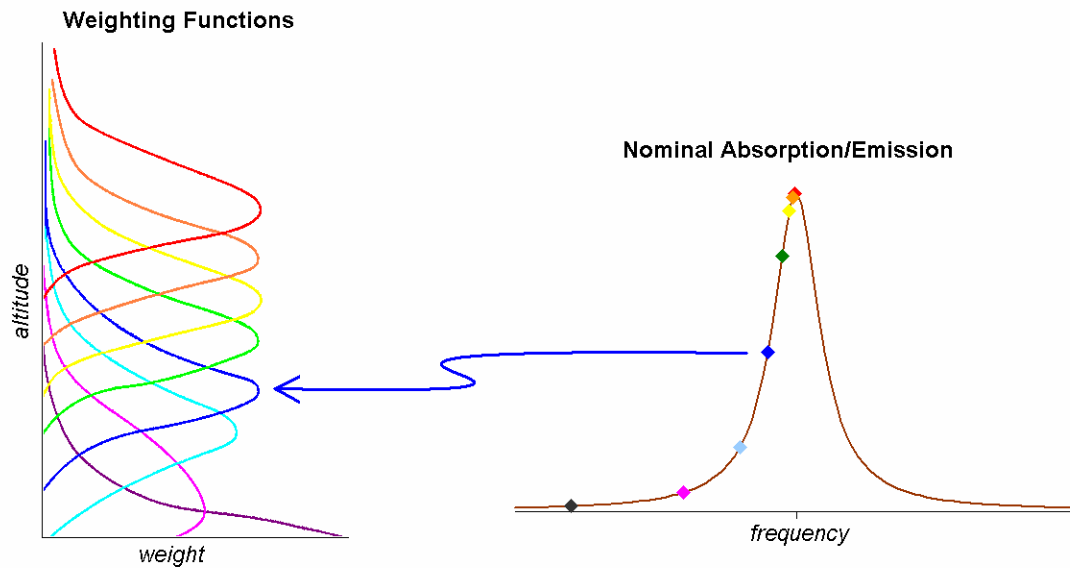

Fig. 1.2. Illustration of weighting functions used for atmospheric sounding.

spectral line. Most of the radiation it sees is coming from the uppermost layer of the atmosphere because the emissions from lower layers are absorbed before they reach the spacecraft. On the other hand, if it is monitoring a frequency on the far wings of the spectral line, most of the observed signal is coming from the bottom of the atmosphere because absorption is very low and the higher density layers of molecules in the lower atmosphere emit more energy than the thinner layers above them. In mathematical terms, there is a *weighting function* associated with each frequency that describes what percentage of the radiation reaching the spacecraft originated in a certain layer of the atmosphere as a function of altitude. Between the two extremes described above, frequency points can be selected for which the corresponding weighting function peaks at any altitude desired. By sampling frequency points around a spectral line, a complete profile of the appropriate atmospheric constituent as a function of altitude can be derived, as illustrated in Figure 1.2. Note that this measurement can only be made from space, as a sensor on the ground would see only the bottom layers of the atmosphere which have the strongest emission and are the least attenuated from that perspective [1].

An alternative to the nadir sounding technique described above, *limb sounding*, can be used to achieve greater resolution in altitude. It is based on the same principle, but instead of looking straight down towards the surface, the sensor looks towards the edge, or limb, of Earth's atmosphere. This is the

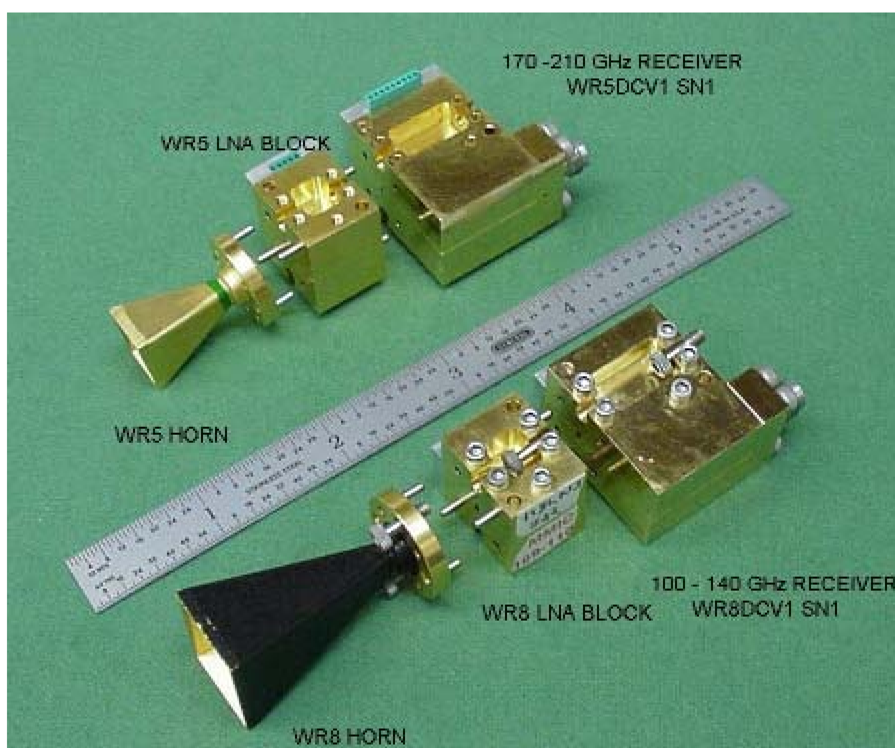

Fig. 1.3. Prototype MMIC-based receiver modules for the Array Microwave Limb Sounder.

approach used by the Microwave Limb Sounders developed at JPL. These instruments contain a variety of radiometers monitoring different spectral lines, thereby providing invaluable information for weather monitoring and forecasting, atmospheric ozone and chemistry monitoring, and climate change research. However, the size, cost, and power requirements of these sensors meant that only a single radiometer per frequency band could be supported on a spacecraft. This limits the mission to taking measurements at discrete, widely separated points as the spacecraft orbits swiftly around the globe.

Recent developments in MMIC technology provide an exciting solution to this problem. The MMIC approach allows new radiometers to be developed with an order of magnitude reduction in volume, mass, and cost, concurrently with an improvement in performance in terms of power requirements, system noise temperature, and bandwidth. A large number of these receivers could then be arranged into a focal-plane array for contiguous imaging of the atmosphere from space. This architecture is part of a proposed mission at JPL known as the Array Microwave Limb Sounder (AMLS). The author of this thesis has participated in the development of two prototype receiver modules for this project, shown in Figure 1.3. The 100-140 GHz module can be used to monitor the oxygen line at 118 GHz for derivation of a

temperature profile in the atmosphere, and the 170-210 GHz receiver can be used to obtain a humidity profile via the 183 GHz water vapor line. The project that funds this development effort is an Instrument Incubator Program (IIP) at JPL known as Microwave Atmospheric Temperature and Humidity Sensors (MATHS).

Both modules incorporate RF and IF low-noise amplifiers, broadband mixers, and LO amplifiers. I was responsible for the mixers in both modules, and their design will be discussed in more detail in Sections 3.1 and 3.2. Originally, both modules were going to use an LO frequency of 80 GHz, with the higher band receiver incorporating a second-harmonic mixer so that both could run off the same LO source. Later, it was decided to run the 100-140 GHz module with a 90 GHz LO so the IF bands of both modules would be equivalent. The integration of LO MMIC amplifiers in the module greatly relaxes the millimeter-wave power requirements. Typically, we have tested these receivers with about –20 dBm of LO power. This means an entire focal plane array with 50 receivers in each band could run with just 1 mW from the local oscillator.

1.3 Passive Millimeter-wave Imaging

Referring back to the plot of Figure 1.1, it can be seen that the absorption due to fog is significantly lower in the millimeter-wave band as opposed to visible wavelengths. It is therefore feasible to consider building a video camera that can penetrate fog by using millimeter waves instead of visible light. This is the basis of an interesting project at TREX Enterprises in San Diego, CA. The Passive Microwave Camera (imprecisely named, since its operating range is in W-band) is funded by the Army Research Lab, which is interested in a passive aircraft landing system that can safely operate under foggy conditions. Other potential applications include the detection of non-metallic contraband (such as plastic weapons) concealed under a suspect's clothing.

A second iteration of the millimeter-wave imager, called PMC2, is currently under development. A mechanical diagram of the camera is shown in Figure 1.4. The antenna (not visible on the diagram) is a

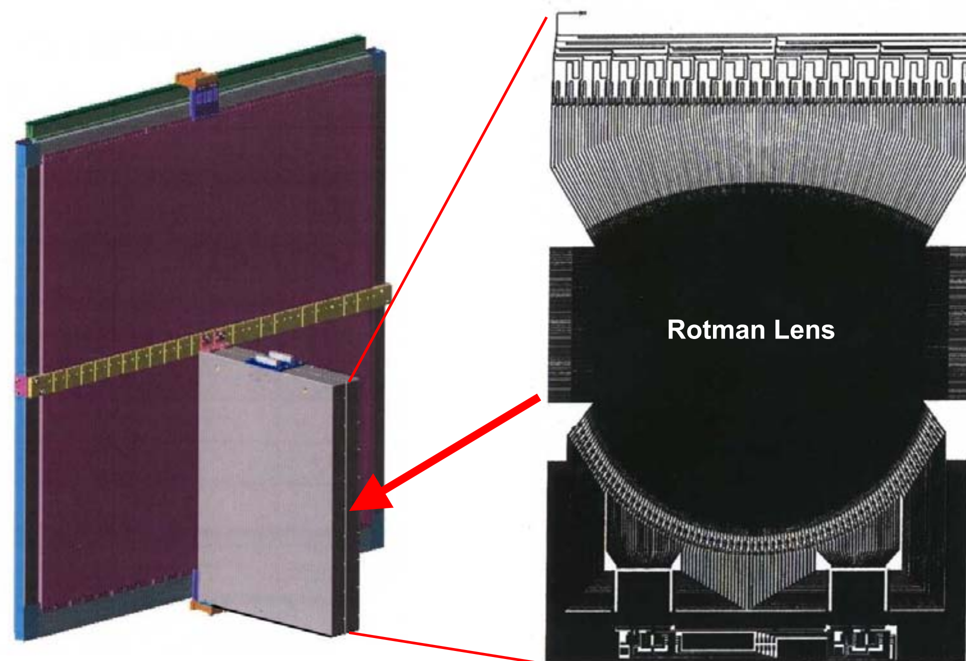

Fig. 1.4. Mechanical assembly diagram and frequency processor board for the Passive Microwave Camera 2 under construction at TREX Enterprises.

phased-array of dispersive radiating elements. That is, each element in the array has a horizontally broad beam that shifts vertically with frequency. The signals from the antenna elements are amplified and then fed to a *phase processor*, a passive network which combines the signals from the array in different phases to produce a distinct channel for each column of the image. Since the antenna is dispersive, the row-information is contained in the relative power at different frequencies. Therefore, each channel is passed through a *frequency processor*, shown on the right in Figure 1.4. This is essentially a Rotman Lens implemented in stripline. The signal for a single channel (or a single column in the image) enters on the transmission line at the top left corner. This signal is split onto a number of feedlines that vary in length such that the wavefront arriving at the lens has a frequency-dependent phase slope. This phase slope produces a beam on the lens that steers left and right as a function of frequency. These channels, and thus the individual pixels of the final image, are picked up by the taps arrayed at the bottom of the lens [3].

TREX is currently using InP low-noise amplifiers in their design, but given the large number that is required for a single imager, they are highly motivated to find a lower-cost alternative. A promising new technology is the Metamorphic-HEMT process which has matured in recent years. This is a process in

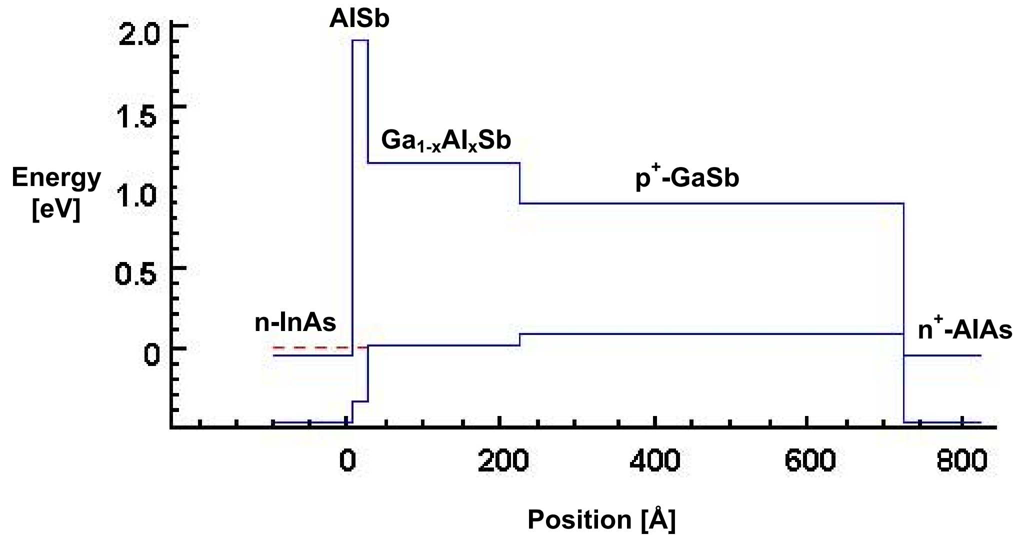

Fig. 1.5. Band diagram of HRL's Sb-Heterostructure Tunnel-Diode.

which InP transistors are grown monolithically on a GaAs substrate. It promises InP performance at lower cost, in part because the processing can be done on a 4-inch wafer as opposed to the 3-inch diameter that is common for InP. The author has designed a W-band LNA using such a process, and that work will be described in more detail in Section 4.1.

Unlike the first imager, which used heterodyne detection, the PMC2 will require a huge number of diodes for direct detection in W-band, one for each of almost 25,000 pixels. These are to be supplied by the Hughes Research Laboratory, which is developing a new Antimony Heterostructure diode that has good sensitivity up into W-band. A band-diagram of the device is shown in Figure 1.5. Tunneling current flows from the InAs contact on the left through the AlSb barrier and is controlled by varying either the barrier thickness or the Al content in the GaAlSb blocking layer. Negative bias induces large tunneling current through the barrier, whereas positive bias blocks it. This asymmetry in current flow produces the non-linearity near zero-bias for detection and mixing [4]. The author has assisted in this development effort by modeling the various generations of diodes and characterizing them in terms of their equivalent circuit and

their responsivity, both at low frequencies and in W-band. I also contributed to the integration of the detectors on the frequency processor board.

These diodes are generated in huge quantities on GaAs wafers and then diced into individual flip-chips which are finally mounted on the frequency processor boards described earlier. The frequency processor is simply too large to fabricate as a MMIC, but the difficulty experienced while dealing with the flip-chips on this project makes abundantly clear the advantage of monolithic techniques in other systems. First, the size and technical specifications of the phase and frequency processor boards required them to be made in stripline using 250 μm thick polypropalene layers supplied by a PC-Board manufacturer. Right away, this causes problems for the detector integration as these materials and processes were never intended for use at so high a frequency. The original plan was to drill out small holes in the top layer of the stripline structure for insertion of the flip-chips, but this led to unavoidable cavity resonances that would have ruined the operation of the imager. Instead, it was decided to transition from stripline to microstrip after the bottom edge of the Rotman Lens where the detectors will be placed. Unfortunately the 250 μm polypropalene layers, acceptable in a stripline configuration, are really too thick for microstrip at 90 GHz. Discontinuities in the transmission line, including matching networks and the transition to microstrip itself, have a tendency to radiate power off the board. This loss must be made up elsewhere in the already loss-stricken system, and the radiated power may lead to crosstalk from one channel to the next.

The parasitic elements of the flip-chip itself were also examined in great detail. The mechanical issues associated with picking and placing over 20,000 diodes precisely on a large circuit board place constraints on the minimum size of the chips and the bonding pads. The shunt capacitance between the two large pads in the high-dielectric constant GaAs material, and the series inductance of the chip which is almost 500 μm long, both have considerable detrimental effects on the performance of the diode. Aside from the radiation described earlier, these parasitic elements are lossless and do not affect the optimum matched responsivity of the detector, but they do limit the bandwidth achievable by any matching network. Although the individual channels of the frequency processor are only 300 MHz wide, the automated placement of the detectors is bound to have small positioning errors that could completely de-tune a narrow-band matching network at this high center-frequency. For this reason, a 50 Ω matching network

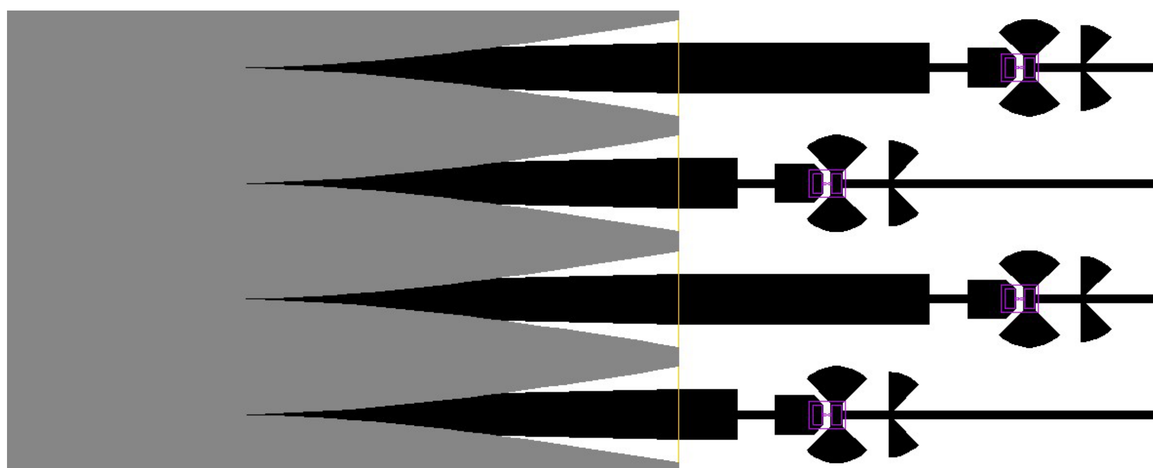

Fig. 1.6. Metallization pattern for transition from stripline to microstrip and diode impedance transformers. Gray area represents top metal, and black represents the center metal. The top dielectric extends from the stripline section on the left over to the orange line. To the right of the orange line is pure microstrip.

was not used, but instead a simpler impedance transformer designed to enhance broadband responsivity without necessarily achieving good return loss was used. The poor return loss expected from the detectors may have implications for the performance of the Rotman-Lens architecture.

A detail of the detector impedance transformers is shown in Figure 1.6, beginning with the transition from stripline on the left. The flip-chip is mounted across a gap in the center conductor. To the right of this gap are a pair of radial stubs which provide a ground return for the millimeter-wave signal. A DC output line extends to the right, and an additional pair of stubs provides another level of filtering to prevent the high-frequency signal from leaking onto the DC line. To the left of the gap are two quarter-wave transforming sections and a length of 50 Ω line leading back to the stripline-microstrip transition. Adjacent transformers are staggered to prevent the fringing fields on the ends of the radial stubs from coupling across from one channel to the next. The dimensions of the transformer sections vary continuously across all 128 channels of the frequency processor to keep the nominal peak of the responsivity curve at the appropriate frequency for each channel. The 3 dB bandwidth of responsivity in each channel is roughly 10 GHz wide which allows plenty of room for slight misalignment of the diode on the board.

The PMC2 is still under construction at TREX Enterprises, but it is hoped that testing of a complete camera will commence within the next year. While the system designers made the best decisions

they could given the constraints of this very ambitious project, the author will always think of it as an example of how difficult things can be when monolithic integration is not used in millimeter-wave systems.

In addition to TREX, other companies are developing millimeter-wave imagers as well. One called Millivision contracted with Caltech to develop a low-cost, low-noise amplifier for their system. Their specifications were somewhat unique in that the chip was required to simultaneously amplify the noisy receive band around 94 GHz as well as a large-signal sub-harmonic pump at 47 GHz. Rather than try to design an awkward "dual-band" amplifier to meet these specs, it was decided to simply make a flat octave-bandwidth circuit that would be more generally useful in other projects. This chip will be described in more detail in Section 4.1.

1.4 Radio Telescope Arrays

It is well known that the sensitivity of any receiver is related to the signal-to-noise power ratio. Even in a radiometer, where the signal is itself noisy in nature, a distinction must be made between the incoming signal noise and the noise generated internally by the system. Although there is still much progress to be made in the area of low-noise electronics, the most sensitive receivers today utilize cryogenically cooled amplifiers which are fast approaching the quantum limit of noise-performance. Indeed, a colleague at Caltech and formerly a student at Chalmers University in Sweden recently demonstrated a 4-8 GHz hybrid amplifier with a mere 3 Kelvin equivalent noise temperature [7]. With so little room left for improvement in the receiver noise, we must find ways to increase the signal power that enters the system. Generally, this means increasing the collecting area of the antenna.

A great deal of effort has been invested in building larger and larger dishes for radio telescopes, culminating in the Arecibo Observatory in Puerto Rico. Almost 305 m in diameter, this ranks as the largest single-dish radio telescope in the world [8]. It also illustrates why dishes are not built any larger. The impracticality of supporting and maneuvering such a large structure led to the fixed-dish design in which the antenna feed is suspended above the reflector and moved around to steer the beam. While it allowed

such a large aperture telescope to be built, it meant using a less-efficient spherical (rather than parabolic) reflector, reducing the *effective* collecting area to a small fraction of the apparent dish size. This approach also severely limits the range of sky to which the telescope can be pointed. For more versatile radio telescopes, the cost of building and positioning a large dish, while maintaining the necessary shape and surface quality in the presence of wind and gravitational stresses, increases almost as the cube of the diameter. A case of diminishing returns is encountered, and building ever-larger antennas is no longer feasible.

The elegant solution is to combine the power of many smaller dishes acting as one, the icon in this case being the Very Large Array in New Mexico. The VLA consists of 27 antennas, each 25 m in diameter, thus achieving sensitivity equivalent to a single 130 m dish. Furthermore, as an interferometer, it can achieve spatial resolution equivalent to an antenna 36 km across [9]. Clearly, this approach can match performance with the largest single-dish telescopes for significantly less cost, but there are other important advantages that are exclusive to an array architecture. Perhaps the most obvious are redundancy and graceful degradation. Expensive radio telescopes operate almost continuously, and time is extremely valuable, so the need to periodically go offline for repairs is a serious problem. With an array environment, repairs could be made to a small number of the antennas without having to cease operation of the telescope and with minimal impact on its performance. Even routine maintenance could be done on a rotating schedule while the telescope is in use, and it is not unreasonable to expect that the instrument may never need to stop working during its useful lifetime. Such a telescope would also have the potential to grow with time as it is upgraded by adding more dishes when they are needed. Additionally, as receiver technology improves, new electronics could be installed on each dish in turn during their routine maintenance cycle, again without ever having to take the telescope offline.

Another advantage to the array architecture is the ability to form sub-arrays by taking only as many dishes as are needed for a given experiment, and leaving the others for use on different projects. By allowing each of the antennas in the array to steer independently, multiple experiments using completely different areas of the sky can be performed simultaneously. However, forming multiple beams does not even require that one divide up the array. Raw data from each element can be recorded, or temporarily

buffered, and then used to construct *virtual beams* in any direction included within the radiation pattern of a single element. In this fashion, multiple beams can be steered electronically and simultaneously, each using the full resources and sensitivity of the array. This process, referred to in some circles as "Virtual Astronomy," would even allow users to "go back in time" to investigate transient phenomena like pulsar glitches, supernovae, and gamma-ray bursts with the full power of the array brought to bear.

It is important to realize that success of the array concept depends on the ability to replicate the electronics in very large quantities at minimal cost. For this reason, MMICs are a critical enabling technology for arrays. After all, the smaller each individual dish element is, the more of them will be required to fill in a desired collecting area. A tradeoff must be made between the cost of larger individual dishes and the cost of larger quantities of the electronics. Rigorous cost estimates are underway to determine the optimum dish size for a given array collecting area. Were it not for the ability of MMIC chips to be turned out in mass quantity on whole wafers, the optimum dish size would probably not be much smaller than the largest telescopes already are, and instruments with large collecting area would be much more expensive.

There are several microwave and millimeter-wave telescope arrays that are currently being designed. The Atacama Large Millimeter Array (ALMA) is a large international effort to build a millimeter-wave radio telescope array of 64 12-meter antennas in the Atacama desert of Chile [10]. The United States effort on this project is being overseen by the National Radio Astronomy Observatory. Some of the work covered in this thesis was performed in support of that program, specifically in the challenging area of millimeter-wave local oscillator generation. A number of broadband power amplifiers, mixers, and frequency multipliers have been designed towards that end, and will be discussed in more detail in later sections.

Another interesting project is the Allen Telescope Array (ATA) under development by the SETI Institute. Currently SETI performs its Search for Extraterrestrial Intelligence by renting time from other facilities such as the VLA and Arecibo observatories. The observing time they have available on these instruments is quite limited. The ATA, on the other hand, could be dedicated full-time to the search, and, by taking advantage of some of the unique array capabilities discussed above, could study many areas of

the sky simultaneously. When a candidate signal is detected, the full array could be steered (either mechanically or electronically) toward the signal's point of origin, perhaps even *retroactively* using buffered raw data from the antenna elements as described earlier. The current array specifications call for about 350 6 m antennas, manufactured cheaply by the makers of commercial satellite dishes, for a net collecting area exceeding that of a 100 m telescope. One of the more interesting challenges for this array is bandwidth. Since the program does not know exactly what frequency they are looking for, they want to observe the widest possible instantaneous bandwidth they can within a range that makes the most sense for communication (current specification is for 0.5 GHz to 11 GHz). This has motivated the development of extremely wideband antenna feed structures and cryogenic low-noise amplifiers [11].

One of the more ambitious projects being discussed today is the Square Kilometer Array (SKA). It is in the planning stages by an international consortium aiming to build an instrument that covers 0.15 GHz to 20 GHz with a square kilometer of collecting area. Such an instrument would revolutionize the field of radio astronomy in many ways. The exact nature, size, and number of the antenna elements have not yet been determined, but a number of feasible approaches have been proposed and are being studied [12].

1.5 Deep Space Communications

Until the ATA receives the first historic transmissions for which it was built, the distinction of being the longest communication link in human experience belongs to the Deep Space Network, a series of large radio telescopes used by NASA to communicate with its remote spacecraft. Currently, the DSN consists of three complexes located at approximately 120° intervals around the globe: one at Goldstone, California, in the Mojave Desert, another near Madrid, Spain, and the last near Canberra, Australia. Each complex houses a number of independent dishes (not arrays) with diameters of 11, 26, 34, and 70 m [13]. While these huge parabolic dishes make the DSN the largest and most sensitive telecommunication system in the world, it is still one of the most severe limitations on the exploration of the solar system today. Our

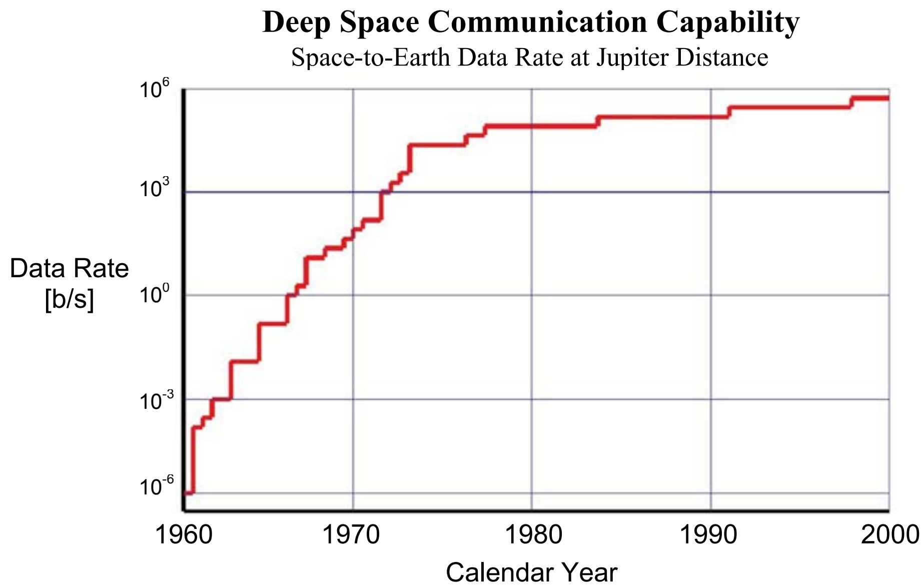

Fig. 1.7. Deep space communications capability since the creation of the Deep Space Network.

best scientific instruments are capable of collecting an enormous amount of useful data, but due to the communication bottleneck, only about 1-3% of it is transmitted back to Earth. Figure 1.7 shows the deep-space communication capability since the DSN was first brought online in the 1960's. Various upgrades have been made through the years for incremental improvements, but the growth of the DSN has leveled off as we approach the limit of what can be achieved with a 70 m dish. At the same time, the demands placed on the DSN have grown at an ever-increasing rate. A significant upgrade of the DSN is desperately needed, but as explained above the cost and technical difficulty of building large dishes prohibits anything other than an incremental improvement. JPL is currently studying arrays as an alternative. The development would begin with an array of roughly equivalent collecting area to that of the existing 70 m dishes, and additional dishes could be added later for perhaps as much as a factor of 100-500 improvement over current capability. This would represent a step forward that is totally infeasible with a single-dish design [14, 15]. The importance of upgrading the DSN sensitivity cannot be overstated. Not only would this enable higher data-rate missions, but it could also be used to reduce the mass and power requirements for spacecraft which currently are required to carry relatively large dishes and powerful transmitters of their own into deep space. The investment in sensitivity on the ground would save money on virtually every space mission for decades to come.

As with the astronomical radio telescopes, there are more significant advantages to arrays in the DSN than just pure, low-cost collecting area. By eliminating single-point failures, allowing for regular maintenance without halting operations, and forming sub-arrays with "just enough" power to communicate with several spacecraft in totally different directions , the array achieves a new standard of reliability and availability. Also, the flexibility afforded by virtual beam-forming would in itself enhance data throughput by using multiple beams for simultaneous communication with a number of spacecraft in orbit around a planet, each harnessing the full potential of the array, and even if all of them are using the same frequency [14].

Another feature of arrays that can be used to great advantage is the order of magnitude sharper beamwidth compared to a single dish of equivalent collecting area. This is simply a result of the nominal spacing of antenna elements and could be further sharpened by the addition of a few elements at large distances from the main cluster. It would be extremely useful in navigation as a means of determining the position of a spacecraft accurately [14]. It undoubtedly could have alerted NASA to the error that occurred on the Mars Climate Orbiter spacecraft that eventually caused it to burn up in the Martian atmosphere in 1999. Had they been using a DSN array at that time, they would have noticed that the spacecraft was off-course, and it is very likely that corrections could have been sent in time to save the mission. It has also been proposed that a DSN array could be made to transmit multiple narrow beams with slightly different frequencies to aid a spacecraft in distress in determining its own position without instruction from the ground.

Finally, the surface accuracy of small stamped aluminum antennas allows them to operate at higher frequencies more readily than very large dish structures. This opens the door for very wide bandwidth communication at frequencies as high as 100 GHz [14]. It would enhance the DSN's capability as both a scientific instrument and a communications array.

A block diagram for the Ka-band receiver in a DSN Array is shown in Figure 1.8. The author has developed many of the chips and modules that will be used in this receiver, and these components will be discussed in more detail in Sections 3.4, 4.2, 4.3, 6.1, 6.2, 7.7, and 7.10.

A comparison of the radio telescope facilities discussed so far is shown in Table 1.1. A useful

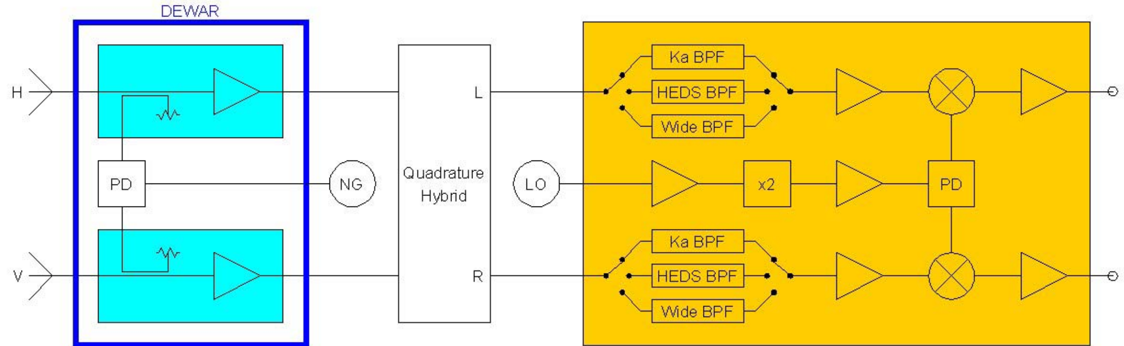

Fig. 1.8. Simplified block diagram of the DSN Array Ka-band receiver. The cryogenic front end (cyan) is discussed in Section 7.7, and the dual-polarization downconverter (orange) is discussed in Section 7.10.

Table 1.1. Comparison of Existing Large Antennas and Future Arrays [14]

Antenna	Elements	Effective Area	Upper Freq.	T_{sys}	A/T_{sys}	Year Finished
DSN 70m	1 x 70m	2,607 m^2	8 GHz	18 K	145 m^2/K	1965
GBT	1 x 100m	5,700 m^2	100 GHz	20 K	285 m^2/K	2000
VLA	27 x 25m	8,978 m^2	43 GHz	32 K	280 m^2/K	1982
Arecibo	1 x 305m	23,750 m^2	8 GHz	25 K	950 m^2/K	1970
ALMA	*64 x 12m*	*4,608 m^2*	*800 GHz*	*50 K*	*92 m^2/K*	*2011*
ATA	*350 x 6m*	*6,703 m^2*	*11 GHz*	*35 K*	*192 m^2/K*	*2005*
DSN Prototype	*100 x 12m*	*7,200 m^2*	*38 GHz*	*20 K @ 8 GHz* *40 K @ 32 GHz*	*360 m^2/K* *180 m^2/K*	*2007*
DSN Goal	*3600 x 12m*	*259,200 m^2*	*38 GHz*	*18 K @ 8 GHz* *36 K @ 32 GHz*	*14,400 m^2/K* *7,200 m^2/K*	*2012*
SKA	*4550 x 12m*	*327,600 m^2*	*22 GHz*	*18 K*	*20,000 m^2/K*	*2016*

future telescopes shown in italics with projected performance values

figure of merit for large radio telescopes is the ratio of collecting area to system equivalent noise temperature, shown in column six.

1.6. Overview of Thesis Work

Because of the large scope of this thesis, it is worthwhile to provide an overview of the work as a whole before discussing the various chip designs and technical innovations in the remaining chapters. My research has included designing some 36 new millimeter-wave MMIC chips, which perform almost every

imaginable function including amplification, attenuation, mixing, multiplication, and switching, as well as innumerable passive structures of both classical and innovative design to perform attenuation, coupling, filtering, power dividing, and transitioning between various cables, transmission lines, and waveguides. These and other chips were then integrated into complex multi-chip modules to form radiometers, communication receivers, signal sources, cryogenic gain blocks, passive imagers, and spectrometers. Tables 1.2 and 1.3 list the most significant of these elements, and indicate where in this thesis a more detailed discussion of each can be found.

Further information is available in the 11 papers that have been published in connection with the work in this thesis:

M. Morgan and S. Weinreb, "A W-band monolithic medium power amplifier," *IEEE MTT-S Intl. Microwave Symp.*, Philadelphia, PA, 2003.

M. Morgan and S. Weinreb, "Octave-bandwidth high-directivity microstrip codirectional couplers," *IEEE MTT-S Intl. Microwave Symp.*, Philadelphia, PA, 2003.

M. Morgan and S. Weinreb, "A millimeter-wave perpendicular coax-to-microstrip transition," *IEEE MTT-S Intl Microwave Symp. Digest*, pp. 817-820, Seattle, WA, 2002.

M. Morgan, S. Weinreb, N. Wadefalk, and L. Samoska, "A MMIC-based 75-110 GHz signal source," *IEEE MTT-S Intl. Microwave Symp. Digest*, pp. 1859-1862, Seattle, WA, 2002.

K. Lin, H. Wang, M. Morgan, T. Gaier, and S. Weinreb, "A W-band GCPW MMIC diode tripler," *32nd European Microwave Conference*, Milan, 2002.

J. Schulman, S. Thomas, D. Chow, E. Croke, H. Dunlap, K. Holabird, W. Clark, and M. Morgan, "High-frequency performance of Sb-heterostructure millimeter-wave diodes," *14th InP and Related Materials Conf.*, pp. 151-154, Stockholm, 2002.

J. Schulman, J. Zinck, S. Skeith, S. Thomas, D. Chow, E. Croke, H. Dunlap, K. Holabird, M. Morgan, and S. Weinreb, "Physics of Sb-heterostructure quantum tunneling millimeter-wave diodes," *44th Electron Materials Conf.*, Santa Barbara, CA, 2002.

V. Radisic, M. Micovic, M. Hu, P. Janke, C. Ngo, L. Nguyen, L. Samoska, and M. Morgan, "164-GHz MMIC HEMT doubler," *IEEE Microwave and Wireless Components Letters*, vol. 11, pp. 241-243, June 2001.

E. Croke, J. Schulman, D. Chow, H. Dunlap, K. Holabird, M. Morgan, and S. Weinreb, "New tunnel diode for zero-bias direct detection for millimeter-wave imagers," *SPIE Intl. Symp. on Aerospace/Defense Sensing, Simulation, and Controls*, Orlando, FL, 2001.

M. Morgan and S. Weinreb, "A full waveguide band MMIC tripler for 75-110 GHz," *IEEE MTT-S Intl. Microwave Symp. Digest*, pp. 103-106, Phoenix, AZ, 2001.

M. Morgan and S. Weinreb, "A monolithic HEMT diode balanced mixer for 100-140 GHz," *IEEE MTT-S Intl. Microwave Symp. Digest*, pp. 99-102, Phoenix, AZ, 2001.

Table 1.2. Overview of MMIC Developments

MMIC	Description	Frequency*	Devices	Foundry	Thesis Section
43TRP1	tripler	36-50 GHz	GaAs Schottky Diode	UMS	2.2
81TRP1	tripler	70-92 GHz	GaAs Schottky Diode	UMS	2.2
93TRP1	tripler	75-110 GHz	GaAs Schottky Diode	UMS	2.1
110TRP1	tripler	90-124GHz	GaAs Schottky Diode	UMS	2.2
33MIX1	balanced mixer	26-40 GHz	GaAs Schottky Diode	UMS	3.1
38MIX1	2nd-harmonic I/Q mixer	31-38 GHz	GaAs Schottky Diode	UMS	3.4
45MIX1	balanced mixer	40-50 GHz	GaAs Schottky Diode	UMS	3.1
53MIX1	balanced I/Q mixer	49-57 GHz	GaAs Schottky Diode	UMS	3.3
81MIX1	doubly balanced mixer	70-92 GHz	GaAs Schottky Diode	UMS	3.5
94MIX1	balanced mixer	75-110 GHz	GaAs Schottky Diode	UMS	3.1
120MIX2	balanced mixer	100-140 GHz	0.1 μm InP pHEMT	TRW	3.1
120MIX3	balanced mixer	100-140 GHz	0.1 μm InP pHEMT	TRW	3.1
132MIX1	doubly balanced mixer	120-144 GHz	GaAs Schottky Diode	UMS	3.5
200MIX1	2nd-harmonic mixer	170-210 GHz	GaAs Schottky Diode	UMS	3.2
35LN2	low-noise amplifier	30-40 GHz	0.1 μm InP pHEMT	TRW	4.3
38LN1B	low-noise amplifier	26-40 GHz	0.15 μm MHEMT	Raytheon	4.2
40LN2B	low-noise amplifier	33-50 GHz	0.15 μm MHEMT	Raytheon	4.2
86LN4B	low-noise amplifier	75-95 GHz	0.15 μm MHEMT	Raytheon	4.1
MV70B	low-noise amplifier	47-96 GHz	0.15 μm MHEMT	Raytheon	4.1
APH417	power amplifier	70-95 GHz	0.1 μm GaAs pHEMT	TRW	5.1
86PA1	power amplifier	77-95 GHz	0.1 μm InP pHEMT	HRL	5.2
98PA1	power amplifier	87-108 GHz	0.1 μm InP pHEMT	HRL	5.2
110PA1	power amplifier	100-120 GHz	0.1 μm InP pHEMT	HRL	5.2
34ATT10	switched attenuator	30-40 GHz	GaAs Schottky Diode	UMS	6.1
34ATT20	switched attenuator	30-40 GHz	GaAs Schottky Diode	UMS	6.1
34SW1	SP3T switch	30-40 GHz	GaAs Schottky Diode	UMS	6.2

Table 1.3. Overview of Multi-Chip Module Developments

Module	Description	Frequency*	Chip Count [active / total]	Thesis Section
KABLOCK1	cryogenic LNA package	26-40 GHz	1 / 3	7.6
EVLA45PA1	filtered post-amplifier	40-50 GHz	1 / 4	7.8
KAFE1	cryogenic front end	30-40 GHz	2 / 5	7.7
WSRC1	20 mW signal-source	75-110 GHz	6 / 12	7.5
EVLA33DC1	down-converter	26-40 GHz	7 / 17	7.9
DSN38A	dual-polarization down-converter	30-40 GHz	15 / 47	7.10

* *output frequency for multipliers, RF frequency for mixers and down-converters*

2 Broadband Frequency Multipliers

Virtually all high-frequency electronic systems, even the so-called "passive" ones, require some sort of locally generated signal to operate. In the millimeter-wave band, these local oscillators are rarely ever generated directly. Instead, a lower frequency source is cascaded with one or more frequency multipliers and amplifiers. This takes advantage of the superior oscillator technology that exists at lower frequencies. This chapter describes recent developments in MMIC multiplier design, particularly for applications in which a relatively wide output bandwidth is required.

2.1. A Full Waveguide-Band MMIC Tripler for 75-110 GHz

Signal sources in W-band, and thus the necessary multipliers, are of interest for various applications including atmospheric remote sensing, automotive radar systems, and test instrumentation. Many types of multipliers can be used. Both doublers [19, 20] and triplers [21-26] have been reported. Some designers favor transistor multipliers [25, 26], citing improved conversion loss. However, diode multipliers are more common in the millimeter-wave range, owing to improved frequency response and stability. Unfortunately, most of the reported circuits do not cover the full waveguide bandwidth. Two notable exceptions are the commercially available components produced by Millitech [21] and Pacific Millimeter Products [22]. These waveguide circuits deliver on the order of 1 mW across W-band with 2% conversion efficiency. However, MMICs are often preferable to waveguide circuits due to their compactness, repeatable performance, and low-cost fabrication in large quantities. This section describes the design and evaluation of a wideband MMIC tripler using planar Schottky diode technology.

The tripler was designed around an anti-parallel diode pair. This configuration is useful for producing the third harmonic of the drive frequency while suppressing the even harmonics [23].

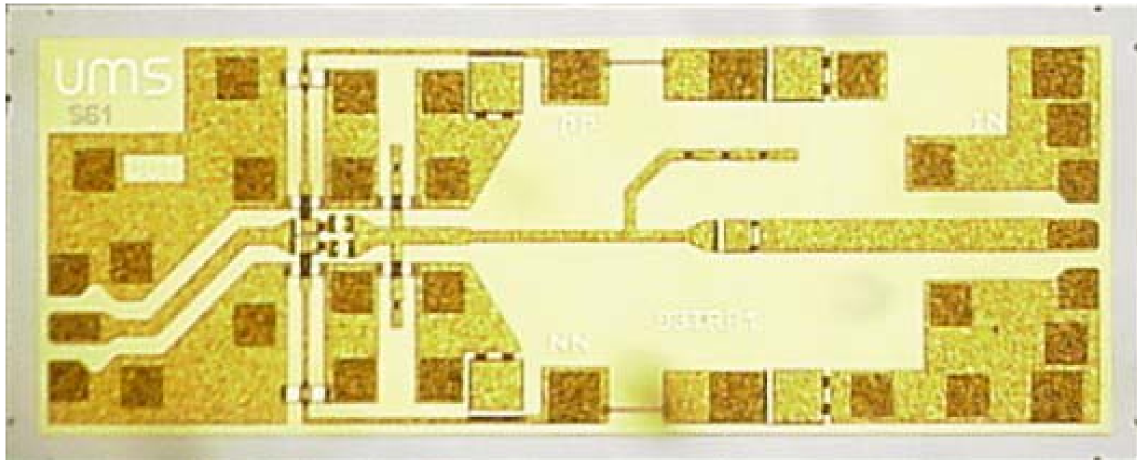

Fig. 2.1. Photograph of the MMIC tripler. Chip dimensions are 2.0 x 0.74 mm. GaAs substrate is 100 μm thick.

Suppression of the fourth harmonic is of particular importance in this design because at some frequencies it will fall within the designed output band. For example, an input signal at 26 GHz will lead to the desired output at 78 GHz, as well as an undesired tone at 104 GHz. This spurious component cannot be rejected by filtering because that would also attenuate the desired signal for inputs at the high end of the band.

A photograph of the chip appears in Figure 2.1, and a schematic is shown in Figure 2.2. The microstrip network on the input port (right side) is designed to provide a conjugate match from 25-37 GHz. The tuning stub incorporates a series of air bridges along its length. This was done in order to allow minor adjustments to be made after fabrication. By selectively breaking one of these air bridges with a needle probe, the length of the stub can be shortened. After the matching network is a pair of open-circuited stubs designed to present an approximate short-circuit at the diodes from 75-110 GHz. This provides frequency isolation as well as a ground return for the output.

The bias line for both diodes is on the output side. Bypass capacitors are located at the appropriate positions on this line to match the diodes to the output port in W-band, while providing a ground return for the input frequency. Thin-film resistors were included in the bias path to protect the sensitive diodes from static damage. The output transmission line network consists entirely of grounded coplanar waveguide. Via holes were placed at quarter-wavelength intervals in the topside ground planes to suppress parallel plate modes.

The circuit design described above was entered into HP's Advanced Design System (ADS).

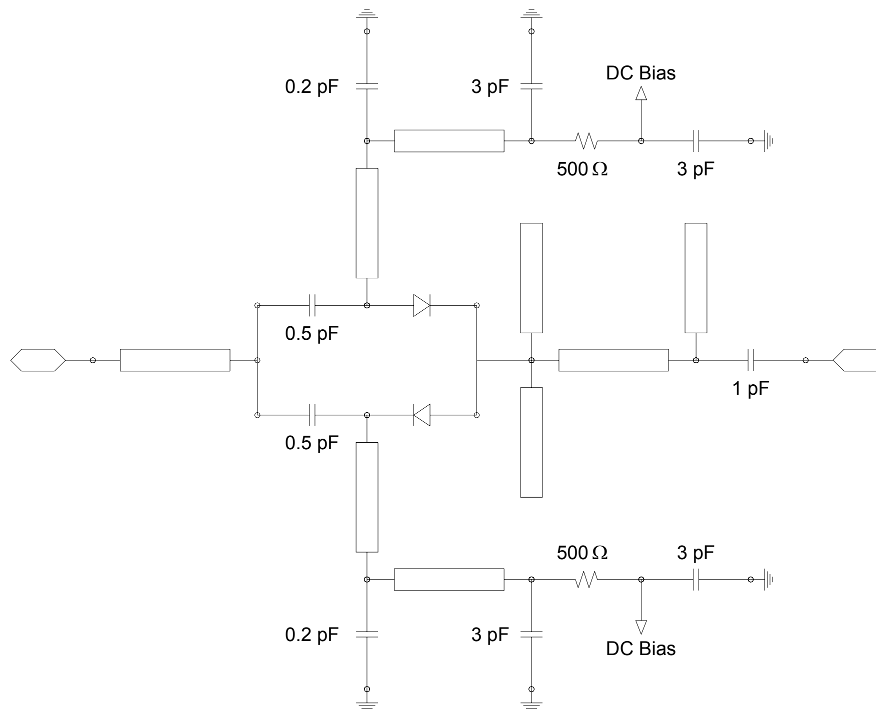

Fig. 2.2. Schematic of the tripler, showing MIM capacitors, thin-film resistors, and transmission-line sections.

Using the optimization routines provided with this software, the passive network parameters, such as transmission line lengths and impedances, were allowed to vary within a 10% range of their original values. A gradient search algorithm was used to explore this parameter space and to design a tripler with output power variation of ±1 dB over the frequency range from 75-110 GHz.

The chips were fabricated by United Monolithic Semiconductor (UMS) using their BES Schottky Diode MMIC process. Anode dimensions of 1 x 3 μm were selected for high-frequency performance. This diode exhibits low junction capacitance of approximately 6 fF and series resistance of 7 Ω, resulting in a calculated cutoff frequency over 3 THz. The GaAs substrate thickness is 100 μm, and the chip dimensions are 2.0 x 0.74 mm.

Scalar measurements were performed on several chips. A block diagram of the test setup is shown in Figure 2.3. The input signal was provided by an active frequency doubler (DBS Microwave model DB99-0356) driven by an HP 83620B signal generator. The input signal was coupled into the chip through a GGB Industries coplanar wafer probe. Output power was measured with an HP W-band power

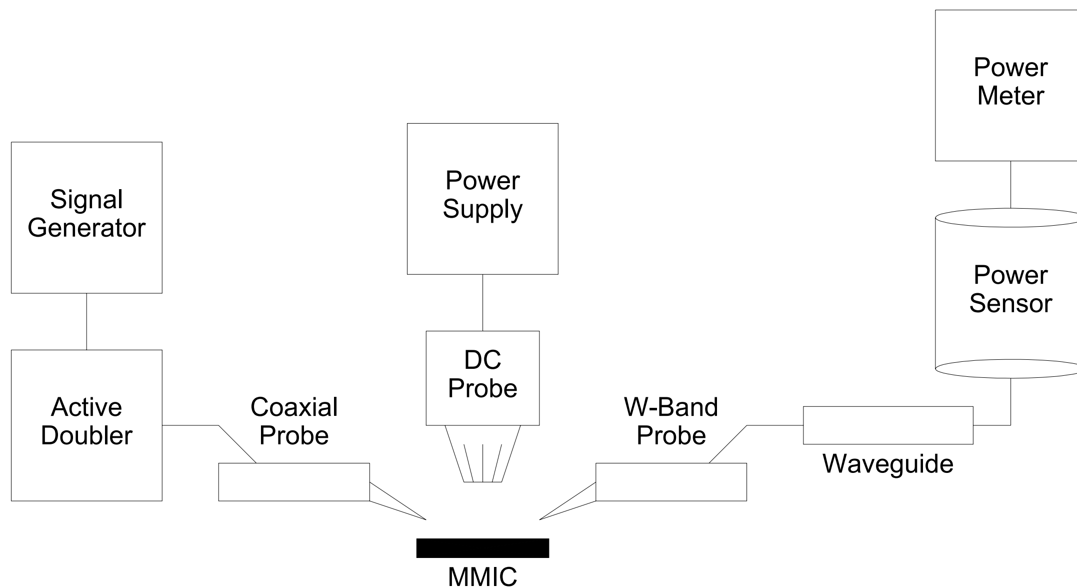

Fig. 2.3. Block diagram of the test setup.

sensor. The losses in the waveguides and probe transitions, typically about 1-1.5 dB, were calibrated out, so the data represents the performance of the chip alone. Bias current was supplied to the chip through needle probes.

Output power versus frequency for various bias conditions and drive levels are shown in Figure 2.4. Between –4 dBm and +2 dBm was measured across the band for high drive level. Figure 2.5 shows the simulated performance along with measurement under the same drive conditions. In general, the chip delivered 1-3 dB less power than predicted. Output power versus input power for several frequency points is plotted in Figure 2.6, showing that the tripler was not saturated during these measurements. This suggests that higher output power is achievable.

An attempt was made to improve the power flatness by trimming the input tuning stub. The middle air bridge on this stub was broken with a needle probe and micro-manipulator. Also, the bias voltage was adjusted to optimize the conversion loss at the worst frequency point, anticipating a sacrifice in output power at other frequencies. The result of this adjustment is plotted in Figure 2.7. For input power of 16 dBm, the chip delivered between –4.6 dBm and –1.3 dBm from 75-110 GHz.

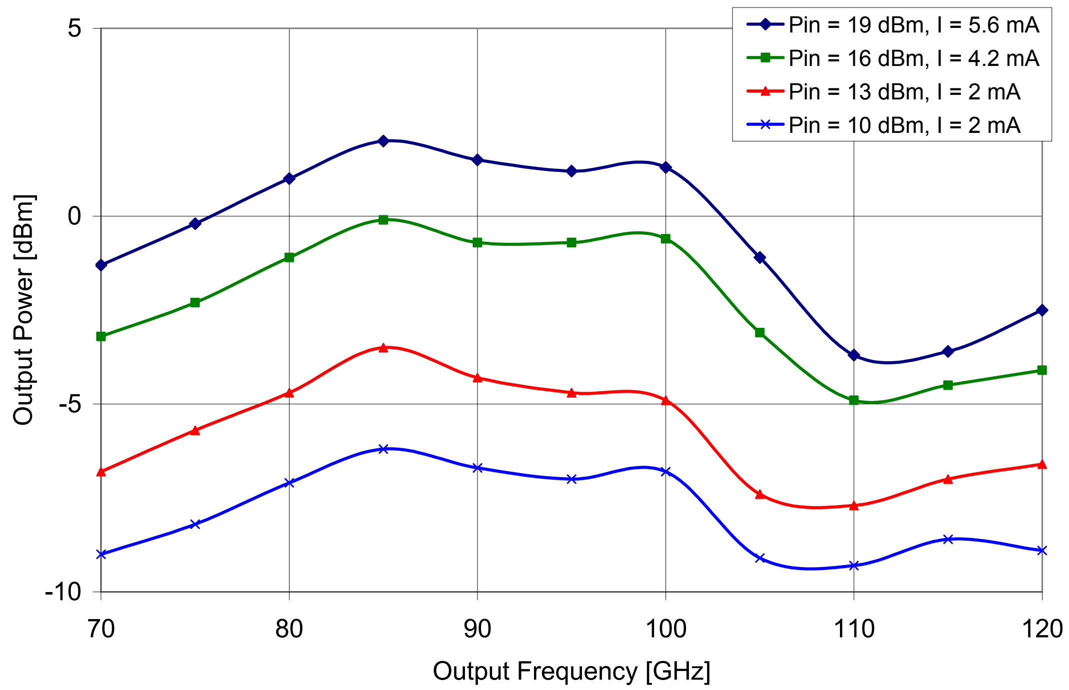

Fig. 2.4. Output power vs. frequency. The chip was biased with the indicated constant current values. Little change was noted with constant voltage bias.

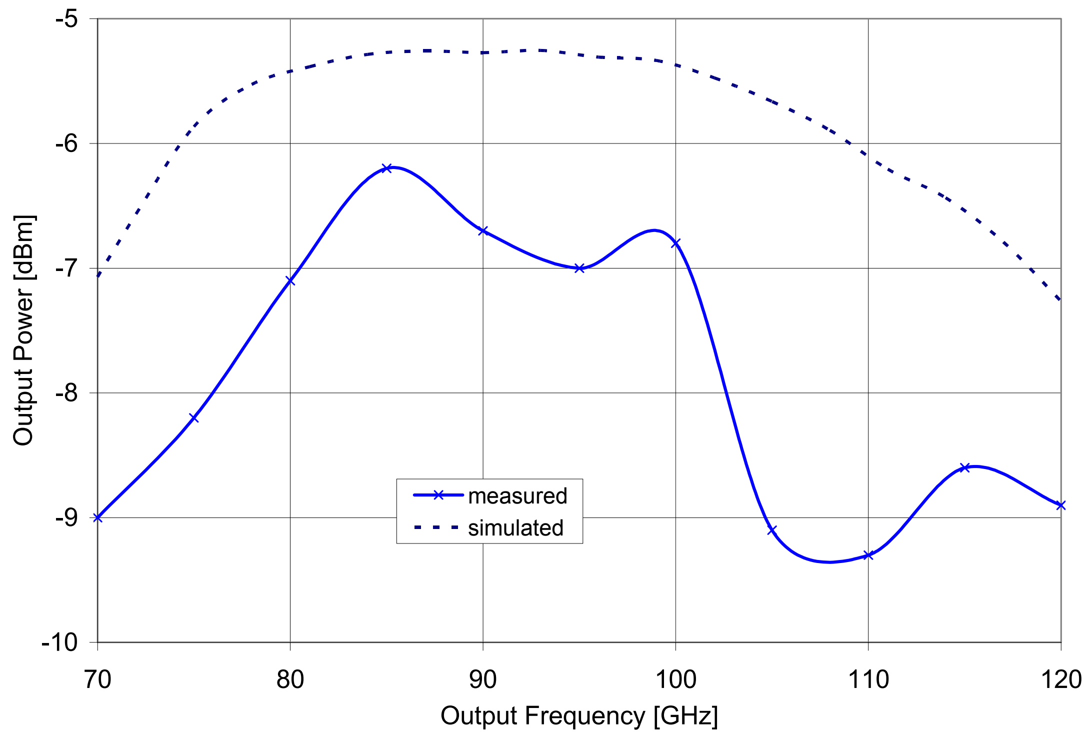

Fig. 2.5. Measured and simulated output power vs. frequency. Input power was 10 dBm, and bias current was held constant at 2 mA.

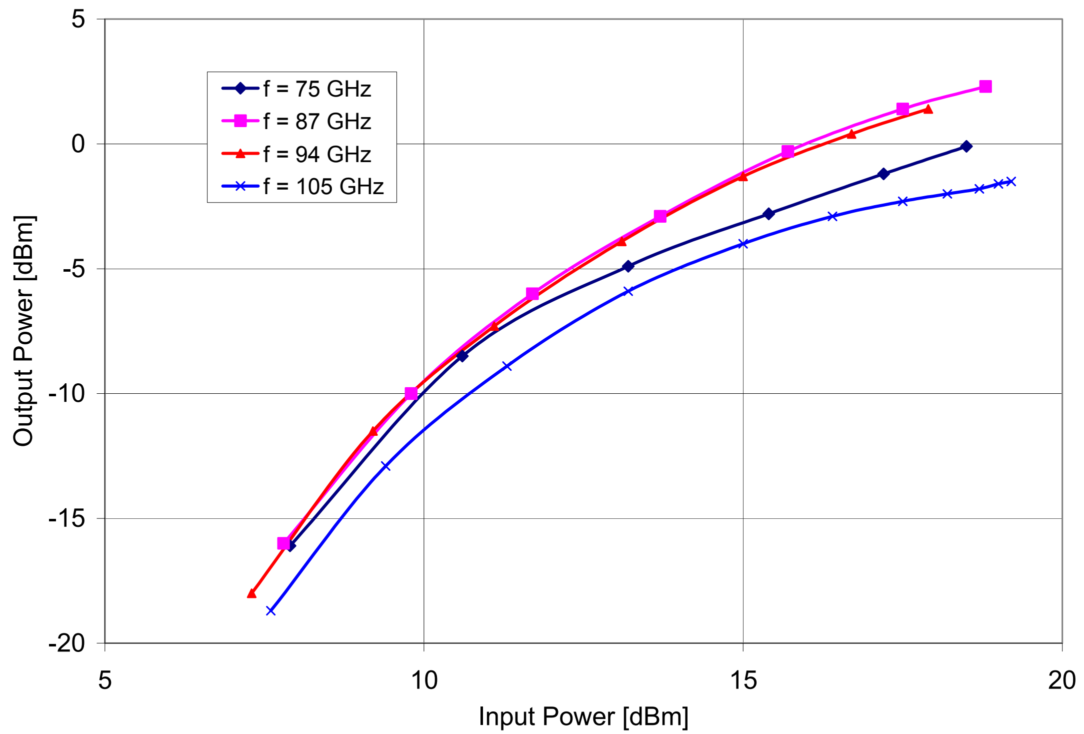

Fig. 2.6. Output power vs. input power. Input power was swept up to the limits of the test setup. The chip was biased with a constant current 4.2 mA.

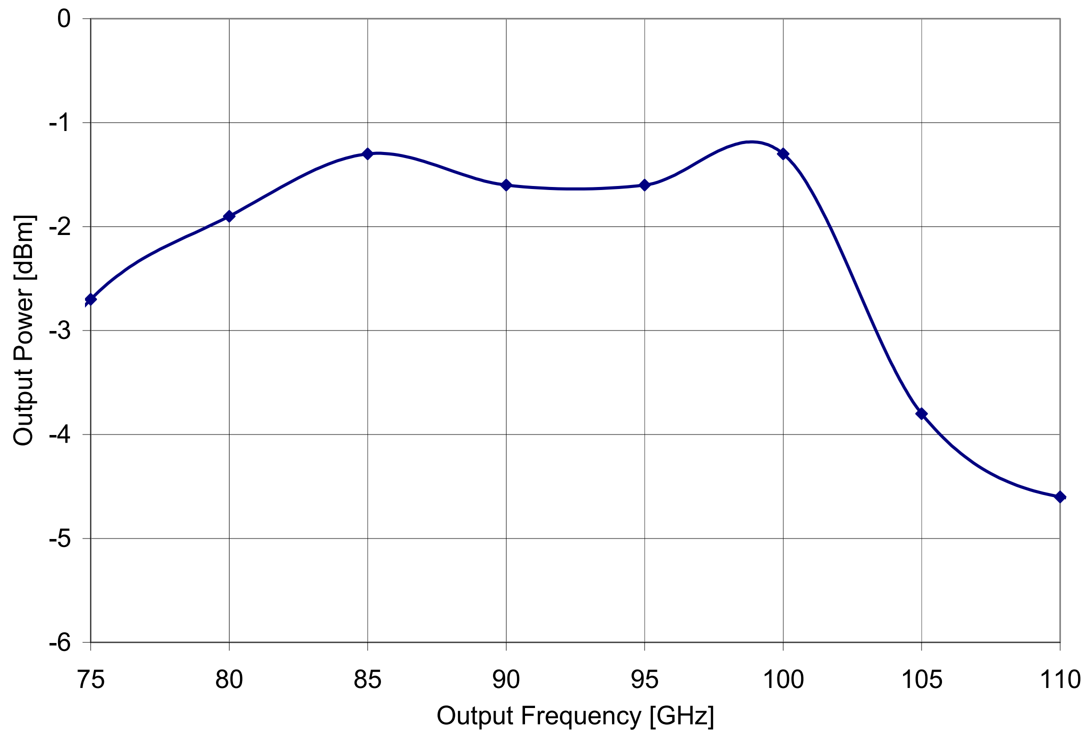

Fig. 2.7. Output power vs. frequency after trimming the input tuning stub and optimizing bias for power flatness. Input power was +16 dBm, and the chip was biased with a constant 3.7 V.

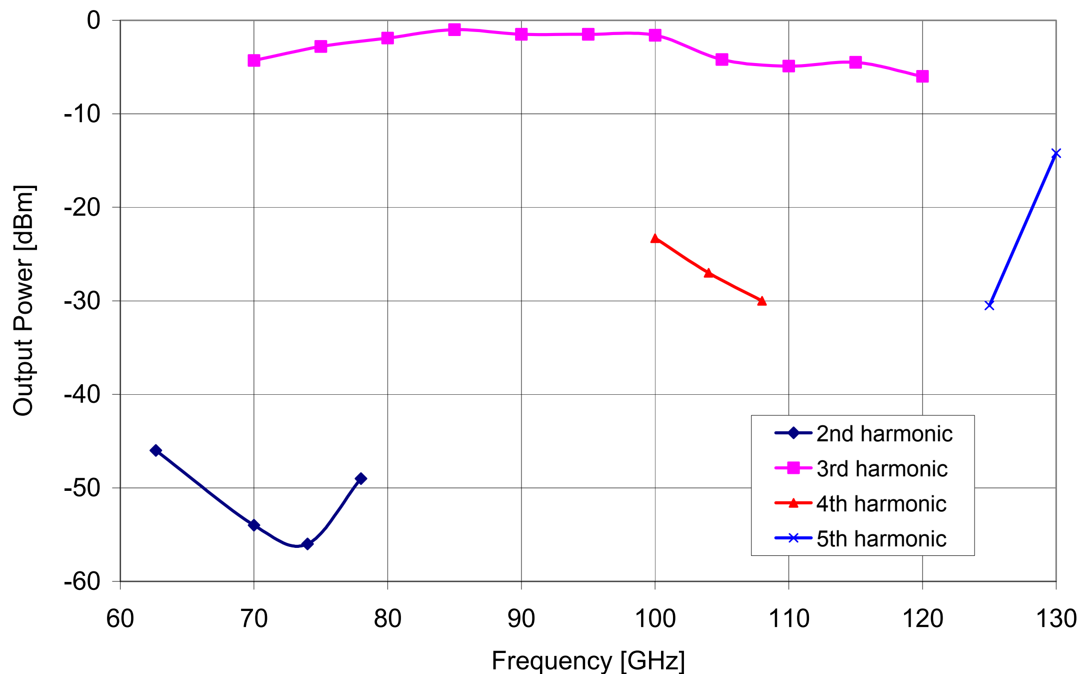

Fig. 2.8. Output power vs. frequency for the second through fifth harmonics. Input power was +16 dBm, and the chip was biased with a constant current of 4.2 mA.

Additional tests were performed to characterize the output power spectrum of the tripler. This data is shown in Figure 2.8. Of critical importance is the fourth harmonic from 100-110 GHz, the range over which both the third and fourth harmonics fall within the designed output band. As the plot shows, the fourth harmonic is more than 20 dB below the desired output. The fifth harmonic is not so well suppressed by the MMIC, measured as high as –14 dBm, but at 130 GHz this tone is far enough out of band to be easily filtered out.

This is believed to be the first MMIC tripler reported to provide relatively flat output power across the entire W-band. It has found many useful applications, including LO signal generation for a millimeter-wave radiometer developed jointly by JPL and Aerojet. A photograph of the module appears in Figure 2.9. The module was developed as part of the IIP program for atmospheric temperature and humidity sensors introduced in Section 1.2. The first two prototype receivers built at JPL, for 100-140 GHz and 170-210 GHz, incorporated RF low-noise amplifiers using the latest InP HEMT technology. There was also a desire for a 240 GHz radiometer array, but it was not believed that a useful LNA could be made with current

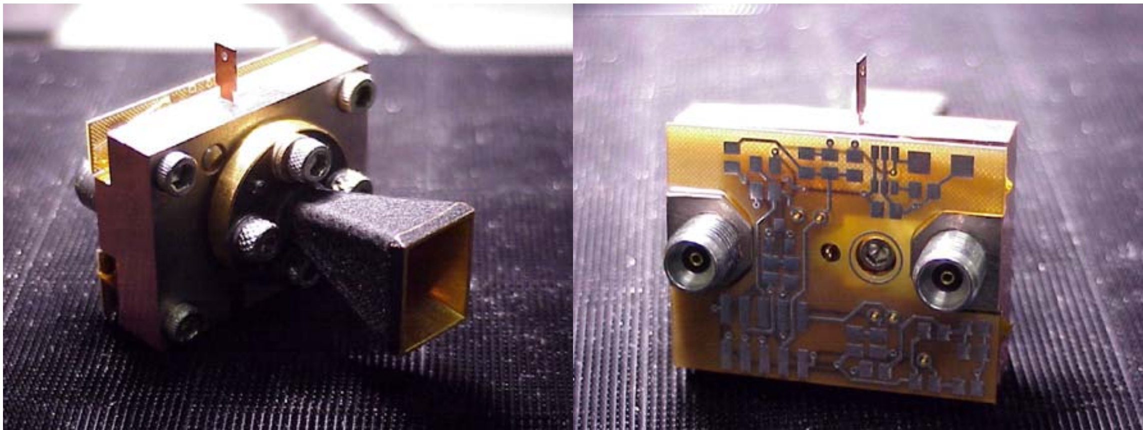

Fig. 2.9. Photograph of the millimeter-wave radiometer developed jointly by JPL and Aerojet.

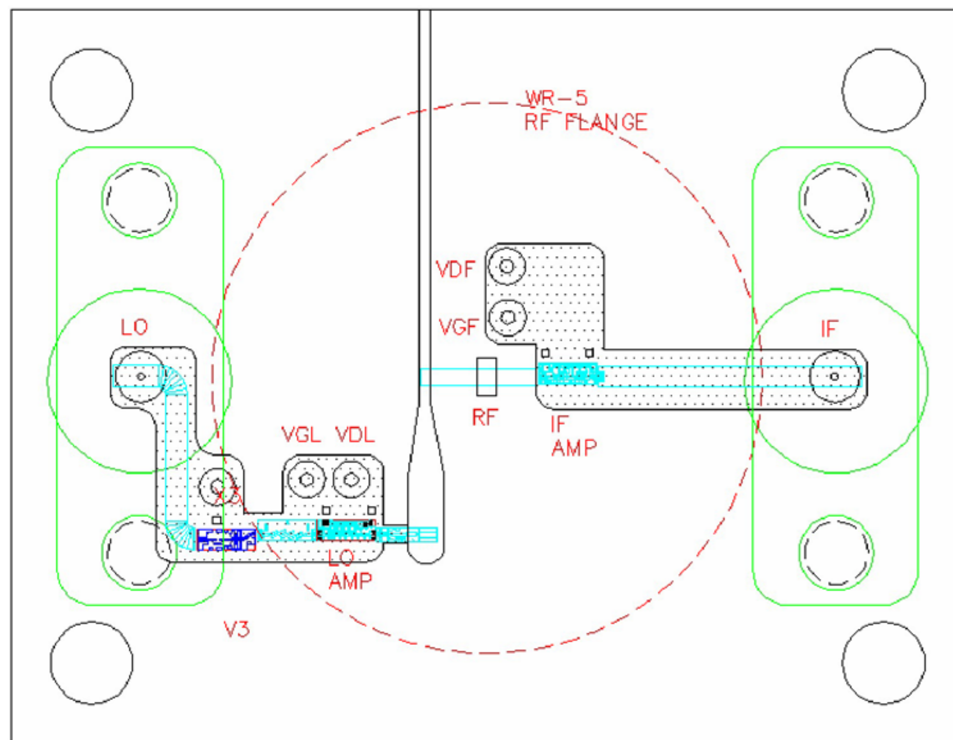

Fig. 2.10. Layout of the 183 GHz JPL/Aerojet radiometer. Module dimension are 2.5 x 3.3 cm.

MMIC technology at that high a frequency. Instead, a new architecture was pursued that uses a highly efficient waveguide mixer as the front end. Aerojet has made some of the best millimeter-wave radiometers in this way, such as the MLS-EOS instrument already in space. As a means of reducing the size of this type of instrument, it was decided to use a MMIC multiplier-amplifier chain to provide the LO

signal for the mixer. This greatly relaxes the LO signal requirements of the sensor and allows a reduction in its mass and cost.

For the 240 GHz radiometer, an LO of 120 GHz would be required to pump Aerojet's second-harmonic mixer. However, it was decided to build a 183 GHz prototype first (Figure 2.9) to prove the integration of MMIC and non-MMIC technology in a single module and compare it with the previously developed all-MMIC module discussed in Section 1.2. The lower frequency band then requires a 91.5 GHz LO. Fortunately, the MMIC tripler described above is capable of driving both frequencies so it was a natural choice for this development effort. A layout of the 183 GHz radiometer is shown in Figure 2.10. The module is driven with a 30.5 GHz local oscillator that enters through the coax on the left and is fed to the frequency tripler. The output of the tripler is filtered, amplified, and launched into a WR-10 waveguide. This simulates the LO source that was used to drive the Aerojet mixer in its original design. The mixer now sits in the center of the block. The RF signal is coupled into the mixer through another waveguide that is perpendicular to the MMIC plane as shown in Figure 2.10. Finally, the IF is amplified with another MMIC chip and exits the block through a second coax connector. DC bias is supplied via glass bead feedthrus that connect to a PC-Board on the opposite side of the metal chassis.

2.2. LO Source Multipliers for ALMA and EVLA

The 75-110 GHz tripler described in the previous section also caught the attention of engineers at the NRAO working on the ALMA project (see Section 1.4). They have need of multipliers like this for the array's LO system and purchased some of the chips to use in their early prototypes. They eventually requested the development of a series of new multipliers to cover a number of different frequency bands from 70 GHz to 150 GHz. Before long, other NRAO engineers working on the EVLA also realized the usefulness of MMIC multipliers for millimeter-wave signal generation and added their own requirements for Ka- and Q-band chips to the list. In order to reduce risk and complete the designs as quickly as

possible, all of these second generation chips were modeled after the proven W-band tripler discussed in the preceding section.

The first new chip that was needed was to provide at least +3 dBm of power from 36-50 GHz with 17-20 dBm input power. The resulting layout is shown in Figure 2.11. Schematically, it is very similar to the W-band MMIC tripler, but size constraints demanded that a different sort of bandpass filter be used. The UMS wafer that these designs would be fabricated on was being shared by three projects: ALMA, the EVLA, and the DSN Array. A very large number of new designs had to be included, and as all three projects were arrays, they needed as many copies as possible. This meant making the very most efficient possible use of space on the wafer. Two standard chip sizes were selected (2000 x 730 μm and 2000 x 1200 μm) so that all the chips would pack neatly into rows and columns for easy dicing. The lower frequency chips like this one became especially cramped and presented some interesting challenges in terms of layout. As is obvious in the figure, much of the input matching network and tuning stubs had to be folded to fit in the allowable space, but one element that could not be folded easily was the usual edge-coupled bandpass filter on the output. Filtering was not explicitly required in the specifications for the chip, but it is still necessary to isolate the diodes from higher-harmonic off-chip loading that in principle cannot be well predicted or controlled. Since these requirements are not too stringent, it was sufficient to use a relatively low-order filter with non-optimal design. A simple two-pole shunt stub, or "comb-line," filter was used, its topology being much easier to fold in a tight space as can clearly be seen in the figure.

Another innovation in this design is the multi-finger diode. The device library available from UMS officially includes only single finger Schottky diodes. They also limit the bias current per finger to 2.5 mA due to long-term degradation from electromigration effects. This became a serious problem in many designs because the large-signal impedance of the diode at that bias level was too high to match over broad bandwidths. Putting several diodes in parallel could solve the problem electrically, but the layout dimensions of several diodes in parallel was large enough to cause distributed phase effects in the higher-frequency chips. Therefore, the author worked with the layout technicians at UMS to develop a three-finger device with compact layout for use in several of our designs.

The passive structures were modeled extensively in the Sonnet 2.5D electromagnetic simulator up

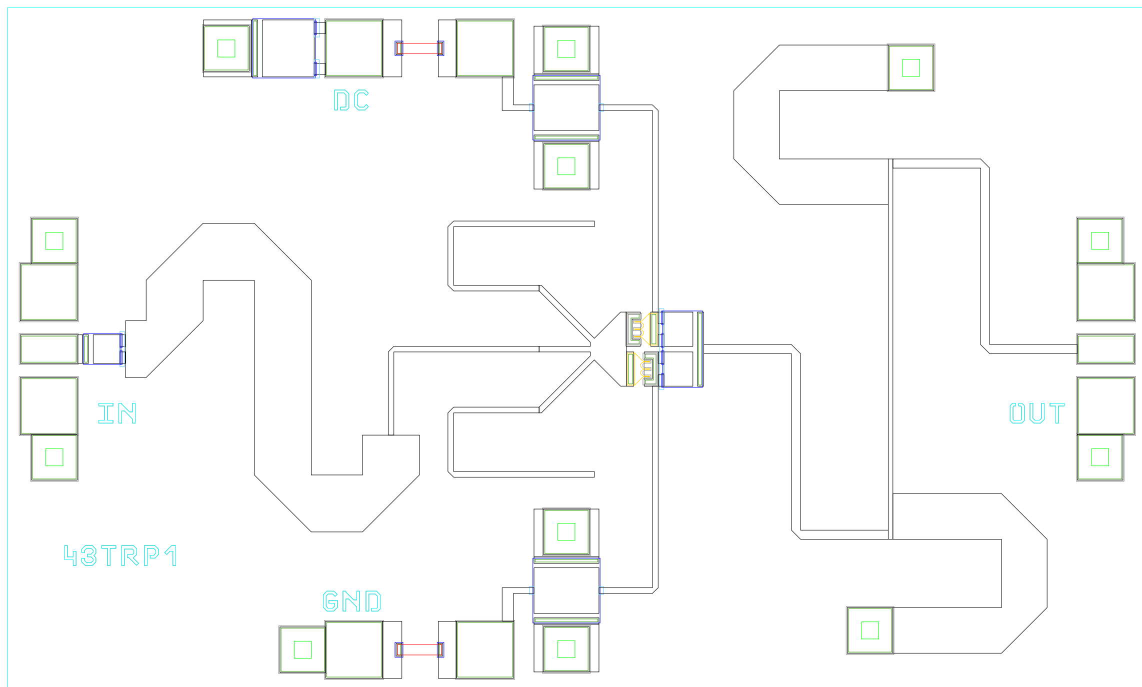

Fig. 2.11. Layout of the 36-50 GHz MMIC tripler. Chip dimensions are 2.0 x 1.2 mm. GaAs substrate is 100 µm thick.

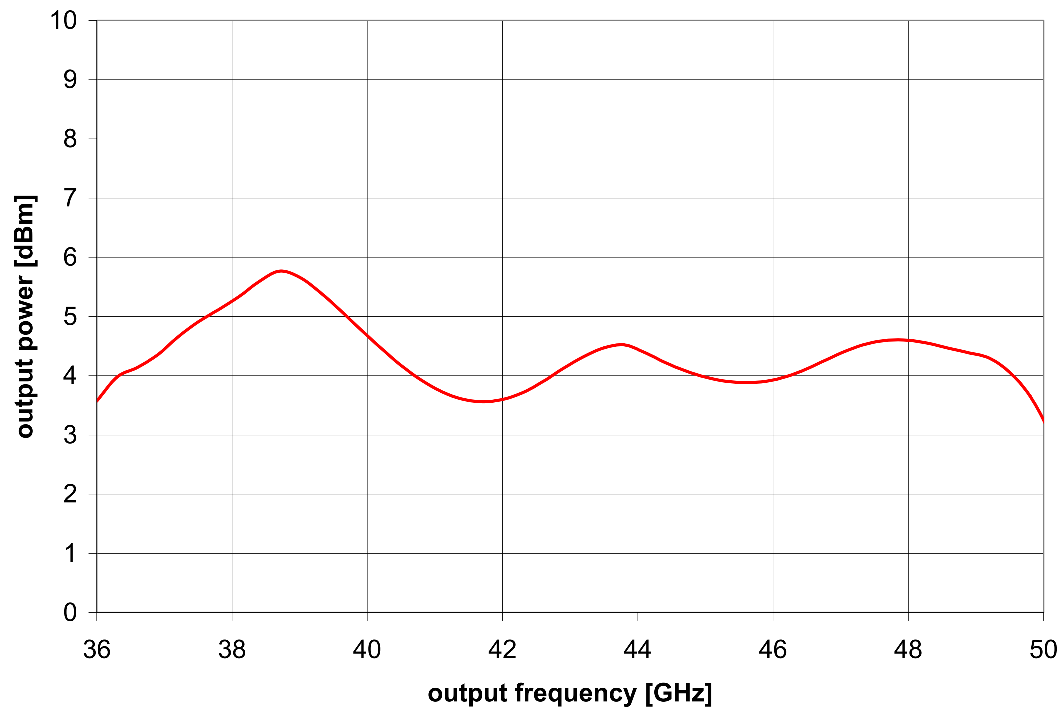

Fig. 2.12. Simulated output power for the 36-50 GHz tripler. DC current is fixed at 7.5 mA, and input power level is +17 dBm.

to the sixth-harmonic of the input band. The results were then imported in to HP's Advanced Design System for Harmonic Balance Analysis. The simulated output power of the tripler is shown in Figure 2.12. Overall, about +4 dBm is predicted with +17 dBm input.

The next tripler that was required had an output frequency range of 70-92 GHz, and similar power specifications. The layout of this design is shown in Figure 2.13. This was high enough in frequency to fit it in the narrower standard chip size (2000 x 730 μm). The traditional edge-coupled bandpass filter was utilized with only moderate folding as illustrated in the layout. Again, the three-finger diodes were incorporated for the same reasons laid out above. The simulated response for this chip is shown in Figure 2.14.

Finally, a 90-124 GHz tripler design was completed and is shown in Figure 2.15. Folding of the passive components was no longer necessary, but at the cost of increasing parasitic reactances and dispersion effects from the "thickening" substrate. The simulated performance of this design is shown in Figure 2.16.

Two other triplers were required for the ALMA and EVLA projects, one for 50-60 GHz, and another for 120-144 GHz. There design was completed by another student, following the same precedents established in the designs above.

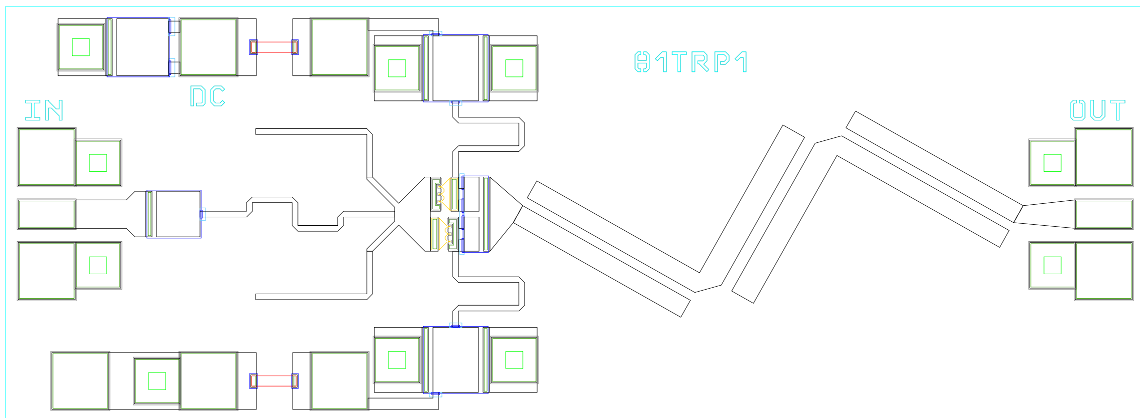

Fig. 2.13. Layout of the 70-92 GHz MMIC tripler. Chip dimensions are 2.0 x 0.73 mm. GaAs substrate thickness is 100 μm.

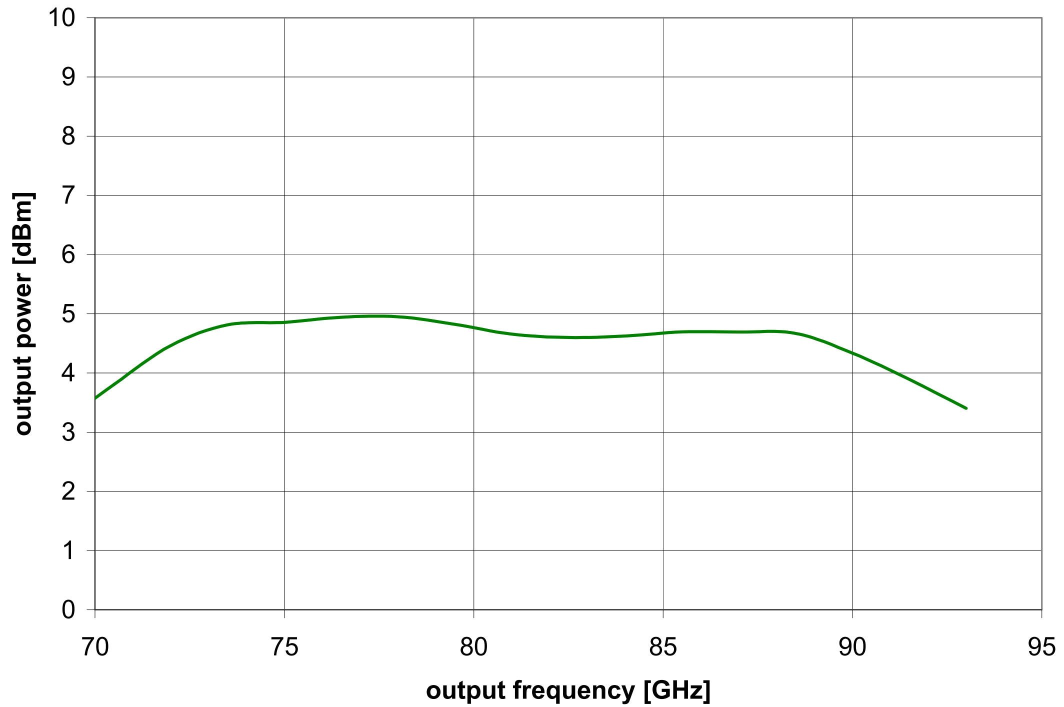

Fig. 2.14. Simulated output power for the 70-92 GHz tripler. DC current is fixed at 7.5 mA, and input power level is +17 dBm.

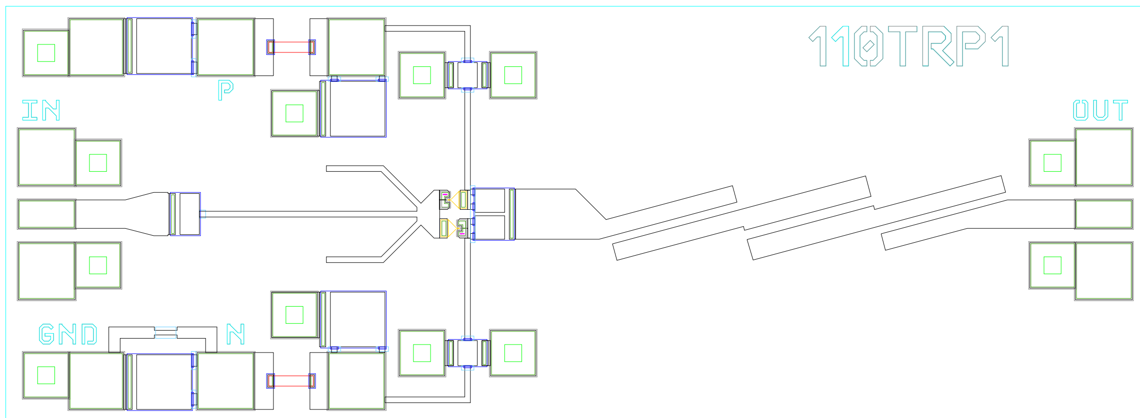

Fig. 2.15. Layout of the 90-124 GHz MMIC tripler. Chip dimensions are 2.0 x 0.73 mm. GaAs substrate is 100 μm thick.

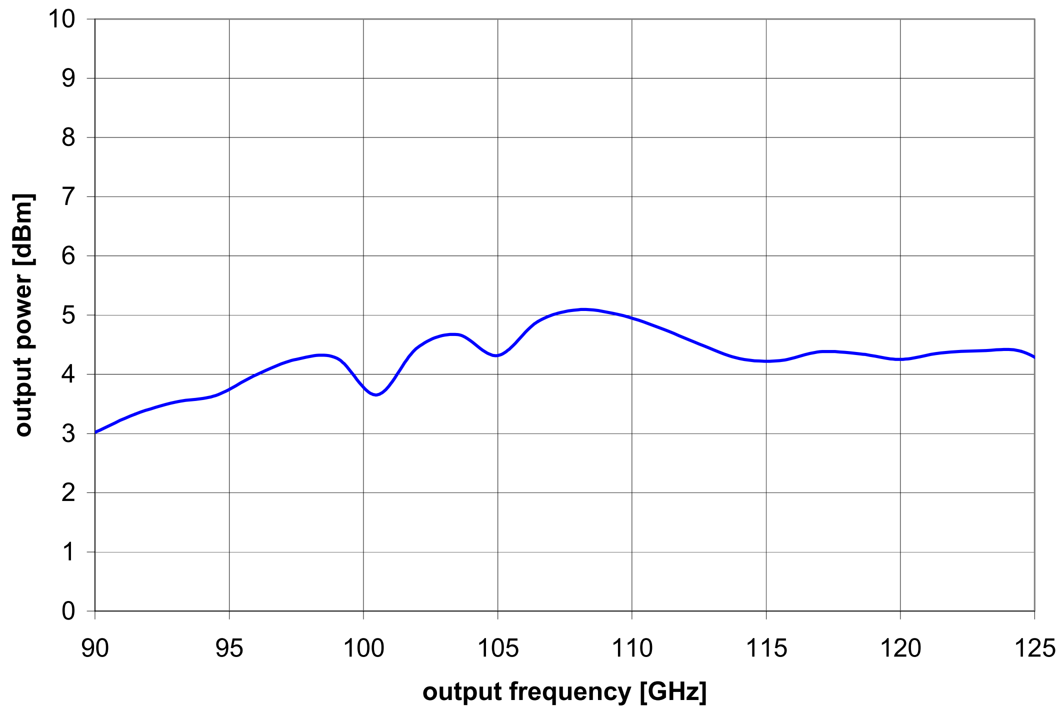

Fig. 2.16. Simulated output power for the 90-124 GHz tripler. DC current is fixed at 2.5 mA, and input power level is +17 dBm.

3 Monolithic Millimeter-Wave Mixers

This chapter describes a number of novel mixer designs that were developed in support of the various programs introduced in Chapter 1. In each case, the particular type of mixer (balanced, image-reject, subharmonic, etc.) was selected based on the needs of the project. Some of the more interesting challenges involved extending advanced mixer concepts (such as the doubly balanced topology) to higher frequencies.

3.1 Broadband Balanced Mixers

Broadband mixers are important components for millimeter-wave radiometers. A monolithic approach enables compact receivers to be assembled into a focal plane array for millimeter-wave imaging applications. HEMT diodes have been used in recent MMIC mixers [32-34] with encouraging results. This approach has the advantage of being compatible with existing LNA technology, thereby allowing a complete millimeter-wave down-converter to be integrated monolithically [33].

Balanced mixers have the useful property of suppressing LO amplitude noise as well as some high order mixing products [31]. Unfortunately, the bandwidth of monolithic balanced mixers is limited by that of the RF/LO coupler, which must have 3 dB coupling and 180° output phase difference across the band to realize these benefits (90° couplers may also be used, but suffer from poor RF-to-LO isolation). For example, the branch-line or ring hybrids are common choices for microstrip balanced mixers, but the bandwidth is typically only 10% to 20% [36].

Here we present the design and evaluation of a broadband balanced diode mixer with RF from 100-140 GHz, and IF from 20-60 GHz. The circuit is fabricated on InP using a standard HEMT MMIC process.

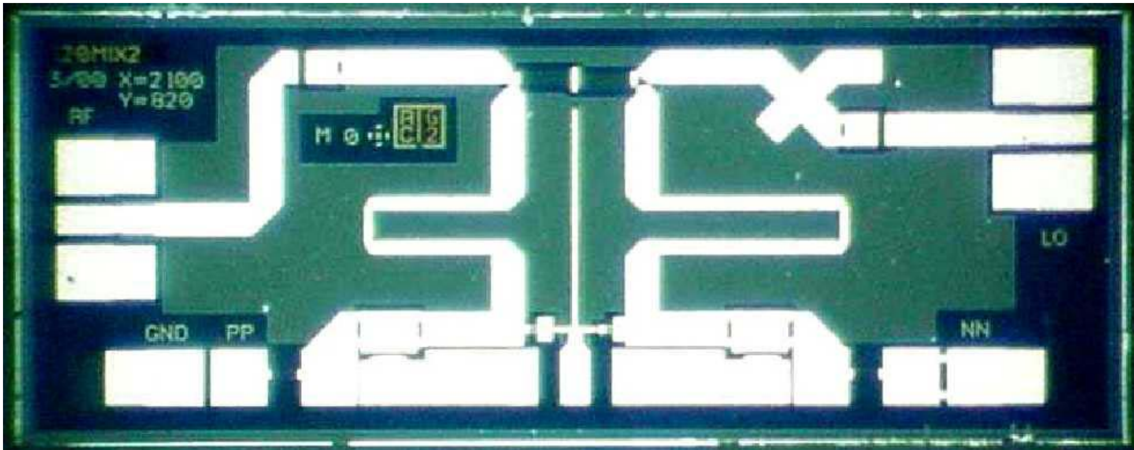

Fig. 3.1. Photograph of the balanced mixer. Chip dimensions are 2.0 x 0.74 mm. InP substrate 75 μm thick.

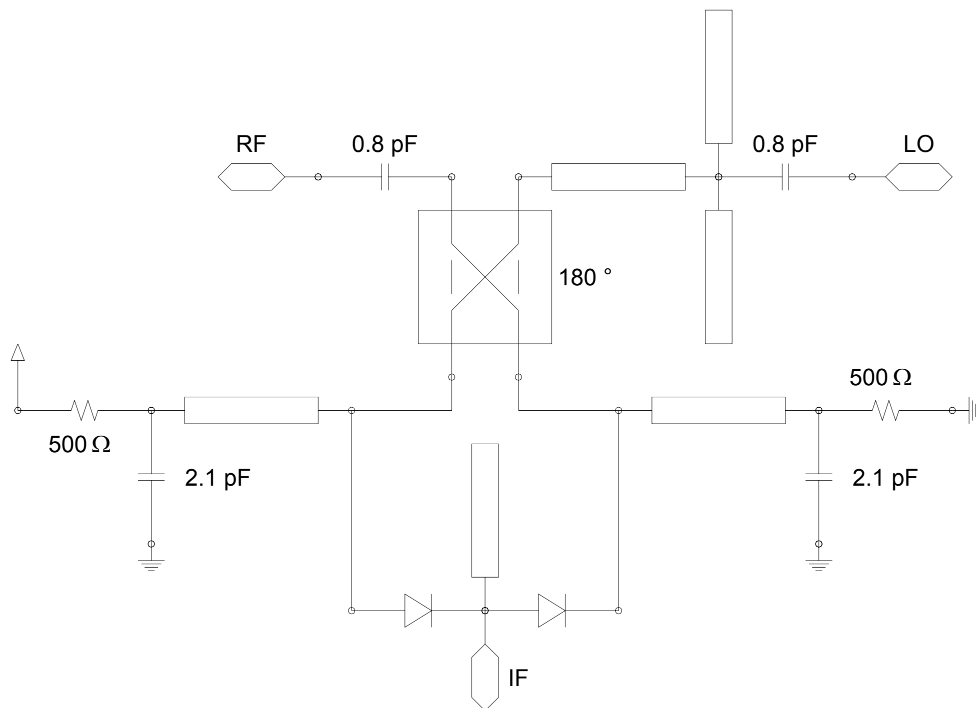

Fig. 3.2. Schematic of the mixer showing MIM capacitors, thin-film resistors, and transmission-line sections.

The circuit is designed to downconvert an RF band of 100-140 GHz to an IF of 20-60 GHz by mixing with a fixed 80 GHz LO. A photograph of the chip is shown in Figure 3.1, and a schematic is in Figure 3.2. As described earlier, the 180° coupler is a key component of this type of mixer, and constrains the bandwidth in many implementations. To overcome this limitation, we incorporated the novel combination of a Lange coupler with 90° coupled-line phase shifters [37, 38] to synthesize a broadband

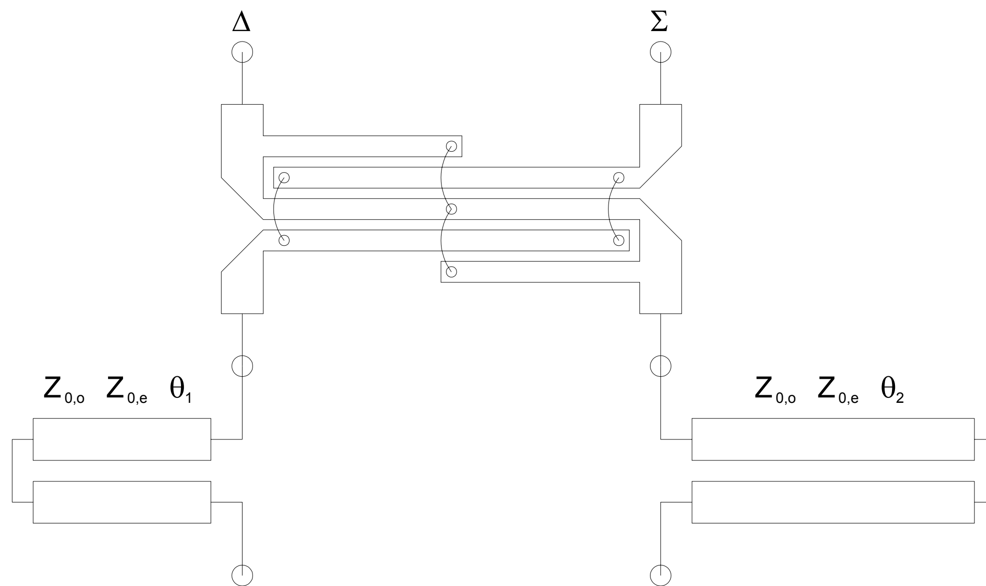

Fig. 3.3. Schematic of the broadband 180° hybrid.

180° coupler, as shown in Figure 3.3. The Lange coupler was fabricated in the First-Level Interconnect (FIC) metal layer, which is thinner and allows tighter spacing between lines than top-metal in this process. Although this approach incurs greater losses, it was necessary to achieve the tight 3 dB coupling that is critical to the operation of the mixer. The coupled-line phase shifters that follow are designed to provide good input match and a differential phase shift of 90° ± 5° from 80-140 GHz. Both the coupler and the phase shifters were simulated using the HP Momentum software. Together they comprise a 180°, 3 dB coupler with approximately 55% bandwidth.

Two HEMT-gate Schottky diodes, available in the TRW InP HEMT Process [39], were used as mixing elements. Based on a 2-finger, 40 μm FET model for this process, the gate structure was designed to simultaneously minimize the parasitic resistance and capacitance of the Schottky diode. Specifically, the diode cell consists of two fingers, each 5 μm long. Our conservative estimate is that this structure has R_s = 33 Ω, and C_{j0} = 16 fF. More rigorous testing of this structure leading to a better model of the diode is planned for future wafer runs.

The diodes are biased in series through low-impedance transmission lines along the bottom edge of the chip. The lines are bypassed at a quarter-wavelength from the diode in the center of the RF band

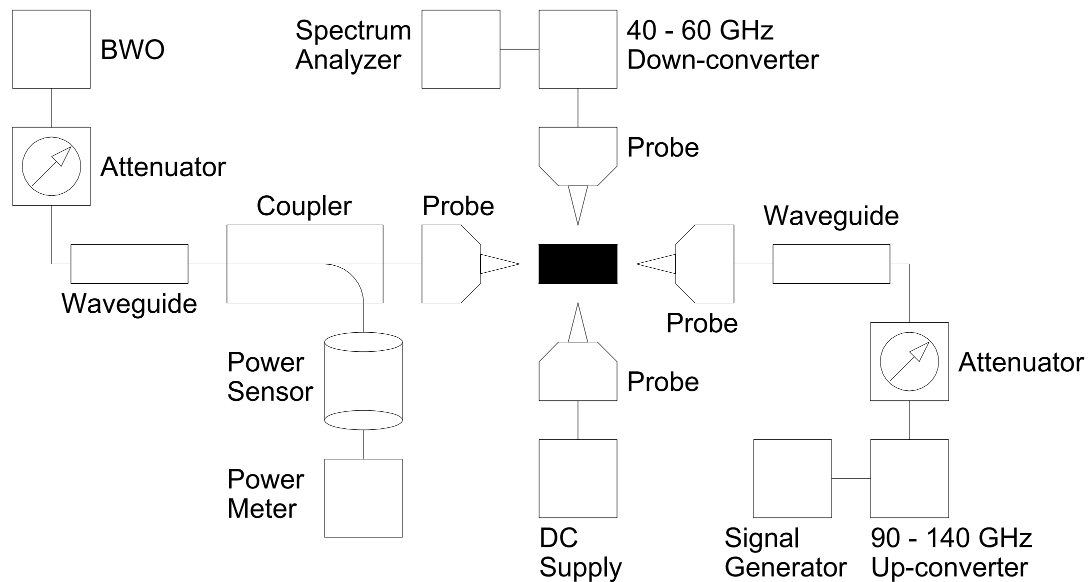

Fig. 3.4. Block diagram of the test setup. The 40-60 GHz down-converter was omitted for IF < 40 GHz.

which provides a ground return and isolation for the IF, while allowing RF and LO frequencies to pass.

Directly on the IF port, between the two diodes, is an open-circuited stub which is intended to be a quarter-wavelength long at the LO frequency. This was done to prevent LO power from leaking at this port. The stub was designed to be tunable by including a series of air bridges near the open end, which could be selectively broken to shorten the stub's length.

A microstrip matching section tuned for 80 GHz was added to the LO side. No matching section was used on the RF port, because this point is too far from the diodes to match the signal over such a wide bandwidth. Nevertheless, simulations indicate that the input return loss should be greater than 6 dB across the band.

The test setup is shown in Figure 3.4. A Thomson Components Backward Wave Oscillator (BWO), model RWO 110S, was used to provide the LO signal. The power from the BWO was adjusted with a WR-10 precision attenuator and monitored through a 10 dB coupler with an HP W8486A power meter. The LO power was coupled into the MMIC through a GGB Industries coplanar wafer probe. The precise coupling of the coupler, always close to 10 dB, was recorded and used in the calibration of the

measurements. The insertion loss of the wafer probe, about 1.3 dB, was also calibrated out of the measurement.

The RF signal was supplied by an HP 83650B Signal Generator, feeding a Millitech 90-140 GHz waveguide mixer utilized as an up-converter. A 120 GHz low-pass filter was attached to the 90 GHz second-harmonic Gunn on the Millitech module to remove a strong, spurious tone at 135 GHz. RF signal power was adjusted with a WR-8 precision attenuator. Finally, the RF signal was coupled into the chip through another GGB Industries wafer probe. The attenuator setting that provided –15 dBm of signal power at the probe tips was measured and recorded for each frequency point. This signal level was strong enough to allow easy measurement of conversion loss without entering compression.

The IF signal was extracted with a 50 GHz wafer probe. For IF below 40 GHz, the output was measured directly with an HP 8564E Spectrum Analyzer. The loss in the coaxial cable, typically on the order of 2-8 dB, was calibrated out. To extend the range of IF measurements, a 40-60 GHz down-converter module was added in front of the Spectrum Analyzer, as shown in Figure 3.4. The conversion loss of this module is about 14-18 dB, and was calibrated out.

The most significant results are plotted in Figures 3.5-3.8. As shown in Figure 3.5, the conversion loss is about 15 dB overall from 100 GHz to 130 GHz. Although the circuit was designed for an 80 GHz LO, additional data was taken with other LO frequencies in order to get some idea how the conversion loss changes with IF and RF frequencies which would otherwise be outside the range of the measurement setup. The results are shown in Figure 3.6. The conversion loss remains in the vicinity of 15 dB for IF from 10-50 GHz, and for RF from 100-135 GHz.

The conversion loss in the center of the band for various LO powers and bias conditions is mapped out in Figure 3.7. Each curve represents a different LO power, and illustrates a different optimum current level. The curves converge at the low current end, implying that the conversion loss can be made relatively independent of LO power if a sacrifice of a few dB in conversion loss is acceptable.

The amount of LO power the circuit can withstand and how it affects the conversion loss would be of interest in some applications. As shown in Figure 3.8, the LO power was swept up to 17 dBm, limited by the test equipment, without any detectable damage to the chip. A minimum of 12 dB conversion loss

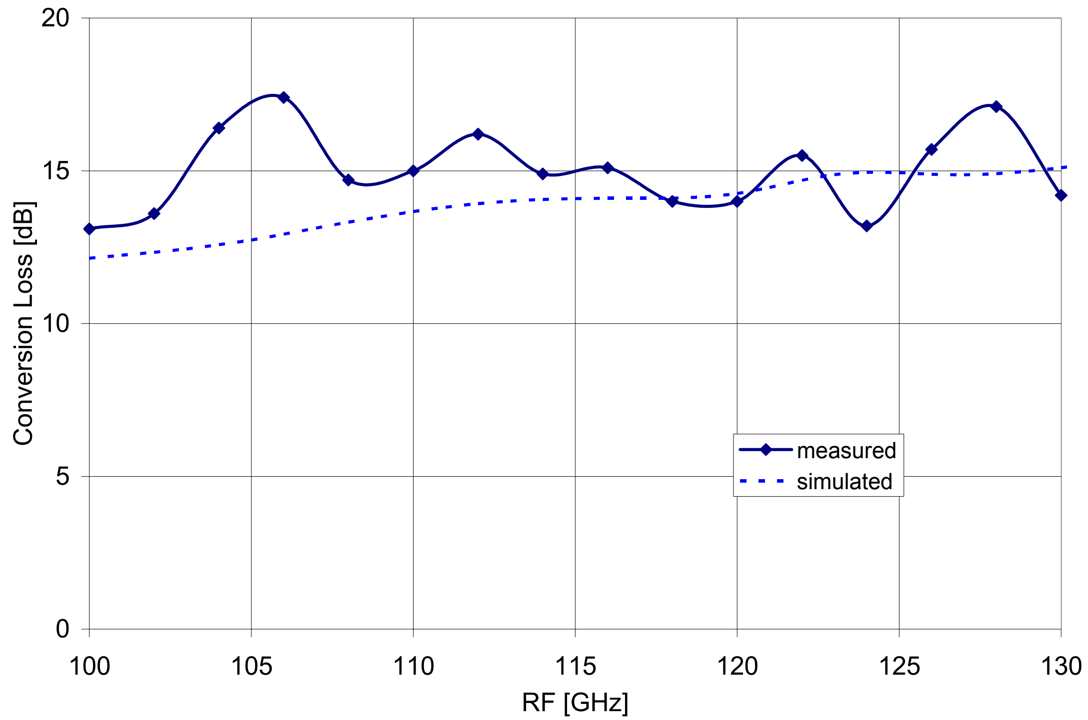

Fig. 3.5. Measured and simulated conversion loss vs. RF frequency. LO was +5 dBm at 80 GHz. RF power was -15 dBm. The circuit was biased with a constant current of 2.4 mA.

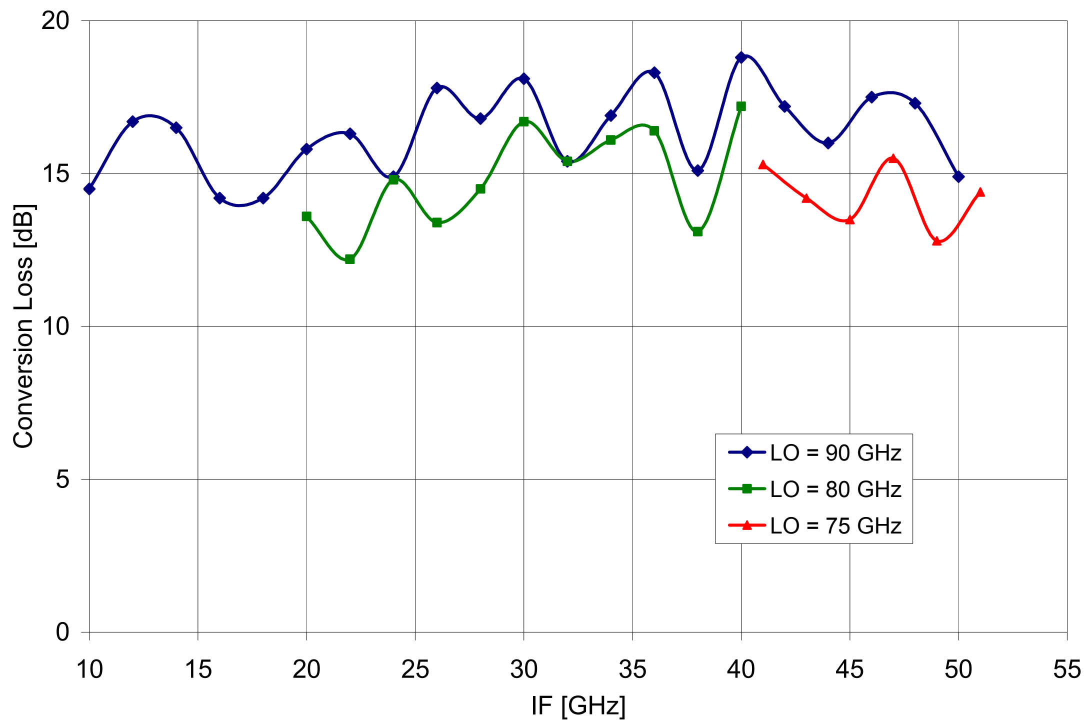

Fig. 3.6. Measured conversion loss vs. IF frequency for various LO frequencies. LO power was +5 dBm in all cases. RF power was -15 dBm, and the bias was held constant at 3.6 V.

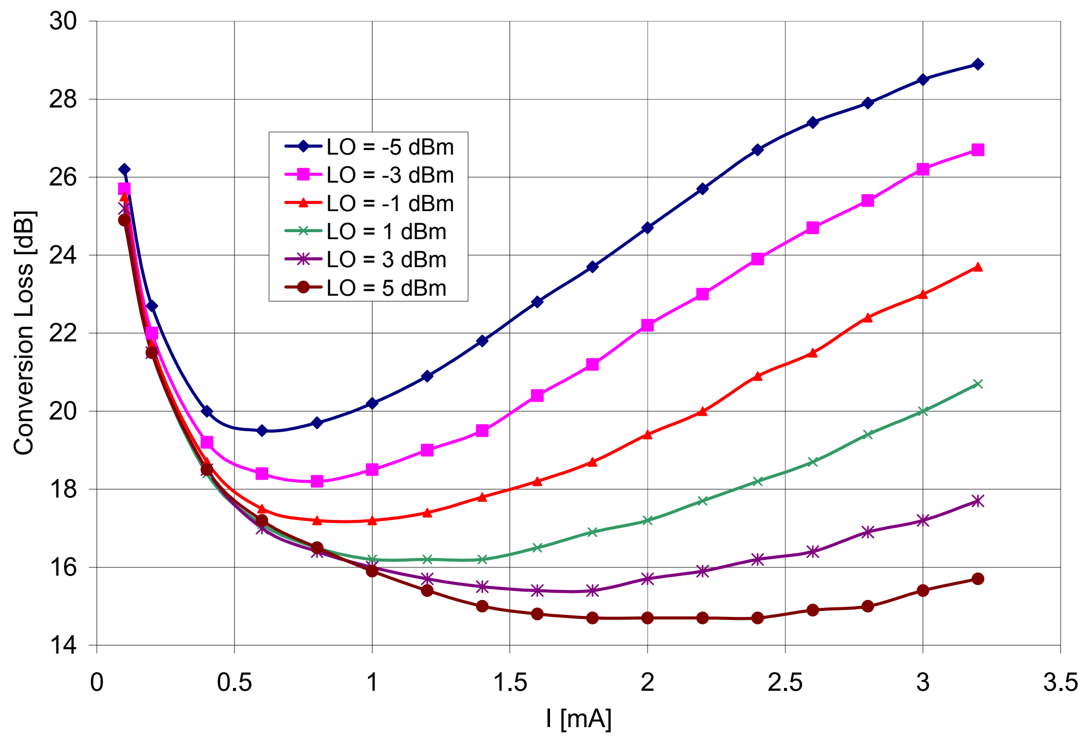

Fig. 3.7. Conversion loss vs. LO power and bias condition. The LO frequency was 80 GHz, and RF was -15 dBm at 110 GHz.

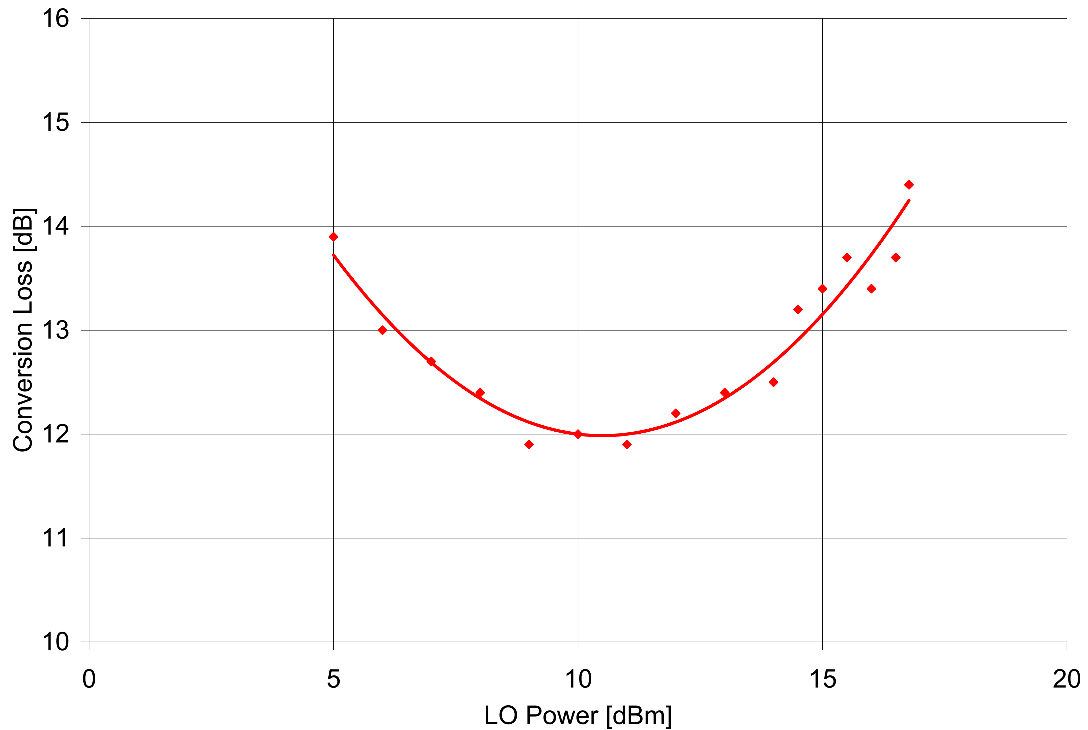

Fig. 3.8. Conversion loss vs. LO power for high drive level. The LO frequency was 88 GHz, and the RF signal was -15 dBm at 132 GHz. Bias was held constant at 2.4 mA.

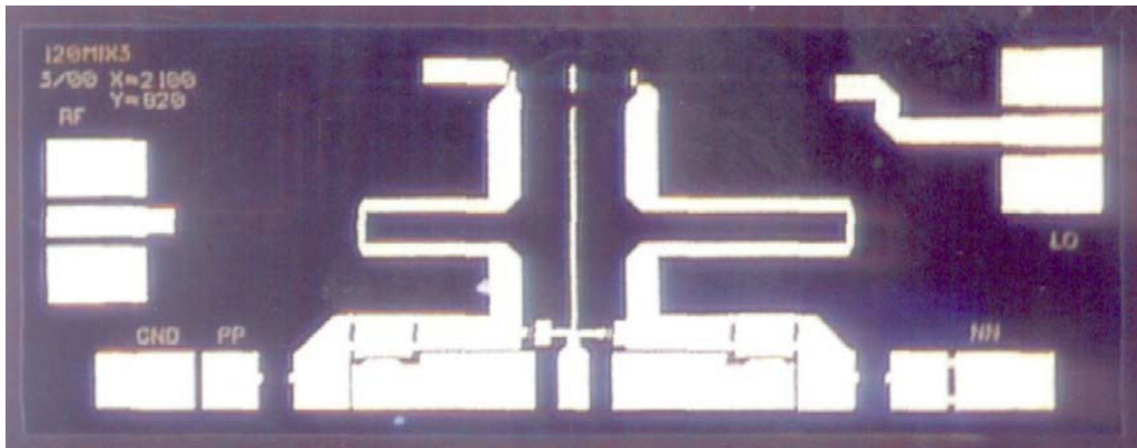

Fig. 3.9. Photograph of the revised 100-140 GHz balanced mixer. Chip dimensions are 2.0 x 0.74 mm. InP substrate is 75 µm thick.

was found with 10 dBm LO power, though one would expect the noise performance of the mixer to suffer at this drive level.

This chip, which was the first monolithic HEMT diode balanced mixer in this frequency range, was used in the 100-140 GHz prototype radiometer introduced in Section 1.2. The module achieved 30 dB conversion gain and equivalent noise temperature of 1000 K across much of the designed bandwidth. This represents a significant improvement in performance over existing sensors concurrent with an order of magnitude reduction in mass, volume, and cost.

A revision of the above 100-140 GHz mixer was made to include an RF band-pass filter, with the intent of rejecting lower-sideband noise from the RF LNA and thus improving the overall noise figure of the radiometer. A photograph of the new chip is in Figure 3.9. As with the Lange Coupler, the RF filter (left side of the chip) required tighter spacing then normally allowed in the thick metal of this MMIC process, so it was fabricated in the thinner FIC layer. Tests indicate roughly the same conversion loss and other characteristics as the first chip. Unfortunately, the IIP program to develop the 100-140 GHz radiometer ended before this chip could be integrated into the module.

The success of the 100-140 GHz mixers prompted the author to develop a W-band version, as there is even more interest in MMIC components at that frequency range. The filter and 180° hybrid were re-tuned and the circuit layout refined to better isolate the three ports and lessen the mixer's sensitivity to out-of-band terminations. A photograph is shown in Figure 3.10. Due to refinements in the design as well

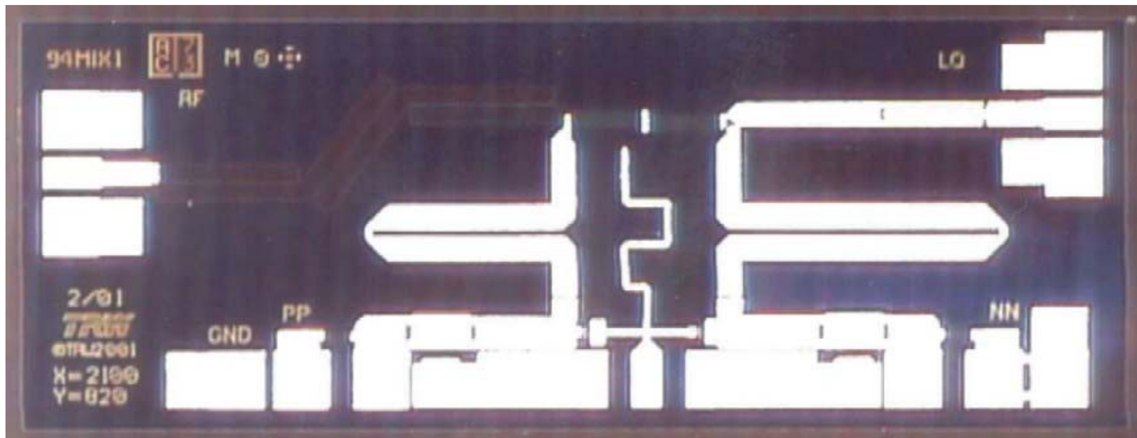

Fig. 3.10. Photograph of the W-band balanced mixer. Chip dimensions are 2.0 x 0.74 mm. InP substrate is 75 μm thick.

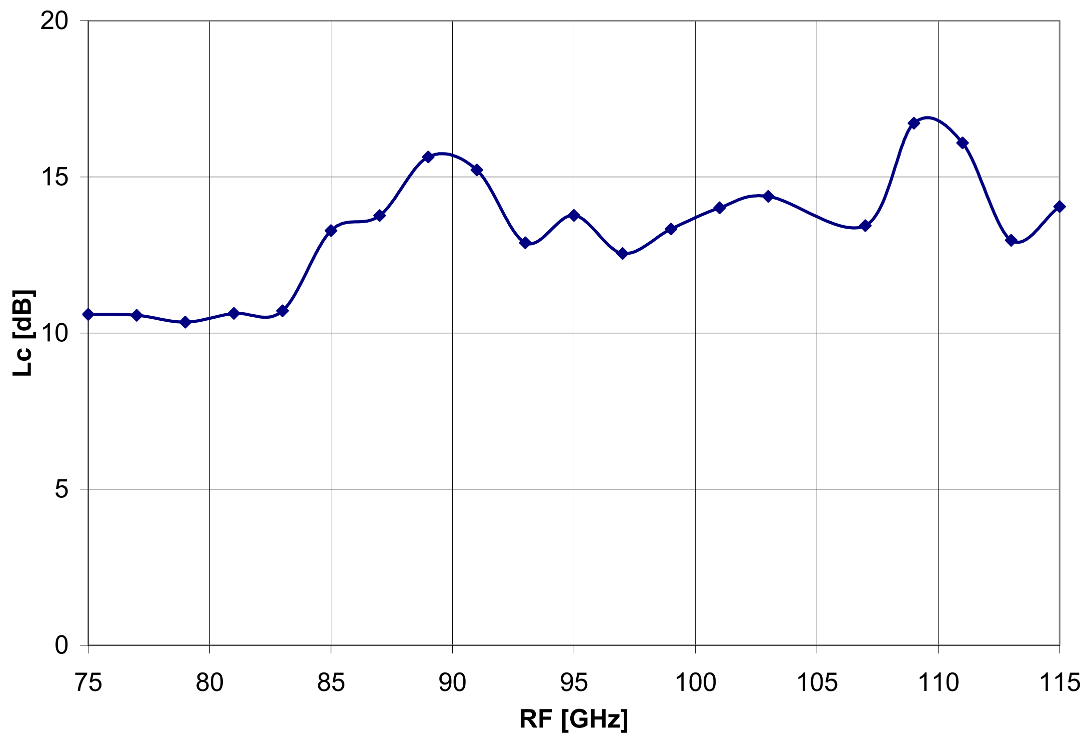

Fig. 3.11. Conversion loss vs. frequency for the W-band balanced mixer. LO power was +8 dBm at 65 GHz. RF power was fixed at -20 dBm. The chip was biased with a constant 3 V, drawing a nominal current of 1.5 mA.

as the lower frequency, this chip has somewhat better performance than the first two. Conversion loss is shown in Figure 3.11.

Once again, engineers at the NRAO working on the EVLA project recognized that the same principles demonstrated in these earlier mixers could be used in their system, and two additional circuits

were requested. Both were required to be balanced mixers with unusually wide bandwidths, one for Ka-band and another for Q-band.

The layout for the Ka-band mixer is shown in Figure 3.12. The balun is similar in design to that used in the broadband balanced mixers described above, though in this case the lower frequency required a dramatic re-arrangement of the layout. The RF and LO signals enter through the ports in the upper and lower left corners, respectively. They immediately go through a Lange coupler (shown in blue) on the FIC layer, followed by the coupled-line phase-shifters which stretch almost the full length of the chip from left to right and back. Two pairs of diodes are used in place of the single diodes from the earlier mixers, in part to improve the impedance match at this lower frequency, but also to increase the compression point of the mixer, which was an issue for the EVLA. The IF signal is extracted from between the diode pairs on the left through a large coupling capacitor. The LO signal is fed to the diodes out of phase, putting a virtual ground between the diodes, but the RF signal which is fed in-phase requires a quarter-wavelength open-circuited stub for ground return. This also helps to prevent the RF and LO signals from leaking out of the IF port. DC bias is brought into the diodes through a pair of capacitor-shorted stubs. They provide a ground return for the IF signal as well as impedance matching for the RF and LO.

The optimization of this mixer was exceedingly difficult because of the bandwidth. The required RF frequency range was 26-40 GHz, with an LO of 36-50 GHz, and an IF band of 8-18 GHz. The balun is thus required to cover almost a full octave of bandwidth (26-50 GHz). Even more problematic, the top of the IF band (18 GHz) comes so close to the bottom of the RF (26 GHz) that isolation between these ports becomes a serious problem. The simulated response of this mixer, plotted in Figure 3.13, shows increasing loss at lower RF frequencies. This slope is present on all curves regardless of the LO frequency and is a result of increasing leakage of the IF signal to the RF port as the IF gets close to 18 GHz. In spite of these problems, it was possible to keep the conversion loss under 10 dB, which meets the EVLA specification. Furthermore, low loss at high RF frequency is often acceptable since most other components in the system will have the opposite trend.

The Q-band balanced mixer for the EVLA was required to have an RF band of 40-50 GHz, with an LO frequency range of 50-60 GHz, and an IF band of 8-18 GHz. It was designed quickly by re-

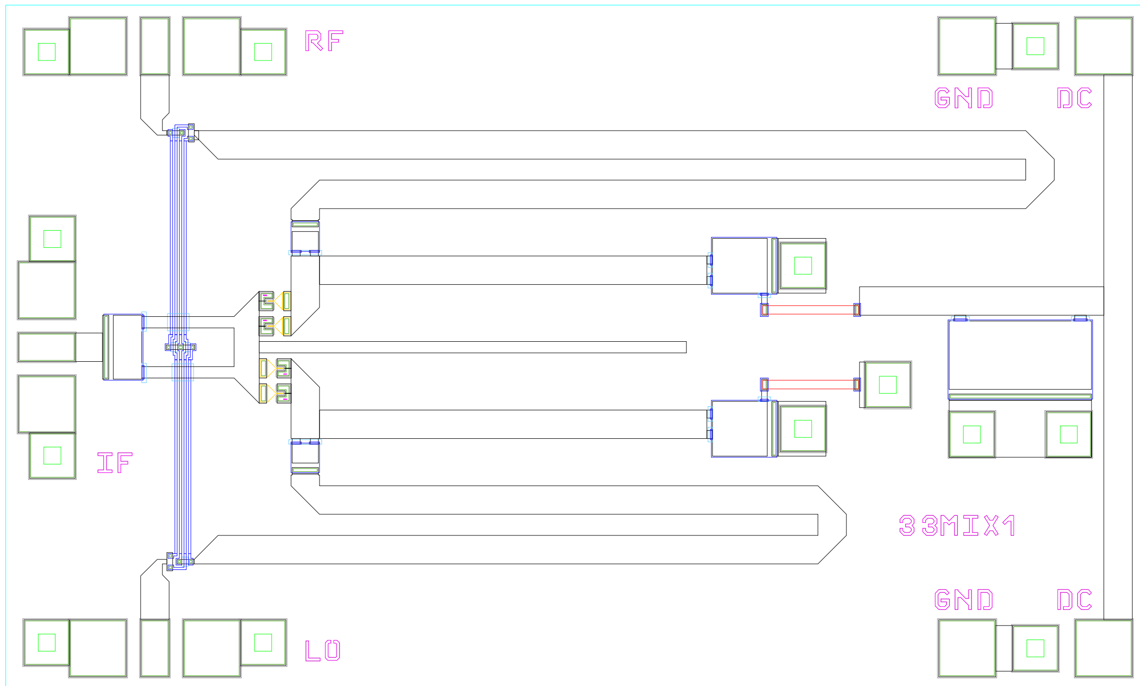

Fig. 3.12. Layout of the 36-50 GHz balanced mixer. Chip dimensions are 2.0 x 1.2 mm. GaAs substrate is 100 µm thick.

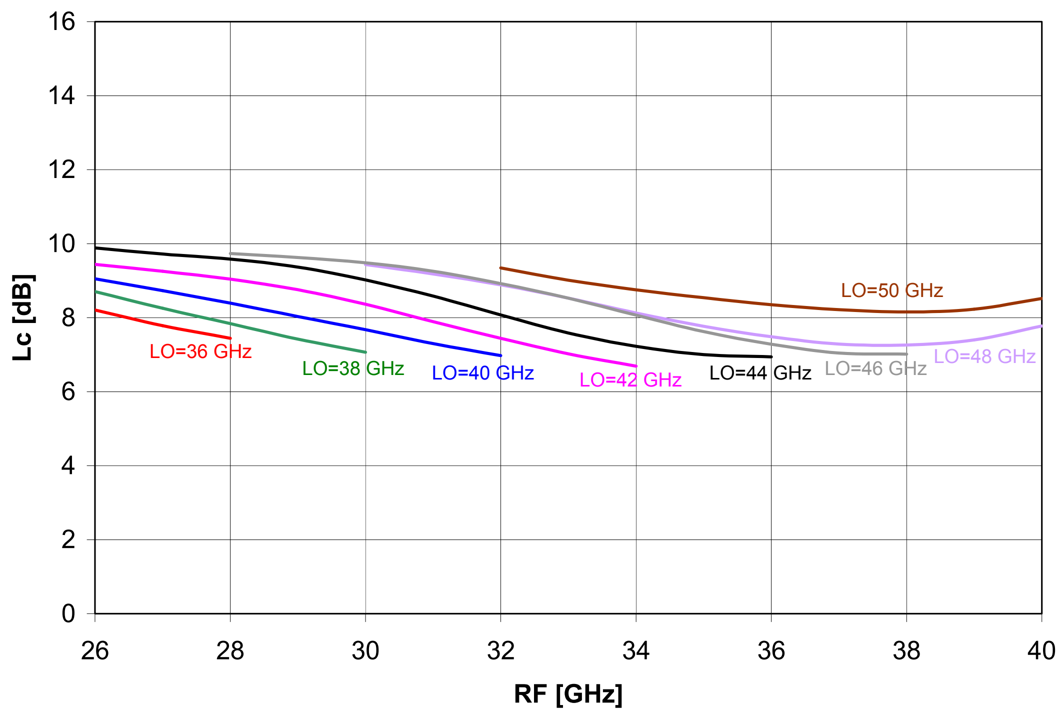

Fig. 3.13. Simulated conversion loss of the 36-50 GHz balanced mixer. IF bandwidth was limited to 8-18 GHz. DC current fixed at 5 mA. LO power level was +13 dBm.

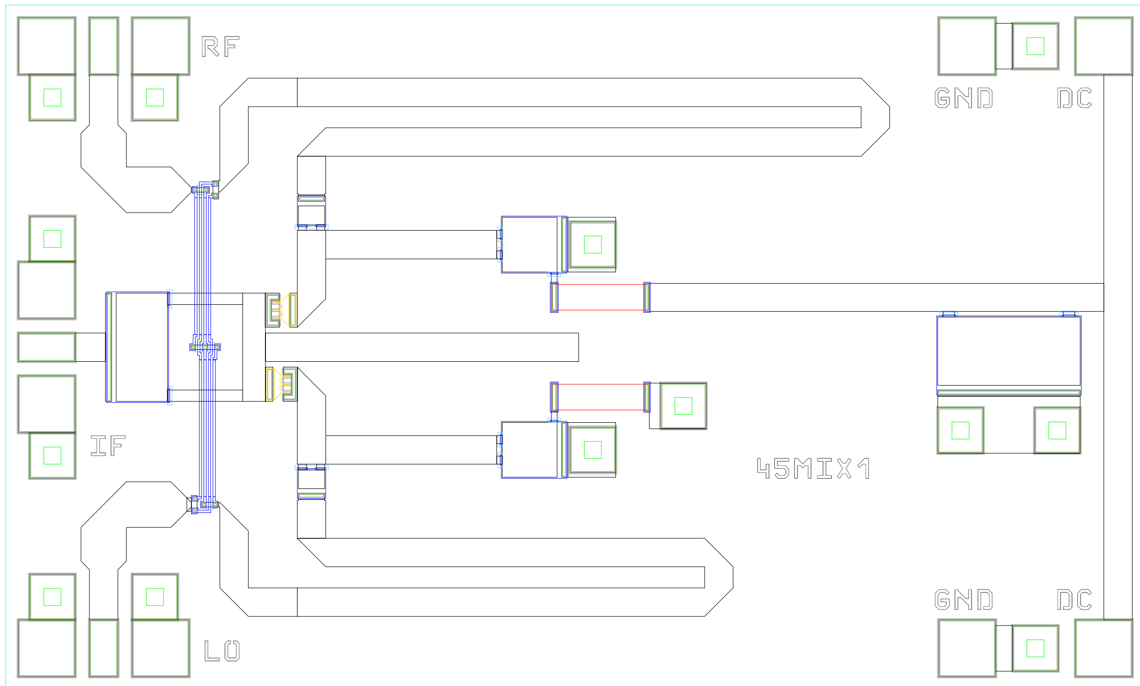

Fig. 3.14. Layout of the 40-50 GHz balanced mixer. Chip dimensions are 2.0 x 1.2 mm. GaAs substrate is 100 µm thick.

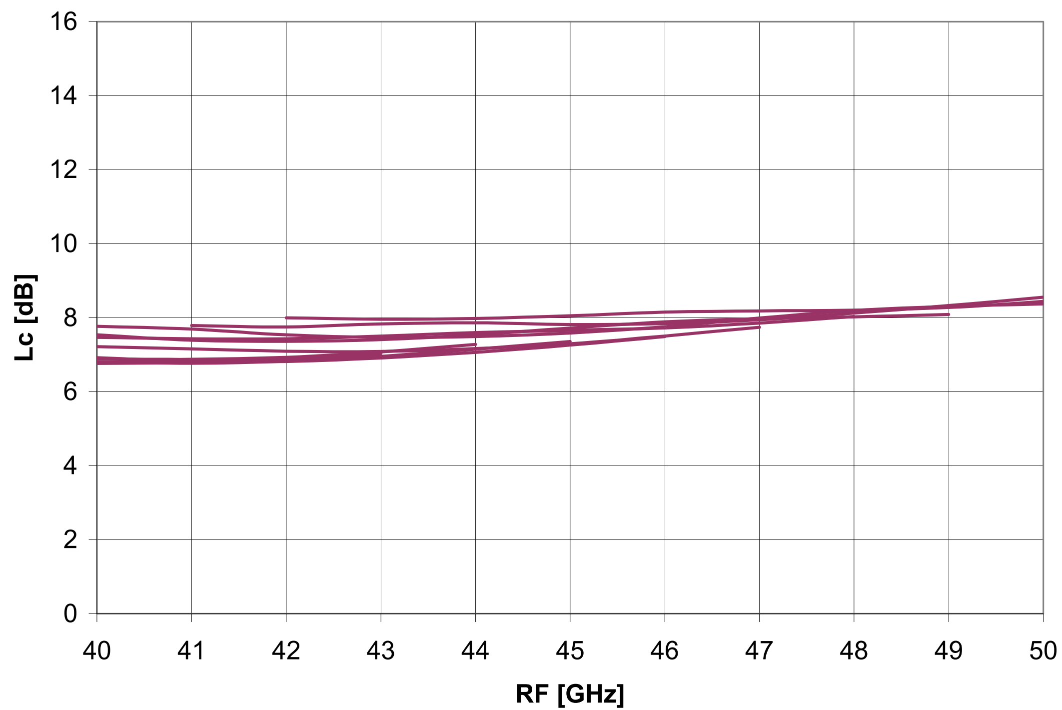

Fig. 3.15. Simulated conversion loss of the 40-50 GHz mixer. IF bandwidth was limited to 8-18 GHz. DC current fixed at 7.5 mA. LO power level was +13 dBm.

tuning the elements from the Ka-band mixer. The layout is shown in Figure 3.14. While this mixer also had a broad RF/LO bandwidth, it was not as broad as the first circuit, and the IF band was of course further from the RF, simplifying the isolation of these ports. In addition, the diode pairs were replaced with three-finger diode cells as these will have fewer problems with distributed effects at higher frequencies. The simulated performance is plotted in Figure 3.15.

3.2. A 170-210 GHz Second-Harmonic Mixer

Among the most prevalent challenges in millimeter-wave receiver design is generating local oscillator signals to drive mixers. One or more frequency multipliers, like those described in Chapter 2, can be used to generate the necessary pump from a lower frequency oscillator. It may be more practical or efficient in some cases, however, to combine this harmonic generation with the mixing function itself. This is the approach taken by a *sub-harmonic mixer*. These circuits are designed to isolate a higher order mixing product than most other mixers, usually involving a harmonic of the input LO frequency.

In this section a 170-210 GHz second-harmonic mixer is described, which was designed for the same program as the 100-140 GHz mixer in Section 3.1. Originally, both mixers were intended to operate with the same 80 GHz LO driver to simplify the combined system. The 170-210 GHz circuit, pictured in Figure 3.16, employs two Schottky diodes in an anti-parallel configuration. The second harmonic of the LO, nominally at 160 GHz, is mixed with the 170-210 GHz RF band to produce an IF between 10 and 50 GHz.

It may seem paradoxical at first that an anti-parallel diode pair was used in the previously discussed triplers for its ability to *reject* even harmonics, and then employ one again in this circuit specifically to *generate* an even harmonic. The difference is that in this case there is no need to couple the 2*LO signal out of the circuit, it needs only to be present in the nonlinear element so it can be mixed with another signal. Even in the tripler, the second harmonic was present on the diodes, but it was trapped there in the loop formed by the two elements, unable by symmetry to excite a wave on the outgoing transmission

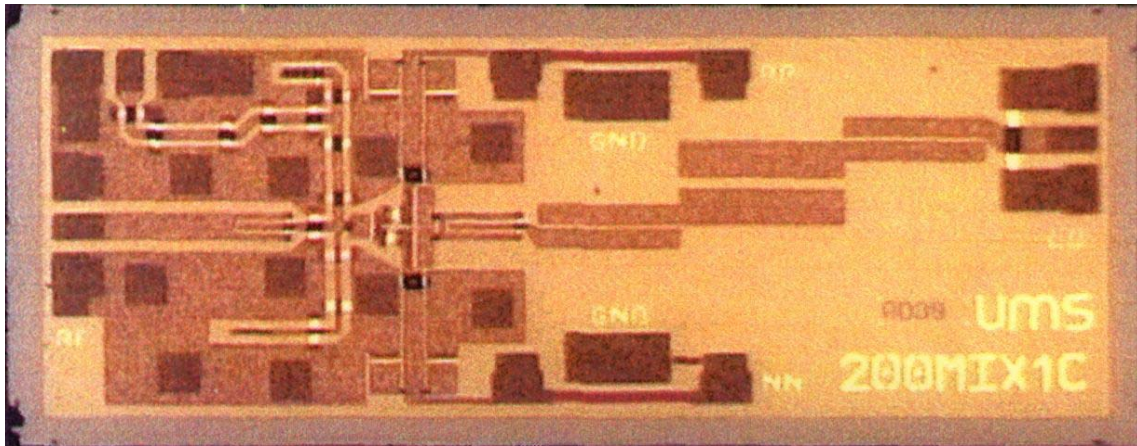

Fig. 3.16. Photograph of the 170-210 GHz second-harmonic mixer. Chip dimensions are 2.0 x 0.74 mm. GaAs substrate is 100 μm thick.

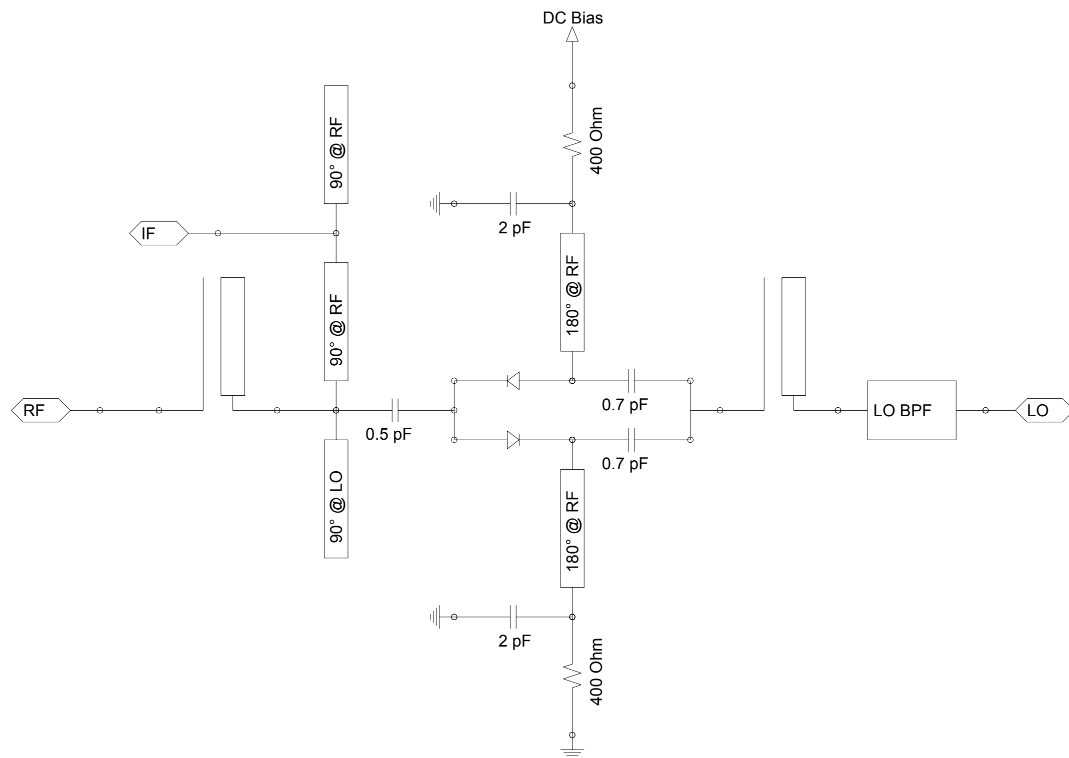

Fig. 3.17. Schematic of the 170-210 GHz second-harmonic mixer.

lines. This same effect can be used to our advantage in this mixer, since the second-harmonic energy cannot leak out from the nonlinearity except by secondary multiplication or mixing.

The high frequency of this circuit relative to the substrate thickness (100 μm) required that the RF side be implemented entirely in coplanar waveguide (CPW) rather than microstrip. As usual, air bridges

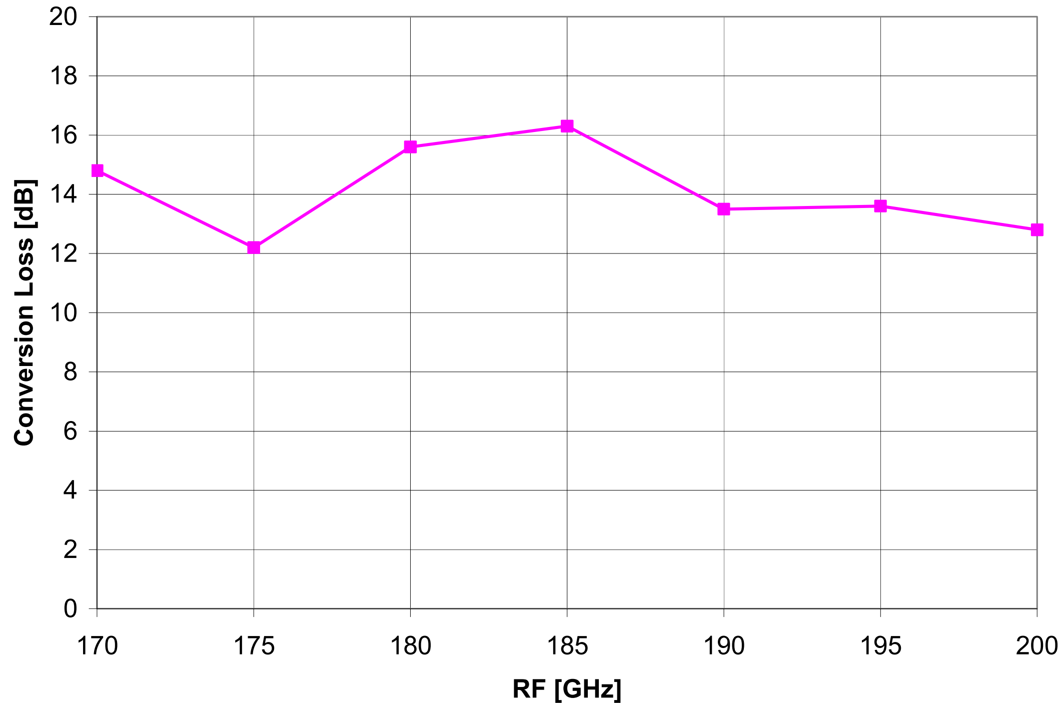

Fig. 3.18. Conversion loss for the 170-210 GHz second-harmonic mixer. LO power was +10 dBm at 80 GHz. Bias current was held constant at 1.1 mA.

were used at various discontinuities to ensure that only the even-mode could propagate, and via holes were distributed throughout the ground areas to prevent parallel plate modes from forming. As shown in the schematic of Figure 3.17, the RF circuit consists of a stub matching network that incorporates the DC bias lines and a rudimentary diplexer for isolating the IF port from the RF. The bias transmission lines are bypassed by small capacitors an RF-quarter-wavelength away from the diodes. They serve to provide ground return for the 80 GHz LO signal but are too low in value to short out the IF output. The IF output transmission line has an open-circuited stub that is a quarter-wavelength long at the RF frequency, shorting out the RF signal at that point. The separation of the junction for this stub from the main RF line is used to tune the input match at the higher frequency. On either side of the diodes are capacitors for coupling in the millimeter-wave signals and routing the DC bias through the diodes. This bias current also passes through a pair of 400 Ω resistors in series, in place to protect the diodes from over-voltage or static damage. Finally, on the LO side is a coupled-line bandpass filter which masks out any spurious harmonics that may have been generated by the LO source and also isolates the unknown termination of the LO port in the RF

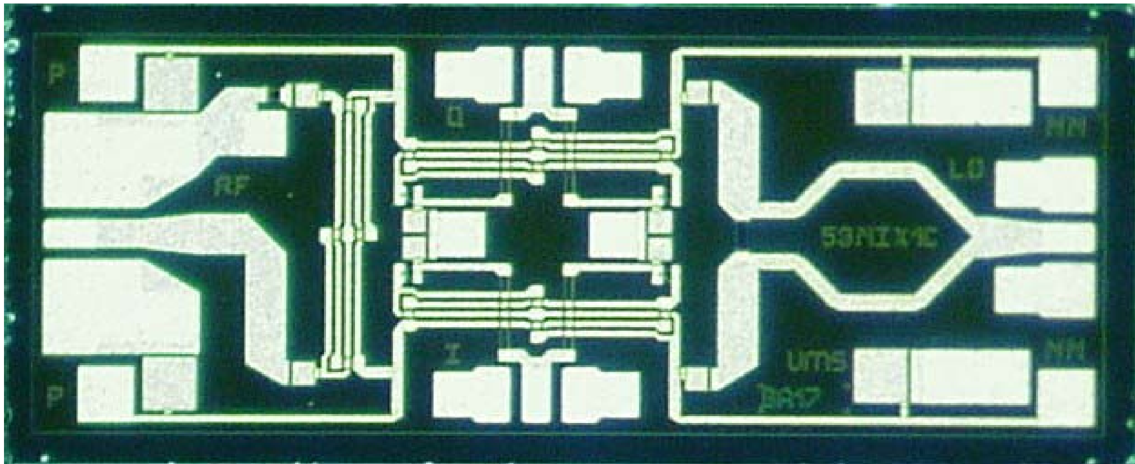

Fig. 3.19. Photograph of the 49-57 GHz I/Q mixer. Chip dimensions are 2.0 x 0.74 mm. GaAs substrate is 100 μm thick.

and IF bands.

This chip was tested on-wafer with a Backward-Wave Oscillator (BWO) as the LO source and an active multiplier chain as the RF. Both sources were measured ahead of time and their power levels recorded. During the measurements, the loss of the interconnects and wafer probes was taken into account and calibrated out of the measurement. The IF output was measured on a spectrum analyzer in order to isolate it from spurious mixing products, but it was calibrated via comparison with measurements using a power meter. Conversion loss is plotted in Figure 3.18. The data is only shown for 170-200 GHz because the IF instrumentation was limited to 40 GHz, but over the band that was tested, the mixer shows good conversion loss of about 14 dB.

3.3. I/Q Mixers

Another useful form of mixer is what some call an *I/Q mixer*, such as that photographed in Figure 3.19. The RF band for this mixer is 49-57 GHz. It consists of two balanced mixers driven by the same local oscillator in-phase, and the same RF signal fed in-quadrature, as shown in Figure 3.20. The LO signal is applied to the port on the right and passes through a Wilkinson power divider. The RF signal enters through the left and is directed to both mixers via a Lange coupler. The other two Lange couplers visible

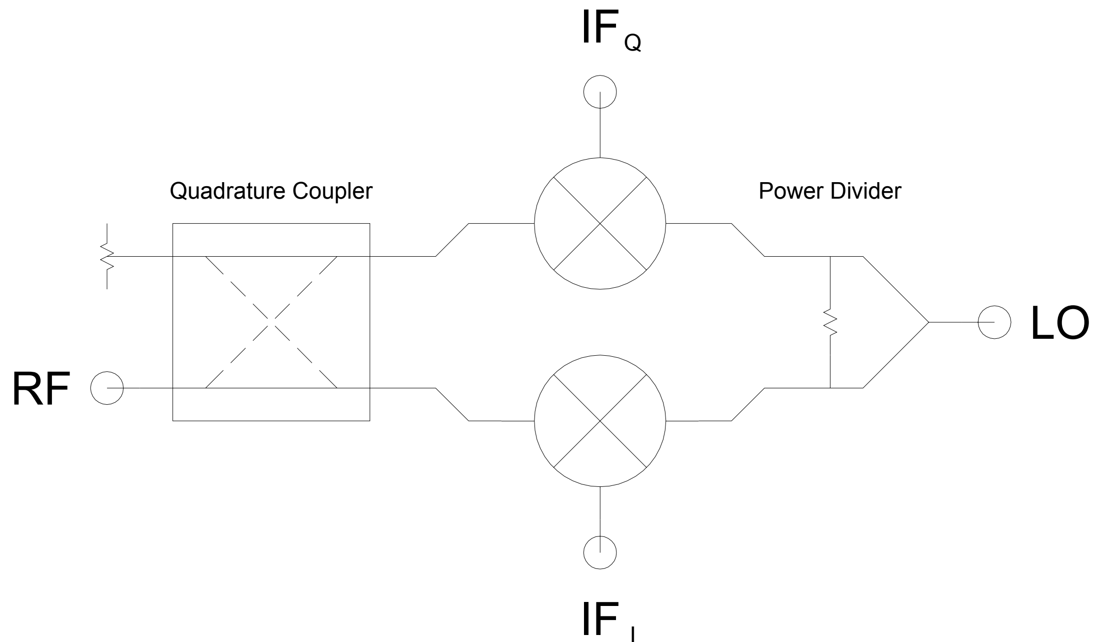

Fig. 3.20. Conceptual diagram of an I/Q mixer.

in the photograph form hybrids for the two smaller balanced mixers of the chip. The chip has two IF outputs labeled "I" and "Q", for "in-phase" and "quadrature," respectively.

The advantage of combining two mixers in this way is that it allows you to isolate the upper- and lower-sidebands of an RF signal with sharper selectivity than a physically realizable filter could normally achieve. The principle can be illustrated simply as follows. Denote the local oscillator entering the chip as

$$LO = A_{LO} \cos(\omega_{LO} t) \tag{3.1}$$

and the RF signal as

$$RF = A_{USB} \cos((\omega_{LO} + \omega_{IF})t + \phi_{USB}) + A_{LSB} \cos((\omega_{LO} - \omega_{IF})t + \phi_{LSB}) \tag{3.2}$$

where A_{USB} and A_{LSB} represent the amplitudes and ϕ_{USB} and ϕ_{LSB} represent the phases of the upper- and lower-sideband components, respectively. After passing through the Wilkinson divider and Lange coupler, the signals entering the I- and Q-mixers are

$$LO_I = LO_Q = \sqrt{\tfrac{1}{2}}A_{LO}\cos(\omega_{LO}t) \tag{3.3}$$

$$RF_I = \sqrt{\tfrac{1}{2}}A_{USB}\cos((\omega_{LO}+\omega_{IF})t+\phi_{USB}) + \sqrt{\tfrac{1}{2}}A_{LSB}\cos((\omega_{LO}-\omega_{IF})t+\phi_{LSB}) \tag{3.4}$$

$$RF_Q = \sqrt{\tfrac{1}{2}}A_{USB}\cos((\omega_{LO}+\omega_{IF})t+\phi_{USB}-90) + \sqrt{\tfrac{1}{2}}A_{LSB}\cos((\omega_{LO}-\omega_{IF})t+\phi_{LSB}-90) \tag{3.5}$$

The IF outputs of both mixers are then given by

$$IF_I = \sqrt{\tfrac{1}{2}L_C}A_{USB}\cos(\omega_{IF}t+\phi_{USB}) + \sqrt{\tfrac{1}{2}L_C}A_{LSB}\cos(\omega_{IF}t-\phi_{LSB}) \tag{3.6}$$

$$IF_Q = \sqrt{\tfrac{1}{2}L_C}A_{USB}\cos(\omega_{IF}t+\phi_{USB}-90) + \sqrt{\tfrac{1}{2}L_C}A_{LSB}\cos(\omega_{IF}t-\phi_{LSB}+90) \tag{3.7}$$

where L_C is the conversion loss of both mixers, and we have neglected the higher-frequency and higher-order mixing products. Finally, the upper- and lower-sidebands can be isolated by combining these two outputs with one last quadrature hybrid (not included on this chip). Thus,

$$\begin{aligned} IF_{USB} &= \sqrt{\tfrac{1}{2}}\left[IF_{I,-90} + IF_Q\right] \\ &= \sqrt{\tfrac{1}{2}}\begin{bmatrix} +\sqrt{\tfrac{1}{2}L_C}A_{USB}\cos(\omega_{IF}t+\phi_{USB}-90) + \sqrt{\tfrac{1}{2}L_C}A_{LSB}\cos(\omega_{IF}t-\phi_{LSB}-90) \\ +\sqrt{\tfrac{1}{2}L_C}A_{USB}\cos(\omega_{IF}t+\phi_{USB}-90) + \sqrt{\tfrac{1}{2}L_C}A_{LSB}\cos(\omega_{IF}t-\phi_{LSB}+90) \end{bmatrix} \\ &= \sqrt{L_C}A_{USB}\cos(\omega_{IF}t+\phi_{USB}-90) \end{aligned} \tag{3.8}$$

$$\begin{aligned} IF_{LSB} &= \sqrt{\tfrac{1}{2}}\left[IF_{I,+90} + IF_Q\right] \\ &= \sqrt{\tfrac{1}{2}}\begin{bmatrix} +\sqrt{\tfrac{1}{2}L_C}A_{USB}\cos(\omega_{IF}t+\phi_{USB}+90) + \sqrt{\tfrac{1}{2}L_C}A_{LSB}\cos(\omega_{IF}t-\phi_{LSB}+90) \\ +\sqrt{\tfrac{1}{2}L_C}A_{USB}\cos(\omega_{IF}t+\phi_{USB}-90) + \sqrt{\tfrac{1}{2}L_C}A_{LSB}\cos(\omega_{IF}t-\phi_{LSB}+90) \end{bmatrix} \\ &= \sqrt{L_C}A_{LSB}\cos(\omega_{IF}t+\phi_{LSB}+90) \end{aligned} \tag{3.9}$$

This is often a more practical means of isolating the two sidebands than filtering, since a very low IF frequency (in this case less than 100 MHz) will place very stringent rejection requirements on the filters. The disadvantage is that this method will generally require 3 dB more local oscillator power to achieve the same conversion loss as a single balanced mixer with image-filtering.

Measurements indicate that the I/Q mixer of Figure 3.19 has about 8 dB conversion loss into each IF channel (5 dB if they are re-combined) with 7 dBm LO power. The Lange couplers appear to be slightly under-coupled, but this could be remedied by redesigning the couplers for the thinner metal layer as was done with the higher-frequency balanced mixers described earlier.

3.4. A Second-Harmonic I/Q Mixer for the DSN Array

Among the more interesting mixer designs the author has had the opportunity to work on is that for the DSN Array. For this project, the system designers wanted to take advantage of both I/Q mixing and the sub-harmonic LO pump concepts. It was required to downconvert the DSN Ka-band channels at 32 and 38 GHz, to a wide IF band of 0.5-2.0 GHz (wide for a communication system), using a sub-harmonic LO signal at 15-18.5 GHz, and to reject the lower sideband by at least 20 dB. This combination of requirements led to some interesting challenges in the chip's design.

A layout of the MMIC appears in Figure 3.21, and a schematic is shown in Figure 3.22. The RF signal enters through the port on the top edge of the chip, and is immediately split via a Lange quadrature coupler. As with the TRW chips from Section 3.1, the tight coupling required in this 3 dB hybrid led to the decision to place it in the FIC metal layer where it was possible to etch narrower lines and spaces. The I and Q sub-mixers on the chip are implemented with an anti-parallel diode pair, which we learned earlier was a useful configuration for second-harmonic mixing. A short inductive transmission line is used to match the impedance of the diode pair to nearly 50 Ω. It is important to note that although the presence of the quadrature coupler will automatically create a good input match for the chip, it is still necessary to

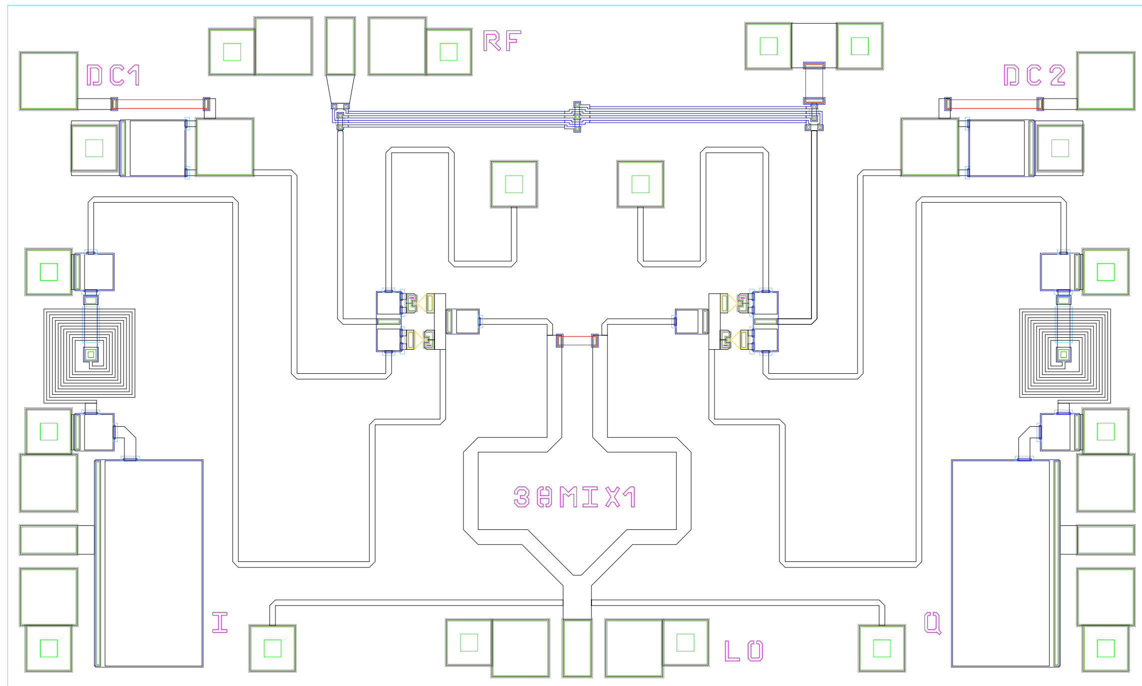

Fig. 3.21. Layout of the 31-38 GHz second-harmonic I/Q mixer. Chip dimensions are 2.0 x 1.2 mm. GaAs substrate is 100 µm thick.

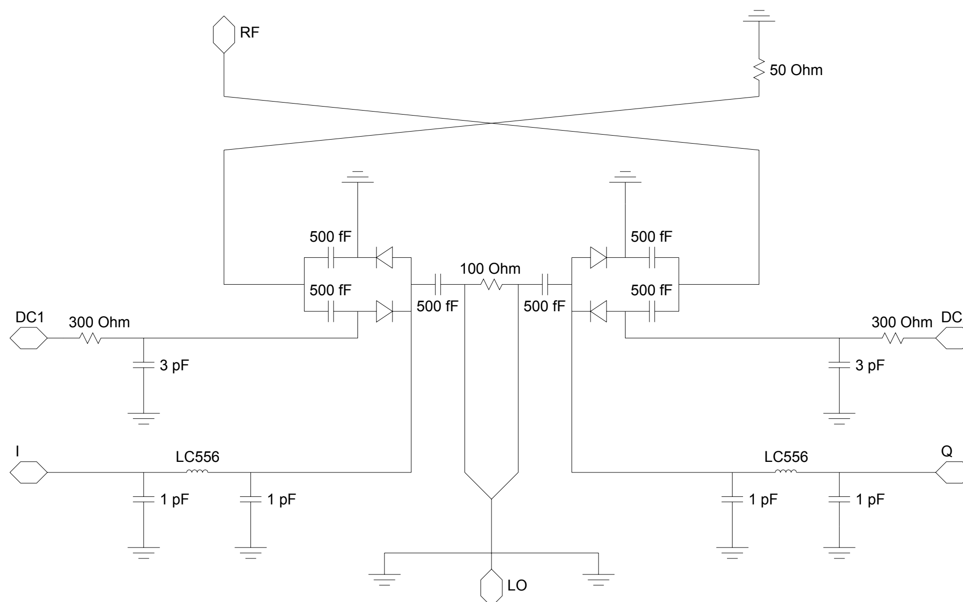

Fig. 3.22. Schematic of the 31-38 GHz second-harmonic I/Q mixer. Diodes are 1x3 µm.

match the two sub-mixers to 50 Ω to avoid dumping energy from the RF signal into the load resistor on the "isolated" port and thus increasing the conversion loss.

The LO signal enters through a port on the bottom edge of the chip, and is distributed to the two sub-mixers via a Wilkinson in-phase power divider. Astute readers may notice that the arms of the Wilkinson divider appear roughly equivalent in length to the Lange coupler on the RF side, whereas a divider tuned to the LO frequency in this sub-harmonic mixer should have been twice as long. This was not a mistake, however. Consider that all that is required for the LO splitter is an in-phase and magnitude-balanced division of the signal which could have been accomplished with a simpler T-junction. The point of a Wilkinson in this context is simply to provide some isolation between the two sub-mixers, since cross talk between them would degrade the image rejection. Since the LO signals are fed to the mixers in phase, so will be the LO reflections. Cross talk will therefore not occur at this frequency, but instead at the RF frequency (whose signals are phased in quadrature with one another), and to a lesser extent the higher-order mixing products. That is the reason the Wilkinson power divider was tuned to the RF frequency, even though its primary function is in the LO circuit. The matching network on the LO port includes the arms of this divider ($\lambda/8$ long in this band), preceded by a short inductive transmission line, and followed by shunt inductive stubs to ground.

The two sub-mixers are biased independently, allowing the image rejection to be fine-tuned by adjusting the DC current on each side. Bias current is routed through the diodes in series, connecting to a pair of coupling capacitors on the RF side. The bias lines are a quarter-wavelength long at the RF frequency, allowing that signal to pass unimpeded to the diodes while providing a somewhat inductive ground return for the LO.

The IF signal is extracted from the diodes on the LO side through a long high-impedance transmission line. A bypass capacitor shorts it to ground a quarter LO-wavelength away from the diodes. Thus, it serves as a ground return for the RF and does not play a significant role in the LO circuit. The bypass cap forms the first element of a simple low-pass filter along with an on-chip spiral inductor and a second shunt capacitor. The inductor was modeled in Sonnet up to several harmonics of the RF band, and in spite of passing through several resonances in that range, it does not have a significant impact on the

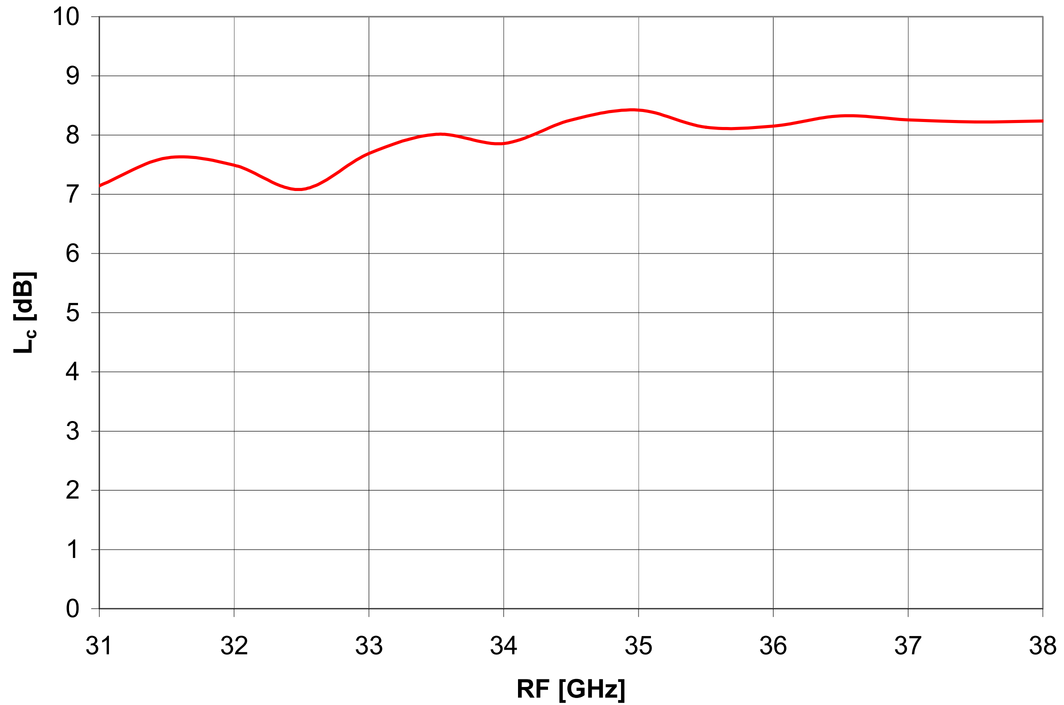

Fig. 3.23. Simulated conversion loss versus RF for the 31-38 GHz second-harmonic I/Q mixer. IF was fixed at 1 GHz, LO power was +10 dBm, and bias current in each sub-mixer was 1.1 mA.

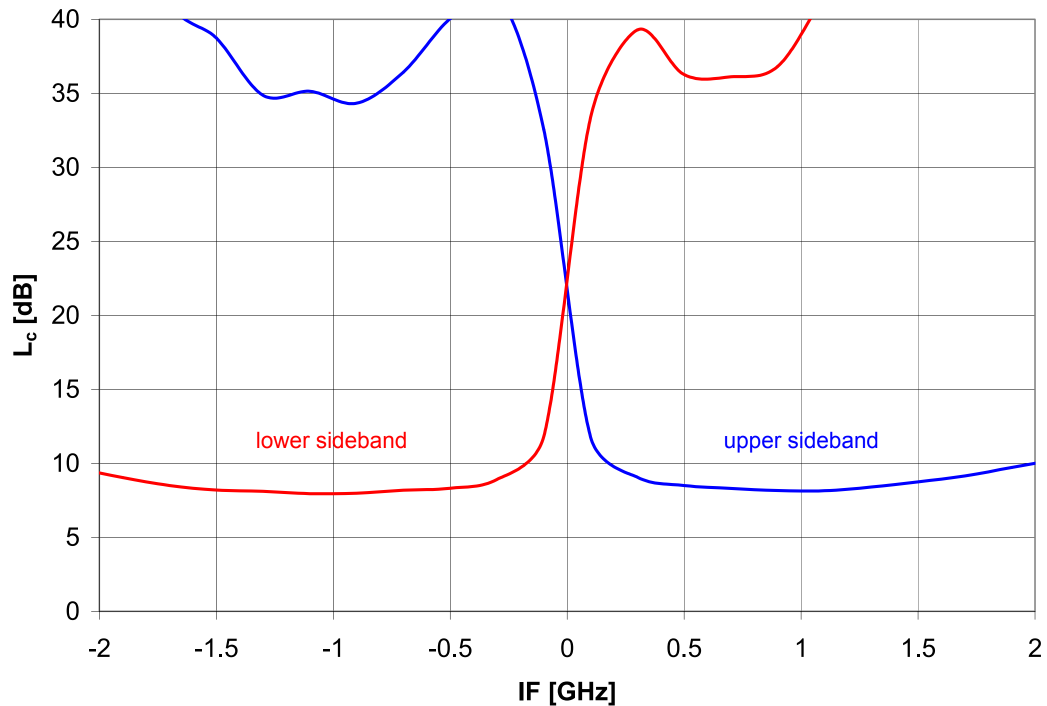

Fig. 3.24. Simulated conversion loss versus IF for the 31-38 GHz second-harmonic mixer. Plot shows theoretical image rejection using an ideal (off-chip) IF hybrid. RF frequency was 34 GHz, LO power was +10 dBm, and bias current was 1.1 mA.

behavior of the rest of the circuit. Finally, just before the IF port is a 20 pF coupling capacitor, allowing the circuit to operate to a lower IF limit of about 250 MHz. The parasitic shunt capacitance of this unusually large element was not significant in the IF band and was isolated from the rest of the circuit at higher frequencies by the aforementioned low-pass filter.

Almost all the passive elements in the circuit were modeled with Sonnet from the IF band up to the third harmonic of the RF with Sonnet's 2.5D EM-simulator. These were then imported into HP's Advanced Design System along with a Schottky diode model for Harmonic Balance Analysis. The chip is currently in fabrication at United Monolithic Semiconductor using the BES Schottky Diode MMIC process. Simulated results, shown in Figures 3.23 and 3.24, predict about 8 dB conversion loss across all frequency ranges, with +10 dBm LO power. Image rejection with an ideal off-chip IF hybrid is approximately 30 dB. The actual image rejection will of course depend on the off-chip components as well as the selective biasing that was described earlier.

3.5. Doubly Balanced Mixers

The benefits of singly balanced mixers were explained in Section 3.1. Those same useful properties can be extended by using a doubly balanced mixer. They have greater LO noise and spurious signal rejection than singly balanced mixers and provide inherent isolation between all ports without the need of filtering [31]. In the microwave range where they have been most widely used, these mixers are generally believed to have greater conversion loss than their singly balanced counterparts. It will be argued in this section, however, that the simplification of the rest of the circuit in terms of port isolation and impedance matching reduces the parasitic losses to such a degree that conversion efficiency is actually improved in the millimeter-wave band over singly balanced topologies.

There are two standard doubly balanced mixer topologies in the literature: the so-called "ring" and "star" mixers, both illustrated in Figure 3.25. In both cases, a 180° hybrid is required on both the LO and

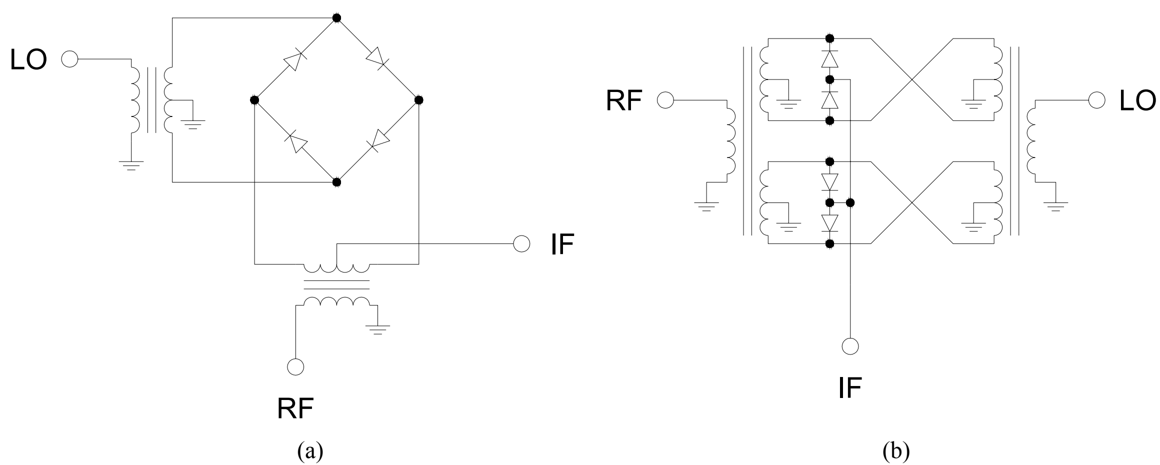

Fig. 3.25. Basic a) ring- and b) star-configurations of a doubly balanced mixer.

RF ports (often implemented with a transformer at lower frequencies). The IF signal is taken from the common, or isolated, port of one of the hybrids in the ring mixer, and from the common node in the center of the diodes in the star mixer. Isolation of all three ports from one another is guaranteed by symmetry. The ring or star of diodes, when pumped by a strong LO signal, acts as a polarity-reversing switch, to which the RF signal is then applied, and mixing occurs.

Two doubly balanced mixers were designed by the author for the ALMA project at NRAO (see Section 1.4). Their specifications were for balanced-mixers covering three bands: 70-92 GHz, 91-124 GHz, and 120-144 GHz. The IF band was quite low at 20-200 MHz, dual-sideband. These mixers were needed as part of a phase-locked-loop in the local oscillator system. *Doubly* balanced mixers were not required but turned out to be relatively easy to implement as a result of the low IF range, and the elimination of port isolation and biasing networks made for an elegant solution that in simulation met all specifications and exceeded the NRAO's conversion loss requirement by 6 dB!

Layouts of the 70-92 GHz and 120-144 GHz mixers are shown in Figures 3.26 and 3.28. The middle-band design was worked by another student. All three mixers utilize the ring topology. Ratrace hybrids were used to implement the baluns on the LO and RF ports.

For the 70-92 GHz design, the hybrids were large enough to fit around the diode ring, allowing an almost direct connection to the nodes between diodes. The resultant interlocking of the two hybrids was included in the simulation and did not have a serious affect on the circuit's operation. A quarter-

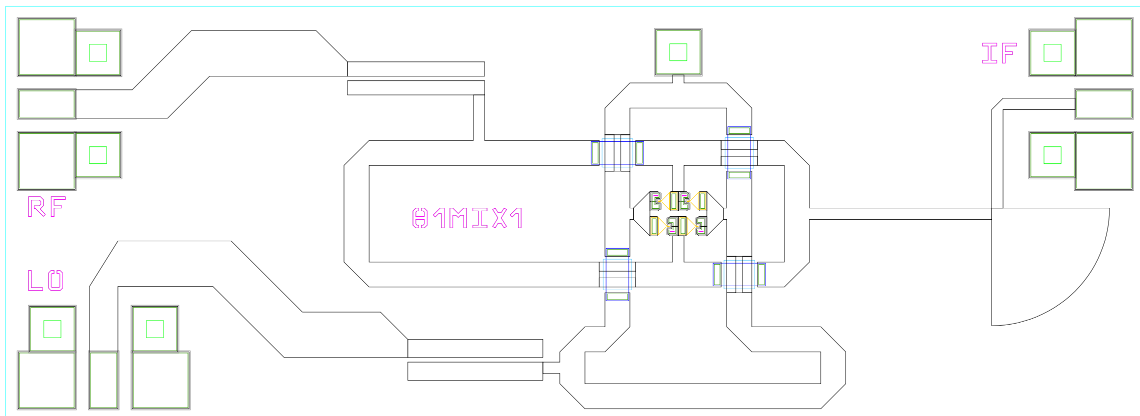

Fig. 3.26. Layout of the 70-92 GHz doubly balanced mixer. Chip dimensions are 2.0 x 0.73 mm. GaAs substrate is 100 μm thick.

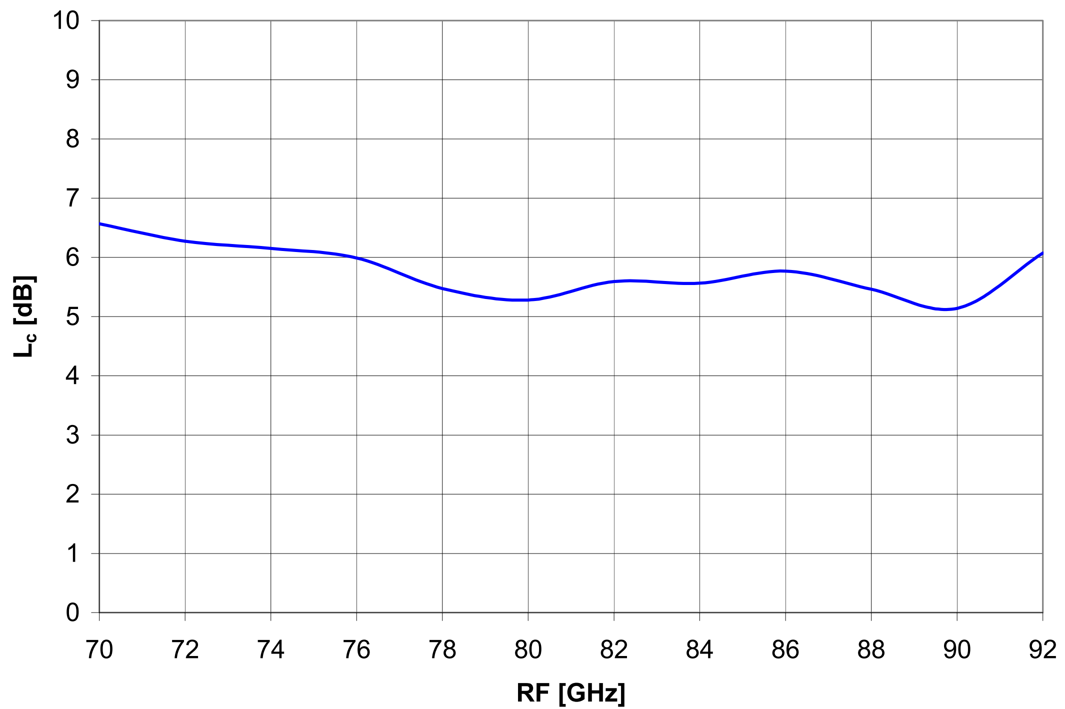

Fig. 3.27. Simulated conversion loss of the 70-92 GHz doubly balanced mixer. LO power was +5 dBm, and IF was fixed at 100 MHz.

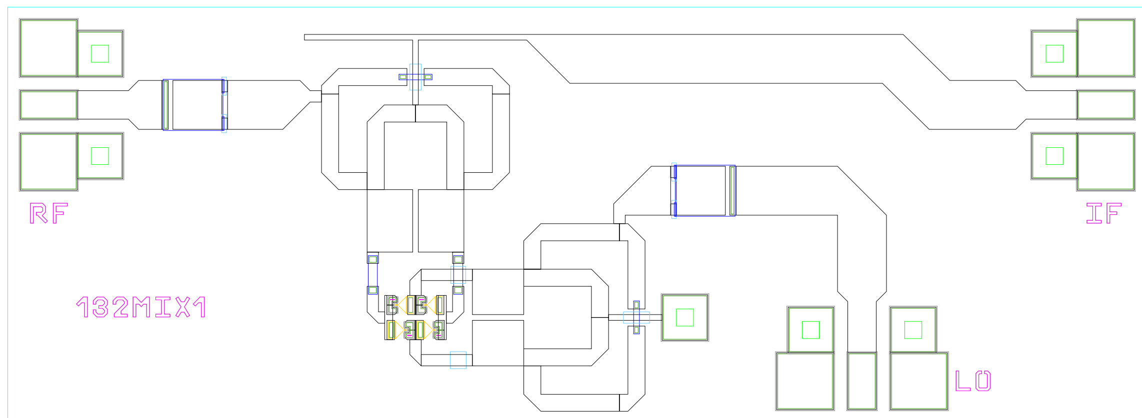

Fig. 3.28. Layout of the 120-144 GHz doubly balanced mixer. Chip dimensions are 2.0 x 0.73 mm. GaAs substrate is 100 µm thick.

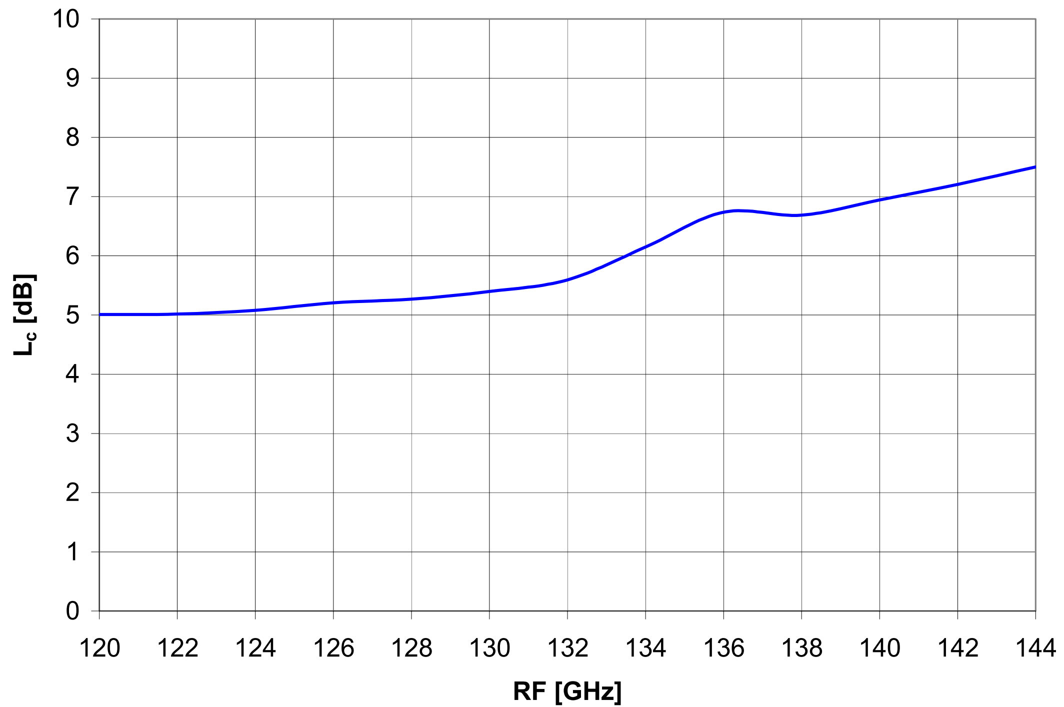

Fig. 3.29. Simulated conversion loss for the 120-144 GHz doubly balanced mixer. LO power was +5 dBm, and IF was fixed at 100 MHz.

wavelength coupled line section was used on both ports for impedance transformation and IF-blocking. The IF port is connected to the isolated port of the RF hybrid. On the isolated port of the LO hybrid is a via hole which serves as an IF ground return. While the hybrids themselves provide some LO-to-IF isolation, the IF output line includes a radial stub to further notch out the LO pump signal.

The 120-144 GHz mixer is similar topologically but with a different layout approach. The hybrid rings in this case were too small to fit around the four diodes, so they could not be interlocked as before. The hybrids then had to be folded into a "pac-man" structure to put the differential ports on the same side, and the isolated port was directed backward across the ring. The transmission line was necked-down around the crossover point to minimize coupling across different areas of the ring which would affect its behavior. While this new approach complicates the layout of the hybrids, it allows the matching networks to be closer to the diodes, which in turn has the potential for greater bandwidth. As before, the IF port is connected to the isolated terminal of the RF hybrid, and the IF ground connection was on the LO hybrid. A simple stub was used to further notch out the LO pump on the IF output line.

The middle-band mixer, designed by a colleague at Caltech, takes yet another approach to the layout of a ring mixer. His idea was to use a crossover in the diode ring itself, eliminating the need for crossovers in the hybrids. As usual, the passive elements were modeled in Sonnet up to several harmonics of the highest operating frequency, and imported into ADS for Harmonic Balanced simulation. All three mixers were fabricated by United Monolithic Semiconductor using their BES Schottky diode MMIC process, and are currently in testing at the NRAO. Simulations predict that each mixer will have roughly 6 dB conversion loss with +5 dBm of LO power. If the measurements agree with simulation, than this will be an extraordinary success, as it exceeds the performance of any MMIC mixer at this frequency that the author has designed before.

4 Millimeter-Wave Low-Noise Amplifiers

We turn our attention in this chapter to amplification, specifically in the case where noise is a concern. Many of the projects the author has been involved in are noise-limited systems, such as passive radiometers or radio telescopes. The ultimate sensitivity of these instruments depends more strongly on the front end low-noise amplifier than anything else in the system. This makes MMIC LNAs a critical component in many applications.

4.1 W-Band Low-Noise Amplifiers for Millimeter-Wave Imaging

Among the more interesting emerging applications in W-band is that of passive, real time imaging. Such cameras would have a broad range of uses, including security, environmental remote sensing, and adverse-weather aircraft landing systems [40]. As described in Section 1.3, development projects are underway at both TREX Enterprises and Millivision. The design of the latter system leads to some unique requirements for a MMIC low-noise amplifier. The chip they requested would need to amplify a 94-96 GHz band with minimum noise figure while at the same time passing a large signal sub-harmonic pump at 47 GHz. Rather than design an awkward dual-band amplifier, it was decided to try for an octave-bandwidth version which would be more widely applicable to other projects.

Because of the large number of amplifiers that are typically required for a single imager, the developers are highly motivated to keep the chip cost down as much as possible. One way that this has been accomplished is to utilize a relatively young transistor technology known as the Metamorphic-HEMT. This is an InP pHEMT transistor grown on a GaAs substrate. The hope is that it can match or even exceed the performance of InP transistors, but at lower cost.

The octave-bandwidth LNA for Millivision, photographed in Figure 4.1, was designed using a

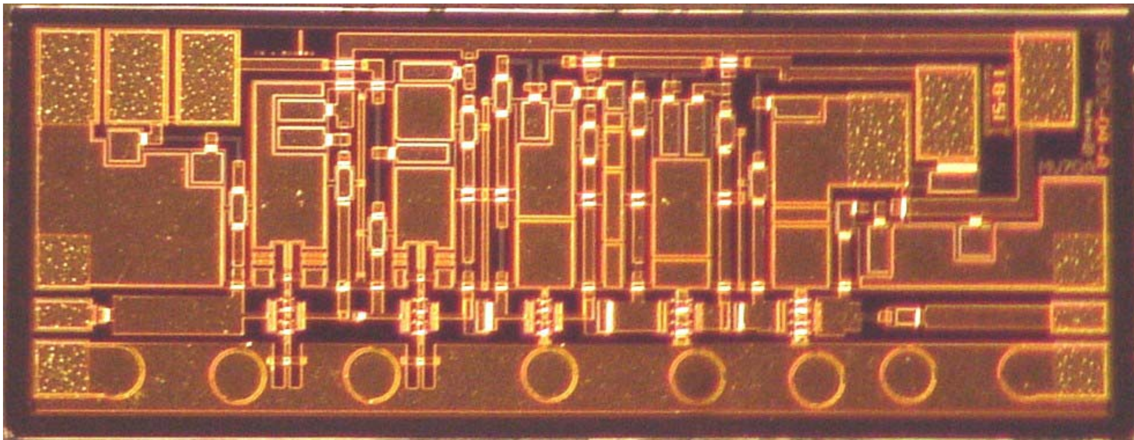

Fig. 4.1. Photograph of the 47-96 GHz LNA for Millivision. Chip dimensions are 2.0 x 0.73 mm. GaAs substrate is 100 μm.

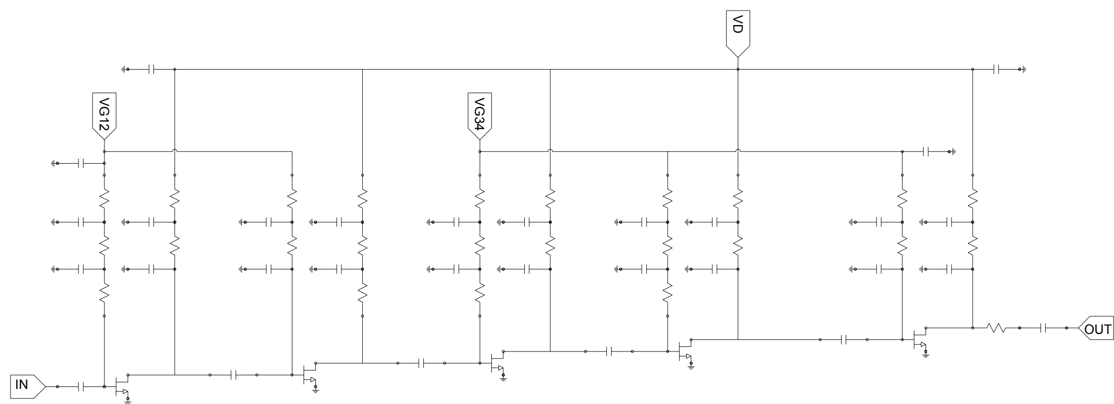

Fig. 4.2. Schematic of the 47-96 GHz LNA.

0.15 μm MHEMT process available from Raytheon. This chip would be substantially less expensive in large quantities than its InP counterparts, in part because the MHEMT wafers are 10 cm in diameter instead of 7.5 cm which is common for InP. Further, the MHEMT process at Raytheon is a streamlined production process, unlike the experimental InP processes that have been used in the past.

The circuit was realized with Grounded Coplanar Waveguide (GCPW) technology. Vias holes were used in the grounded areas to suppress parallel-plate mode leakage. It is a five stage common-source design with output gate periphery of 100 μm. Bias for each stage was supplied through transmission lines that are shunted by small MIM capacitors, effectively making short-circuited stubs at the RF frequency. The impedance at each stage is tuned by adjusting the lengths of these stubs. Inductive stubs were also used on the sources of the first two stages to bring the noise-optimum impedance of the transistor stage closer to the maximum-gain impedance [41].

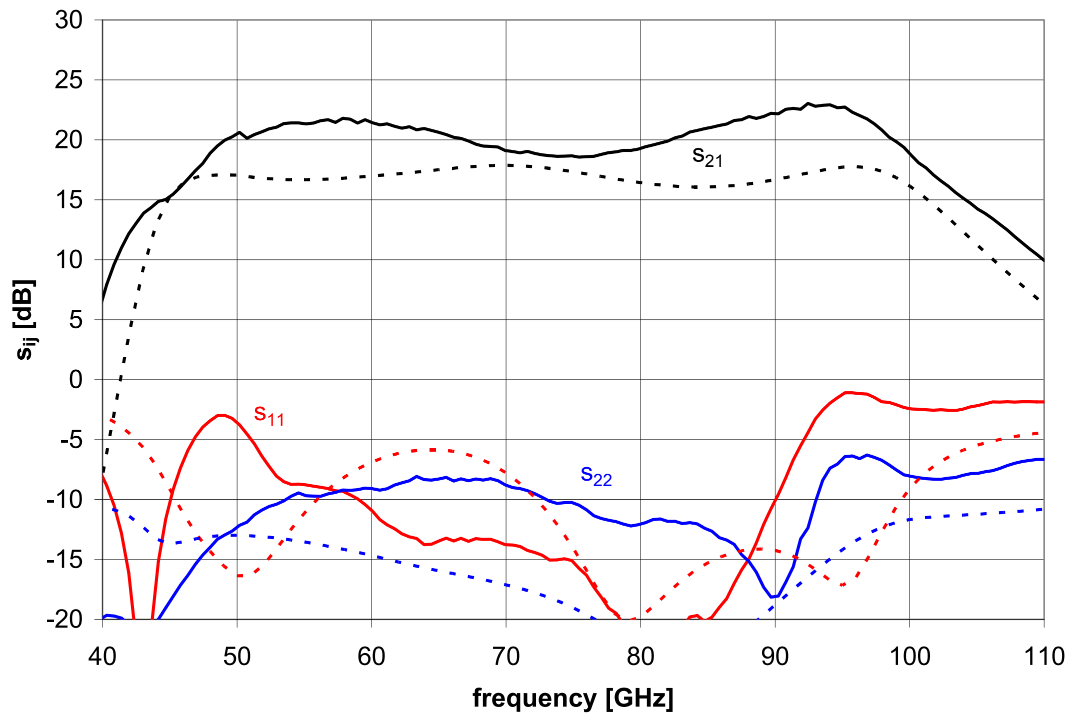

Fig. 4.3. S-parameters for the 47-96 GHz LNA. V_G = -0.55 V, V_D = 1.5 V, I_D = 46.1 mA. Simulated data is shown with dashed lines, measured data with solid lines.

Series resistors were placed in the bias lines to improve stability below band where the transistor gain is very high. Smaller resistors were used in the drain lines to avoid burning too much DC power in biasing the circuit.

The chip was tested on a 110 GHz Vector Network Analyzer at Raytheon. The results are plotted in Figure 4.3. While the circuit achieves about 20 dB of gain over the desired band, the input return loss is significantly worse at 95 GHz than expected. This may be related to the relatively crude transistor model that was used. The model was extrapolated from measurements below 50 GHz on samples provided by the foundry. Unfortunately, the samples did not come with calibrated test structures, leading to some uncertainty in the reference planes of the model. Further attempts to model the Raytheon devices for W-band applications have had limited success.

4.2 KA- AND Q-BAND LOW-NOISE AMPLIFIERS FOR RADIOMETRIC APPLICATIONS

Of course, millimeter-wave imagers are not the only applications that would benefit from reducing the cost of LNAs. Two lower frequency LNAs were developed in parallel with the above W-band MMIC, taking advantage of the same MHEMT technology provided by Raytheon. The primary motivation for these chips was the EVLA (see Section 1.4).

The first of these new chips is photographed in Figure 4.4. It is a 3-stage amplifier with 50, 50, and 100 μm transistor cells, respectively. Inductive source degeneration was used as before to improve the input match of the circuit while maintaining good noise performance. Bias was again supplied to the active devices via short-circuited stubs which serve the secondary purpose of impedance matching.

Series resistors were once again introduced into the bias lines for stability purposes. One issue that has come up with MMIC LNAs like this one is the realization of very high valued thin-film resistors for gate bias, like the two 100 Ω elements connected to the gates of stages 2 and 3 in this design (see Figure 4.6). Such a resistor acts as an RF choke in the absence of broadband inductors which are very difficult to realize at millimeter wavelengths. However, the impedance of the resistor must be very high in order to avoid loading the main RF transmission line. Therefore resistor values of several kΩ are not uncommon. The problem is that while *DC* resistance can in principle be made as large as desired by lengthening the thin-film element, the effective *RF* impedance is degraded by distributed effects. In other words, a long thin-film resistor on a MMIC substrate can be thought of as a very lossy transmission line. The RF signal is essentially absorbed after some characteristic distance, preventing the wave from ever reaching the far-end of the resistor. Simulations have verified that there is an upper-limit to the resistance value that can be realized at high frequency, beyond which more resistive material, or even open- and short-circuit termination of the resistor, will have no effect. This limit depends on the substrate characteristics, as well as the sheet-resistance of the film used.

Unfortunately for these circuits, the resistive TaN film available in Raytheon's MHEMT process has an unusually low sheet resistance, 6 Ω/□, which severely restricts the use of resistors as chokes (mesa-resistors are also available in the process, but their temperature sensitivity precludes their use in cryogenic

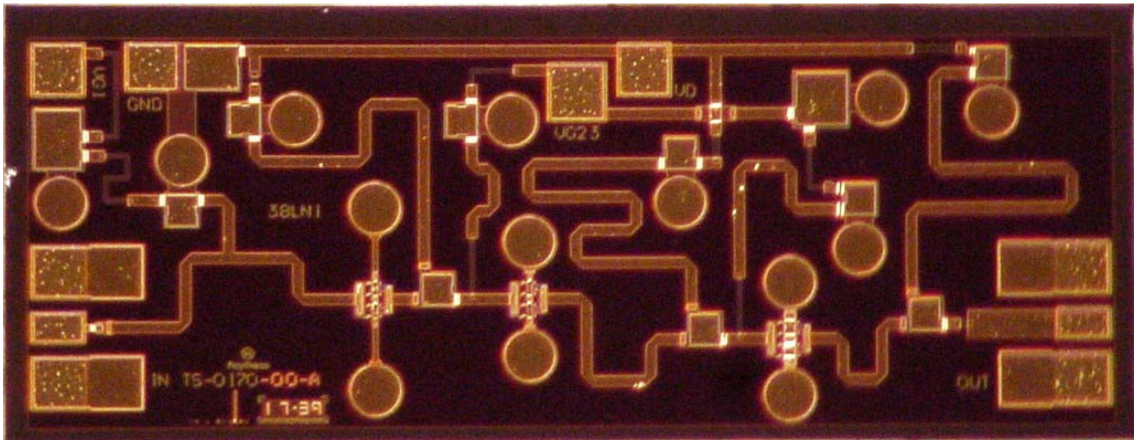

Fig. 4.4. Photograph of the 26-40 GHz low-noise amplifier. Chip dimensions are 2.0 x 0.74 mm. GaAs substrate is 100 μm thick.

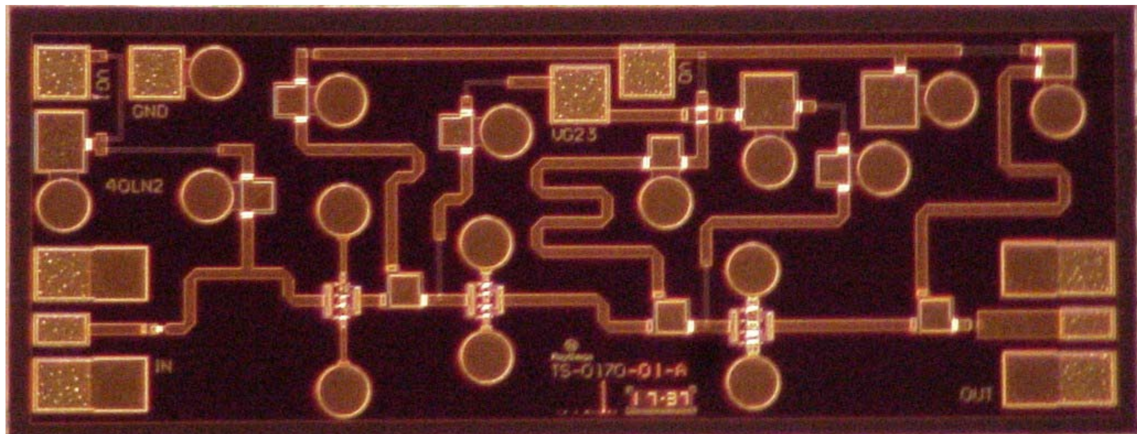

Fig. 4.5. Photograph of the 33-50 GHz low-noise amplifier. Chip dimensions are 2.0 x 0.74 mm. GaAs substrate is 100 μm thick.

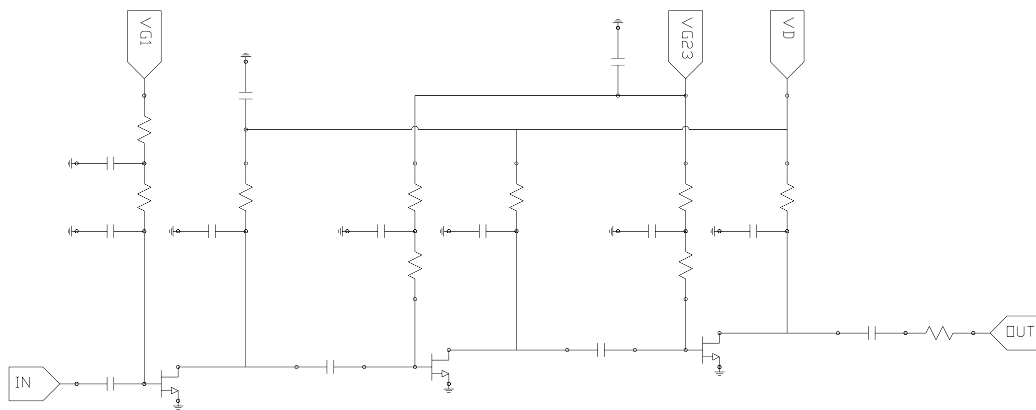

Fig. 4.6. Schematic of the 26-40 GHz and 33-50 GHz low-noise amplifiers.

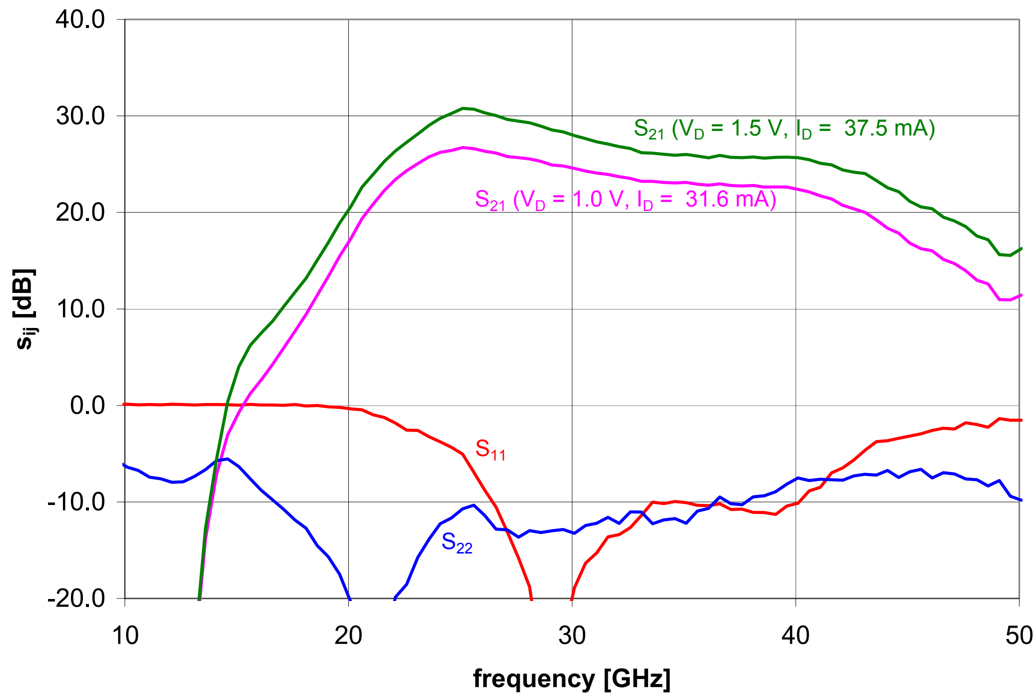

Fig. 4.7. S-parameters for the 26-40 GHz low-noise amplifier. VG1 = -0.3 V, VG2 = VG3 = -0.4 V, and drain voltage and current are as shown on the plot.

applications). The upper limit to RF resistance that can be achieved is only about 100 Ω so that is what was utilized in the 26-40 GHz design. This element was left out of the first stage, because in that position it would have had an unacceptable impact on the overall noise figure of the amplifier.

The chip was first tested on an HP 8510C Vector Network Analyzer. The key results are in Figure 4.7. The circuit achieves a gain of approximately 25 dB over its design bandwidth with input and output return loss of about 10 dB. Its noise characteristics were also measured in a cryogenic dewer cooled to 15 K. The equivalent noise temperature of the LNA was under 25 K from 32-38 GHz. While these results are not as good as current InP amplifiers are capable of, and thus not suitable for the front-end LNA in either the DSN Array or EVLA, it is still an acceptable low cost RF post-amplifier for both of these projects.

A similar LNA design, shown in Figure 4.5, was completed for the EVLA Q-band receivers. While it was designed for a nominal gain of 23 dB from 33-50 GHz, the engineers at NRAO were

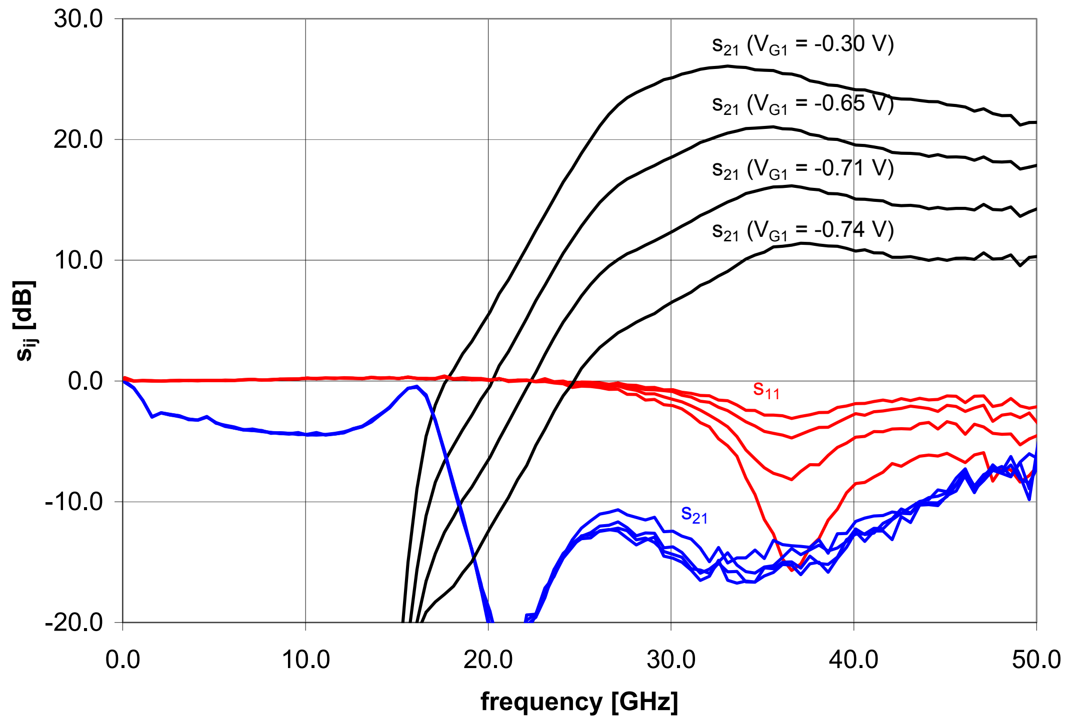

Fig. 4.8. S-parameters versus V_{G1} for the 33-50 GHz low-noise amplifier. $V_{G2,3}$ = -0.5 V, V_D = 1.5 V, I_D = 14.6-27.6 mA.

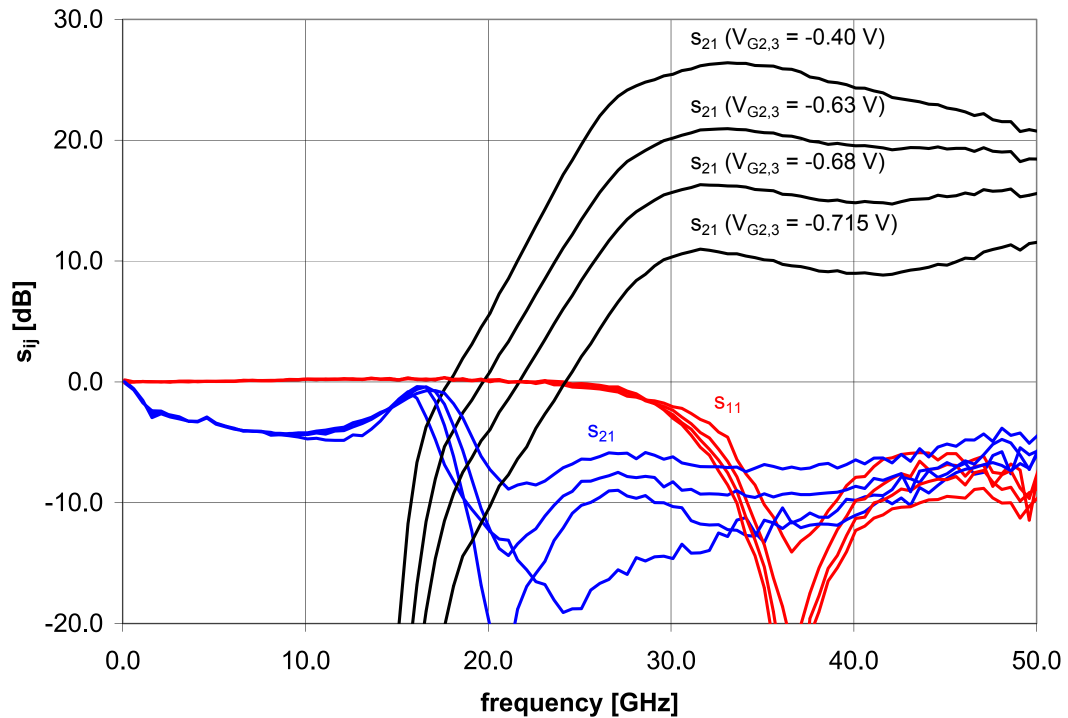

Fig. 4.9. S-parameters versus $V_{G2,3}$ for the 33-50 GHz low-noise amplifier. V_{G1} = -0.3 V, V_D = 1.5 V, I_D = 14.7-35.5 mA.

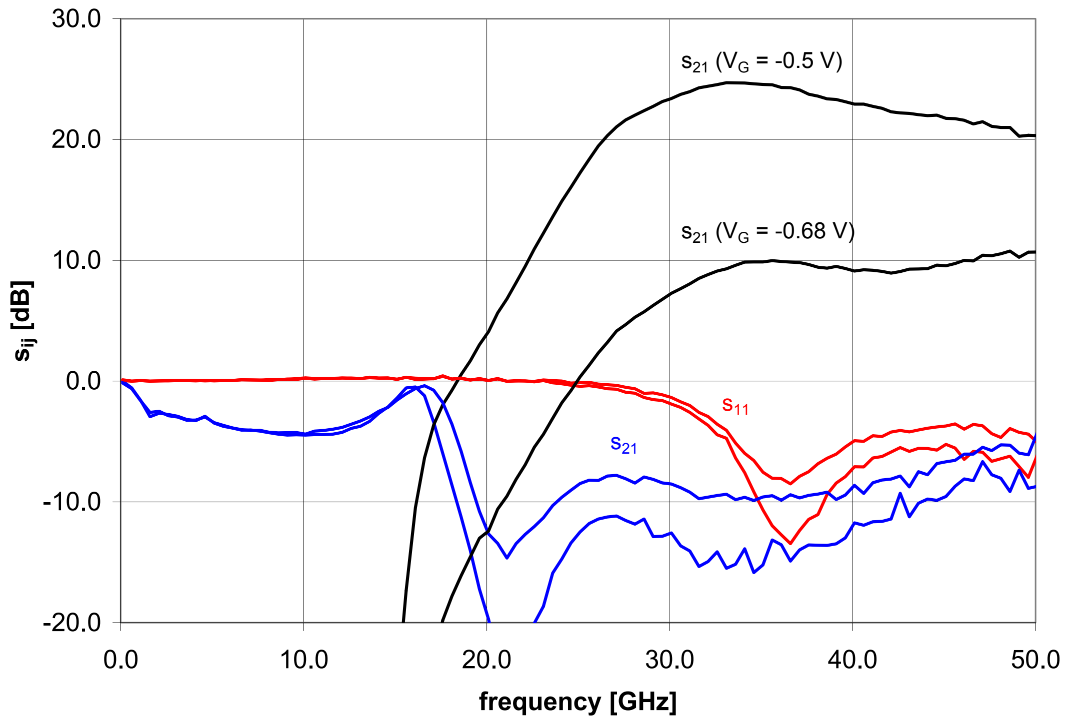

Fig. 4.10. S-parameters versus $V_{G1,2,3}$ for the 33-50 GHz low-noise amplifier. V_D = 1.5 V, I_D = 3.6-20.1 mA.

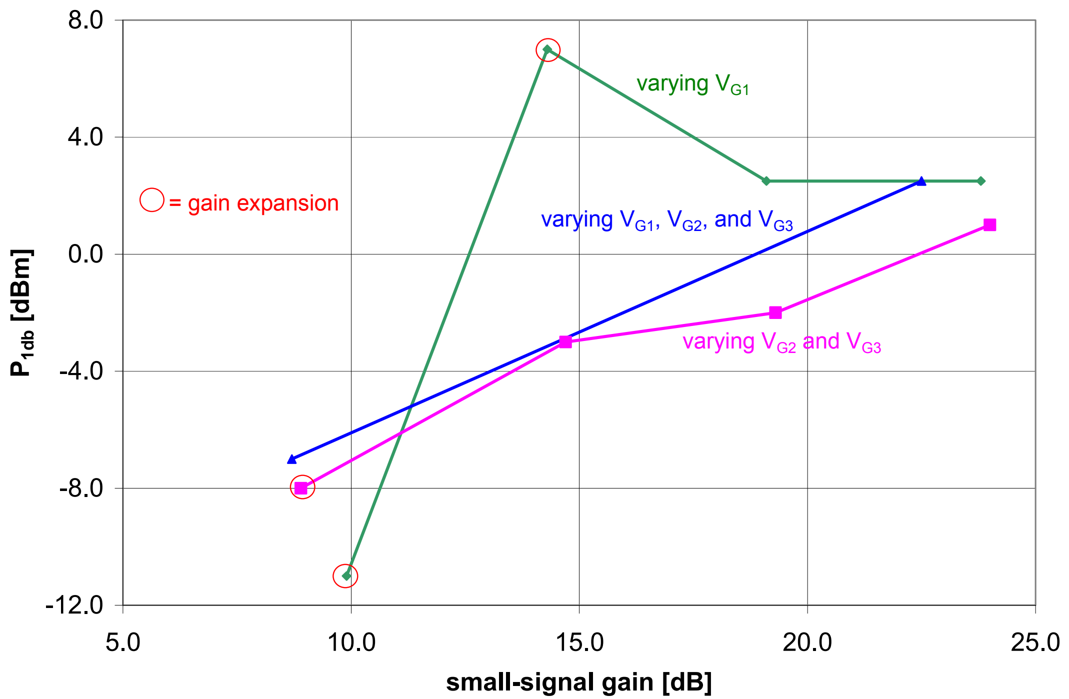

Fig. 4.11. Output powers corresponding to 1 dB gain distortion for the 33-50 GHz low-noise amplifier. The points circled in red correspond to 1 dB gain expansion rather than compression.

interested in possibly controlling the gain by varying the bias conditions. They were motivated in part by a desire to improve the "headroom" of their system, which they define as the difference between the expected signal power and the 1% compression point of any active component, which in turn is assumed to be 12 dB below the 1 dB compression point. It was generally agreed upon that the drain bias would remain constant, but there was some uncertainty about which gate voltages were best used for this purpose. Thus, several sweeps were taken, and are plotted in Figures 4.8-4.10. In Figure 4.8, it can clearly be seen that a relatively uniform change in gain can be achieved by turning down the first stage gate voltage. However, in order to reduce the gain by 10 dB with this single stage, it is necessary to nearly pinch off the transistor, which significantly degrades the input return loss. In Figure 4.9, we also show a relatively uniform change in the gain by turning down the second- and third-stage gates. In this case the output return loss is degraded, but since two stages are affected simultaneously, the voltage does not have to be reduced as much and the return loss is not inflicted as badly as in Figure 4.8. Finally, Figure 4.10 shows how the gain can be reduced by turning down all three stages. The gain is still relatively flat, and the return loss is only slightly degraded, even with a 15 dB reduction in gain.

Large-signal measurements at 40 GHz were also performed under the same bias conditions that were used above. The VNA was switched to CW mode and used as a signal source, while the output signal of the amplifier was monitored with a power meter. Under high-gain bias conditions, the amplifier behaved exactly as one would expect, with the gain dropping as input power is increased beyond a certain limit. The 1 dB compression point, where the gain had dropped by 1 dB relative to its small-signal gain, was recorded. For the low-gain bias conditions, however, a somewhat different behavior was observed. During these tests, in which one or more of the stages was nearly pinched off, a large input signal would actually begin to turn those transistors back on, causing the gain to initially increase at moderately high power rather than decrease. This "gain expansion" is presumably just as damaging to linearity requirements as compression, so for the purposes of discussion, "P_{1dB}" shall be defined as the lowest output power level at which large-signal gain is changed (either by expansion or compression) by more than 1 dB from its small-signal gain.

Figure 4.11 shows a plot of P_{1dB} versus small-signal gain at 40 GHz for each of the three biasing scenarios described earlier. What is most interesting about this plot is the fact that P_{1dB} can actually *increase* at some bias points while reducing the gain. This can be explained as cancellation between the gain expansion and compression phenomena described above. While the effect is clearly illustrated in the curve for V_{G1}-variation, it may also be present to some degree in the other two curves, but the measurement was not taken at enough bias points to detect it.

The data presented here clearly shows that it is possible to reduce the gain of this amplifier from 25 dB to 15 dB without prohibitively degrading the gain flatness, return loss, or headroom. Even without the P_{1dB} "peaking" that occurs at some bias points, it may still be advantageous to reduce the amplifier gain (from strictly a linearity perspective) since in none of the three curves does the output compression/expansion point fall as quickly as the small-signal gain. In other words, P_{1dB} referred to the *input* was always increased at lower gain during these measurements, regardless of how it was done.

4.3 A Ka-Band Low-Noise Amplifier for the DSN Array

While the Metamorphic-HEMT transistor promises to be an important low-cost alternative to InP pHEMTs, they have not yet achieved the level of noise performance that is required for the front-end LNAs of a sensitive radio telescope like the DSN. It is for this express purpose that another Ka-band low-noise amplifier, covering 30-40 GHz, has been designed using the 0.1 μm InP process at TRW.

A layout of the chip appears in Figure 4.12, and a schematic is in Figure 4.13. As with the other Ka-band LNA, this is a 3-stage design with inductive source degeneration on the first stage. All three transistor cells use a four finger topology with 50 μm total gate periphery. A common DC bus supplies bias current to all three drains, but a separate pin is provided for each gate bias to allow maximum flexibility in tailoring the gain and noise of this circuit.

The MMIC was designed using a small-signal transistor model extracted from 0-50 GHz measurements made on sample transistors at JPL. Noise was simulated using Pospieszalski's approach [43]

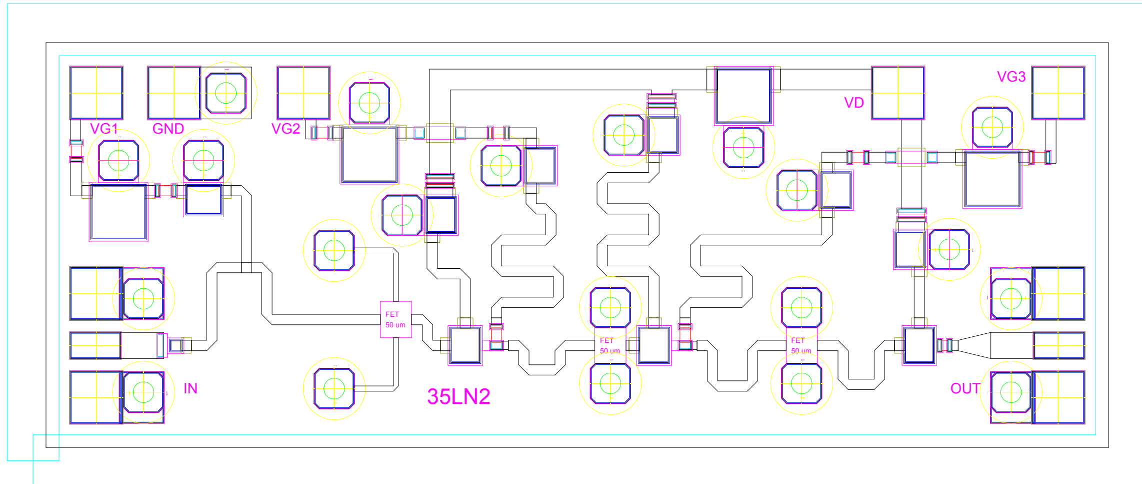

Fig. 4.12. Layout of the 30-40 GHz low-noise amplifier. Chip dimensions are 2.1 x 0.83 mm. InP substrate is 75 μm thick.

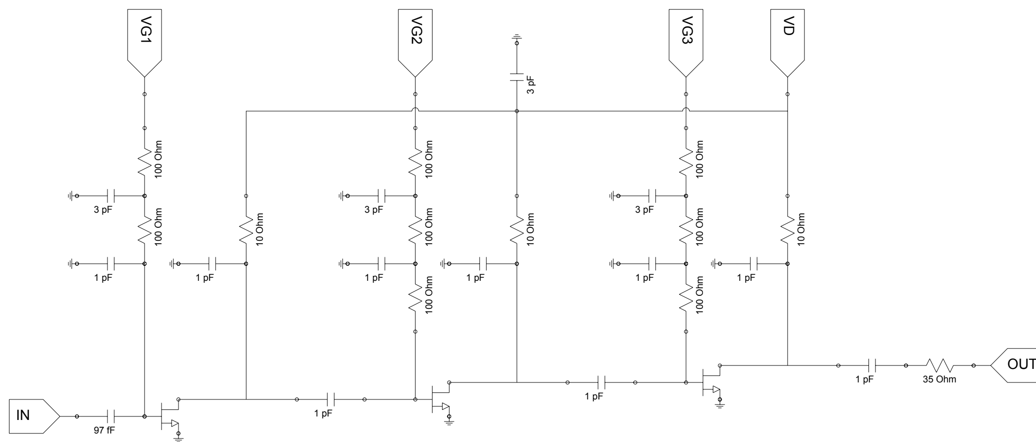

Fig. 4.13. Schematic of the 30-40 GHz low-noise amplifier. All FETs have 4 x 12.5 = 50 μm gate periphery.

with an assumed drain temperature of

$$T_{drain} = 300 + 6T_{amb} \tag{4.1}$$

where T_{amb} is the ambient physical temperature of the device. This approximate equation has been arrived at empirically, based on past amplifier designs.

The simulated performance of the chip is shown in Figure 4.14. It achieves flat small-signal gain of about 21.5 dB over the design band of 30-40 GHz. The equivalent noise temperature is 13 K at 32 GHz

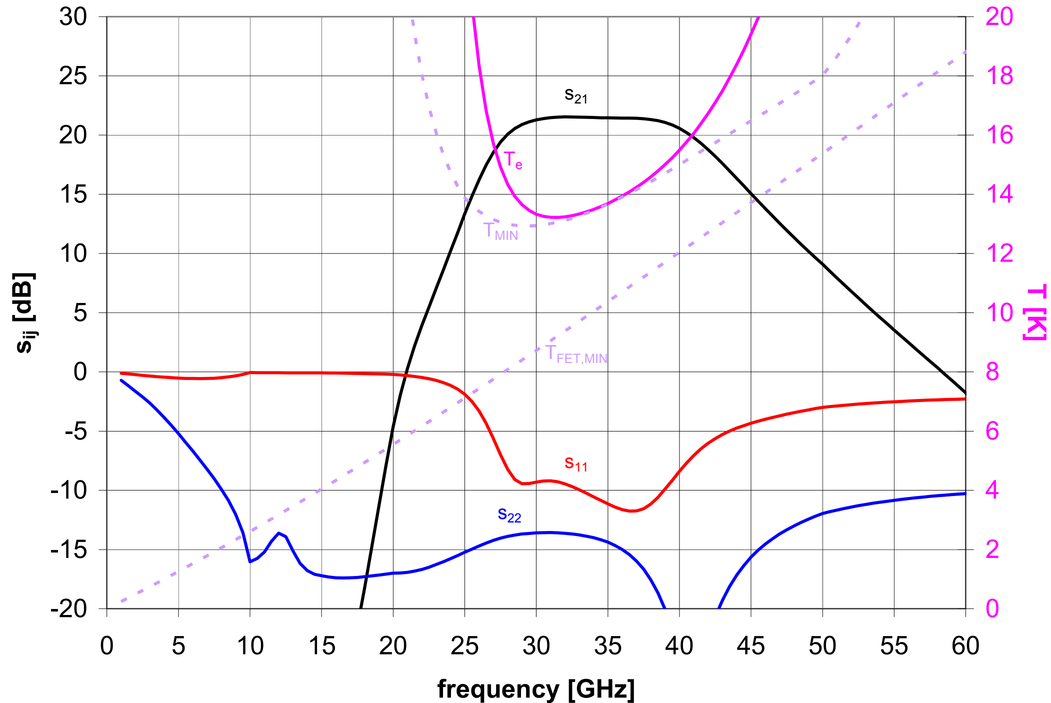

Fig. 4.14. Simulated s-parameters and equivalent noise temperature for the 30-40 GHz low-noise amplifier. V_D = 0.5 V, I_D = 40 mA. T_e is the equivalent noise temperature of the chip, T_{MIN} is the minimum noise temperature of the chip, and $T_{FET,MIN}$ is the minimum noise temperature of a single transistor.

when cooled to 15 K. Input return loss is approximately 10 dB, and output return loss is about 15 dB.

The minimum noise temperatures for the amplifier and a single transistor are also plotted in the graph, which provide good information for diagnosing the limitations and tradeoffs of the design. T_e and T_{MIN} are tangential within the band, indicating a good noise match for the amplifier. However, the minimum FET noise reveals that roughly 4 K was added by the second and third stages. Optimally, if we assumed that the first stage contributes 6 dB of gain (slightly less than a third of the total gain due to source degeneration), and given that $T_{FET,MIN}$ = 9 K at 32 GHz, then we would have expected the second stage to contribute roughly (9 K)/4 = 2.25 K to the noise temperature of the amplifier. The extra 2 K may be present because the first stage has less than 6 dB of gain, or that the second stage falls short of achieving the optimum noise performance of the FET. Source degeneration could have been added to the second stage to improve its noise, but this would have reduced the overall gain further.

It is worth noting at this point that there has been some debate over the use of MMIC technology for the front-end LNA of a radio telescope, even in large arrays such as the DSN. Some argue that MMIC

LNAs will never be able to compete with hybrid circuits in which the individual transistors may be hand-selected for optimum noise characteristics, at least at sufficiently low frequency where discrete component assembly techniques are accurate and repeatable. Indeed, the very best LNAs currently being produced by the DSN team at Ka-band are made in this way. The critical active devices for these hybrid circuits are selected from a particular InP wafer, made at TRW, that is known from past measurements to possess record-breaking cryogenic noise performance (an accomplishment that as yet is not repeatable, despite the best efforts of the foundry and JPL researchers for the better part of a decade).

While it cannot be refuted that hand-picked devices will always outperform a random assortment such as would be produced on a MMIC chip, the questions one must ask are as follows: How much time and money does it take to select the individual transistors and assemble the circuits in large quantities, and how much noise reduction does this effort buy you? MMIC technology may still have an edge if the performance gap is not too great, in that the system noise temperature may be traded off for collecting area by adding more elements to the array, thus achieving the same system performance for less cost.

The LNA described in this section is predicted to have an equivalent noise temperature of about 13 K at a physical temperature of 15 K, which is comparable to the best measurements to date using discrete FETs in this band. While noise performance is not the easiest metric to simulate accurately, it is hoped that this chip will be good enough to end the debate over implementation for the DSN front end.

5 Millimeter-Wave Power Amplifiers

Just as low-noise amplifiers dominate the performance of high-sensitivity receivers, power amplifiers are equally crucial components in the systems in which they are used. Power amplifier device technology and circuit design is now one of the most heavily researched subjects in the fields of microwave and millimeter-wave engineering. Much of a system's architecture and ultimate performance hinges on the available power and efficiency of its signal source.

Whereas the critical stage of an LNA is the input, which dominates the overall noise figure, most of the attention on a PA is focused on its output, which dominates the overall power level and efficiency. While these goals may not appear to be mutually exclusive, the practical constraints, specifications, and operating environment of a PA are much different than those of an LNA, which naturally leads MMIC engineers to make very different design decisions and results in circuit implementations that bear little resemblance to their low-noise counterparts.

The maximum power available from an amplifier, if it is designed well, is proportional to the physical size of the output stage, often measured by the total gate periphery in millimeters. To first order, the best output power is then achieved by selecting a *load-line*, or trajectory in the I-V plane, that allows the maximum swing in current and voltage [44]. Better efficiency can be obtained by using non-linear load-trajectories that stay close to the current and voltage axes, minimizing dissipation of power in the transistor [45]. Unfortunately, such techniques are difficult to realize at millimeter-wave frequencies.

Because the optimal power condition implies a load impedance that is not conjugately matched to the transistor, a high-power output stage will often have too little gain to be useful by itself, particularly at high frequencies. Therefore, a practical millimeter-wave PA has to be designed with multiple stages. The preceding stages will generally be smaller, but one must be careful that the increase in size from stage to stage does not "outrun" their gain. Otherwise, one of the drivers will saturate first, and the lion's share of DC power feeding the last stage will be wasted.

The difficulty in modeling excessively large transistors in the millimeter-wave range, where distributed effects become significant, usually means several smaller devices will have to be power combined at the output. On-chip, two-way [46], four-way [47], and eight-way [48] power-combining networks are common, but much beyond that the increasing losses of these passive networks become prohibitive. An exciting field of research is in *quasi-optical* power-combining in which the outputs of large numbers of transistors are combined in free space [50]. Such grand schemes are beyond the scope of this thesis, however.

5.1 A W-Band Monolithic Medium Power Amplifier

New applications in W-band, such as automotive radar, millimeter-wave imaging, and even communications are driving millimeter-wave power amplifier research forward. Recent developments in MMIC W-band PA's have shown output powers approaching 0.5 W at 95 GHz [48], and power added efficiencies of almost 20% [48, 49].

However, in the race to establish new records for output power, the trend of circuit designers has been toward narrow-band designs, requiring highly customized chips to be developed for each new application at great cost. The role of a more general purpose, medium power amplifier has been largely neglected. A literature search has only turned up one reference fitting those requirements, wherein two InP MMIC amplifiers are reported, covering 65-145 GHz and 75-110 GHz, with power outputs of 25 mW and 50 mW, respectively [46].

Here, we present design and test results of a 75-95 GHz medium power amplifier with 100 mW power capability and with associated large-signal gain of 11 dB. This amplifier would be useful for millimeter-wave applications requiring moderately high power over a broad frequency range.

A photograph of this chip appears in Figure 5.1. The circuit was fabricated at TRW on a 50 μm GaAs substrate using 0.1 μm AlGaAs/InGaAs/GaAs pseudomorphic-HEMT technology. The circuit dimensions are 2600 x 840 μm.

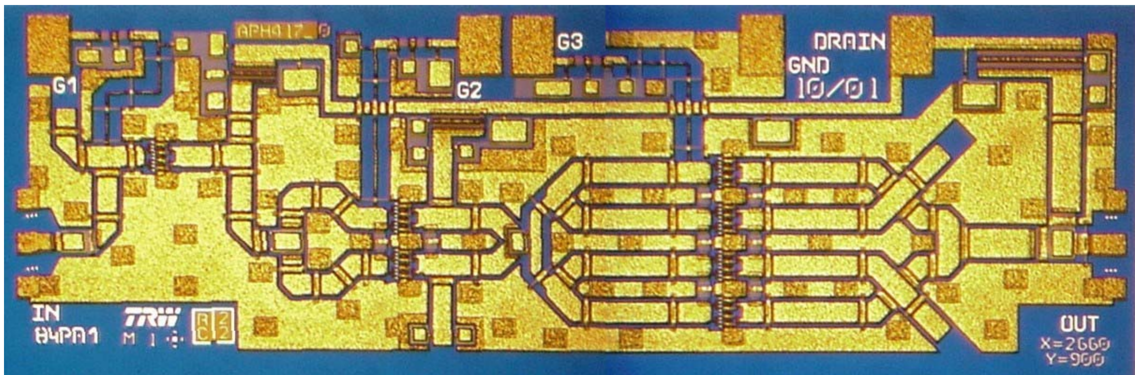

Fig. 5.1. Photograph of the 75-95 GHz power amplifier. Circuit dimensions are 2.6 x 0.84 mm. GaAs substrate is 50 μm thick.

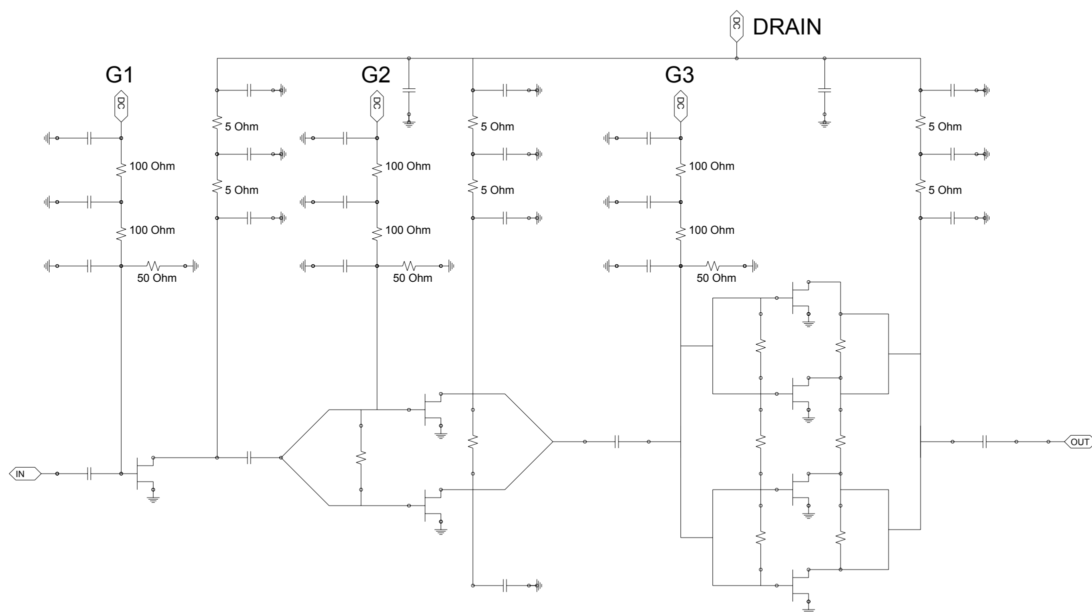

Fig. 5.2. Schematic of the 75-95 GHz power amplifier. All transistor cells are 8 x 20 μm for total peripheries in three stages of 160 μm, 320 μm, and 640 μm.

The MMIC amplifier is a 3-stage design with 1, 2, and 4 identical transistor cells in each stage, sequentially. This geometric increase in gate periphery from stage to stage ensures that the output transistors will enter compression first, as long as the preceding stages have at least 3 dB gain. All transistor cells are 8-finger devices with 20 μm gate widths, resulting in 640 μm total output periphery for the chip. A small-signal model of this device was extracted from on-wafer measurements of calibrated test-structures below 50 GHz.

The circuit is designed with grounded coplanar-waveguide (GCPW) technology. The advantage of this approach over microstrip layouts is the availability of low-inductance connections to ground. Via

holes were placed at less than quarter wavelength spacing to suppress parallel-plate modes in the substrate. Air bridges were used at all asymmetric discontinuities to prevent the odd-mode from propagating.

A schematic of the circuit is shown in Figure 5.2. The inter-stage networks consist of coupling capacitors, gate and drain bias lines, stub matching networks, and CPW power combiners and splitters. All transistors are power combined after each stage before re-dividing for the next stage. This facilitates DC bias, since one pair of gate and drain bias supplies can then be shared among all transistors in each stage. The final power combiner consists of low-impedance transmission lines with shunt capacitive stubs connected at the intermediate junctions between transistor pairs. Balancing resistors were incorporated as closely as possible to the transistors in all combiners and splitters to suppress odd-mode oscillations.

Resistors were also placed in the gate and drain bias lines to improve low frequency stability, which is a recurrent problem with W-band amplifiers. While it degrades the efficiency, this approach was successful in making the chip easier to use, since it has never shown signs of oscillation under any bias condition, drive level, or packaging environment in which it has been tested. The gate bias lines have two 100 Ω resistors in series and one 50 Ω shunt resistor, forming a 5:1 voltage divider. Bypass capacitors short-out these resistors in-band and isolate the rest of the amplifier from the power supply. The drain lines have much smaller series resistors, 5 Ω, and no shunt element except the bypass capacitors described above.

The Rollett stability factor [52-54], K, for the amplifier was simulated greater than 20 for all frequencies between DC and 120 GHz. Many designers argue that stability must be examined at each individual stage as well as for the entire circuit, but the author's opinion is that such additional tests are redundant. For one thing, it is not necessary that internal stages be *unconditionally* stable, or stable under all passive load conditions, simply because not all passive loads are possible at those points — and some non-passive loads are! The termination of internal transistors are buffered from the external world by the outer stages, so their source and load impedances are well known and controlled. Furthermore, consider the case that an oscillation is present on some internal stage and does not directly involve an outer stage. Under these conditions the oscillation's signal will *still* have some coupling or leakage through the surrounding stages to the ports of the circuit, even if said coupling is unimaginably small, and this signal

will be picked up mathematically by the circuit's stability test. The only scenarios the author can imagine in which an internal oscillation is fully contained are one, the designer is using a device model that is perfectly unilateral (rarely a good assumption in any case) or two, the oscillation occurs in an odd-mode amongst a set of power-combined transistors, and the external ports are coupled to a *perfect* symmetry point of the oscillation. While odd-mode oscillations can definitely be a problem for circuits like this one, the general necessities of bias lines and layout concerns will disrupt the symmetry. Despite a designer's best efforts to keep the circuit electrically symmetrical, the odd-mode rejection must almost never be mathematically zero once a reasonably detailed circuit model is constructed.

In any case, oscillation in a millimeter-wave amplifier is more often the result of unaccounted for feedback across the chip which is generally introduced during packaging. This can be avoided if the chip is mounted inside a small metal cavity that is cutoff at all operating frequencies. In turn, that influences the way the chip is laid out, since it requires the chip to be narrow enough to fit in such a cavity. The power amplifier described in this section does allow this type of packaging, and is one way in which it differs from most of the other W-band MMIC PAs being produced today [48]. The disadvantage of cutoff-channel packaging is that it presents a highly reactive and widely varying impedance to the circuit below-band, making low-frequency oscillations a near certainty if the overall circuit is not unconditionally stable below the operating frequency range.

On-wafer, small-signal measurements were performed using an HP 8510C Vector Network Analyzer with WR-10 waveguide extensions from Oleson Microwave Labs. The VNA extenders from Oleson enable 2-port measurements with good dynamic range across the full waveguide bandwidth. Calibration was performed at the probe tips using CPW calibration standards on an Alumina substrate.

The results are plotted in Figure 5.3. The data shows that the amplifier has small-signal gain of 19±1 dB from 72 to 95 GHz. Output return loss is better than 5 dB across the band, while input return loss exceeds 10 dB from 75 to 90 GHz. The input return loss gets close to 0 dB at 70 GHz, but the measurement could be a few dB off because of calibration errors that occur outside the WR-10 band. In spite of the highly reflective input below band, the amplifier remained stable even when packaged.

Large-signal measurements were also done using a Backward Wave Oscillator as the source. A

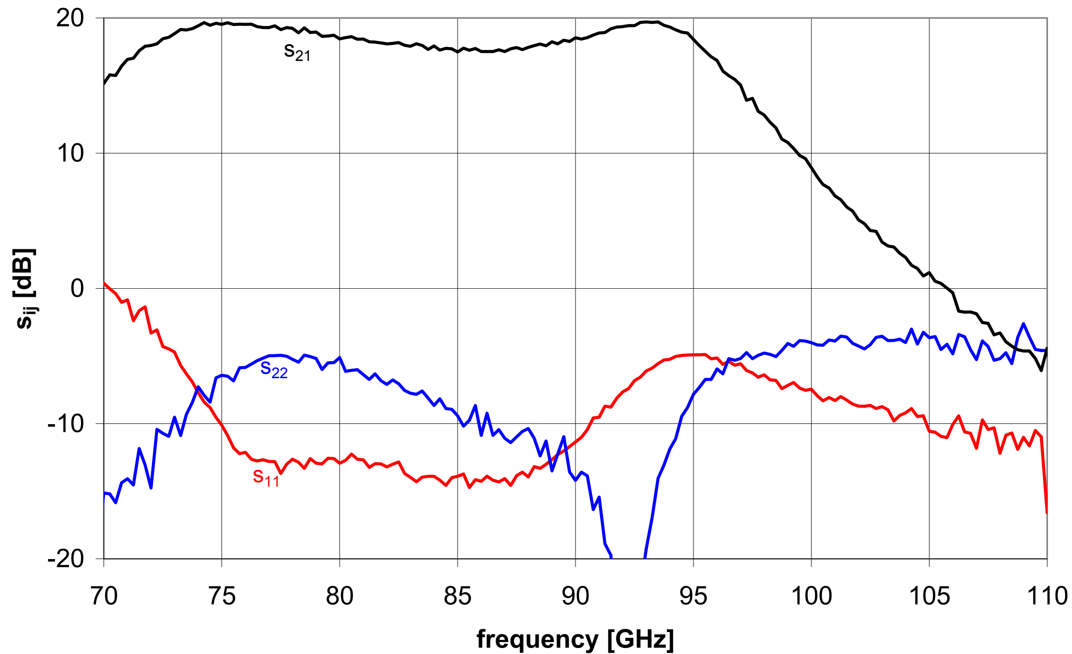

Fig. 5.3. S-parameters for the 75-95 GHz power amplifier. V_G = -0.15 V, V_D = 2.5 V, and I_D = 280 mA.

diagram of this test setup is shown in Figure 5.4. Immediately following the BWO is a precision attenuator for controlling the power level, which is monitored by a power meter connected through a 10 dB directional coupler. Another power meter on port 2 measures the output power. The signal is coupled into and out of the chip through the same wafer probes that were used during the s-parameter measurements. In this case, however, the insertion loss of the probes had to be calibrated out manually. This was done using data supplied by the probe manufacturer and verified by landing the probes on a short microstrip through-line. The loss of the interconnecting waveguides was also measured and calibrated out of the measurements so that the data represents the power levels at the ports of the chip. The MMIC was epoxied to a copper plate for heat-sinking during these measurements.

Figure 5.5 and 5.6 show the output power versus frequency for various input powers and bias levels. For +10 dBm input power and V_D = 5 V, the chip delivered more than 100 mW from 75 to 93 GHz, with a corresponding large-signal gain of 11 dB. Peak PAE was about 8%.

Output power versus input power at 91 GHz is shown in Figure 5.7. The power saturated at about

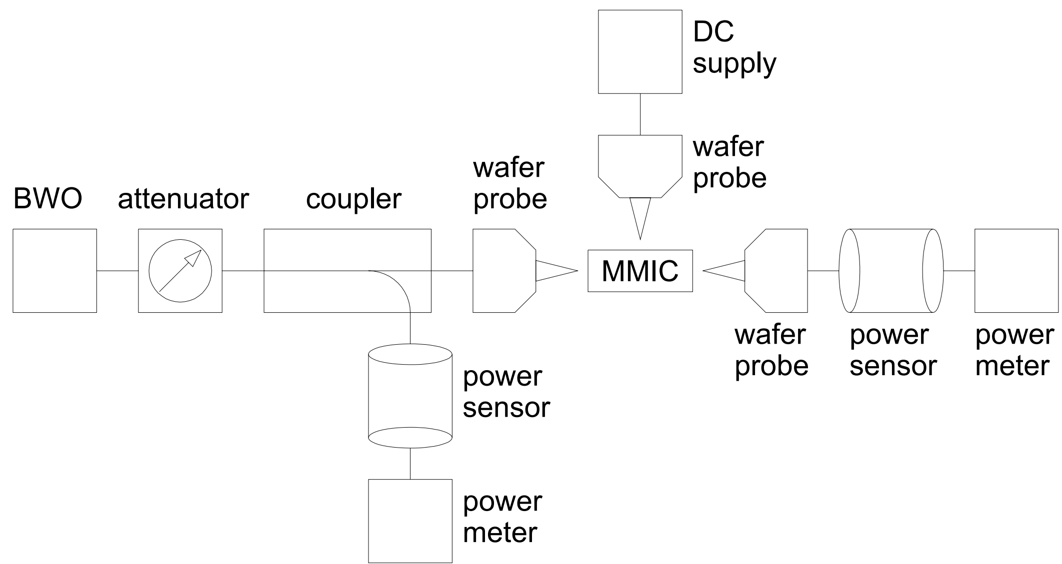

Fig. 5.4. Diagram of the large-signal measurement setup. The input signal was provided by a Backward Wave Oscillator. The chip was mounted on a small metal plate for heat-sinking.

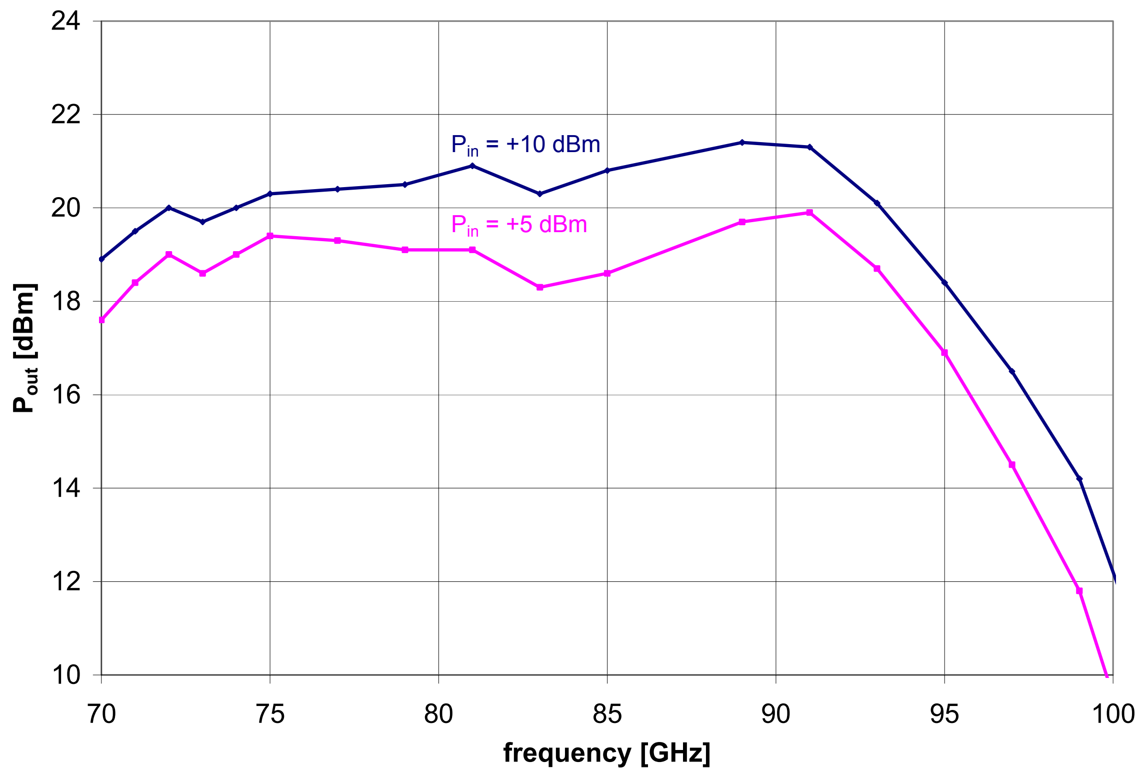

Fig. 5.5 Output power versus frequency for different input powers. V_{G1} = 0 V, V_{G2} = V_{G3} = -0.3 V, V_D = 5 V, I_D = 320-360 mA.

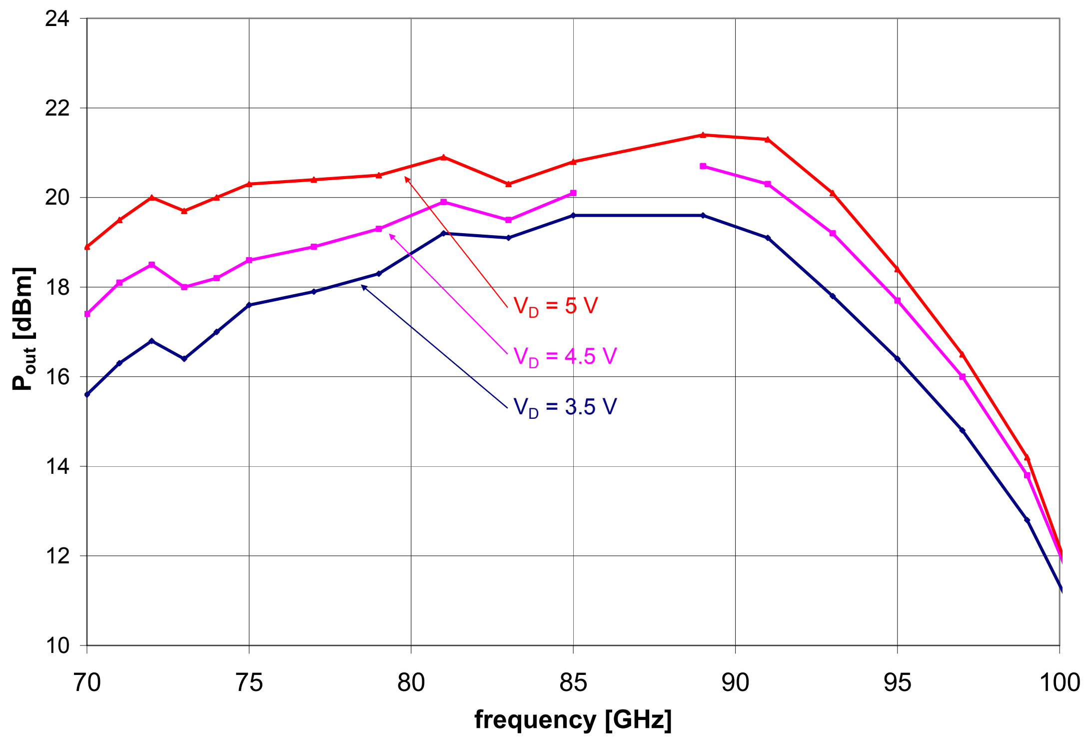

Fig. 5.6. Output power versus frequency for several bias voltages. Input power was fixed at +10 dBm. I_D = 250-350 mA.

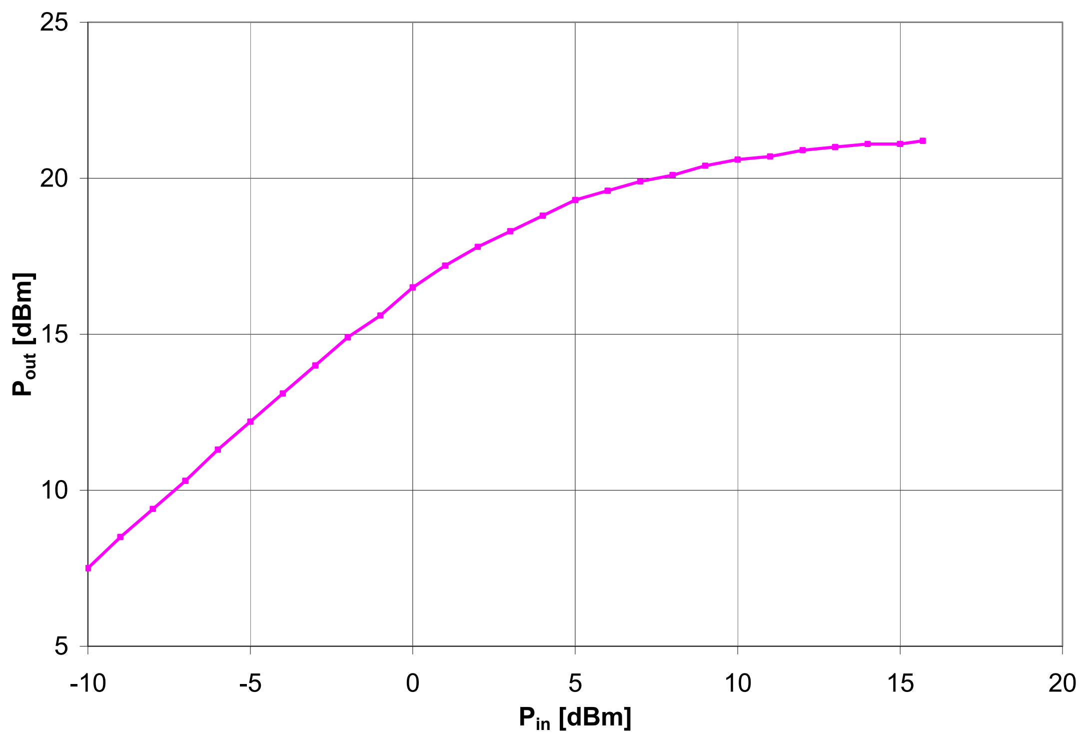

Fig. 5.7. Output power versus input power at 91 GHz. $V_{G1} = V_{G2} = 0$ V, $V_{G3} = -1.5$ V, $V_D = 4.5$ V, I_D = 285-300 mA. P_{1dB} = 16.5 dBm.

130 mW. This data also shows that the 1 dB compression point is +16.5 dBm.

5.2 More W-Band Power Amplifiers

Three other MMIC power amplifiers similar to the one described in the preceding section were designed specifically for the ALMA project at the NRAO (see Section 1.4). They were required to cover 77-120 GHz in three bands with approximately 50 mW of power. The foundry in this case was HRL using a 0.15 μm InP pHEMT process.

The layouts of these chips are shown in Figures 5.8-5.10. Once again, they have three stages, with 1, 2, and 4 transistor cells power-combined at each stage, respectively. Each transistor cell consists of a four-finger device with 148 μm gate periphery. A schematic of the 100-120 GHz circuit, which is representative of all three, is shown in Figure 5.11. They are very similar to the previous W-band amplifier, though some additional measures were taken to improve low-frequency stability of the high-gain InP devices. In particular, the 0.1 pF coupling capacitors after stages 2 and 3 were shunted with a series RC network designed to introduce resistive loss at low frequencies while maintaining the necessary DC block. The layout of the chips also had to be wider to accommodate the via holes between the four output-

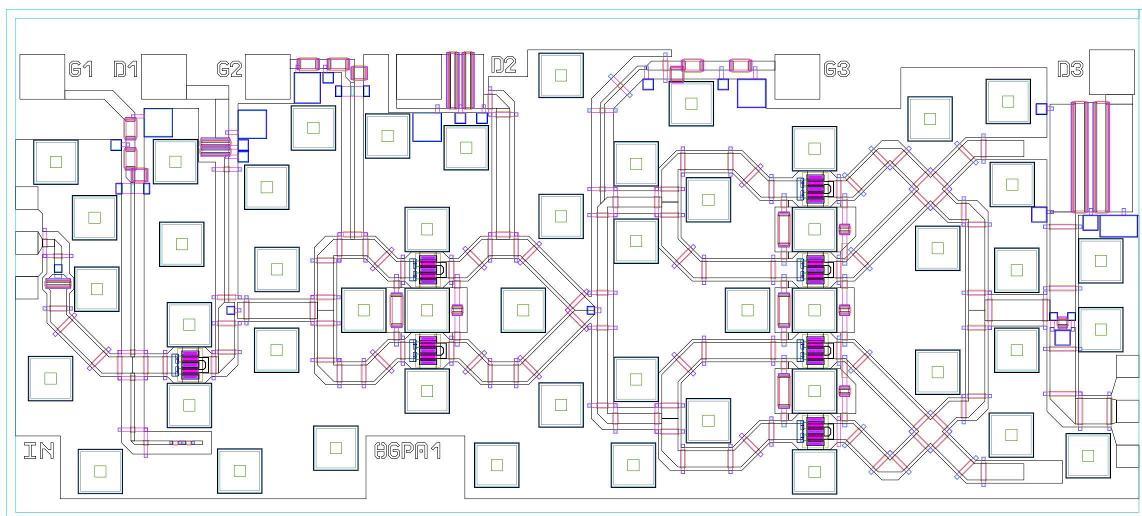

Fig. 5.8. Layout of the 77-95 GHz power amplifier. Chip dimensions are 2.5 x 1.1 mm. InP substrate is 50 μm thick.

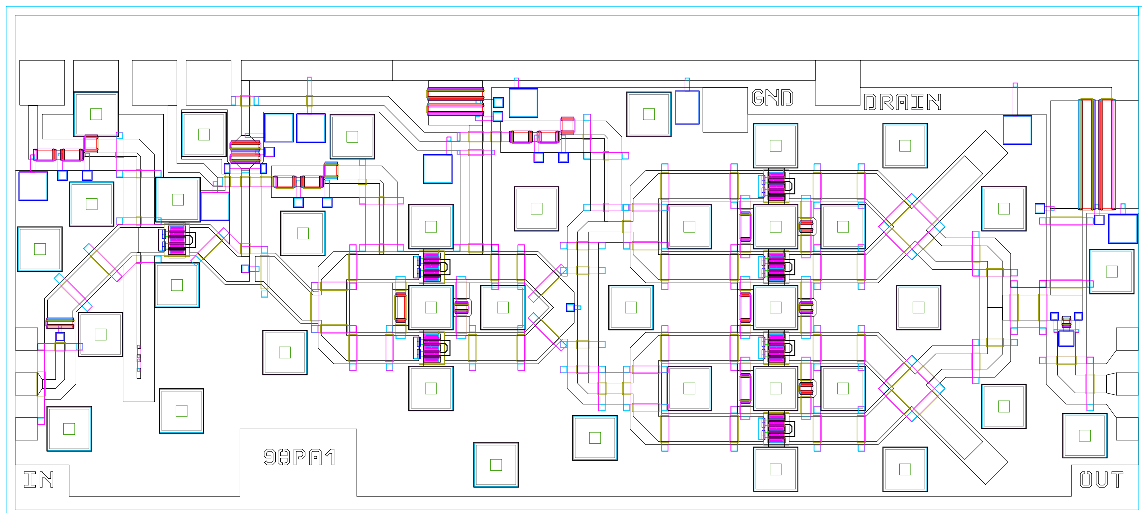

Fig. 5.9. Layout of the 87-108 GHz power amplifier. Chip dimensions are 2.5 x 1.1 mm. InP substrate is 50 µm thick.

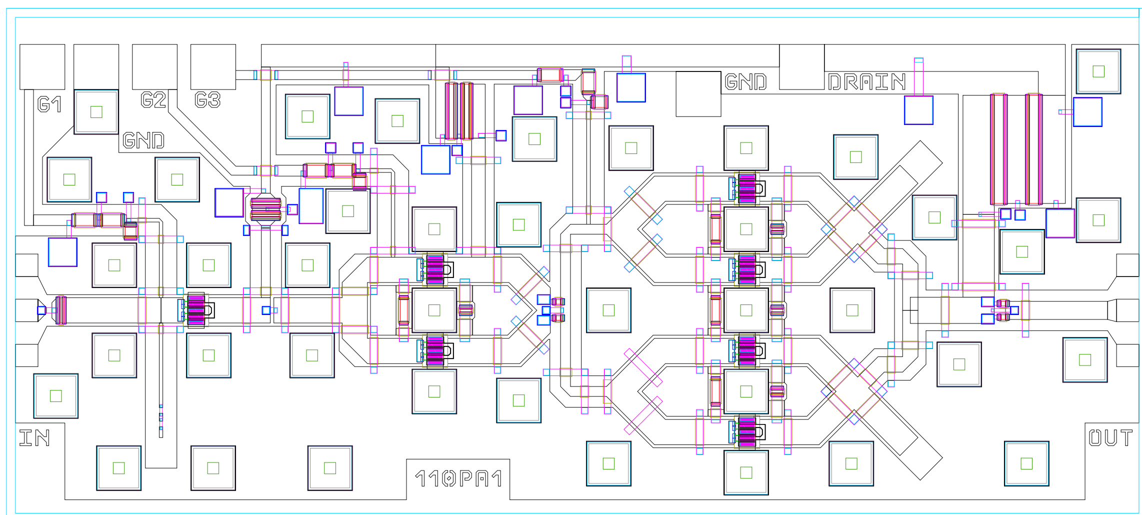

Fig. 5.10. Layout of the 100-120 GHz power amplifier. Chip dimensions are 2.5 x 1.1 mm. InP substrate is 50 µm thick.

stage transistors since the top-metal pads for vias are larger in this process.

Unfortunately, the wafer run that was carrying these designs ran into some fabrication problems, and the masks have not yet been repeated. Simulated data for these amplifiers is shown in Figures 5.12-5.14. The plots indicate that each amplifier is expected to produce 50 mW of power within their design bands.

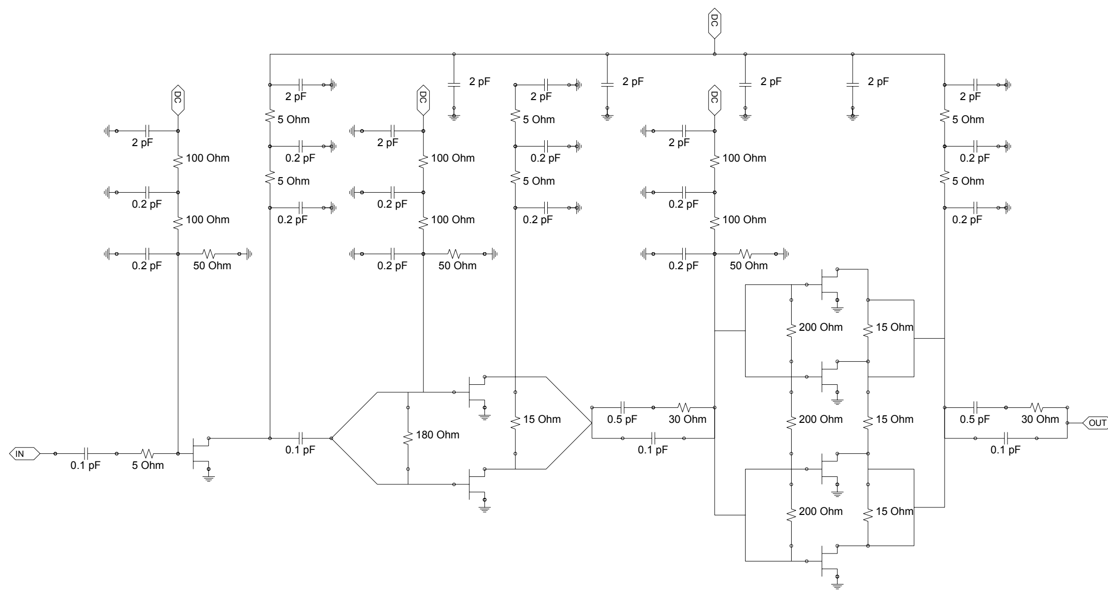

Fig. 5.11. Schematic of the 100-120 GHz power amplifier. Chip dimensions are 2.5 x 1.1 mm. InP substrate is 50 µm thick.

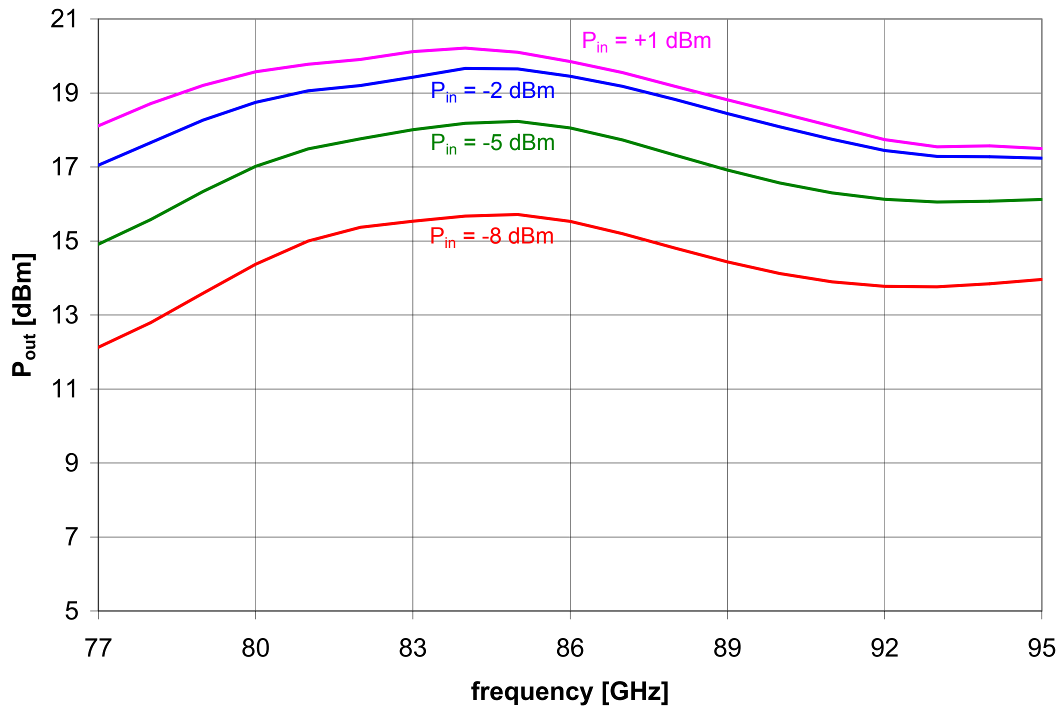

Fig. 5.12. Simulated output power for the 77-95 GHz amplifier.

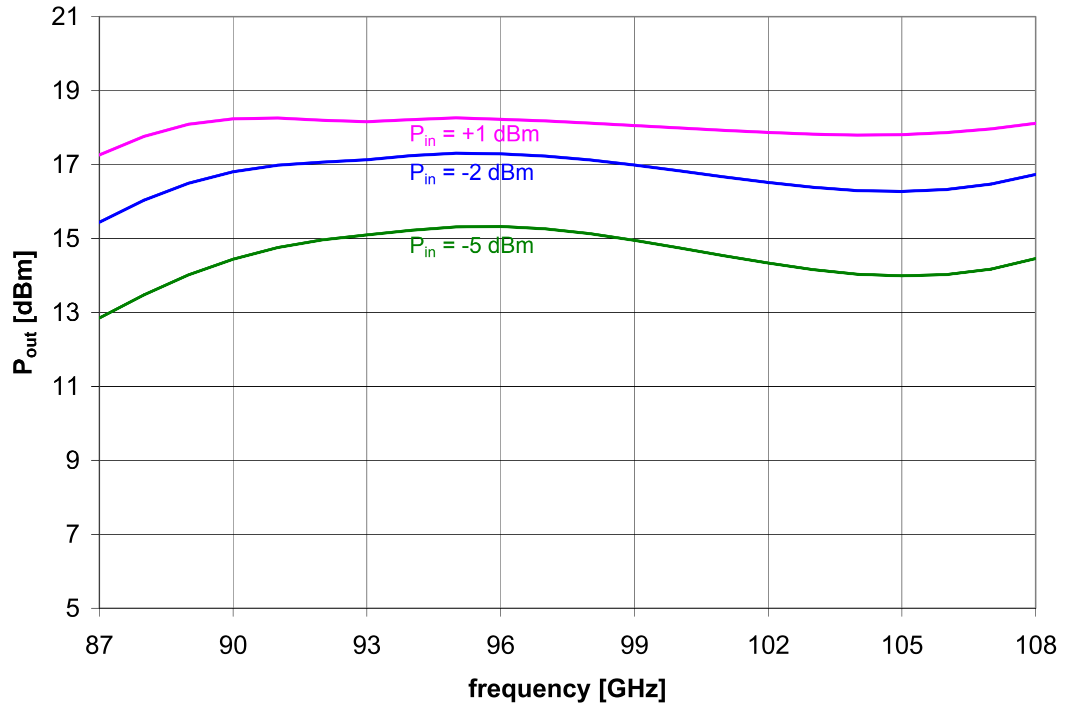

Fig. 5.13. Simulated output power for the 87-108 GHz amplifier.

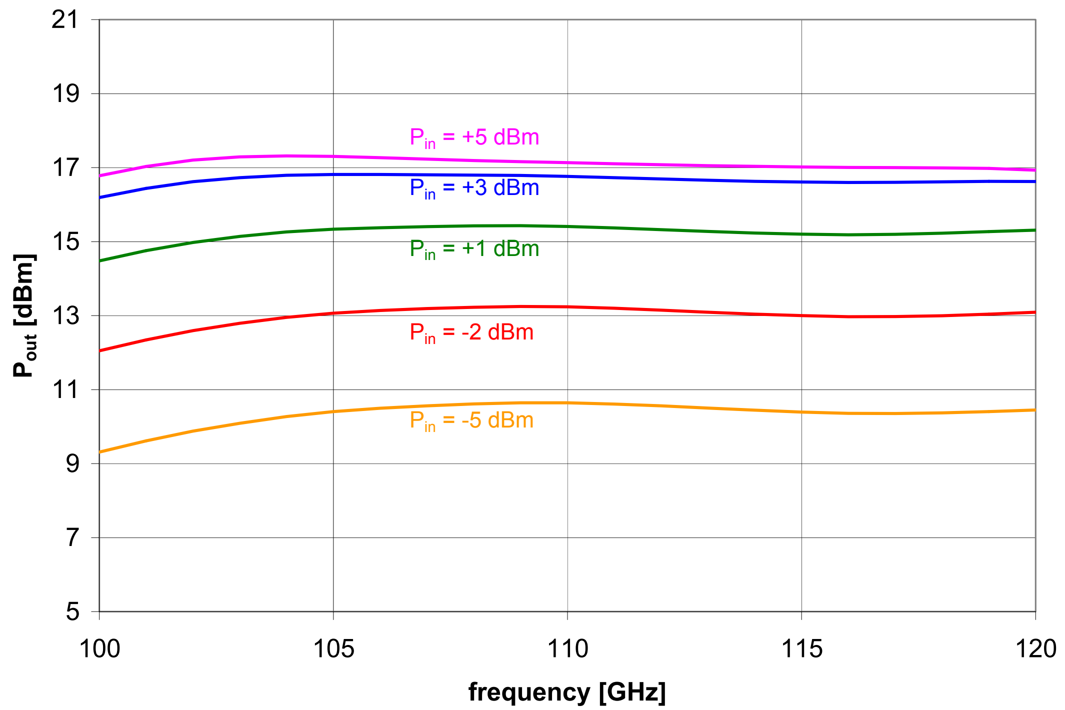

Fig. 5.14. Simulated output power for the 100-120 GHz amplifier.

6 Custom Millimeter-Wave Control Circuits

In this chapter, the often oversimplified topic of switching is discussed. While control circuits like these rarely attract as much attention as power amplifiers, they are nonetheless important parts of any sufficiently sophisticated millimeter-wave application. If not designed carefully, they can quite easily become the limiting factor in overall system performance.

The switches is this chapter were designed for the BES Schottky Diode MMIC process at UMS, the same one that was used for many of the mixers and multipliers described in earlier chapters. This allowed a great number of these new designs to be fabricated cheaply on the same wafer, though it is not really a good process for making switches. In contrast to PIN diodes, which are the device of choice for high-frequency switching applications, Schottky diodes will not usually be able to support as much RF power before the signal itself, rather than DC bias, starts turning the switch on and off. An even more critical problem is that diodes in the BES process are limited to 2.5 mA of bias current per contact finger. Any more would result in long-term degradation due to electromigration effects. Regrettably, at 2.5 mA the series resistance of the diode is too high for use as a low-loss element. The resistance can be reduced, of course, by combining diodes in parallel, or by using multi-finger diodes like those introduced for the mixers and multipliers in Chapters 2 and 3. One should not forget, however, that this will also increase the off-state capacitance, thereby sacrificing isolation.

The author explored many combinations of series and shunt diodes, with single and multiple fingers, and concluded that the best compromise between loss and isolation could be achieved by using only three-finger shunt diodes in the low-loss path of any switch. Series diodes could only be used in paths that were already lossy, such as the on-chip attenuators that will be discussed in Section 6.1.

6.1 Ka-Band Switched Attenuators

It is always easier to add loss to a system than gain. Even in highly sensitive receivers where great care is taken to ensure the lowest possible noise temperature, it is wise to provide some means for cutting down the RF power that enters the module to avoid saturating the amplifiers on those instances when an unusually strong signal is present. Such is the case for a Ka-band receiver being developed for the DSN Array, which will be discussed in more detail in Section 7.10. For this application, it is desirable to be able to switch on up to 30 dB attenuation at the very front of the downconverter module. Furthermore, it is crucial that the switches have as little loss as possible, to avoid degrading the noise temperature when the attenuators are turned off.

It was decided to use two separate chips to implement the stepped attenuator for this module. One would have an on-chip 10 dB attenuator, and the other would have a 20 dB attenuator, either one of which could be switched out. Thus, attenuation settings of 0, 10, 20, and 30 dB would be available using two DC control signals.

Layouts of the two switched attenuators are shown in Figures 6.1-6.2. A schematic is shown in Figure 6.3. The input and output ports are located at the top and bottom edges of the chips, with the low-loss paths looping to the right, and the attenuators in the paths on the left. Two shunt diodes are used in the right arm of each switch a quarter wavelength away from the T-junctions, and two series resistors are placed in the left arm. A simple T-network of resistors forms the on-chip attenuator, with a 3 pF shunt capacitor serving as the RF ground. Bias is supplied across the shunt capacitor. When negative bias is applied, all the diodes are turned off, and the RF signal passes through the right arm. Since no diodes are conducting in this state, the circuit does not suffer from the high series resistance that was described at the beginning of this chapter. When positive bias is applied, all four diodes turn on, shorting out the path on the right, while connecting through to the path on the left. In this state, the RF signal does have to pass through diodes with high series resistance, but it does not matter since the attenuator is turned on anyway.

While this design elegantly avoids the issue of series resistance in the diodes, it does have a drawback. In the off-state, negative bias is applied across two sets of diodes in series, which can lead to

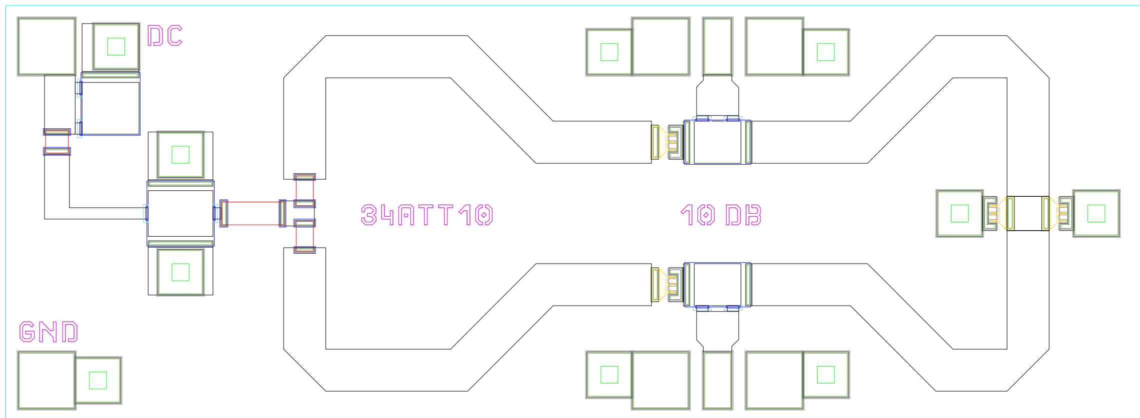

Fig. 6.1. Layout of the 10 dB switched attenuator. Chip dimensions are 2.0 x 0.74 mm. GaAs substrate is 100 µm thick.

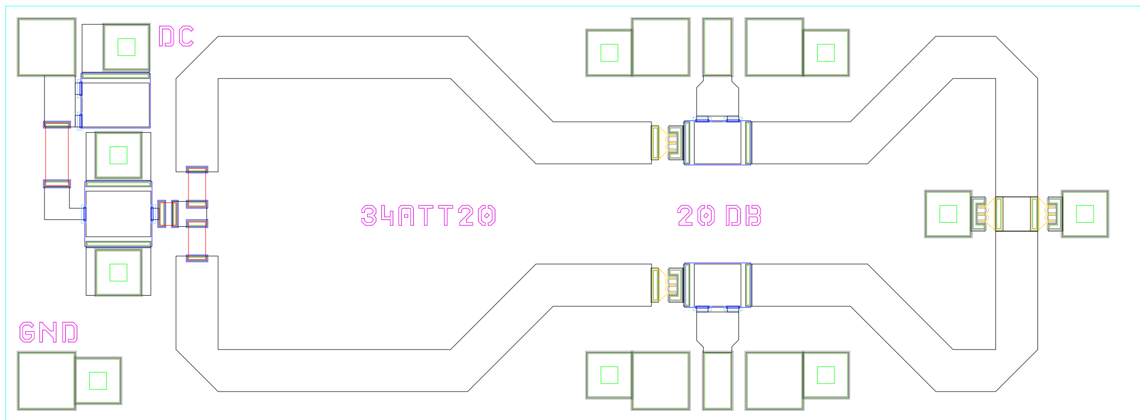

Fig. 6.2. Layout of the 20 dB switched attenuator. Chip dimensions are 2.0 x 0.73 mm. GaAs substrate is 100 µm thick.

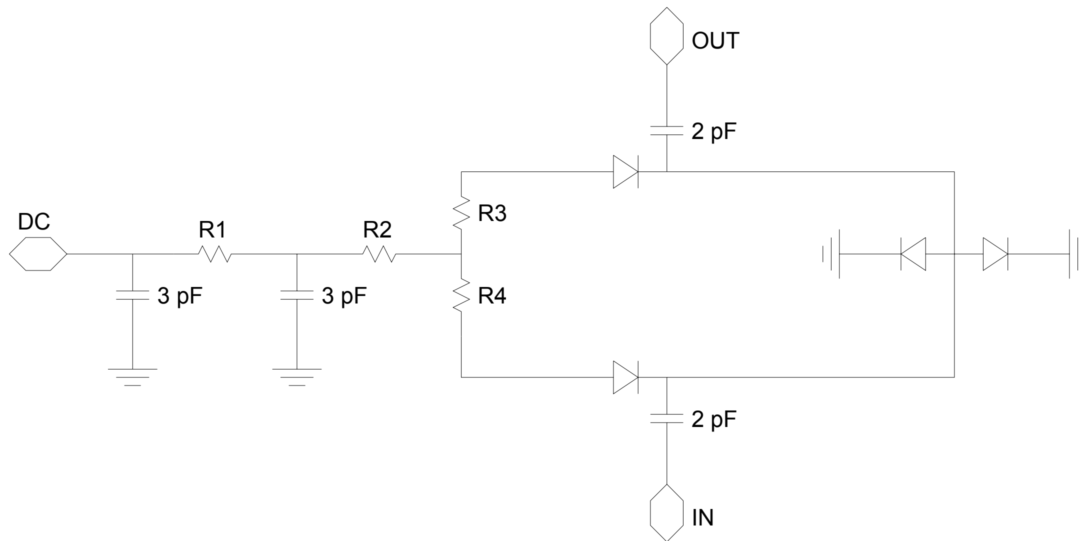

Fig. 6.3. Schematic for the Ka-band switched attenuators. All diodes are 3 finger devices with 1x3 µm contact areas. The resistor values determine what attenuation the chip will have when the diodes are turned on.

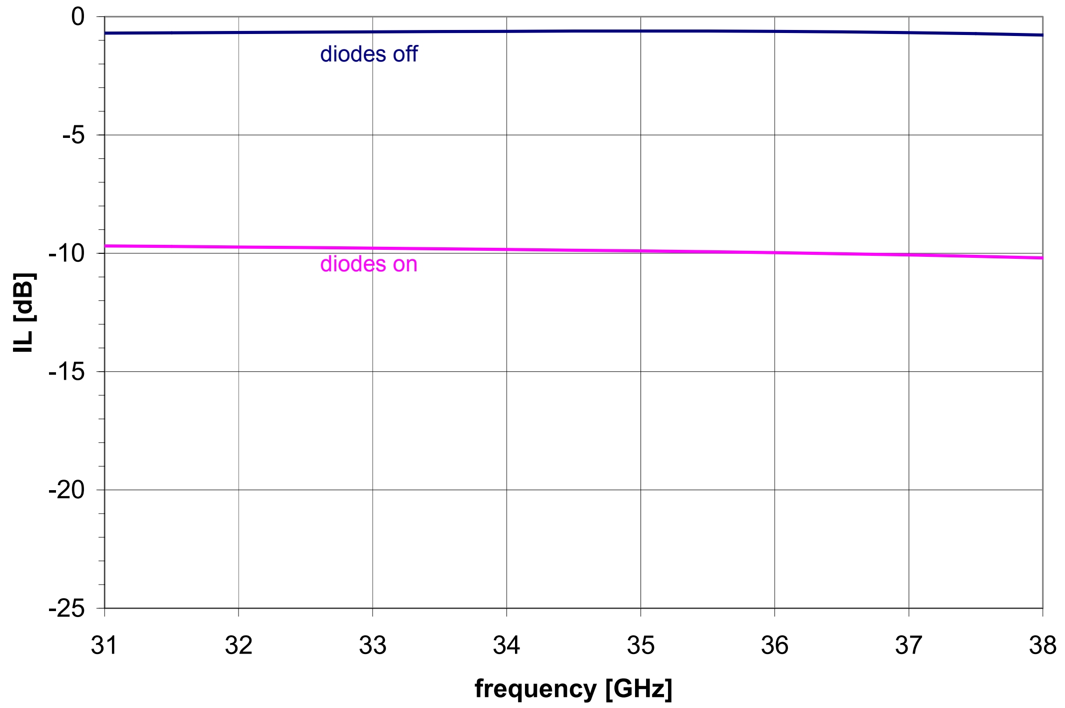

Fig. 6.4. Simulated s-parameters for the 10 dB switched attenuator.

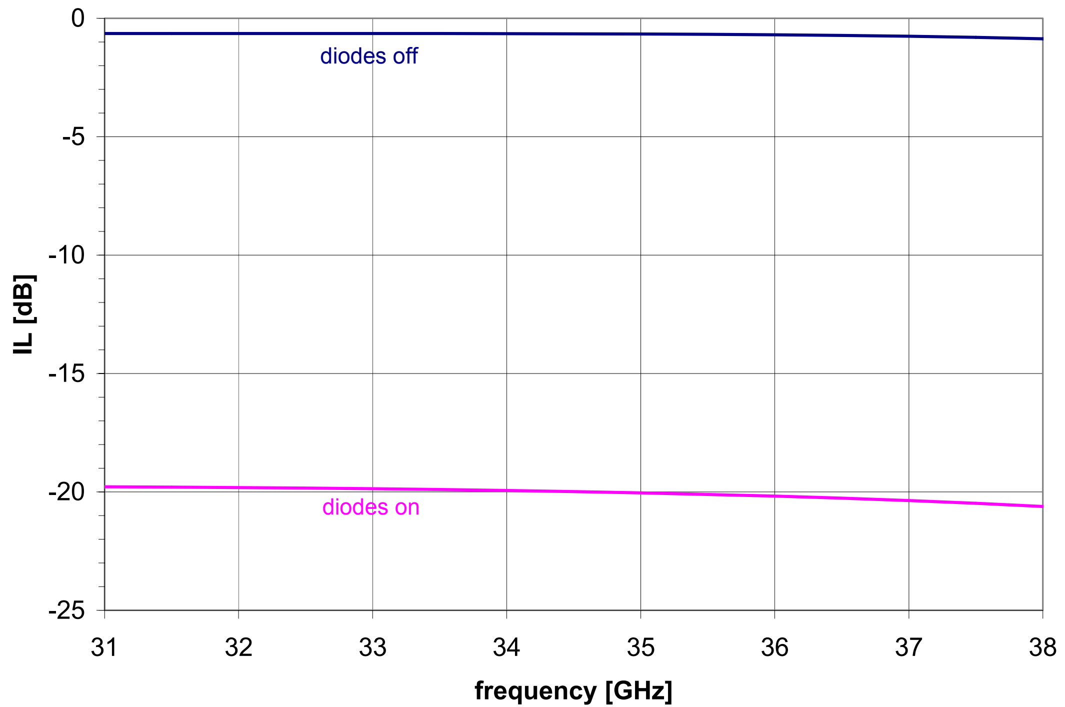

Fig. 6.5. Simulated s-parameters for the 20 dB switched attenuator.

problems if the reverse leakage of the diodes is not well-matched. If this turns out to be a problem, a revision will have to be made that includes balancing resistors across the diodes, at the cost of some extra loss in the circuit.

Simulated data for the switched attenuators is shown in Figures 6.4 and 6.5. They each achieve off-state insertion loss of less than 1 dB across the design band. Return loss (not shown) was better than 15 dB for both chips in both states, and the input-referred 1 dB compression points were greater than +5 dBm.

6.2 Ka-Band SP3T Switches

Switched filters are also required in the DSN Ka-band downconverter in order to select one of three receive bands: 31.6-32.4 GHz, 36.9-38.1 GHz, and 31-38 GHz. While the switches and filters could have, in principle, been integrated onto a single substrate, printed-circuit filters do not provide sufficient rejection to meet the DSN's requirements. Instead, the author chose to use high-Q waveguide filters with a pair of single-pole, triple-throw switches at either end, as will be discussed in Section 7.10. Here we describe the MMIC switch that was designed in the BES Schottky diode process for this purpose.

The layout of the chip is shown in Figure 6.6. The common port is at the bottom of the chip, and the three other ports are along the other three edges of the chip. Again, only three-finger shunt diodes were used in order to keep the insertion loss down. They were connected to each of the 50 Ω transmission lines a quarter-wavelength away from the branch point. A capacitor was used in this connection to isolate the DC bias from the rest of the circuit. Each port has a separate bias line, which is bypassed by another capacitor at a quarter wavelength from the diode. Bias is also supplied through a 100 Ω resistor to protect the diodes.

The simulated performance of the switch is shown in Figure 6.7. It has less then 1 dB insertion loss and better than 15 dB return loss across the band. Isolation is more than 20 dB. There are two sets of curves because the performance is slightly different when the middle port is selected rather than one of the outer ones, primarily due to the four-way branch point.

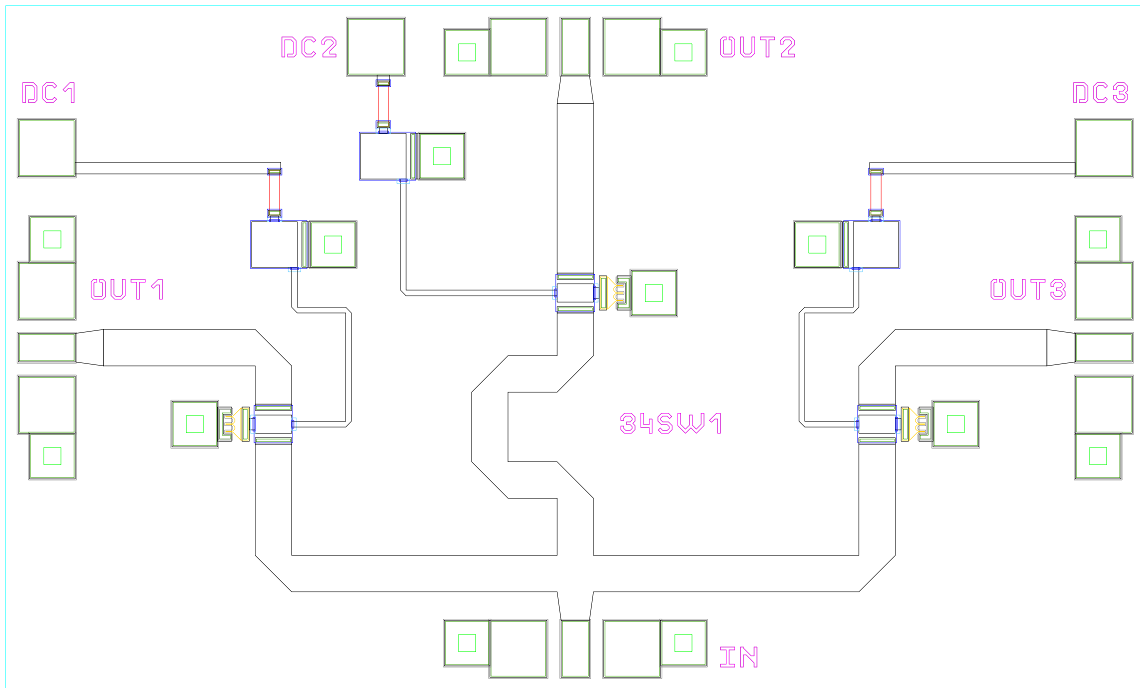

Fig. 6.6. Layout of the 31-38 GHz SP3T switch. Chip dimensions are 2.0 x 1.2 mm. GaAs substrate is 100 µm thick.

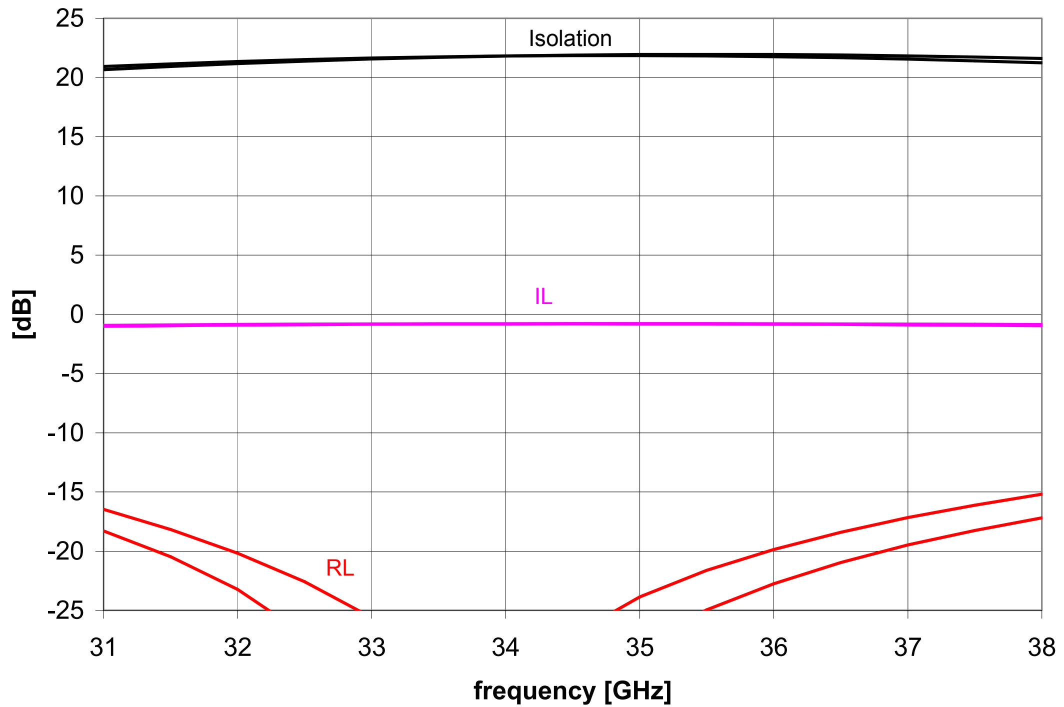

Fig. 6.7. Simulated s-parameters for the 31-38 GHz SP3T switch.

7 Multi-Chip Module Design

This thesis has described at great length the *potential* advantages of monolithic IC's in millimeter-wave systems. However, they can only be realized in practice when careful attention is paid to multi-chip integration and packaging. It will not matter, for example, how small, efficient, or inexpensive a certain MMIC is if it requires an excessively large, lossy, or complex housing in order to use it. MMIC designers often quote chip performance as measured on wafer, which is useful when several chips are strung together, but one should not forget that ultimately, in any millimeter-wave system, it will be necessary to transition from printed circuits to a waveguide, antenna, coax, or other form of connector. This interface between the chip and the outside world can dominate the system in terms of loss, noise performance, bandwidth, and especially the size. As a result, it is somewhat rare to find a millimeter-wave device that contains a single, standalone MMIC chip. It is only practical to combine the functions of several MMICs together in a single module before transitioning to external connectors.

7.1 Multi-Chip Integration

Multi-chip module design can be just as difficult as the individual chip designs, for some of the same reasons that led us to monolithic integration in the first place. Most significantly, the millimeter-wave performance will be sensitive to submillimeter size features in the RF signal path, so one must ensure that the methods of fabrication and assembly can reliably control the dimensions on that scale. Whenever possible, the critical features should be defined lithographically on a printed circuit. Poorly controlled assembly processes must be avoided or at least confined to the non-critical areas of the system.

Keeping in mind that MMIC-based modules will often be used in large quantities, as in an array, the package itself must be as compact, lightweight, and inexpensive as possible. Further, the module must

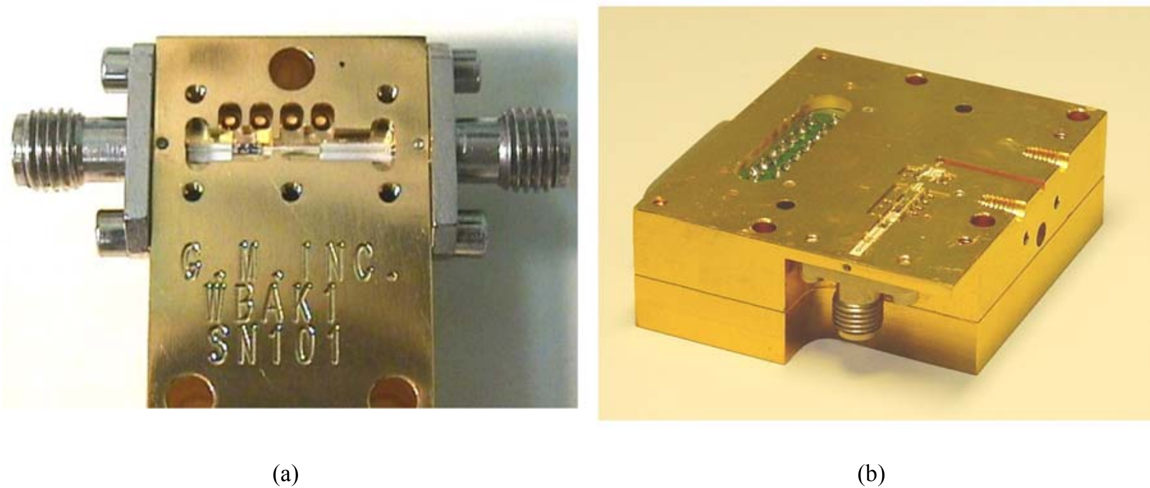

(a) (b)

Fig. 7.1. Multi-chip modules incorporating (a) conventional end-launch coax connectors and (b) a new perpendicular coax connector which allows the chips to be mounted near the top surface of the split block.

consume as little DC and RF power as possible, since the signal and power supplies of an array system will have to be shared among possibly hundreds of elements. This is particularly true of spacecraft instrumentation, where power has been critically limited.

Module fabrication and assembly must not be too difficult or time-consuming either, as the labor involved in building and testing large numbers of identical elements can be the dominating cost of a project. It is therefore important that the module allows the easiest possible access to the chips during all stages of assembly and verification. It is extremely helpful if the MMICs are mounted on a nearly flat surface with no connectors, screws, pins, flanges, cavity walls, or other obstacles extending too far above the top surface of the chips, thus ensuring that wire-bonders and wafer probes will be able to reach them unobstructed. See, for example, the two multi-chip modules pictured in Figure 7.1a and b. The module on the left has deep trenches into which the various chips are placed, making them very difficult to reach with most MMIC test and assembly equipment. The depth of this trench is fixed by the support structure for the coaxial connectors. The module on the right, however, is almost completely flat on the side where the MMICs are mounted, despite having a coaxial connector, a waveguide flange, and a large 15-pin DC plug built into it. It does have a very shallow trench for the chips, but is only deep enough that the module could safely rest face-down without damaging the MMICs, and does not impede probes and tools from working on them. The design allows for this easy access even after assembly is complete, requiring only removal of

the other half of the block (not shown) which easily bolts back into place. This module was designed by the author and will be discussed in more detail in Section 7.5.

Eventually, however, the chips must be covered for protection and shielding from RF interference. Even the lid must be carefully designed, as large cavities will have resonances in the millimeter-wave band that upset the normal operation of the MMICs. It is common practice in our group at JPL to mount chips in a small waveguide-like channel that is cutoff at the frequencies of interest, wherever it is possible to do so. It is particularly useful around MMIC amplifiers where a larger cavity would introduce a feedback path that could easily render the chip unstable. Great care was taken in the layout of the amplifiers described in this thesis to make sure that they were narrow enough to fit in a cutoff waveguide, something that becomes surprisingly difficult above 100 GHz. The author's experience has been that physically wider amplifiers in this frequency range are fraught with stability problems when packaged, even if they were unconditionally stable on-wafer. This serves as an example of why MMIC design and module design should not be considered two separate and independent phases of a project. The necessities of the module will have an impact on the design of the chip, and vice versa.

Typically, the chips in a module are fixed with epoxy into the chassis, and wire-bonds form the interconnection from chip-to-chip. With respect to the wire-bonding, something that is too often overlooked is the difference in performance that is achieved with three-wire (ground-signal-ground) interconnects rather than single wire, microstrip-style interconnects. When a single wire is used, the interconnect introduces what is often a very large parasitic inductance to the circuit. Many microwave engineers invest a great deal of time in trying to model this inductance and incorporate it into their chip design. Unfortunately, this inductance is usually very difficult to predict or control. The length, height, and shape of the bond wire, all of which have a direct influence on the overall inductance, vary from machine to machine, operator to operator, and even among consecutive bonds in a single wire-bonding session. With three-wire links, however, the ground current follows nearly the same arc through the air between the chips as the signal current, making the interconnect look more like a *uniform* transmission line than a lumped inductance. The exact characteristic impedance and phase of this three-wire transmission line is not precisely controlled either, but in the end, is still a much more benign discontinuity than the

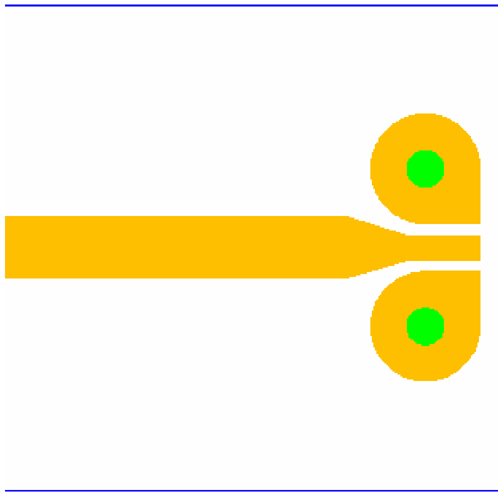

Fig. 7.2. A microstrip-to-CPW transition at the end of a microstrip MMIC chip allows three bond wires to be used in the chip-to-chip interconnection.

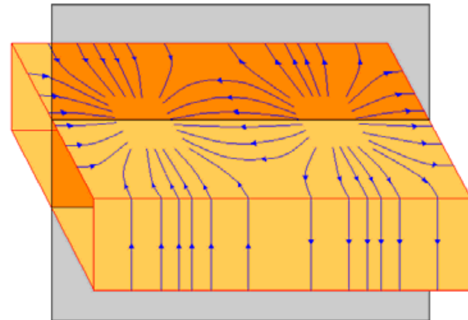

Fig. 7.3. Symmetry of the TE_{10} mode ensures that no current crosses the boundary shown here. This is a convenient place to split the waveguide in a multi-chip block.

single-wire alternative, particularly at higher frequencies. Once again I point out the need for MMIC designers to consider how their chips will be used in a system before committing to a particular layout or design. All of the chips in this thesis are designed with CPW ports, even if the rest of the circuit is entirely microstrip. The transition from microstrip to CPW on the printed circuit can be nearly ideal, and is largely just a function of the spacing between ground vias on either side of the signal line, as shown in Figure 7.2. Most importantly, that transition is well controlled and repeatable, since it is defined through photolithography, and it allows the more reliable CPW interconnect to be used. Further improvement can made by using bond ribbon instead of wire, and by keeping the RF bonds between chips as short as possible. The author has seen this method applied successfully, *without ever modeling the bond wires*, at frequencies exceeding 200 GHz.

Finally, the interface between the chips and the outside world should be reliable, repeatable, low-loss, and have sufficient bandwidth to avoid degrading the performance of the MMICs. Transitions to coax, for example, should be well matched and low-loss from DC up to the highest frequency expected on that port. A transition that meets these conditions without disrupting the planarity of the chassis is discussed in Section 7.2. For waveguide ports, it is often desirable to cover the full guide bandwidth. Additionally, it is advantageous to split the waveguide longitudinally in the center of the broad wall, as

shown in Figure 7.3. Symmetry of the TE_{10} mode ensures that no current crosses this junction, minimizing loss due to the resistive contact between the two halves of the block. Waveguide transitions will be described in Section 7.3.

7.2. A Millimeter-Wave Perpendicular Coax-to-Microstrip Transition

The transition from coaxial-cable to microstrip is a very common feature of microwave and millimeter-wave systems. It is widely used in commercial products which incorporate printed circuits, and also in microstrip test fixtures that can be found in almost any microwave research lab. Traditionally, the transition is accomplished by aligning the axis of the coaxial connector with the end of the microstrip line, and by connecting the outer conductor of the coax to the microstrip's ground plane and the center conductor to the microstrip.

Over the years, various improvements have been proposed [57-61] that extend the transition's bandwidth and enhance its performance, but the basic end-launch geometry has remained the same. Unfortunately, there are some practical problems associated with this arrangement that have not been addressed. Specifically, in order to hold the coax connector rigidly in position beside the printed circuit, there must be a flange or other fixed structure that rises above the top surface of the substrate. As described in the previous section, such a flange would block most wafer probes, making it difficult to verify the chips independently after they have been mounted in the chassis. Also, in some microwave receivers that employ MMIC technology, a side-mounted coaxial connector can interfere with the narrow profile of the modules which is necessary for packing them in a close-fitting focal-plane array. Under those circumstances, a coax connection that enters or exits through the back of the module, rather than the side, is advantageous.

Perpendicular coax-microstrip connections have been made in the past by attaching a bond wire from the center pin of the coax to the microstrip line [62]. However, the length of the bond wire, which is often difficult to control, is critical to the performance. Often it is necessary to tune the transition for a specific frequency by trimming microstrip stubs or other features, diminishing repeatability of the

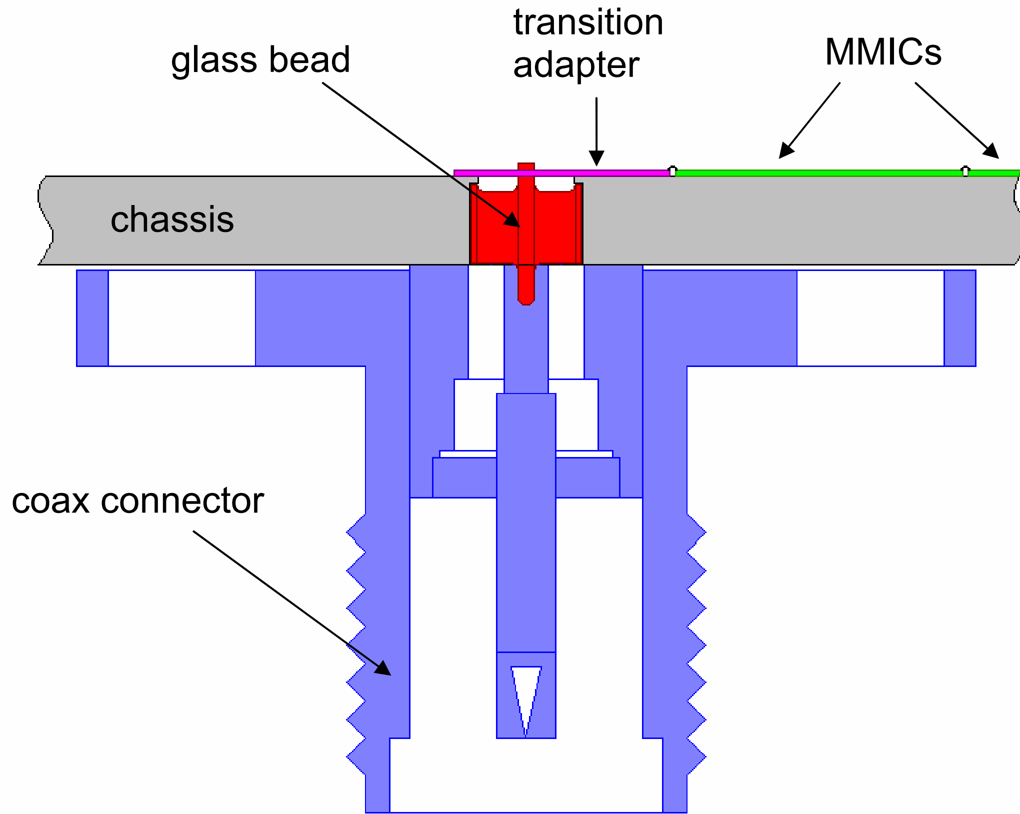

Fig. 7.4. Assembly diagram of the perpendicular coax-to-microstrip transition. A K flange-launcher is shown, but threaded "sparkplug" launchers can be used as well.

transition and limiting the useful frequency range and bandwidth.

With these issues in mind, a novel perpendicular transition has been developed in which wideband compensation of the junction is achieved on the printed circuit through entirely lithographic techniques, allowing easy fabrication and repeatable performance.

A diagram of the perpendicular transition is shown in Figure 7.4. A key component of this design is a "transition adapter," shown in Figure 7.5. The adapter is a two-sided printed circuit on a 100 μm thick Alumina substrate. It has a circular hole that fits over the center pin of a commercially available glass bead mated to a standard K-connector flange or sparkplug launcher [63]. The ground plane of the adapter substrate is electrically connected to the outer conductor of the coaxial bead. The center pin of this bead passes through an aperture in the ground plane, extends through the substrate, and is soldered to a metal ring on the top side, completing the connection to the microstrip line. The critical geometry of the glass

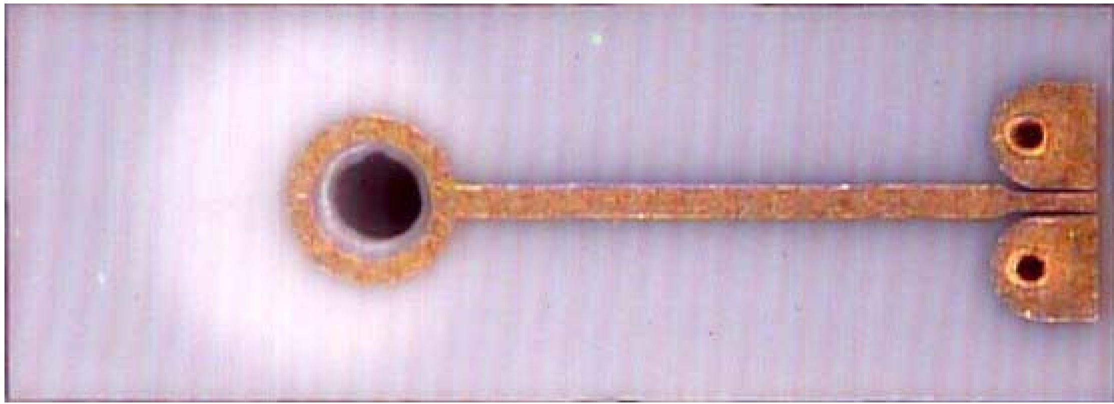

(a)

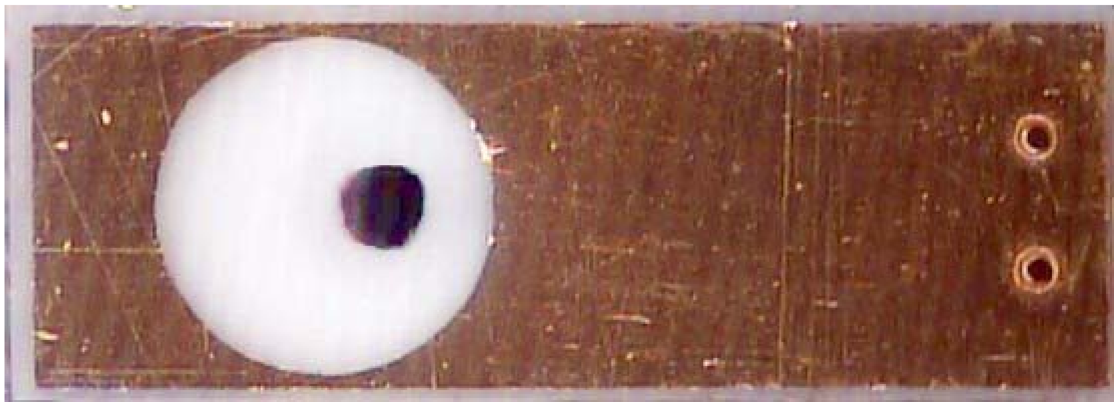

(b)

FIg. 7.5. Top (a) and bottom (b) views of the transition adapter. The hole in the center of the 100 μm thick Alumina substrate fits over the center pin of a standard K-connector coaxial glass bead. The substrate dimensions are 3.75 x 1.35 mm.

bead, the adapter substrate, and the mounting structure was analyzed using Ansoft's High-Frequency Structure Simulator (HFSS).

A key parasitic of perpendicular transitions like this one is the inductance caused by ground currents that must flow around the circumference of the coax outer conductor to reach the underside of the microstrip section. This problem is alleviated by reducing the diameter of the aperture in the ground plane, effectively providing a shortcut for ground currents from the outer edges of the coax shield. If the aperture is made too small, however, shunt capacitance from the center pin to the substrate ground once again degrades the performance of the junction.

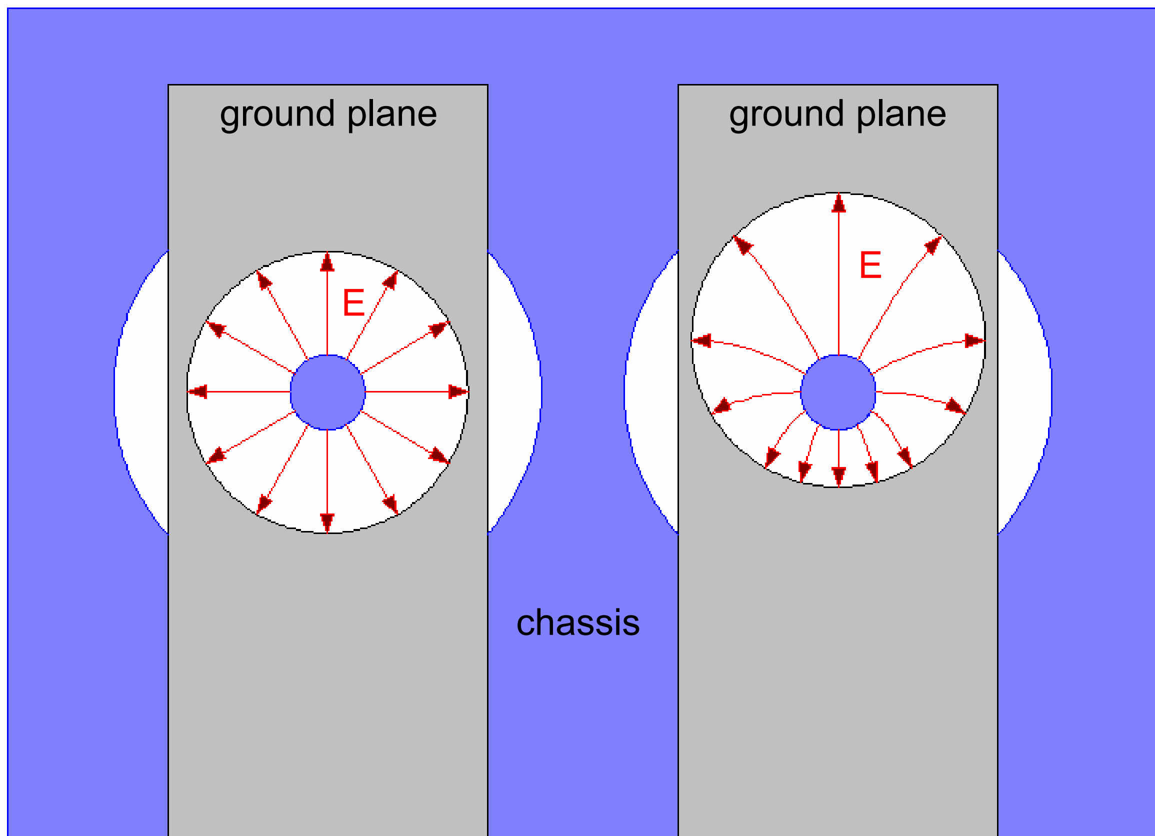

Fig. 7.6. Comparison of the field distribution with concentric and offset ground apertures.

It was discovered that offsetting the aperture as shown in Figure 7.6 can greatly improve the performance of the transition. Doing so redistributes the parasitic capacitance to the side nearest the microstrip, concentrating the fields on that side of the coax line where the ground inductance is least. It also reduces the inductance of the signal line by shortening the distance current must flow to get from the center pin to the 50 Ω microstrip line.

Additional compensation can be included in the form of a microstrip matching network on the top surface of the adapter, but it was found that the ground aperture manipulations described above had sufficient degrees of freedom to fully match the transition, and proved to be a more broadband solution. The resulting structure is low-pass, maintaining good performance from DC to millimeter-wave frequencies, and is limited primarily by over-moding of the coax line itself.

Although it would be best from an electromagnetic perspective to have the adapter's ground plane make contact with the full periphery of the coax line, it was decided to narrow the chip so that the bead was

visible through a gap on either side. Observability of all critical components, such as the glass bead, can be very useful when trying to debug complex multi-chip modules.

Prior to assembly, the short pin of the coax bead was filed down to a length of approximately 375 μm past the rim of the outer conductor. A simple holding fixture was made to fit over the bead to prevent it from being filed too short. Also, a small dome was machined into the cover on the test block to ensure that there was enough clearance for the pin.

The transition is very robust with respect to assembly. Critical dimensions are defined lithographically on the adapter and proper alignment of those features is ensured by the snug fit of the coax pin in the hole through the substrate. Off-chip features such as the recess of the glass bead, the height of the coax pin, and clearance between the pin and top cover were swept in simulation, and the design was found to be relatively insensitive to those parameters. Because all the critical features are contained on the printed circuit, this transition is easier to assemble than the common end-launch connectors which often require very tight machining tolerances.

For our purposes, the adapters were made to include a CPW port because three bond wire (ground-signal-ground) chip-to-chip interconnects tend to perform better than single bond wire links. However, it does not play a role in the coax-microstrip transition.

A back-to-back configuration was used to measure the characteristics of the transition. A photograph of the test block is shown in Figure 7.7. It was necessary to insert a long 50 Ω transmission line between the transitions, as shown in Figure 7.8, to make room for the two coax connectors.

The back-to-back transitions were measured with an HP 8510 Network Analyzer from 0 to 40 GHz. The raw data is plotted in Figure 7.9. The peaks and nulls in the return loss at 5-6 GHz intervals are caused by reflections between the two transitions separated by a 10 mm long, 50 Ω microstrip line on 100 μm thick Alumina. The loss of the microstrip was measured separately with wafer probes and was approximately 0.08 dB/mm at 40 GHz.

Given that the peaks of the return loss curve occur when the reflections from both transitions add in phase, and taking into account the known loss of the intervening transmission line, it is possible to back out the return loss for a single transition at those frequency points. Specifically, the measured scattering

Fig. 7.7. Photograph of the back-to-back transition test block.

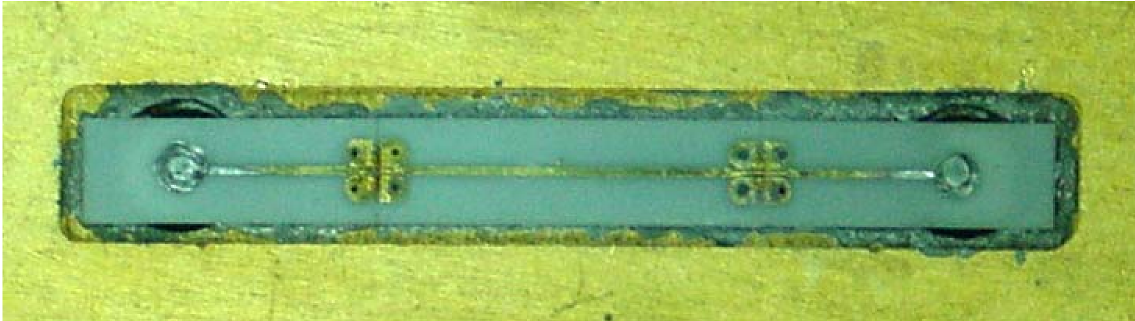

Fig. 7.8. Interior view of the test block, showing the back-to-back transitions with intervening microstrip line.

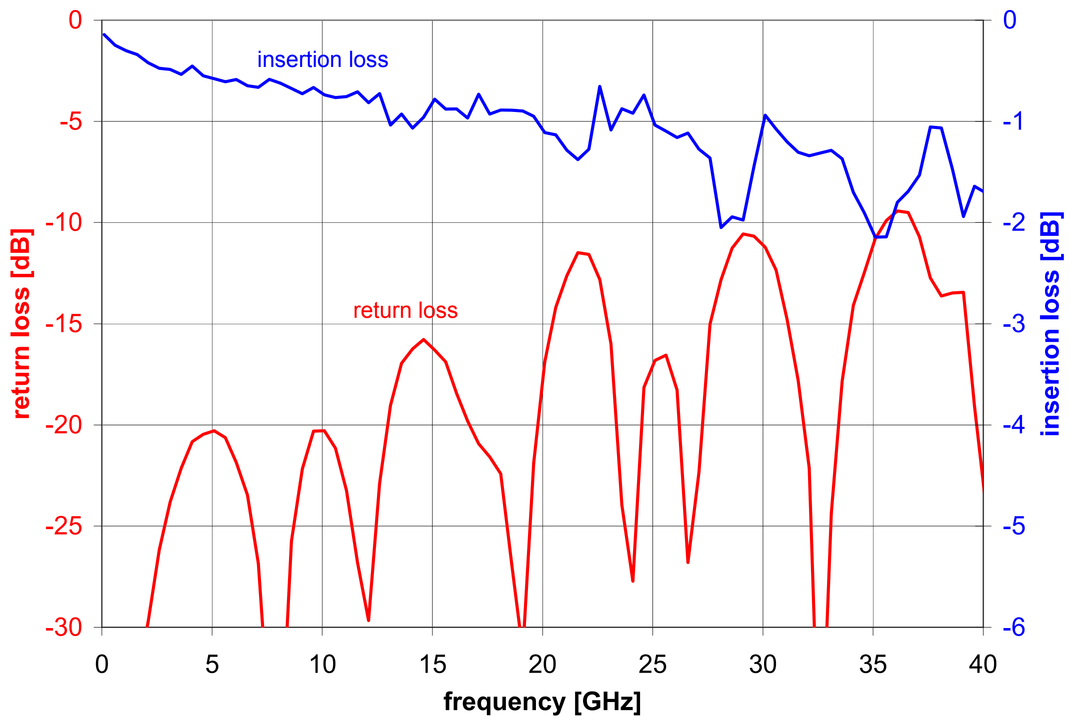

Fig. 7.9. Raw S-parameters for two back-to-back transitions separated by a 10 mm long, 50 Ω microstrip line.

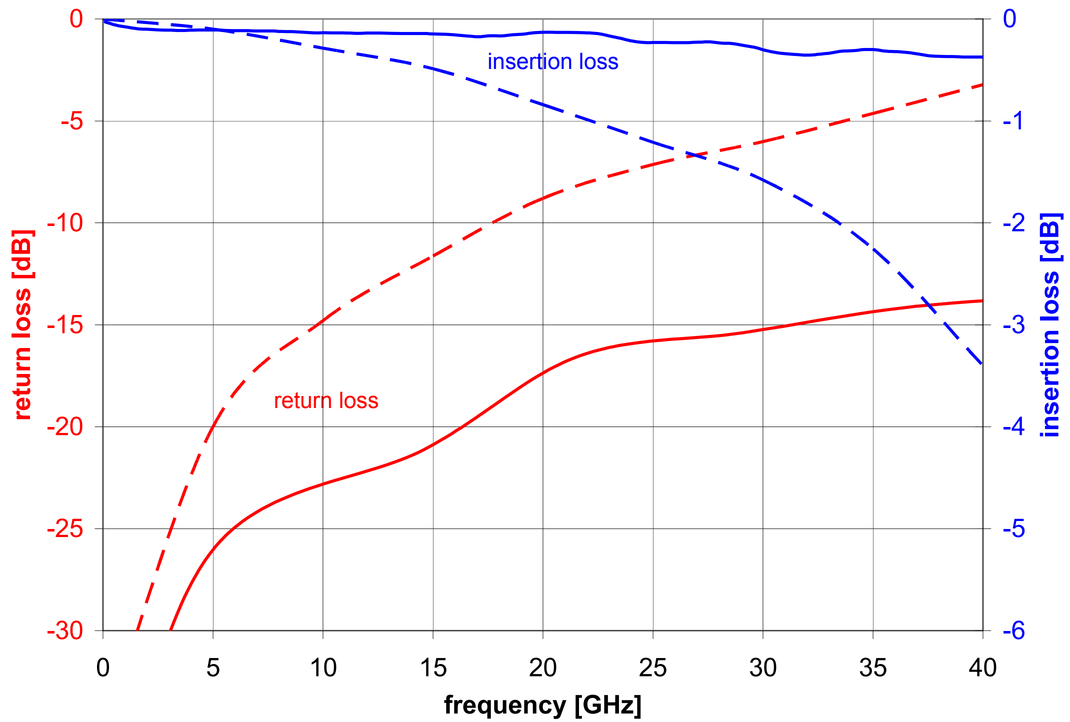

Fig. 7.10. S-parameters for a single transition, corrected for multiple reflections and the loss of the microstrip line. For comparison, the dashed lines show simulated results for a perpendicular transition *without* the ground aperture compensation described in this paper.

parameters are

$$m_{11} = s_{11} + s_{22}\frac{s_{21}^2 t_{21}^2}{1 - s_{22}^2 t_{21}^2} \tag{7.1}$$

$$m_{21} = \frac{s_{21}^2 t_{21}}{1 - s_{22}^2 t_{21}^2} \tag{7.2}$$

where m_{ij} are the measured scattering parameters for the back-to-back transitions, s_{ij} are the scattering parameters for a single transition, and t_{21} is the measured insertion loss of the microstrip line (this analysis assumes that the transmission line is matched, i.e., $t_{11}=0$). From equations (7.1) and (7.2), it follows that

$$\begin{aligned} m_{11} &= s_{11} + s_{22} m_{21} t_{21} \\ &= |s_{11}| e^{j\theta_1} + |s_{22}||m_{21}||t_{21}| e^{j\theta_2} \end{aligned} \tag{7.3}$$

Since θ_2 contains the phase of the long transmission line between the two transitions, it will vary more rapidly than θ_1 with frequency. The peaks in the measured return loss (m_{11}) occur when $\theta_1=\theta_2$. At these points, then

$$|m_{11}| = |s_{11}| + |s_{22}||m_{21}||t_{21}| \tag{7.4}$$

Using the fact that $|s11| \approx |s22|$ (this would be exact for a lossless network), we can solve for the return loss of a single transition:

$$|s_{11}| \approx \frac{|m_{11}|}{1 + |m_{21}||t_{21}|} \tag{6.5}$$

at those points where m_{11} peaks. This correction (which must always be less than 6 dB) was applied to the measured data at the appropriate frequencies. The insertion loss was also corrected by subtracting the known loss of the transmission line, dividing by two, and then smoothing. The result is shown in Figure 7.10. The transition is low-pass, with better than 14 dB return loss from DC to 40 GHz. The insertion loss was less than 0.4 dB over the whole range. Although demonstrated with a K-connector and 100 μm Alumina substrate, the principle can easily be extended to V-connectors or 1 mm coax, and to different substrate materials.

7.3. Waveguide-to-Printed-Circuit Transitions

While coaxial connectors remain an important component in many microwave and millimeter-wave devices, the higher frequency ports are most often rectangular waveguide which is rugged, low-loss, and easier to analyze than other waveguide geometries. As with the coaxial transitions, the interface between MMIC chips and the waveguide must be reliable, easy to manufacture, and should preferably not limit the bandwidth or performance of the system. A useful waveguide transition that meets these requirements is the longitudinal E-field probe, shown in Figure 7.11. More information on this probe can be found in the reference [64]. It is compact and simple, and can even be integrated monolithically with the MMICs [65], though it is more frequently fabricated separately on a ceramic substrate such as Alumina.

The radiating element of the transition is a simple rectangular paddle that extends roughly halfway into the waveguide from a slit in the center of the broad wall aligned with the direction of propagation (hence the term *longitudinal*). The ground plane of the substrate is removed beneath this paddle. A backshort is placed roughly a quarter-wavelength away from the probe. Practical machining of the block requires that the backshort have rounded corners rather than the ideal box-end. This merely introduces a shift in the reference plane of the short which can easily be accounted for, and may even play a role in reducing the loss as the current on the walls of the guide has a smoother path to follow. When modeled in a 3-D EM simulator such Ansoft HFSS, this probe and waveguide structure usually presents a slightly

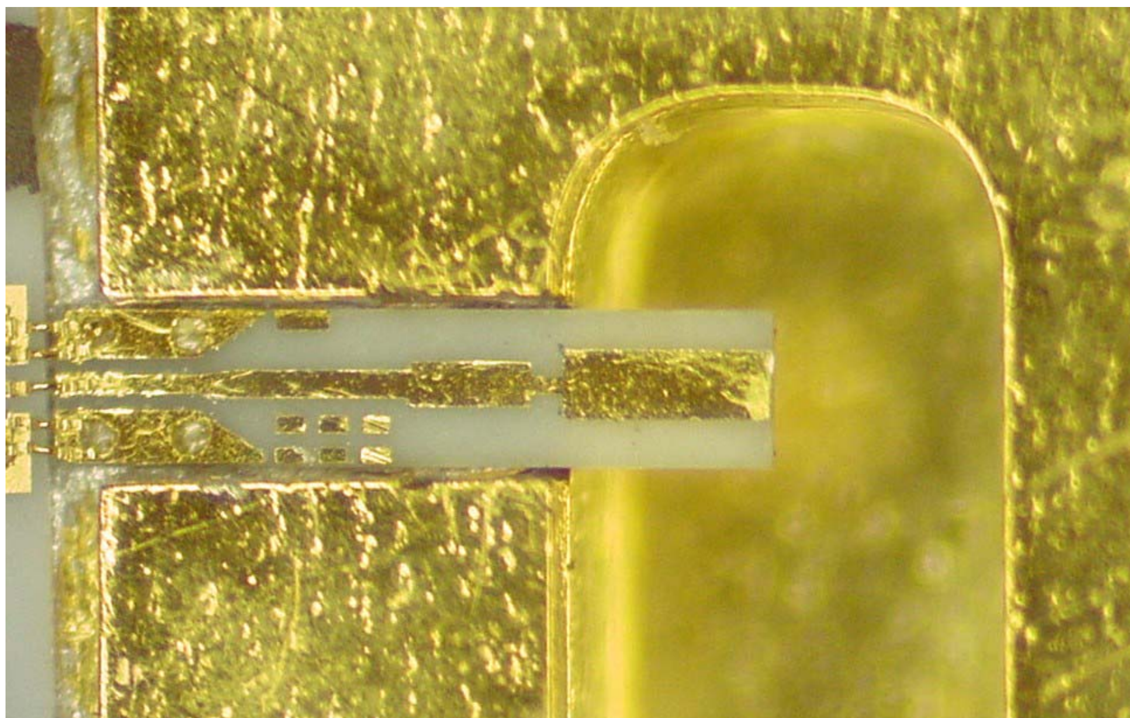

Fig. 7.11. Photograph of a longitudinal E-field probe.

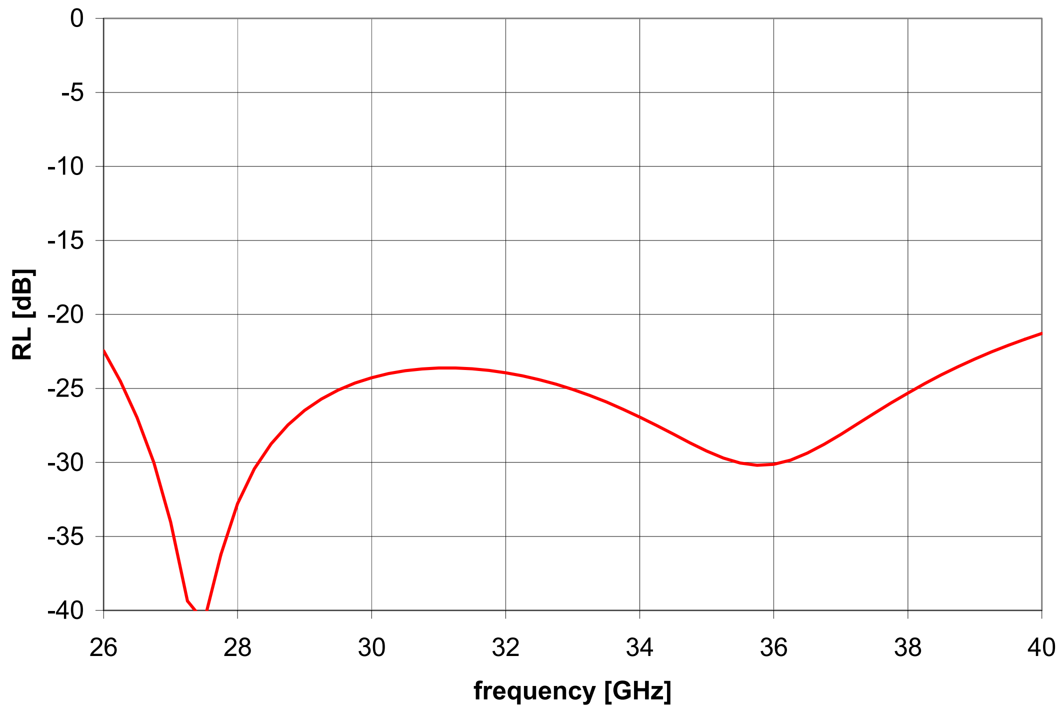

Fig. 7.12. Simulated return loss for a Ka-band longitudinal E-field probe.

capacitive impedance with real part less than 50 Ω. A microstrip matching network is therefore required, consisting of a high-impedance transmission line (series inductor) followed by a low-impedance quarter-wave transformer. Better than 20 dB return loss across the full-waveguide bandwidth is readily achievable with this technique. One must be careful though that the width of the chip is narrow enough that the channel it rests in is cut off to waveguide modes that might otherwise leak in from the main guide. Simulated data for a Ka-band version of this transition is shown in Figure 7.12.

The advantages of the above approach over other types of microstrip-to-waveguide transitions lie in its ease of use and reliability. Some designers use a probe that extends all the way through the waveguide and shorts on the far broad wall, thereby using the current through this contact to couple into the H-field of the dominant mode. Such probes are difficult to match into a full-height waveguide so they are typically designed to use a half-height waveguide which tapers or steps up to full-height further away from the transition, adding size and complexity to its design. Furthermore, constructing and maintaining a low-resistance contact between the probe and the far wall can be problematic, leading to reliability issues. Similar problems exist with another common transition that consists of a tapered ridge that extends from one broad wall of the guide down the center and makes contact with a microstrip line on a substrate resting against the opposite wall. The E-field probe described above has no contact with the chassis (except for the ground plane on the bottom side of the chip) and can easily be matched over the entire bandwidth of a full-height waveguide. A comparison of these approaches is shown in Figure 7.13.

Finally, there are some rare situations in which a MMIC may operate best with a differential output. Rather than construct a balun before transitioning into waveguide, which may be lossy and narrow-band, it would be useful to have a waveguide probe that has a balanced input. Such was the motivation behind the differential loop transition shown in Figure 7.14. This circuit is driven by a pair of coplanar strips in differential mode. Current through the loop couples into the strong H-field against the backshort of the waveguide. As with the microstrip probes, the chip was designed to be mounted on the symmetry plane in the broad wall of the guide so there will be no current between the two halves of the chassis and less loss in the system. This transition has not yet been tested, but simulated results for a 35 GHz probe are shown in Figure 7.15.

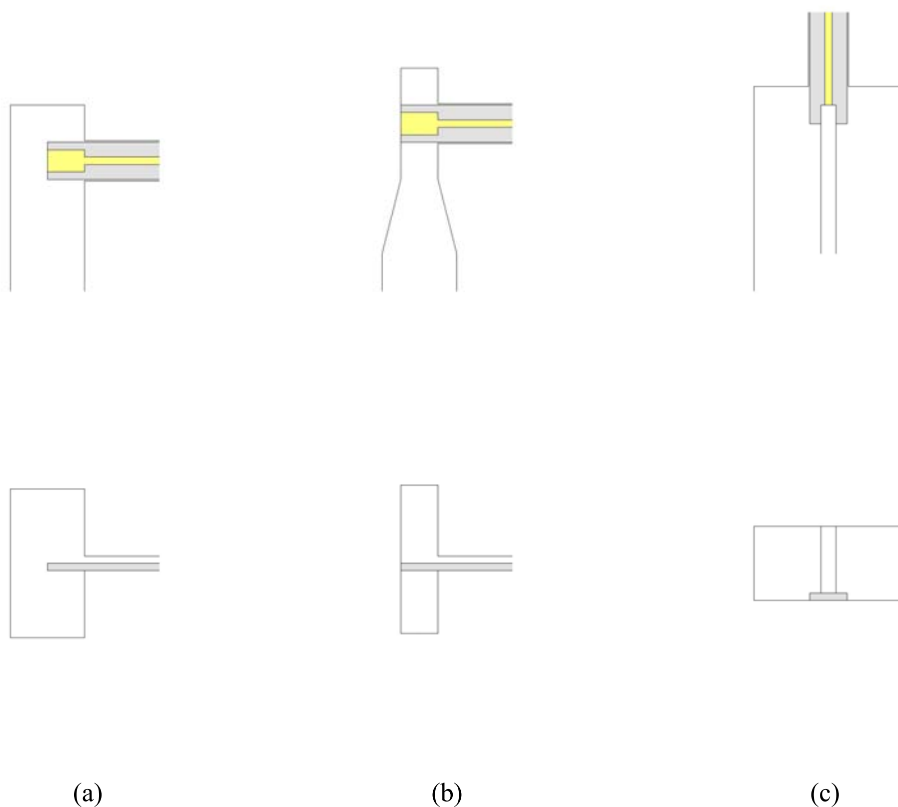

Fig. 7.13. Comparison of three different probe geometries: (a) longitudinal E-Field, (b) longitudinal H-field, and (c) ridge-contact.

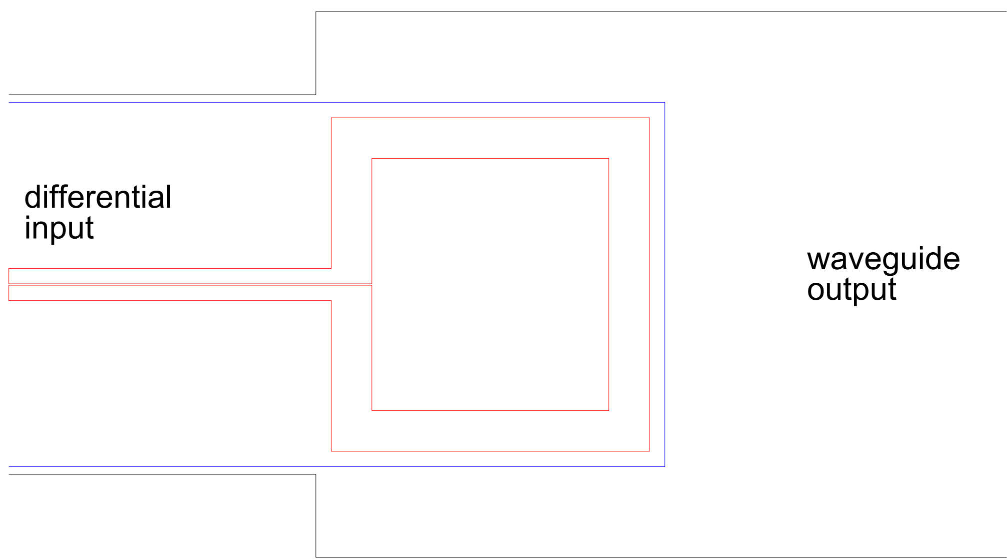

Fig. 7.14. Layout of differential loop probe. The narrow wall of the output waveguide is shown on the right.

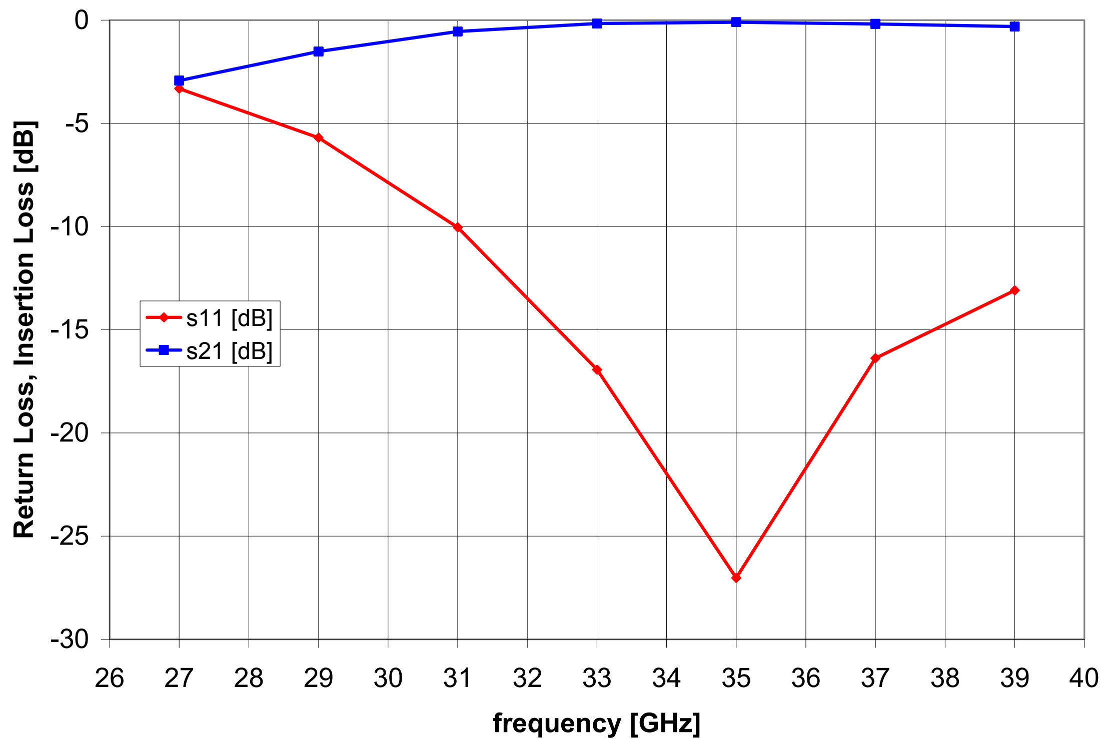

Fig. 7.15. Simulated s-parameters for differential loop probe tuned to 35 GHz.

7.4. Passives in Multi-Chip Modules

In addition to the MMICs themselves, any sufficiently complex multi-chip module will require a number of passive components, such as the waveguide and coax transitions described previously, as well as filters, couplers, power dividers, hybrids, terminations, and attenuators. It is useful to find techniques for implementing these parts that integrate seamlessly with the MMIC chips. A microstrip solution is ideal, but it is usually too costly to waste valuable real estate on a MMIC wafer for something as trivial as a filter. A better alternative is to use ceramic substrates like Aluminum Oxide, commonly called Alumina, or microwave laminates such as Rogers' Duroid. The latter is typically less expensive, but the minimum feature sizes available with those soft-substrates are often not sufficient for millimeter-wave work. *Thin film* manufacturing companies, however, can pattern materials like Alumina with metal traces that have

dimensions as small as 10 μm. These processes include the option of two-sided metal patterning, plated-through via holes, and TaN or NiCr films with sheet resistance that can be specified between about 10 and 200 Ω/□ [66-68].

A good example of an Alumina passive element made to integrate within a multi-chip module is the coupled-line bandpass filter shown in Figure 7.16. Though entirely a microstrip circuit, it includes CPW transitions at both ends to take advantage of the three bond wire interconnect that was described in Section 7.1. Being a fairly high-frequency filter (75-110 GHz), it is doubtful a single bond wire would have produced acceptable results.

The thickness of the substrate should also be considered carefully. When bonding from one MMIC chip or passive substrate to another, it is easiest if the top surfaces of both pieces are at the same level. A large step may force the two chips to be placed further apart in order for the bonding tool to reach the pads of the lower chip, which would result in longer wires and increased inductance. It is possible to machine pedestals for the thinner chips to rest on, thus leveling the top surfaces of all the chips, but one should note that doing so places a large discontinuity in the ground path which may be equally detrimental to the module's performance. A passive substrate thickness of 5 mils is typically close enough to the MMIC substrate thickness, which usually falls between 2 and 4 mils, to avoid any serious problems.

Also, when making a connection between a MMIC and a passive circuit, it is best to bond to the MMIC first, and the passive substrate second. This is because the wire bonder must break off the wire after making the second bond, which places a larger amount of stress on the pad of the second chip. There is a greater risk of peeling up the top metal of a GaAs or InP MMIC, which usually has smaller pads, than on the Alumina substrate which is more rugged and less costly to replace should something go wrong.

Microstrip filters like the one described above are relatively compact and easy to design and use, but they may not be suitable in situations which call for a very high-Q filter. Waveguide filters may offer better characteristics, but it is not obvious how best to integrate them into a MMIC-based system. One approach is illustrated in Figure 7.17. Here, we have used the well proven microstrip-to-waveguide transitions to couple into a short waveguide channel which houses a septum-resonator filter. The vanes of the filter are made by lithographically etching a piece of 2 mil thick shim-stock which is sandwiched

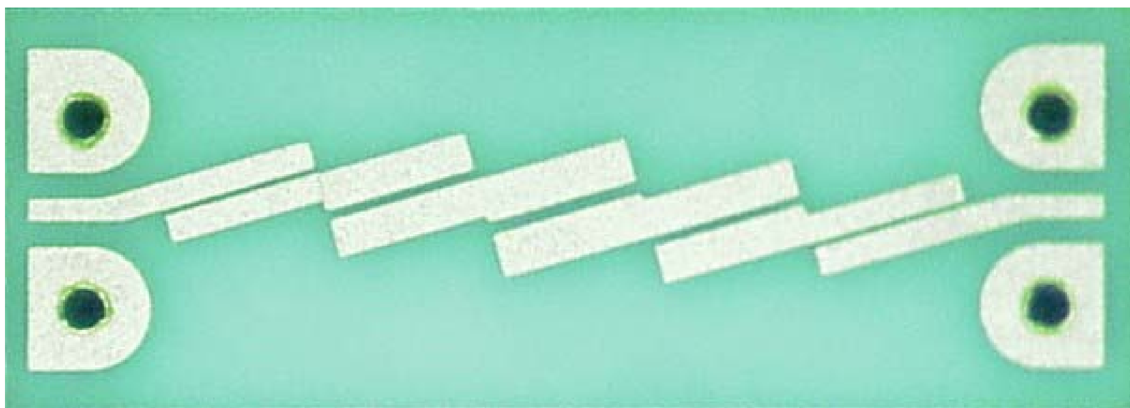

Fig. 7.16. Microstrip bandpass filter fabricated on a 127 μm thick Alumina substrate.

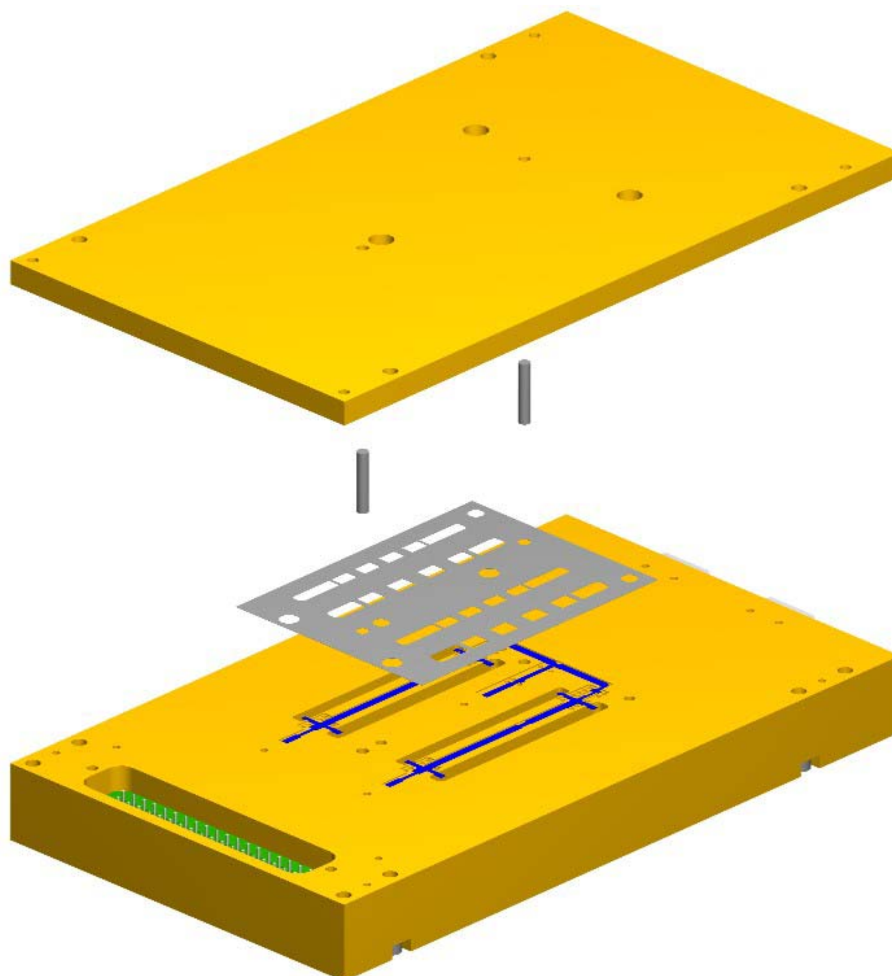

Fig. 7.17. Multi-chip module utilizing fully integrated waveguide filters. A photochemically etched metal shim is held between the two halves of the split block, forming septum resonators that make up the filter. Guide pins ensure good alignment of the shim with the waveguide channels. MMICs and passive chips are shown in blue.

between the two halves of the split-block. As always, such construction allows the block to be split longitudinally along the broad wall of the waveguide to minimize loss. The waveguide channel is entirely internal to the block, eliminating the need for bulky waveguide flanges or separate housings for MMICs and filters.

Another common passive needed in millimeter-wave systems is the directional coupler. The simplest microstrip solution is the backward-wave coupler formed by a quarter-wavelength section of edge-coupled transmission lines. It is commonly known, however, that microstrip implementations of this coupler suffer from poor directivity as a result of the differing even- and odd-mode phase velocities, which is why commercial couplers of this type are almost exclusively built in stripline. Unfortunately, stripline circuits are more difficult to integrate with microstrip or CPW MMIC-based modules. The problem of phase velocity compensation in microstrip couplers has been studied by many researchers, and a number of techniques have been proposed [70]. For example, some improvement can be achieved with lumped capacitors between the lines at both ends of the coupler, or by meandering the gap between the coupled lines (the so-called "wiggly" or "serpentine" couplers) to slow down the odd-mode without much affecting the even-mode [70]. The former option requires discrete parts to be soldered into place by hand (since capacitors are not usually available in a ceramic or soft-board manufacturing process), and the latter method really only works well when the lines are very close together, i.e., when the component has tight coupling.

For loose couplers, an easier, fully-planar alternative is to use a codirectional coupler. In the common backward-wave coupler, one uses the fact that the even- and odd-mode waves have differing impedances, but it is assumed (incorrectly, as described above) that their phase velocities are equal. Therefore, when the two modes reach the end of the coupled-line section, which is usually terminated with 50 Ω loads, the higher-impedance even-mode reflects with 180° phase shift and the lower-impedance odd-mode reflects with no phase inversion. The two modes then add constructively on the coupled-port in the reverse-direction, launching the coupled wave backward. In a codirectional coupler, however, one uses the differing phase velocities to build up a coupled-wave in the forward direction, and the task is simply to ensure that no reflection of the even- and odd-modes occur which would launch a backward wave and

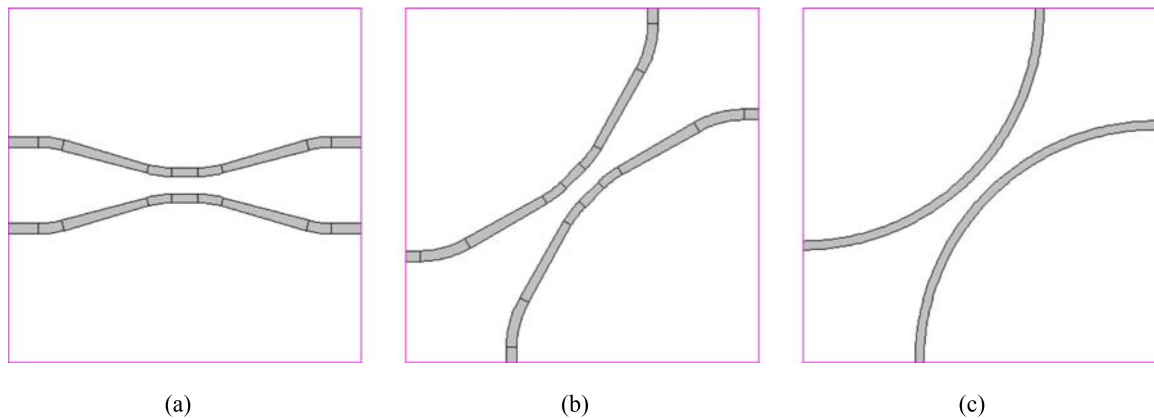

Fig. 7.18. Evolution of the arc-coupler topology. (a) standard codirectional coupler. (b) rotated codirectional coupler. (c) arc-coupler geometry.

degrade the directivity. It is possible to match both modes, even though they have different impedances, by gradually tapering the exits from the coupled-line section at both ends.

Charged with the task of designing a millimeter-wave coupler for a MMIC-based application, the author began with the basic topology of a codirectional coupler shown in Figure 7.18a. There are a large number of parameters that all play a role in determining the coupling factor, input match, and directivity of this design. The importance of the tapered end-sections should not be underestimated, since they are precisely what makes this codirectional, rather than the backward-wave variety, and will directly influence the directivity of the final circuit. The taper must be long enough to provide a good match to both modes at the lowest operating frequency and should separate the feedlines by a great enough distance to completely decouple the transmission lines. Radiusing the bends is also critical to matching both modes, and cannot be done too sharply. Unfortunately, it also makes analyzing the overall structure more difficult since the gradual turn will effectively lengthen the coupled-line section and thereby change the coupling factor and operating frequencies. One inevitably ends up having to optimize a large number of design parameters in a numerical simulator which is both tedious and time consuming.

A practical detail that one should also consider is that a multi-chip system in which this coupler is used will be more difficult to layout if any two of the ports come out on the same edge of the chip. It is more convenient if each of the four ports lies on a separate side. Thus, it is useful to rotate the whole structure 45° as shown in Figure 7.18b. The critical dimensions are exactly the same, so the initial

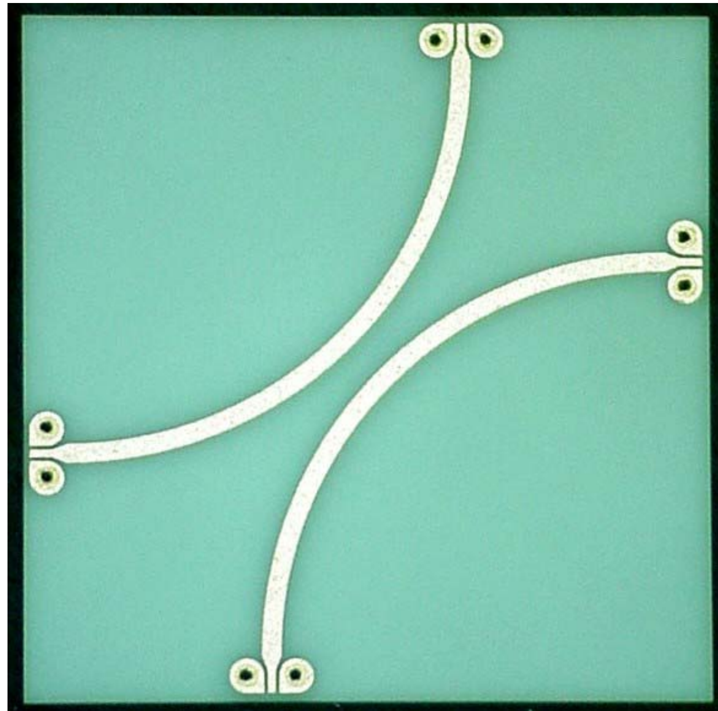

Fig. 7.19. Photograph of the 50-110 GHz codirectional coupler. Chip dimensions are 4.6 x 4.6 mm. Alumina substrate is 127 µm thick.

simulation need not be revised, but having drawn this picture, the author noticed how much the two metal traces resembled quarter-arcs of circular rings. Out of sheer curiosity, I tried simulating the simpler arc-coupler structure shown in Figure 7.18c. This is, of course, much easier to optimize as it only has two parameters for us to deal with, the radius of the arcs and the minimum separation between them (the width of the trace was fixed to that of a 50 Ω microstrip line). The structure is so much simpler, in fact, that my first best-guess dimensions resulted in better performance (in terms of directivity and input match) than the optimized version of the coupler shown in Figures 7.18a-b.

Taking advantage of this serendipitous discovery, the authors quickly prototyped a broad 50-110 GHz coupler (Figure 7.19) which was needed for a MMIC-based Vector Network Analyzer. Theoretically, the coupling of a codirectional design will vary as

$$s_{31} \approx -j \sin\left(\frac{\pi \Delta n_{eff} L}{c} f\right) \tag{7.6}$$

$$\Delta n_{eff} = \sqrt{\varepsilon_{eff}^{even}} - \sqrt{\varepsilon_{eff}^{odd}} \tag{7.7}$$

where L is the length of the coupled-line section, and Δn_{eff} is the difference between the square roots of the effective dielectric constants of the two modes [71]. So, an octave-band coupler like this one would normally have about 3 dB coupling variation. That amount of variation is perfectly tolerable in a VNA since the precise coupling is not critical and will be taken out in the usual calibration of the instrument. Further, the stronger coupling occurs at the high end of the band, and may help to offset the usual roll-off that amplifiers and other components tend to experience at higher frequencies. For this particular project, it was decided to design for a nominal 9-12 dB coupling factor.

The simple coupler geometry shown in Figure 7.18c was modeled with Ansoft's High-Frequency Structure Simulator (HFSS). The simulation predicted that the arc-geometry would have slightly more variation in coupling factor over the octave bandwidth than the 3 dB that was calculated for a straight codirectional coupler, but the directivity remained very good. Final dimensions for the line spacing and radius were selected after only a few iterations.

In order to verify the design, it was necessary to make test pieces which had 50 Ω terminations on two of the four ports. Since the quality of the termination limits the measurable directivity, it was important to design a load that would have good return loss over the full bandwidth of the coupler. A dot-termination was used, which consists simply of a disc of thin-film material with sheet-resistance equal to 50 Ω/□ [62]. This termination has a lower-frequency limit set by the diameter of the disc, and upper-frequency limited only by moding of the microstrip line. A sketch of the dot termination used for this project is shown in Figure 7.20. The dot diameter used was 800 μm which simulations predicted would have excellent return loss above about 30 GHz.

Three test pieces were fabricated, and are shown in Figures 7.21-23. The first was used to measure forward-coupling, the second for isolation, and the third for insertion loss. Standalone terminations were included on the piece in Figure 7.21 for verifying the dot's performance. All test pieces as well as the final coupler (Figure 7.19) were fabricated by American Technical Ceramics on 127 μm thick Alumina substrates.

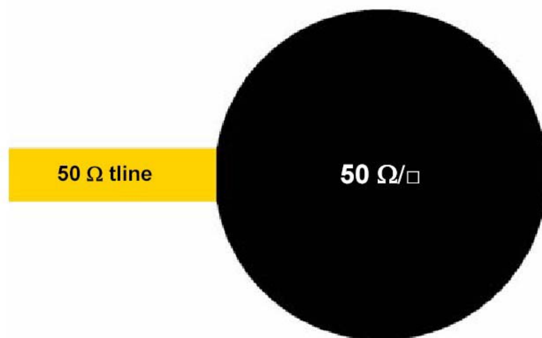

Fig. 7.20. Diagram of the dot termination The diameter of the thin-film disc was 800 μm, setting a lower frequency limit of about 30 GHz.

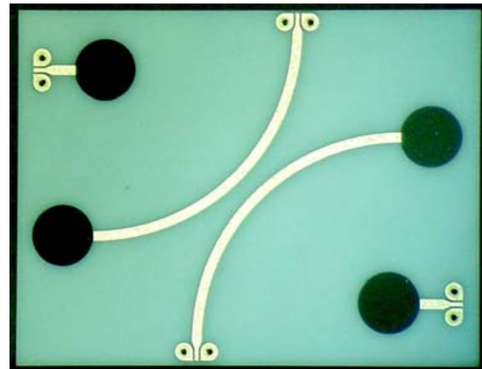

Fig. 7.21. Photograph of the test substrate for measuring dot terminations and forward-coupling of the 50-110 GHz coupler.

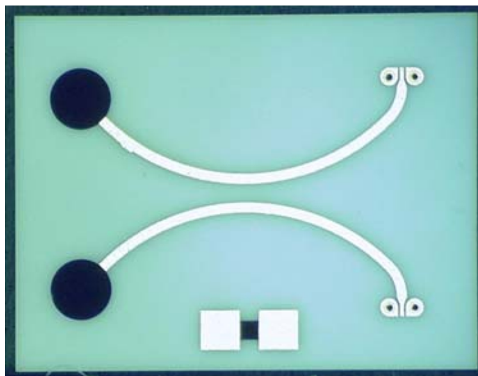

Fig. 7.22. Photograph of the test substrate for measuring isolation of the 50-110 GHz coupler.

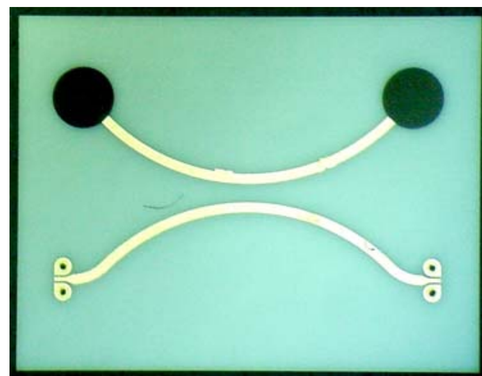

Fig. 7.23. Photograph of the test substrate for measuring insertion loss of the 50-110 GHz coupler.

Measurements were performed with an HP 8510C Vector Network Analyzer. Above 50 GHz, external VNA extensions from Oleson Microwave Labs were used to test the circuits in WR-15 and WR-10 bands. The 1-port measurement of the dot-termination is shown in Figure 7.24. The return loss is better than 25 dB from 30 to 75 GHz. It degrades to 16 dB by 110 GHz but is consistent with the expected performance of the microstrip-to-CPW transition that was necessary to land the wafer probes, and is not an indication of the dot's high-frequency return loss. Fortunately, the transition is not present on the terminated ports of the test couplers, and will not therefore limit the directivity that is measured. Based on simulation, the dots alone are believed to operate very well up to and beyond 110 GHz.

The measured performance of the coupler is plotted in Figure 7.25. The coupling factor was a bit lower than the simulation, but as expected, the maximum coupling occurred at 110 GHz with a value of

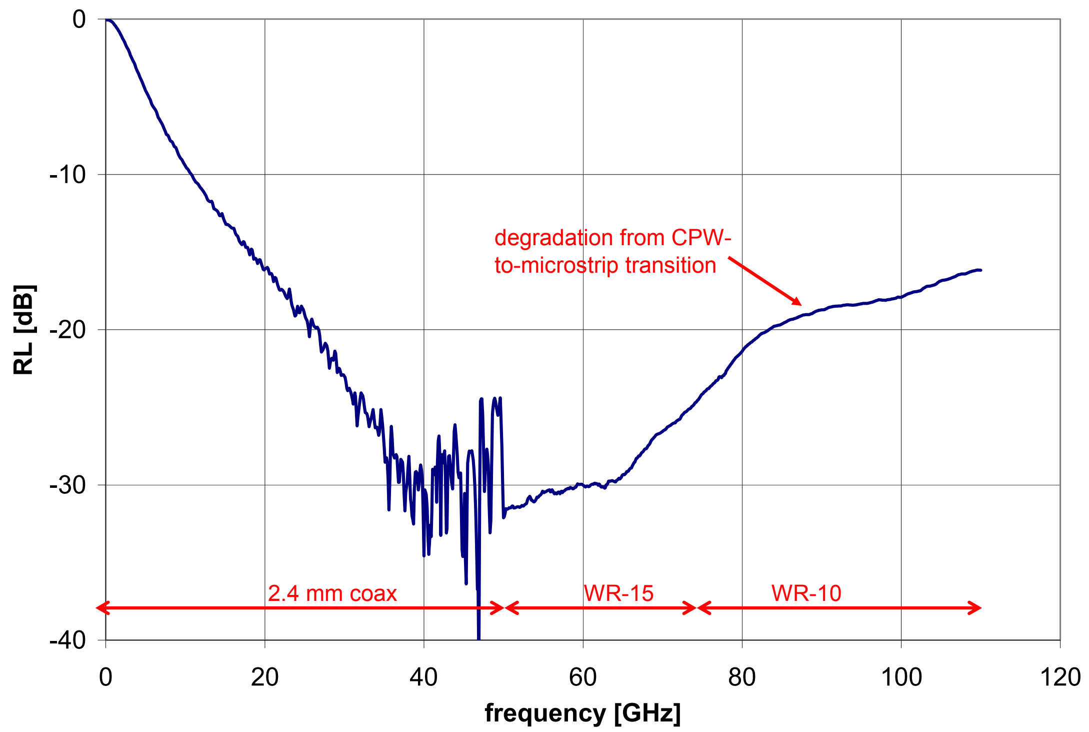

Fig. 7.24. Return loss of the 800 μm dot termination measured in three VNA bands. The degradation above 70 GHz is believed to be due to the CPW-microstrip transition rather than the termination itself.

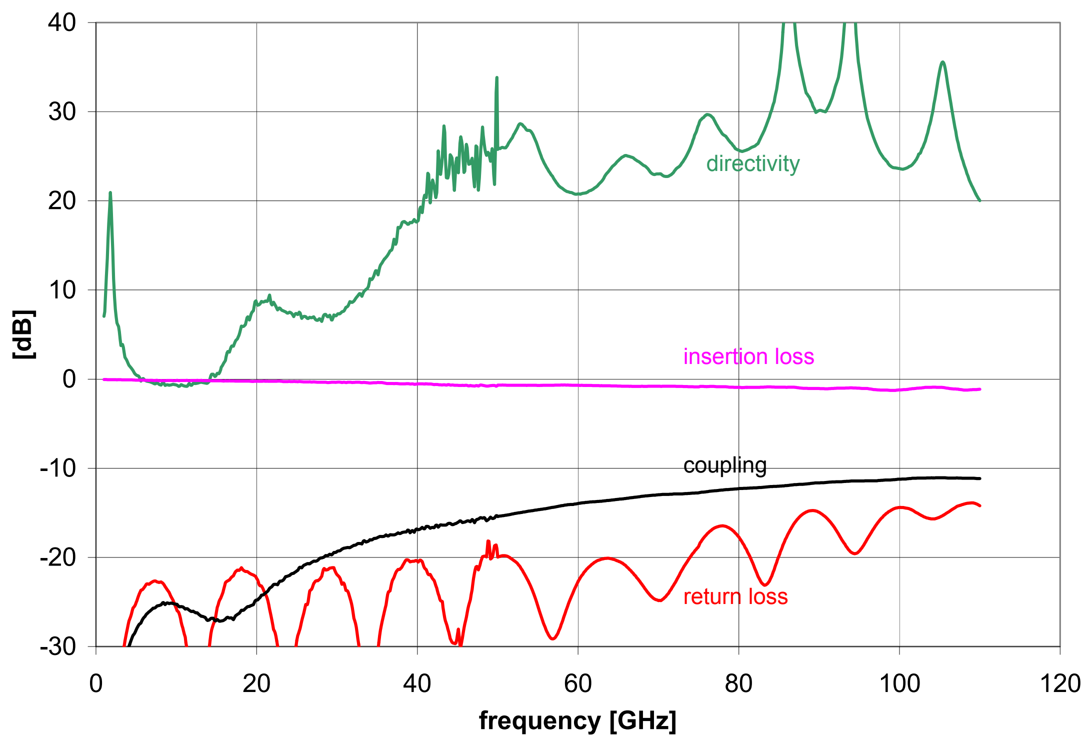

Fig. 7.25. Measured coupler performance.

11.2 dB. It fell to 12.8 dB at 75 GHz, and 15.4 dB at 50 GHz. Input return loss was at least 15 dB, and directivity was better than 20 dB across the full octave of bandwidth. Maximum insertion loss was 1.1 dB at 110 GHz. This data was corrected for a small error in the transmission line impedance by renormalizing the s-parameters to 48 Ω, but this amounted to less than a 2 dB correction in the directivity and input match.

7.5. A MMIC-BASED 75-110 GHZ SIGNAL SOURCE

There is growing interest in W-band electronics for various applications including automotive and meteorological radar systems, atmospheric radiometry, and even communications. However, development efforts in this area are hindered by the difficulty in finding solid-state signal sources with sufficient power, low spurious tones, and the large bandwidth necessary for general use in a variety of projects. Traveling-Wave Tube oscillators and amplifiers are also available in this frequency range, but the auxiliary requirements for high-voltage power supplies and cooling systems make them inconvenient in many settings, particularly when it is necessary to mount them on a probe station for on-wafer measurements. The 75-100 GHz Active Multiplier Chain from Millitech (AMC-10-R0000) is compact and capable of providing about 5 mW of power through much of the waveguide band, but it has several dB conversion loss and is unleveled [73]. Finally, Agilent makes a sophisticated millimeter-wave source module (83558A), but it is much larger and has a maximum leveled power of 1 mW [74].

Here, we report on the development of a compact, 20 mW, broadband signal source suitable for measurement setups in the 75 to 110 GHz range. A photograph of the module appears in Figure 7.26. It makes use of recently developed Monolithic Millimeter-wave Integrated Circuits (MMICs) as well as other commercially available chips. The MMIC approach results in a light, compact module (60 cm^3). Additional features such as an integrated reflectometer and voltage-controlled gain make this a flexible and user-friendly instrument in a laboratory setting.

This module was made possible by the recent development of two key W-band, integrated

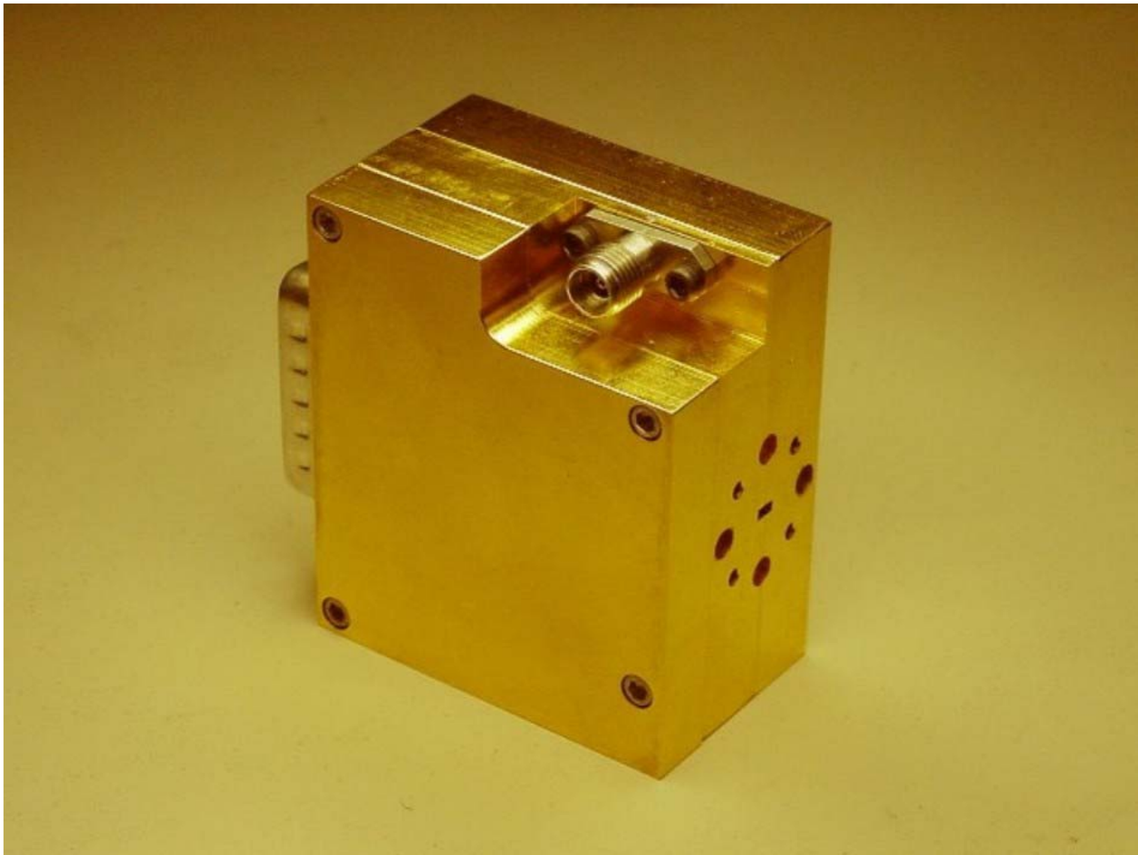

Fig. 7.26. Photograph of the W-band signal source. The module dimensions are 5.1 x 4.3 x 2.6 cm.

circuits: a full waveguide band tripler (Section 2.1) and a broadband power amplifier [46]. The maximum output power of the tripler is only about 1 mW, so amplification is necessary for practical use. The power amplifier delivers 16 dBm of power across the band. Although designed independently for unrelated projects, the concurrent development of these two chips inspired the idea to combine them in a multi-chip module that would be useful in future millimeter-wave research.

A schematic of the module is shown in Figure 7.27. The input signal is fed into a commercially available MMIC driver amplifier and a commercial frequency doubler. The output of the doubler is filtered with a custom designed hairpin-style bandpass filter. It was fabricated by UltraSource Inc. on a 125 μm Alumina substrate. The next chip is a variable-gain amplifier that is used to level the power output of the module. It is nominally biased to deliver about 10 mW from 25 to 37 GHz which is sufficient to drive the frequency tripler and W-band power amplifier described earlier. A second bandpass filter blocks spurious signals that may have been generated by the tripler outside of W-band. The tripler itself has rejected

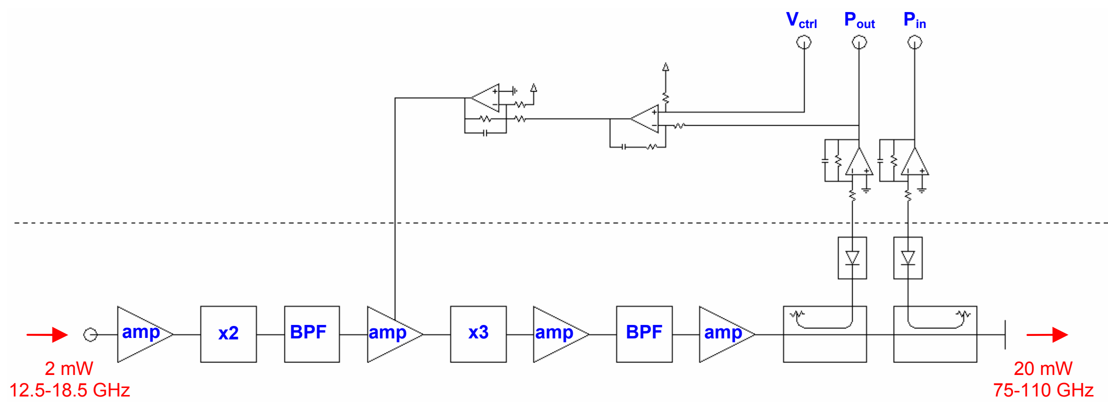

Fig. 7.27. Schematic of the W-band source module. Components above the dotted line are on a small PC-Board, while the higher frequency components below the line are mounted in a small cavity inside the split block

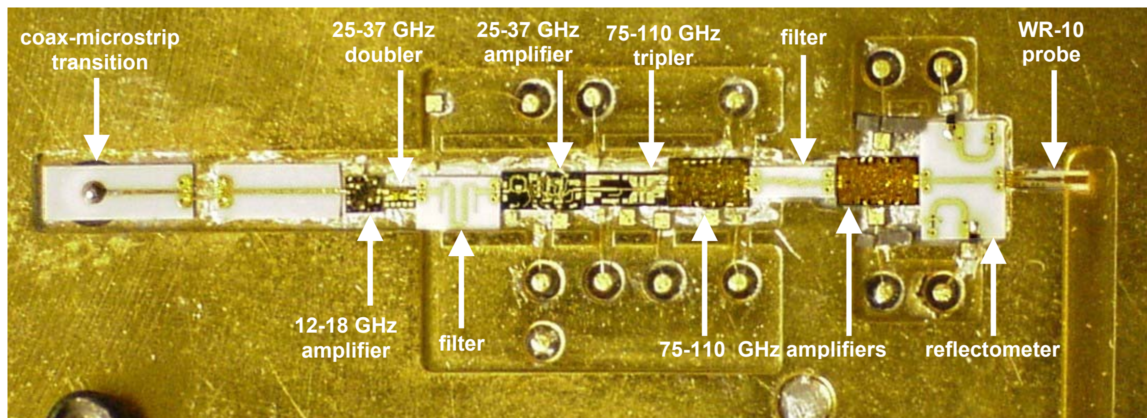

Fig. 7.28. Photograph of the interior of the split block, showing the coaxial input on the far left, the MMIC amplifiers, multipliers, and passive circuits, and finally the WR-10 waveguide output on the far right. The small holes above and below the row of chips are glass-bead DC feedthrus that connect the bias and control points of the MMICs to the PC-Board on the opposite side of the metal chassis. A schematic of this network is shown in Figure 6.21.

spurious tones that fall within W-band, as described in Section 2.1. A second output amplifier is included to ensure the maximum power is obtained from the module. Finally, the output signal passes through a dual directional-coupler with integrated millimeter-wave detectors. Like the bandpass filters, this microstrip reflectometer was fabricated by UltraSource on 125 μm Alumina. The couplers are codirectional in design, thus overcoming the directivity problems inherent in microstrip backward-wave couplers [76]. Integrated on the substrate are lossy impedance transformers that are designed to match the detector-diodes across W-band. They are also designed to compensate the natural downward slope of the diode's responsivity so that the detected voltage is relatively independent of frequency and is small enough to keep the diodes in square-law operation.

The module is constructed as a split-block with the dividing plane bisecting the broad wall of the output waveguide. This minimizes loss in the waveguide as the propagating mode has no current across the junction. The MMIC chips lay in a 280 μm deep cavity machined into one of the blocks, as shown in the photograph of Figure 7.28. The transition from coaxial cable to microstrip is a perpendicular design in which the coax comes up to the microstrip section from below. Unlike more common end-launch connectors, this geometry maintains a planar top surface of the block so that the chips can be wafer-probed during initial testing. A novel transition adapter (Section 7.2) allows the junction to perform well up into the millimeter-wave band. On the output side, an E-plane, longitudinal probe accomplishes the transition into WR-10 waveguide.

DC signals, such as the bias, gain control voltage, and detected output and reflected power monitors, are connected to glass-bead feedthrus which pass through the block and contact a small PC-Board mounted on the opposite side (Figure 7.29). The PC-Board contains voltage regulators for the bias points and op-amps for power control and leveling. The module power supply, control voltage, detected voltages, and several current monitor points are accessible through a 15 pin D-subminiature connector mounted on the PC-Board. A protective metal cover fits over the exposed electronics. Fully assembled, the module is 5.1 x 4.3 x 2.6 cm and weighs 335 grams.

A diagram of the measurement setup is shown in Figure 7.30. The input signal was generated with an HP 8340A Synthesized Sweeper. The input power was monitored with a 16 dB directional coupler and power meter. A 10 dB WR-10 coupler was attached to the output of the module and a W-band power meter was connected to the thru arm to measure the output power. On the coupled arm was a WR-8 down-converter with a 90 GHz Gunn Oscillator for the LO. The down-converted output was then displayed on an HP 8564E Spectrum Analyzer. In this way, the output spectrum was monitored during the measurement, ensuring that the power meter was reading the main desired signal and not some unusually strong spurious tone. Although no well-calibrated measurement of the harmonics was made, it was clear on the spectrum analyzer that the harmonic rejection was on the order of 20 dB or more, at least within the frequency range of the WR-8 down-converter. Both the loss of the waveguides (typically on the order of 1 dB) and the precise coupling of the couplers were known ahead of time and calibrated out of the measurement, so the

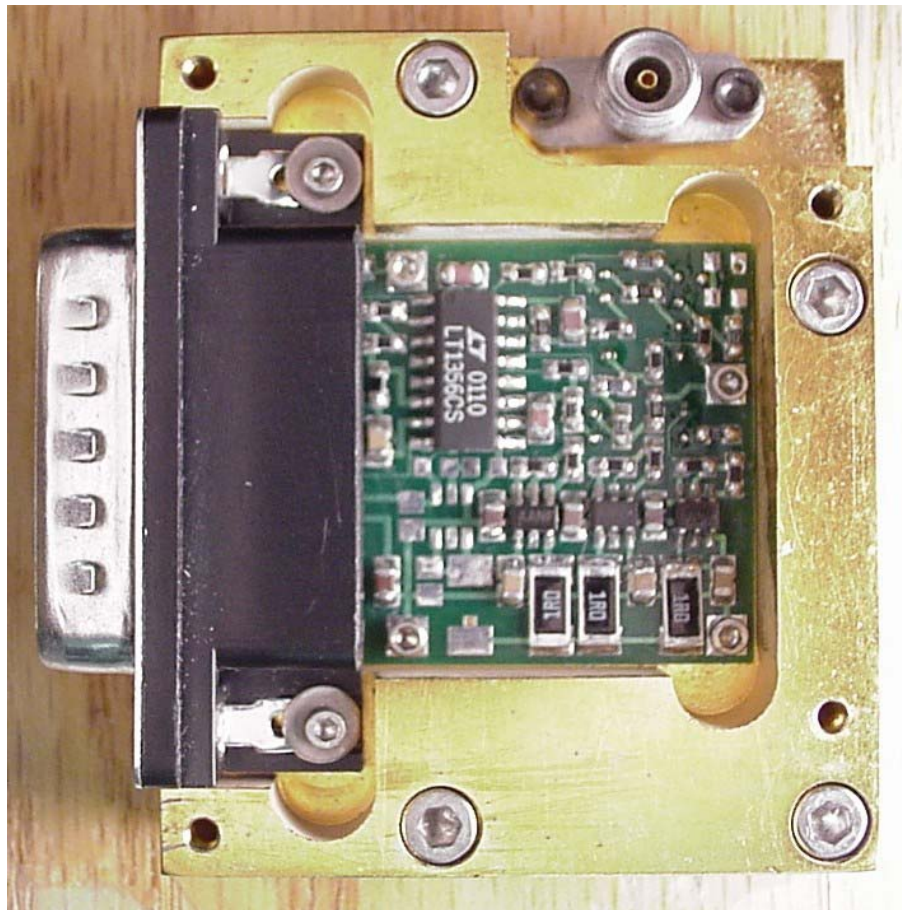

Fig. 7.29. Photograph of the module with the top cover removed, showing the PC-Board containing bias and leveling control circuitry.

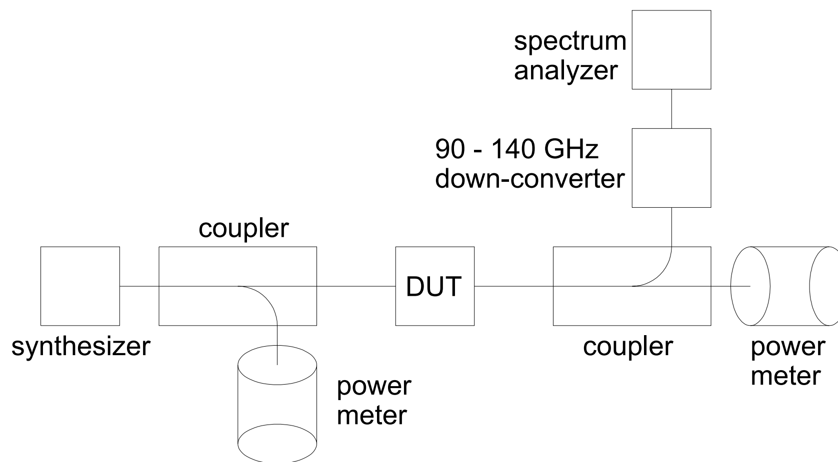

Fig. 7.30. Diagram of the test setup.

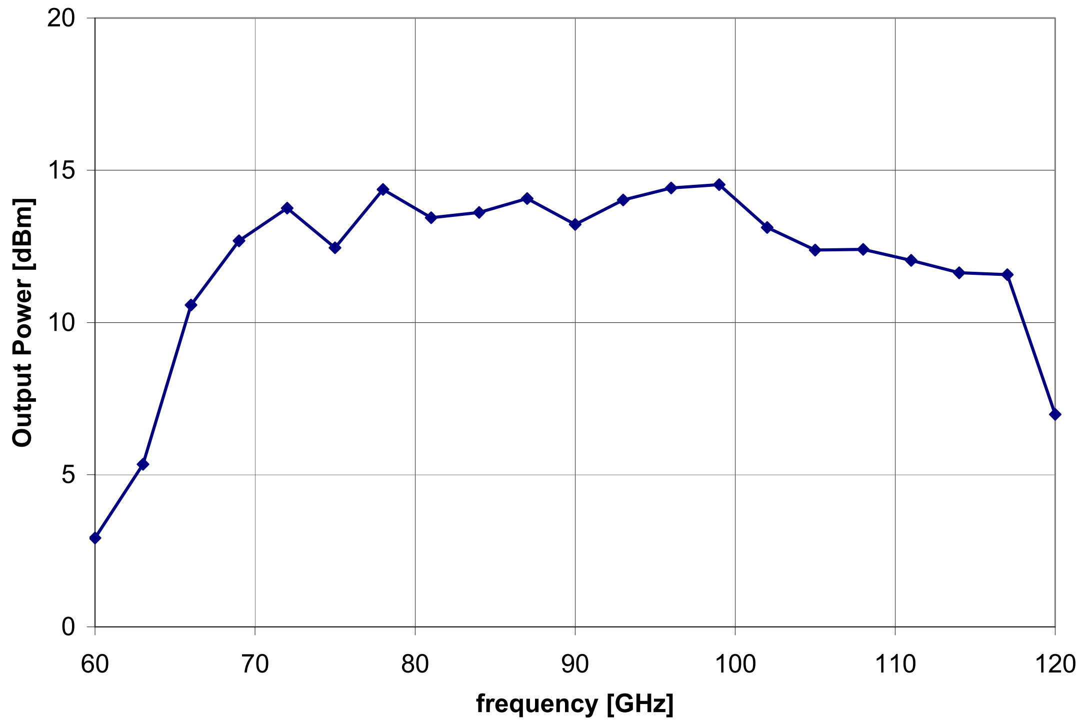

Fig. 7.31. Output power versus frequency. Input power was +3 dBm, and the control voltage was fixed at -1 V for maximum gain.

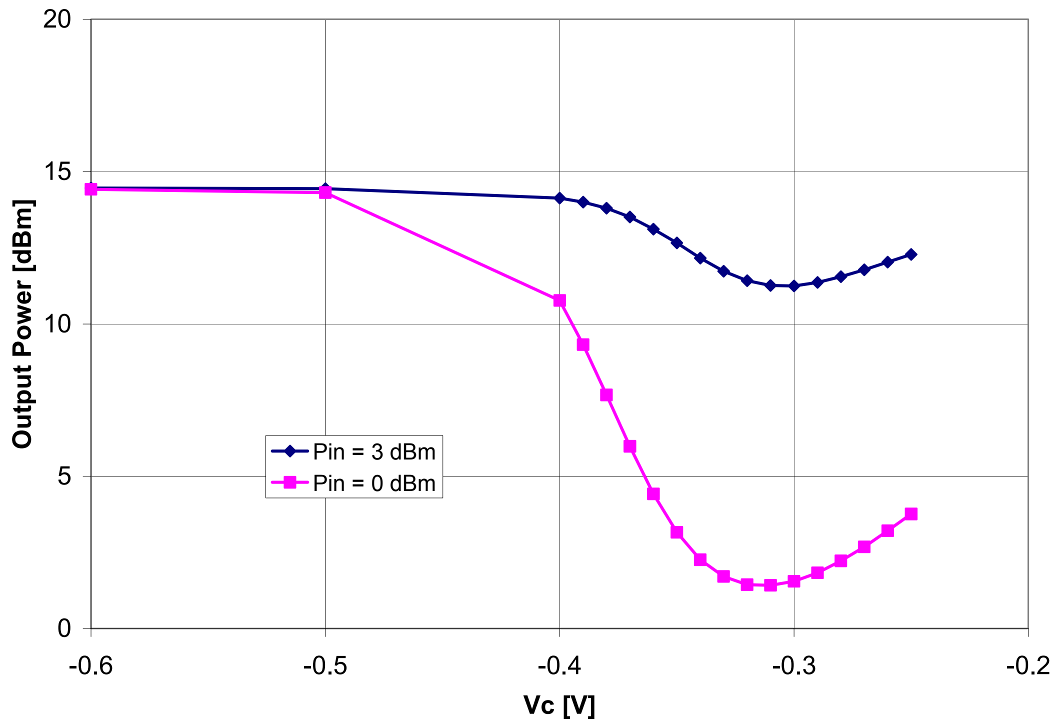

Fig. 7.32. Output power versus control voltage at 96 GHz.

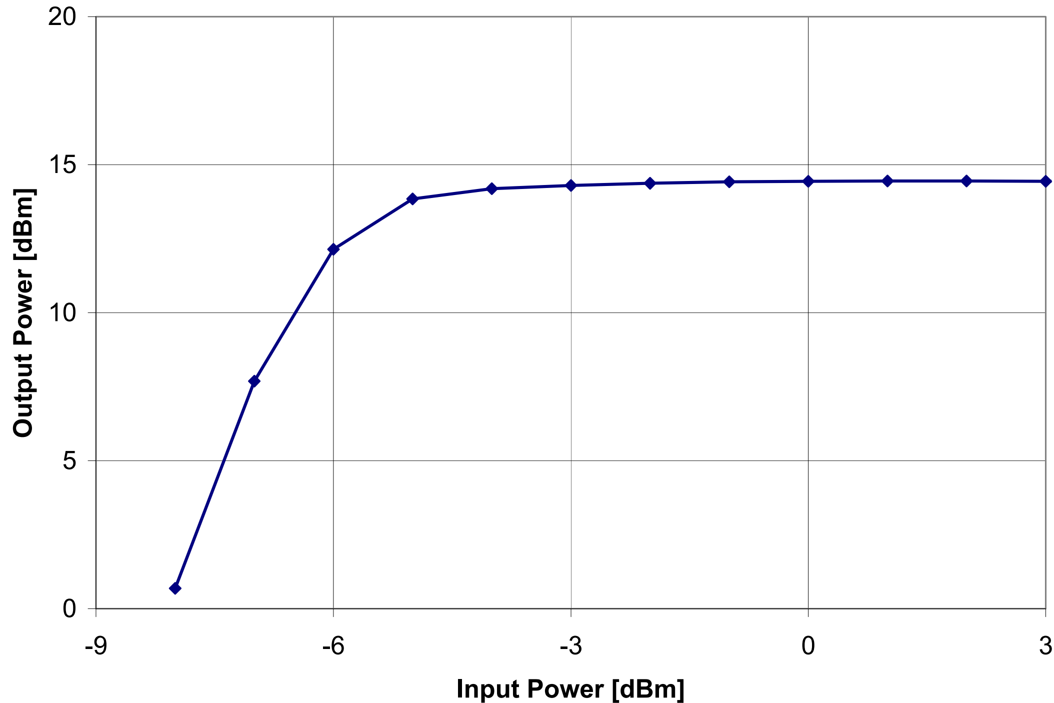

Fig. 7.33. Output power versus input power at 96 GHz. The gain control voltage was fixed at -1 V for maximum gain.

data represents the power at the ports of the module itself.

The key results are plotted in Figures 7.31-7.33. With 3 dBm input, the output power was 13.4 ± 1 dBm across W-band, as shown in Figure 7.31. Output power versus control voltage near the center of the band is plotted in Figure 7.32. The location of the minimum in the gain curve, about -0.3 V, is consistent with the response of the variable gain amplifier used in the module. The leveling loop was carefully designed to limit the control voltage within the monotonic range of this curve to prevent it from latching up on the low-gain end of the curve. Finally, output power versus input power is plotted in Figure 7.33.

Measurements reveal that the reflectometer is not responding correctly to the output power, in turn throwing off the operation of the leveling loop. A careful revision of the coupler and detector matching network is under way, and it is hoped that these features will be restored. However, in spite of these problems, this module still represents a step forward in millimeter-wave signal generation. Such a module is widely useful as a laboratory test instrument. A comparison with three commercial instruments is made in Table 7.1.

Table 7.1. Comparison with Commercially Available Instruments

Module	Output Freq.	Power	Conv. Gain	Volume	DC Power	Leveled	Flatness
Agilent 83558A	75-110 GHz	+1 dBm	-16 dB	1344 cm^3	???	yes	**±2.0 dB**
Millitech AMC-10-R0000	75-100 GHz	+4 dBm	-6 dB	20 cm^3	6.4 W	no	**±1.5 dB**
Spacek AW-6XW	75-95 GHz	+6 dBm	-6 dB	36 cm^3	2.1 W	no	**???**
this work	75-110 GHz	+13 dBm	+10 dB	60 cm^3	1.8 W	potentially, yes	±1.3 dB

7.6 A Ka-Band Low-Noise Amplifier Module

Although MMICs are used to their greatest potential when integrated together, occasionally a project comes along that requires a single chip to be packaged in its own block. Such was the case for the module described in this section: a Ka-band cryogenic low-noise amplifier package.

The module was developed to solve problems with a previous amplifier block used in radio astronomy at the University of California in Santa Barbara, and to serve as a testbed for MMC LNA's designed for the DSN Array (see Section 1.5). Though the Ka-band front end for the DSN will ultimately include more components (Section 7.7), it is useful to have a standard package in which cryogenic noise measurements and fair comparisons can be made on various LNA chip designs. The original UCSB block was fully functional and could have served this purpose, but it was not without problems. The chassis split into four pieces and utilized a coaxial probe to transition from the MMIC to the waveguide ports. This transition was delicate, difficult to assemble, and forced the chassis to be split along an unfavorable plane with regard to loss in the waveguide. It also sunk the MMIC into a relatively deep trench in the block where it was difficult to reach with a wire-bonding tool. A new block was designed to get around these

difficulties. The goal was to make a block that was simple, compact, easy to machine, and as fast and easy to assemble as possible.

To begin with, the awkward coaxial transition was replaced with the planar, E-field longitudinal probes described earlier. Such probes had not been used in this band before, so new ones had to be designed. The design procedure is quite straightforward and was discussed in Section 7.3. Though developed initially for this specific module, the general utility of these transitions is so great that both Ka- and Q-band versions were requested by the NRAO (with whom the author was collaborating on other projects) even before the designs had been proven.

This one change from coaxial to planar waveguide probes had a cascading effect on the rest of the module. The block could now be machined from just two pieces. The MMICs could be brought closer to the surface of the base block where chip mounting, wire-bonding, and wafer-probe testing were much easier. The seam between the two halves of the chassis was now centered on the broad wall of the RF guides, minimizing loss. The time it took to assemble a complete package was reduced, which would have tremendous and obvious advantages in an array where thousands might be required.

A drawing of the LNA block without the top half is shown in Figure 7.34. The input and output ports are standard WR-28 waveguide. Space is hollowed out behind the flanges, not only to make the block lighter, but to allow screws to pass in either direction, which is useful when multiple blocks like this one are connected directly together.

The input signal is coupled into microstrip with the Alumina waveguide probe described above. The MMIC LNA follows this probe. The output signal is then coupled back into waveguide at the output. The waveguides are curved so that the flanges are directly opposite one another, which is often the simplest configuration to use in larger systems. The length of the module accommodates chips up to 2 mm in length, which is the standard dimension for MMICs designed by our group at Caltech and JPL. Shorter chips can be tested in this module with a small, 50 Ω, transmission line extension, usually placed to the right of the chip (the output) to minimize its impact on noise figure.

The cavity that houses the LNA is 1320 μm wide and 270 μm deep. These dimensions ensure that the cavity is cutoff in Ka-band to prevent feedback across the chip that might lead to instability. The depth

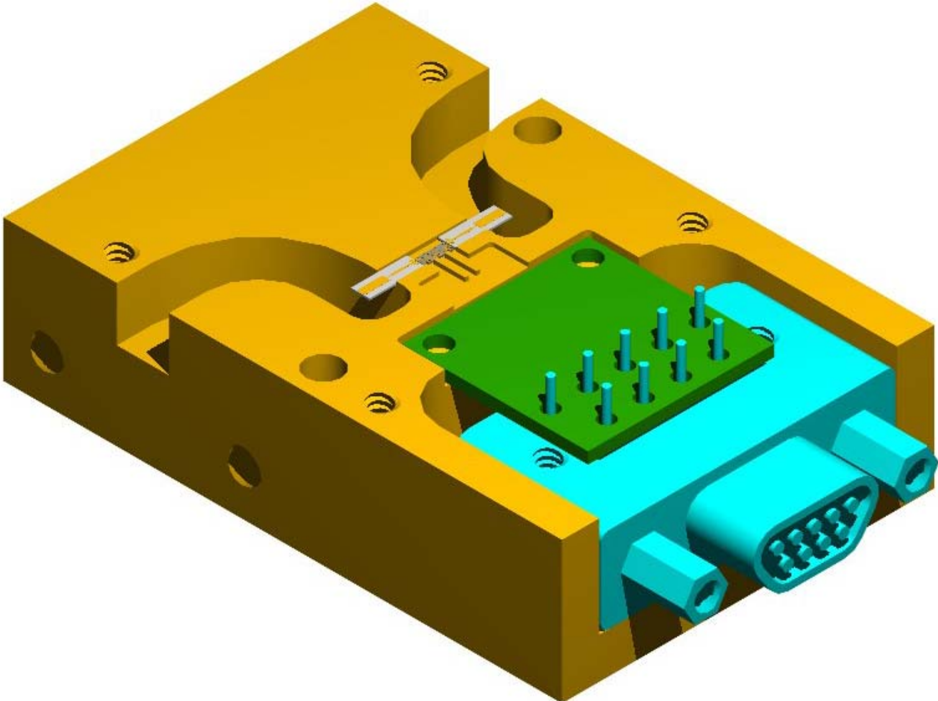

Fig. 7.34. Drawing of the Ka-band LNA package. Finished chassis dimensions are 2.5 x 3.8 x 1.9 cm.

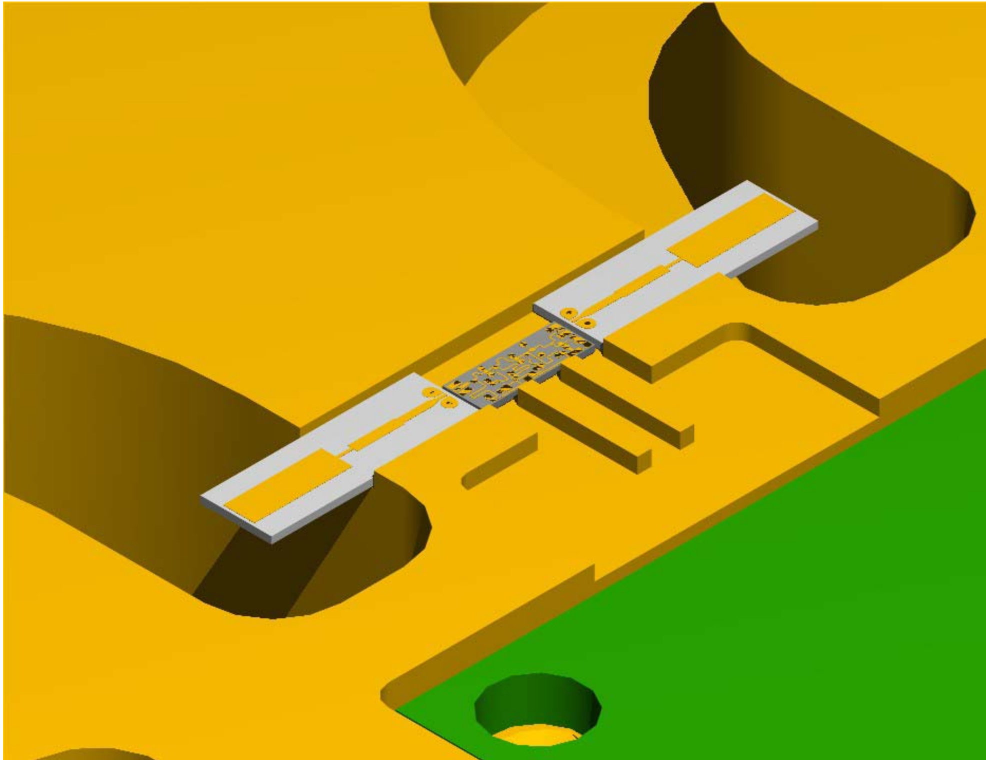

Fig. 7.35. Detail view of the MMIC LNA and longitudinal waveguide probes.

is enough to ensure that the chip would not be damaged if the block were placed face down, but not enough to hinder access to wafer probes or wire-bonders. Along the north edge of the chip are pathways for three DC connections, presumably two gates and a drain. Chip capacitors are used to bypass the DC supply lines and also as tie points for bond wires on the way to a small PC-Board. The PC-Board supports a very simple bias circuit with larger bypass caps and current monitor resistors, and also provides a transition to the 9-pin micro-D connector.

Simple by design, this module has been useful for testing and comparing various MMIC designs and foundry processes at cryogenic temperatures. It was also the model for a slightly more sophisticated package in development for the NRAO's Expansion of the VLA (EVLA), which will be discussed in more detail in Section 7.8.

7.7 A Ka-Band Cryogenic Front End

A single-chip LNA package suitable for cryogenic testing in Ka-band was presented in Section 7.6. The front end of a real telescope, however, requires a few more components, and it was asserted earlier in the chapter that MMICs are used to their best advantage when several are packaged together. This is especially true for parts that come before the first LNA in a cryogenic receiver, since they too will have to be cooled in order to avoid adding too much noise to the system, and separate packages would only add thermal mass to the load on the refrigerator.

In this section the design of a cryogenic front end package is presented that consists of a 30 dB directional coupler, two LNAs, and a fixed attenuator. Drawings of the module are shown in Figures 7.36-7.37. The RF input is through the WR-28 waveguide in the lower right. The first component in the block is a waveguide directional coupler for injecting calibration signals from an external noise source. The coupling value of 30 dB is a compromise. If the coupling were too strong, then a considerable amount of noise would leak in through the calibration port, which is at 300 K even when the noise source is turned off. If the coupling were too weak, then the external noise source would have to have a very large Excess

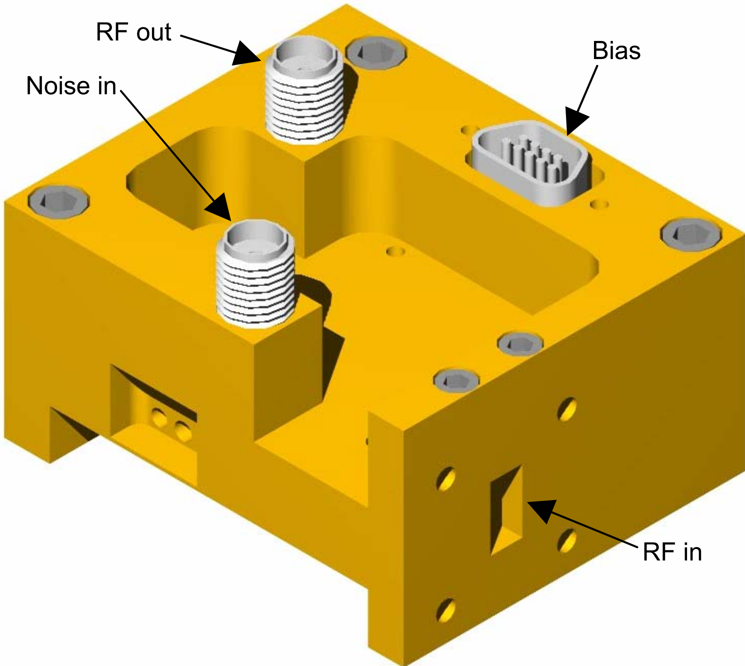

Fig. 7.36. Drawing of the Ka-band cryogenic front end.

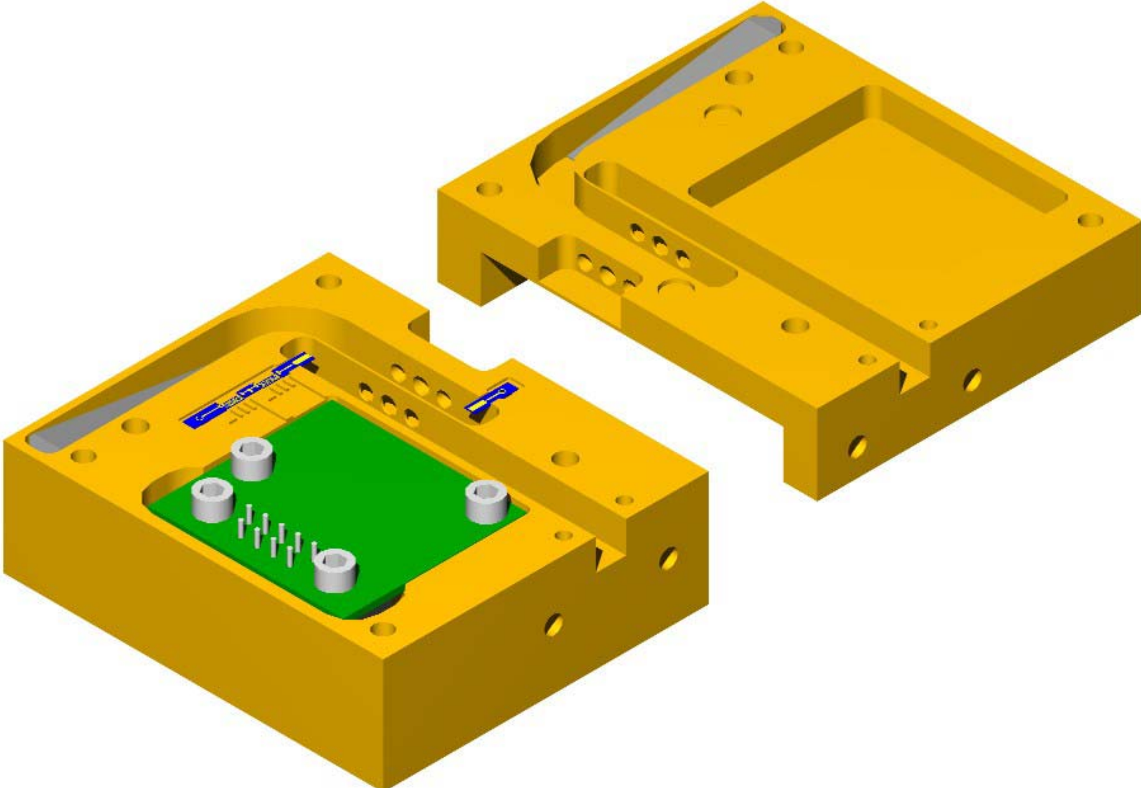

Fig. 7.37. Interior view of the Ka-band cryogenic front end.

Noise Ratio (ENR), which is difficult to realize in practice. A waveguide multi-aperture coupler design was chosen to minimize loss in this critical part of the system. Using a fabrication technique pioneered by Neal Erickson [77], the apertures are drilled through the side of the chassis, leaving holes to the outside. These holes have negligible impact on the coupler operation since they are relatively long and too small in diameter to support a propagating mode. It is only through the very thin wall of the coupler that even -30 dB can leak through these apertures.

While a second waveguide flange would have been the simplest choice for the calibration port, the specifications call for a coaxial input. As usual, a perpendicular transition is used to keep the top surface of the chassis flat, only this time it is combined with a longitudinal waveguide probe on the same substrate. While this coax-to-microstrip-to-waveguide transition may seem awkward, it has the best combination of desirable properties. A standard coax-to-waveguide transition would be difficult to machine in a block that splits on this plane, and would most likely create a vertical obstruction that blocks access to the chips. An external adapter was another option, but would have added another part to the system and more load to the cryocooler. Remember also that we are not sensitive to loss on this side of the coupler, so multiple transitions and a bit of microstrip line can be tolerated. The coupler is terminated with a built-in tapered load.

On the RF side, another waveguide probe picks up the signal after the coupler. Following that are two LNAs separated by a fixed attenuator. The system design calls for at least 35 dB of gain in the cryogenic portion of the receiver. That much gain would be difficult to achieve in a single chip, as well as risky in terms of stability, but is easily accomplished in two chips. The attenuator between them, which is set in a channel that is well cutoff in Ka-band, is a good way to isolate the LNAs from each other. Additionally, it reduces VSWR and provides a means of adjusting the gain of the module while the bias can be optimized strictly for noise performance.

Finally, the RF signal leaves the module through a coaxial connector. Bias is supplied to the chips through a small PC-Board with diagnostic and protection circuitry. Attached to the PC-Board is a 9-pin, Micro-D connector. Fully assembled, the module measures 5.1 x 4.1 x 2.0 cm. At the time of this writing, the module is still undergoing revision, but it is hoped that a prototype will be completed by June of 2003.

7.8 A Q-Band Filtered Post-Amplifier Module for the EVLA

As explained in Chapter 1, the Very Large Array in Socorro, New Mexico, is a powerful and important facility in the field of radio astronomy, but its age is beginning to show. In spite of various upgrades over the years, its receivers do not achieve the best performance available with present technology, and there are gaps in the frequency coverage. The correlator is also far behind the times, and the LO/IF transmission system rests on one of the world's only circular waveguide networks, installed just a short time before fiber optics became a superior technology.

In spite of these limitations, the VLA remains one of the most powerful and productive astronomical instruments in the world, so the NRAO is working on a substantial upgrade to all of the above mentioned systems. A brand new correlator is being developed with vastly greater speed, processing ability, and bandwidth. Existing systems are being modified just to provide the IF bandwidth that the new correlator will now be capable of processing. New receivers are being developed to fill in the gaps and allow continuous coverage from very low frequencies up to 50 GHz. A new fiber optic LO/IF distribution system will be installed. Ultimately, more dishes may be added, and connectivity to other widespread telescopes such as the VLBA will also be provided.

As ambitious as these enhancements are, the NRAO is committed to achieving them with minimal impact on the current observing schedule and functionality. This requires modifications to be phased-in a piece at a time, and many pieces need to be designed for compatibility with both the new and old equipment. Further, to minimize cost, the NRAO would like to reuse some of the components they already have which have not become outdated. These factors lead to some rather unusual choices for integration of the new components.

Such is the case for the Q-band receiver, shown schematically in Figure 7.38. The NRAO recognizes the potential advantages and cost savings offered by MMIC technology, but is reluctant to simply discard the very good Q-band mixers they already have in supply, at least in Phase I of the upgrade. New MMIC LNA's are being developed, and the current plan is to integrate them in the package along with

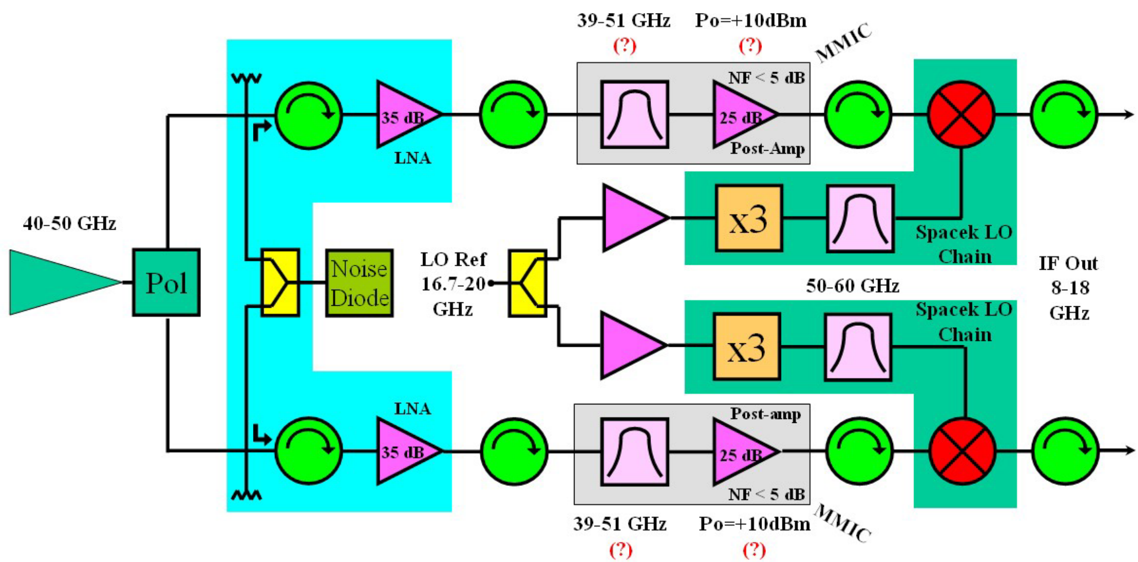

Fig. 7.38. Schematic of the EVLA Q-band Receiver. Caltech/JPL was charged with developing the RF Post-Amp chip and to package it with a suitable filter (gray box).

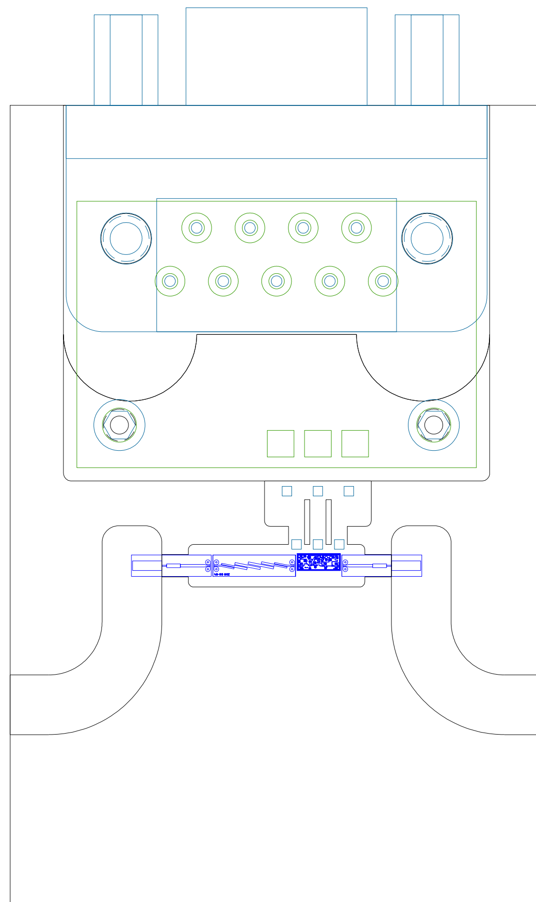

Fig. 7.39. Layout of the Q-band Filtered Post-Amplifier module for the EVLA. Chassis dimensions are 2.5 x 3.8 x 1.9 cm.

a suitable filter. A MMIC mixer is also in development, anticipating that in Phase II of the project the entire downconverter will be implemented as a multi-function MMIC module.

For now, however, the module consists simply of the RF amplifier and an Alumina bandpass filter. The Ka-band LNA block described earlier was the perfect model from which to start. The waveguide probes were re-tuned for WR-22 waveguides, and the module was lengthened to allow room for the bandpass filter. The PC-Board was also made slightly larger to accommodate more sophisticated monitor and control circuitry that the EVLA may require. The initially proposed layout of the module is shown in Figure 7.39.

7.9 A KA-BAND DOWNCONVERTER FOR THE EVLA

The other module required from Caltech/JPL in support of the EVLA program is a Ka-band downconverter. In this case, the NRAO has committed to a full MMIC solution, and several new chips had to be designed, including a frequency tripler (see Section 2.2), a broadband balanced mixer (Section 3.2), and an RF amplifier (Section 4.2). A schematic of the module is shown in Figure 7.40, and the layout is in Figure 7.41.

The RF input is from the WR-28 waveguide on the left of the drawing. As usual, the signal is coupled into microstrip with an E-field longitudinal probe. First in the block is a microstrip bandpass filter on an Alumina substrate. Next is the RF post-amplifier, a broadband balanced mixer, and an IF amplifier. The IF output is through a coaxial connector using the perpendicular coax-to-microstrip transition described in Section 7.2. As explained before, such an arrangement allows the chassis to have a nearly planar surface to mount the chips on, simplifying the assembly of the module.

The LO input also uses the perpendicular transition. The signal is then amplified before being tripled in frequency, and then amplified once more in order to drive the mixer. The output of the tripler is filtered to screen out the higher harmonics as well as the fundamental. One point of concern with this topology was that the input LO frequency (12-16.7 GHz) overlapped the IF band (8-18 GHz). It was

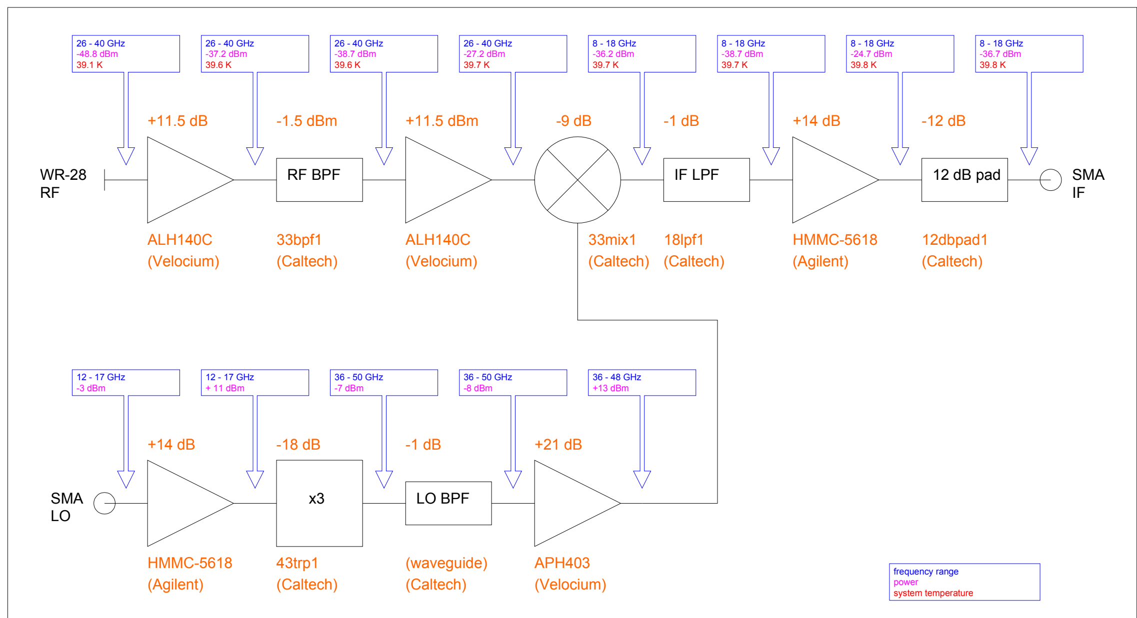

Fig. 7.40. Schematic of the EVLA Ka-band Downconverter.

estimated that a tremendous 70 dB of rejection would be needed in order to ensure that the LO spur would not overwhelm the very weak IF signal. This level of rejection is beyond even the best microstrip filters, and in fact becomes a question of isolation in the multi-chip package itself. For this reason, it was decided to use a waveguide filter in place of the normal microstrip variety, taking advantage of the low-frequency cutoff of the waveguide.

The DC circuitry is located on a PC-Board mounted beneath the MMICs on the opposite side of the chassis, rather than in the same plane with MMICs as was the case with the Q-band module. The latter approach is often simpler to assemble but becomes more difficult as the number of chips (and thus DC connections) increases. For this module, it was easier to route the DC signals down through the chassis with glass-bead feedthrus, rather than laterally using bondwires. The DC circuitry itself may also be more sophisticated in this module, including voltage regulators and greater monitoring capabilities.

The EVLA project is still underway, and further development of these MMIC-based modules is now being undertaken by another student.

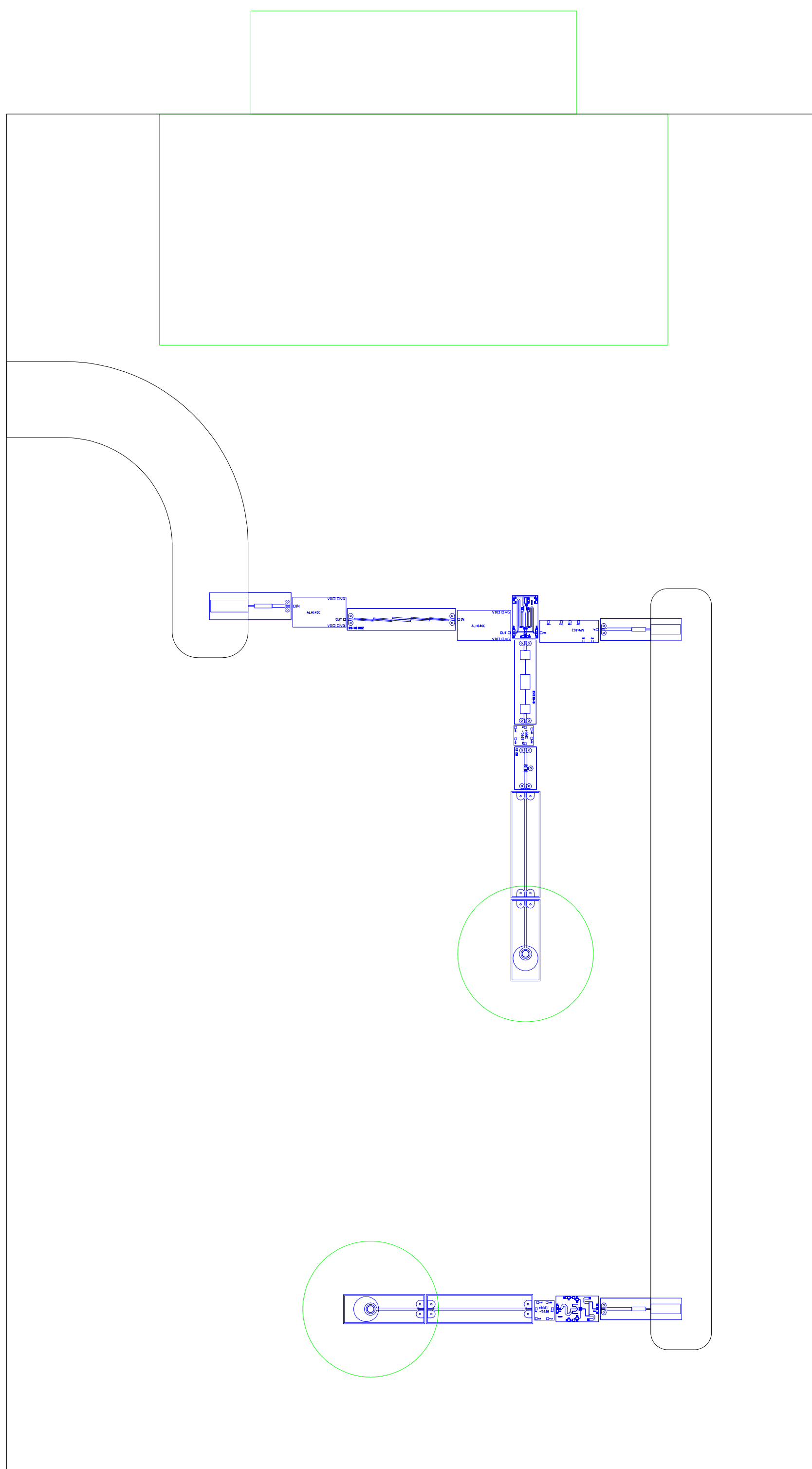

Fig. 7.41. Layout of the EVLA Ka-band downconverter. MMICs and passive substrates are shown in blue, coax connectors are shown in green.

7.10 A Ka-Band Dual-Polarization Downconverter for the DSN

The final module to be discussed is a downconverter for the DSN Array. With a total high-frequency chip count of 47, 15 of which are active MMICs, it ranks as the most complex multi-function module with which the author has ever been involved. Only 3 of the chips will be acquired commercially, the rest having been designed by the author as part of this and other projects.

Referring back to the block diagram of the DSN receiver in Figure 1.8, this module (shown in orange) follows a hybrid, which forms left- and right-circular polarizations from the signals output by the front end (Section 7.7). This module is required to handle both polarizations simultaneously, so as to avoid duplicating the LO multiplier/amplifier chain in separate blocks. The RF frequency can be switched to any one of three bands. The first band is 31.6-32.4 GHz, and is the primary Ka-band downlink frequency for the DSN. The second band is designated HEDS (for Human Exploration of Deep Space), and is 36.9-38.1 GHz. The final receive band covers 30-40 GHz for scientific measurements and diagnostic purposes. The IF frequency for the DSN Array has not been determined, but it will fall somewhere between 0.5 GHz and 2.0 GHz. This module is therefore being designed to cover that whole range.

A block diagram of the downconverter module is shown in Figure 7.42. All the high-frequency components are mounted inside a split block as usual, with the IF and DC circuitry located on a PC-Board. The LO enters through a coaxial connector. A high-valued resistor is used to sample the incoming LO power, which is then detected with a zero-bias diode and passed through the chassis to an Op-Amp on the PC-Board. This is done to permit monitoring of the LO power entering the module which will help determine if an error in the LO system occurs inside the block or elsewhere. The LO signal is immediately amplified, and then doubled in frequency. The output of the doubler is filtered to remove the higher harmonics as well as any leakage of the fundamental, and then amplified once more before being divided equally to the two channels. The amplifiers are commercial chips from Agilent, and the doubler is from Hittite Microwave Corporation. The coax-to-microstrip transition, bandpass filter, and power divider are custom designs implemented on 127 μm thick Alumina substrates.

The RF signals in both polarizations also enter the module through coaxial K-connectors. The

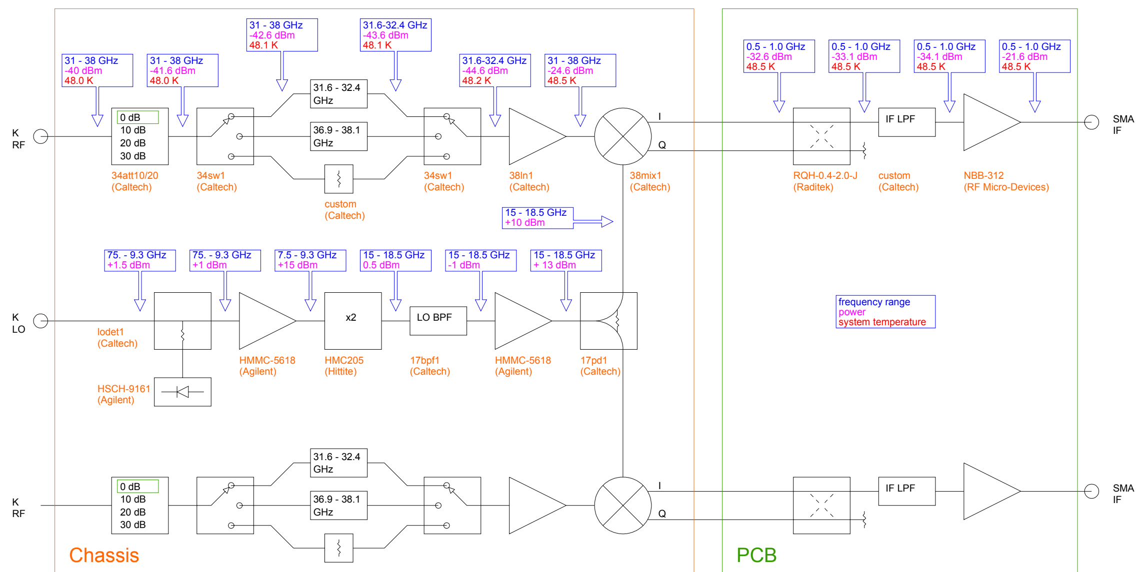

Fig. 7.42. Block diagram of the dual-polarization Ka-band downconverter.

first components in the RF path are the switched attenuators described in Section 6.1. Normally turned off for low-noise operation, these chips are included to allow the user some control over the amount of power entering the module. The P_{1dB} of the front end which will drive this module is anticipated to be about 0 dBm. The attenuators are expected to be able to handle about + 5 dBm without distortion, guaranteeing that the dynamic range of the overall system is limited only by the front end, not this downconverter.

Following the attenuators is a set of switched filters, tuned to the three required receive bands described earlier. A technique for integrating high-Q waveguide filters within multi-chip modules was pioneered in this downconverter. As was shown earlier in Figure 7.17, the approach is to hold a photochemically etched metal shim between the two halves of the split block. On this shim are metal strips that extend across waveguide channels machined into each half of the chassis, forming septum resonators that compose the filters. Signals are coupled into these internal waveguides using the proven longitudinal E-field probes. This technique is fully compatible with all the module construction methodologies endorsed in this thesis, and integrates high-performance filters seamlessly within a printed-circuit environment. Because the filters are entirely internal to the chassis, no bulky waveguide flanges are necessary, and even non-standard guide dimensions can be used.

Two septum filters were designed for this module, corresponding to the two narrow receive bands around 32 GHz and 37.5 GHz. They are both required to reject 34 GHz signals, a DSN transmitter frequency, by more than 30 dB. The 30-40 GHz channel did not have such a challenging specification, so no filter was needed. Instead, a simple microstrip through line will be used, with the possibility of some fixed attenuation to roughly equalize the total noise power to that of the narrower channels.

The 32 GHz filter was designed to fit in a standard WR-28 waveguide. The 37.5 GHz filter, however, would not perform as well in that size waveguide. The dimensions of the metal strips on the shim are easiest to realize in practice when the center frequency of the filter is closer to the middle of the waveguide band. For this reason, the 37.5 GHz filter was designed for a WR-22 waveguide channel. Additionally, this filter gets even better rejection below band because of the nearer cutoff frequency of the waveguide.

As the author had never used this fabrication technology before, multiple versions of both filters were fabricated and then tested in simple split blocks, shown in Figure 7.43-7.44. The shims are 50 μm thick, and gold-plated to minimize loss in the contact with the chassis. Measured results for the filters that are closest to meeting specifications are shown in Figure 7.45. The loss is about 0.5 dB at 32 GHz, and about 0.8 dB at 37.5 GHz. The latter filter has more loss because it has four poles instead of three, as well as being higher in frequency. These measurements show excellent agreement with HFSS simulation.

After the first set of filters was fabricated, extensive dimensional measurements were made of both the shims and the metal chassis under a high-power measuring scope to determine the nature and magnitude of center frequency and bandwidth errors that occur from manufacturing tolerances. The effects on bandwidth turned out to be negligible. A number of center-frequency detuning mechanisms were identified, however, including waveguide machining errors and misalignment of the shim card, but the most significant turned out to be simple over- or under-etching of the metal strips. If all these error mechanisms are taken into account, and the appropriate manufacturing tolerances are factored in, then we estimate a worst-case uncertainty in center frequency of about ±150 MHz at 37.5 GHz. The final filter designs will therefore include 300 MHz extra bandwidth to allow for these variations.

Referring back to the block diagram of the module (Figure 7.42), the next component after

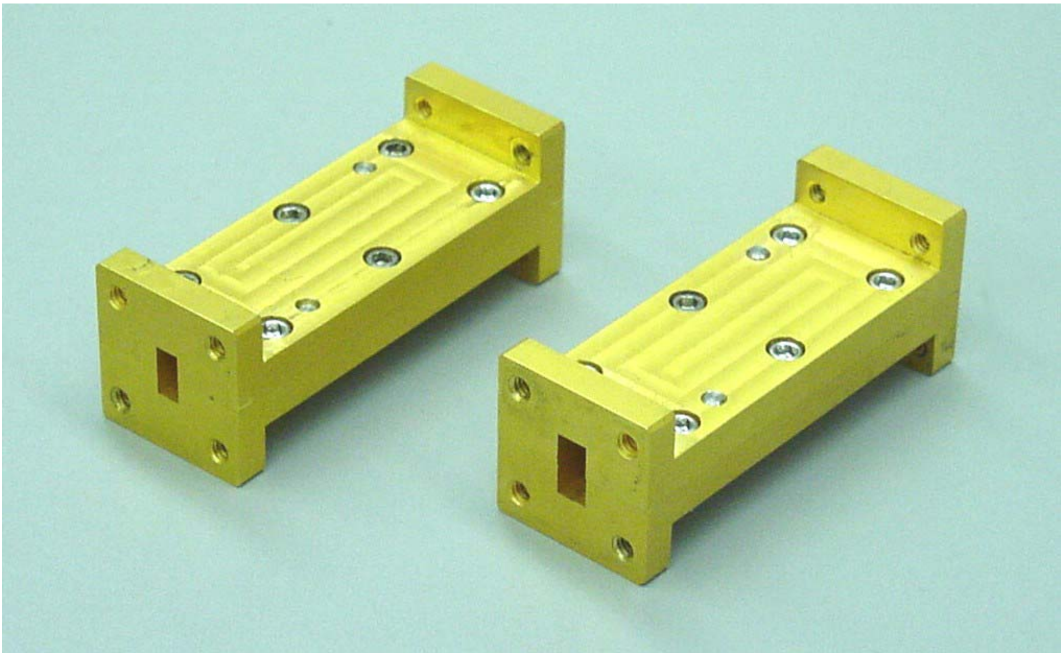

Fig. 7.43. Test blocks for the WR-22 (left) and WR-28 (right) septum filters.

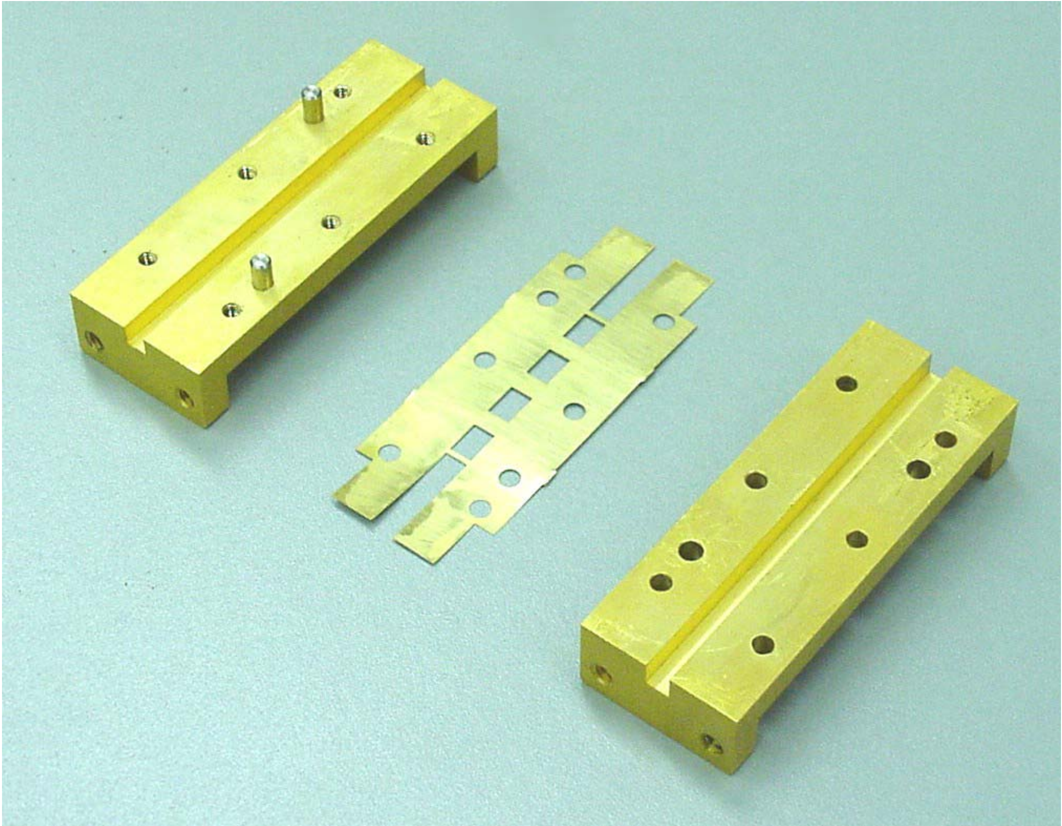

Fig. 7.44. Open WR-22 test block and metal shim for the 37.5 GHz filter.

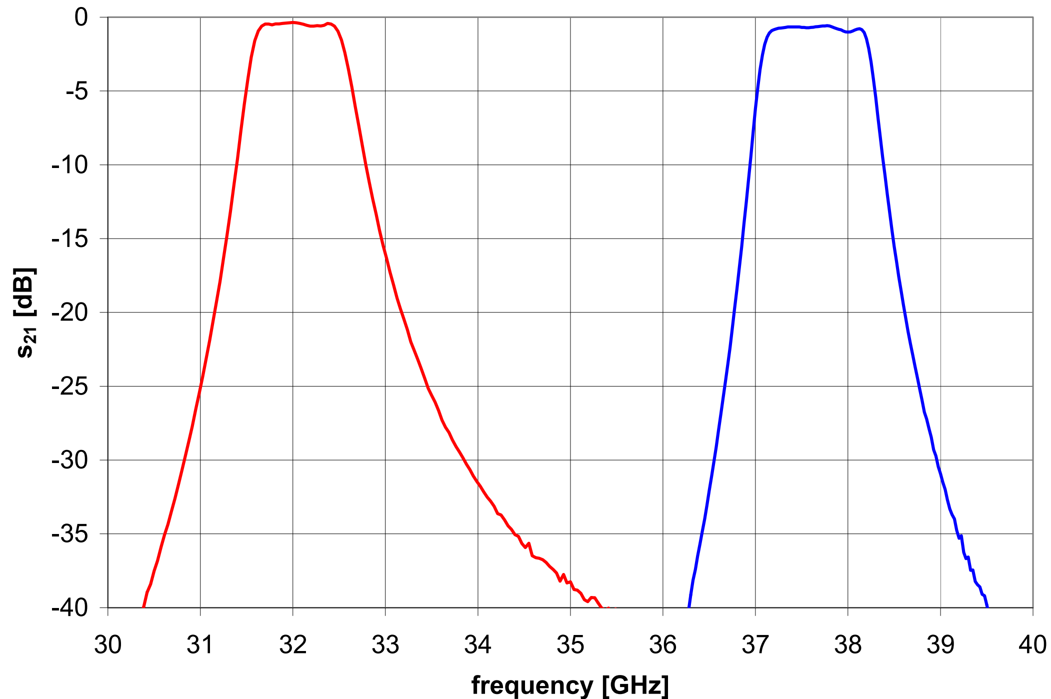

Fig. 7.45. Measured response of the two septum filters. Insertion loss is 0.5 dB in the 32 GHz band, and 0.8 dB in the 37.5 GHz band.

filtering is an RF post-amplifier. For this part the author intends to use the Ka-band MHEMT LNA presented in Section 4.2. Next is the second-harmonic I/Q mixer designed for this project and presented in Section 3.4. The two IF outputs from this mixer pass through coaxial glass-bead feedthrus to the other side of the chassis where they connect to the PC-Board. The remarkable growth of microwave surface mount technology in recent years has made it possible to put virtually all of the IF circuitry on this PC-Board. The first component in the present design is a 0.5-2.0 GHz quadrature hybrid, purchased from Raditek, which isolates the upper sideband from the mixer's I and Q outputs. The lower sideband is simply terminated. Following the hybrid is a lumped-element low-pass filter and IF amplifier. The IF signal leaves the block through an SMA connector.

A drawing of the module appears in Figure 7.46, and a detail of the inner layout is in Figure 7.47. There are no waveguide flanges. All external high-frequency connections are made through coaxial connectors. Perpendicular transitions are used in all cases to keep the MMIC side of the chassis flat for easy assembly and maintenance. The DC power supply, along with monitor and control signals all pass

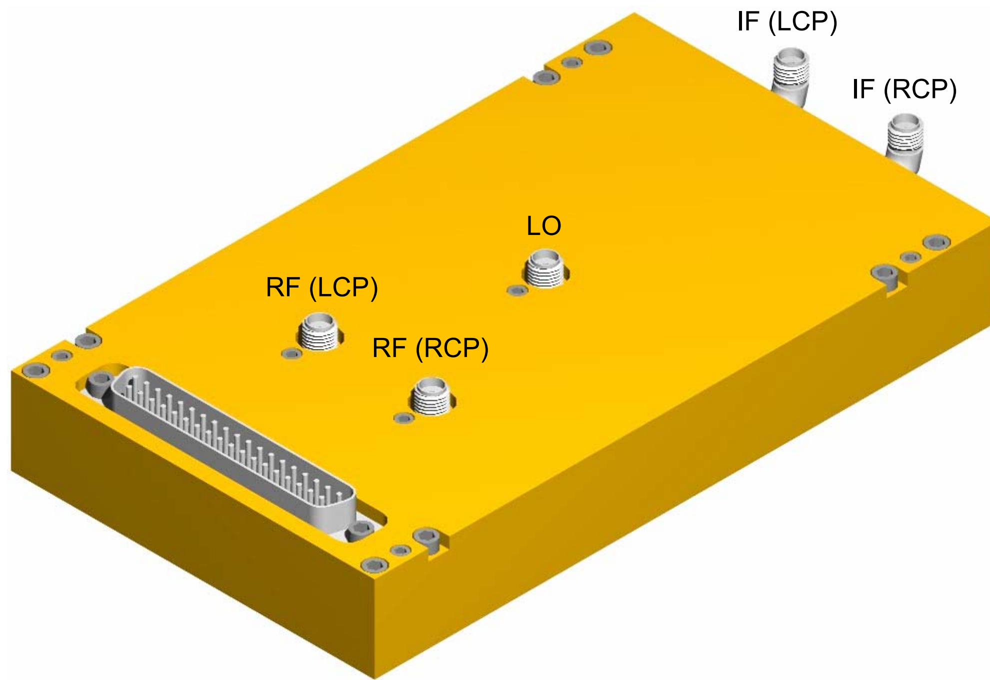

Fig. 7.46. Drawing of the Ka-band downconverter for the DSN Array. Module dimensions are 15 x 9 x 2 cm.

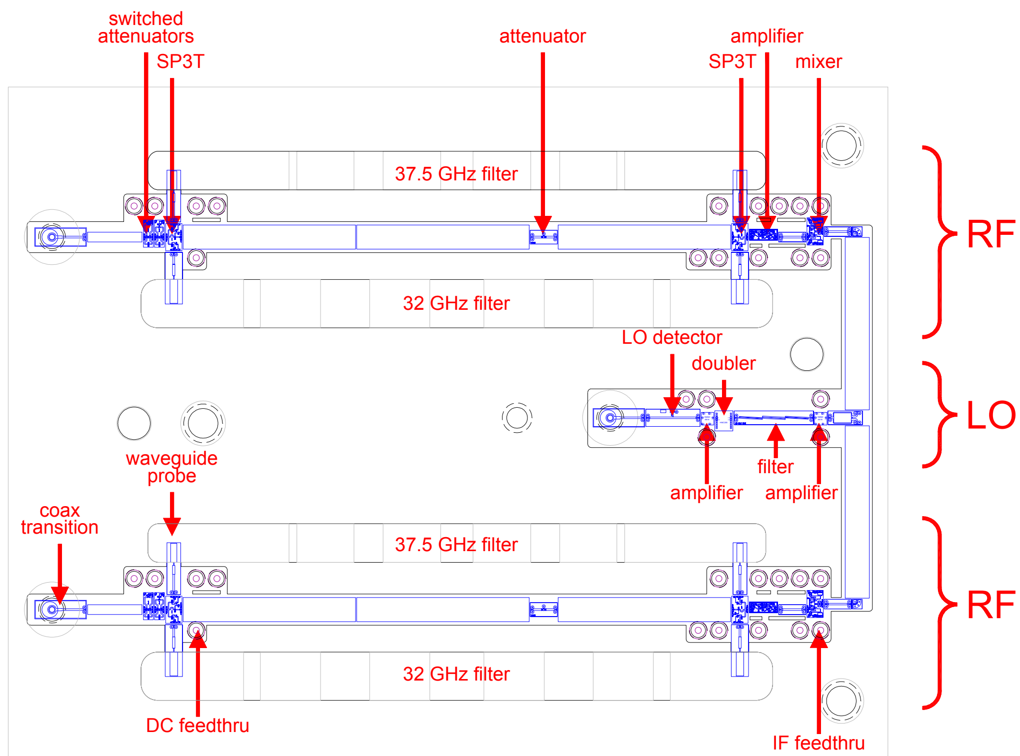

Fig. 7.47. Interior layout of the Ka-band downconverter. MMICs and passive substrates are shown in blue. Upper and lower RF chains process the two polarizations separately while the LO components are shared between them.

through a 37-pin D-subminiature connector. Fully assembled, the module will measure 15 x 9 x 2 cm. While this is large for a MMIC-based module, it is easily an order of magnitude smaller than could be achieved with an assembly of connectorized parts.

The design for this module is undergoing its final revisions, and the author expects to have a working prototype by the end of the year. When complete, it will represent a major step forward in large-scale, multi-chip integration at millimeter-wave frequencies.

8 Conclusions

A multitude of millimeter-wave components and ideas have been presented in this work. I have recounted in detail the design of the first MMIC tripler to exceed the WR-10 waveguide bandwidth in its output, the first doubly balanced MMIC mixers in the millimeter-wave spectrum, and the first MMIC amplifier in W-band to exceed 100 mW of power over a wide frequency range. I have illustrated new and advantageous ways of interfacing with coaxial connectors, synthesizing microstrip directional couplers, and packaging waveguide filters within a multi-chip module. I have described the benefits of MMIC technology in a wide variety of millimeter-wave projects, but there is still a great deal more to explore about this relatively young field.

Completing the work in this thesis has convinced me that this portion of the electromagnetic spectrum *can* be used effectively, and MMIC technology is the tool we need to do so. As with most new paradigms, it requires us to re-evaluate some of our basic assumptions about the way things should work. That does not have to be a drawback. In fact, I foresee many of the techniques we develop as we learn to exploit the millimeter-wave region having a positive effect on the way lower frequency systems are built. MMICs may be one of those rare technologies that is widely accepted at higher frequencies first, before becoming the dominant implementation of circuits in the RF and microwave regions as well.

The true strength of MMIC technology, in my opinion, is the type of system that it suggests. Mass production, repeatability, miniaturization, all the key advantages that MMICs have to offer point to the same thing — arrays. I find it interesting that so many of the great advances in applied science have depended on breaking a large problem down into several smaller ones. This is how modern supercomputing is accomplished, this is how you take a Fourier Transform fast, and this is definitely how you build a large radio telescope. Not only can a constellation of small antennas do the same job as a single large one, but it also brings extraordinary new flexibility and functionality with it. Similar statements can be made about arrays of virtually all sizes and functions. MMICs do not just make an array a feasible architecture, they can often make an array the optimal architecture.

My hope for this work is that it has advanced the *practice* of millimeter-wave engineering. I wanted to raise the bar in our minds that separate the "normal" frequencies of industry from the "high" frequencies that people only talk about in academia. I have attempted to innovate, to indulge my inner scientist's curiosity in the intricate patterns of physics, without losing sight of the practical forces of engineering. The road has been difficult, full of both victory and failure, discovery and disappointment, and I believe I have been much improved by the journey.

References

[1] C. Elachi, *Introduction to the Physics and Techniques of Remote Sensing*, New York, NY: John Wiley & Sons, 1987.
[2] J. Wertz and W. Larson, *Space Mission Analysis and Design*, 3rd ed., El Segundo, CA: Microcosm Press, 1999.
[3] PMC Quarterly Review Briefing, February 20, 2002.
[4] E. Croke, J. Schulman, D. Chow, H. Dunlap, K. Holabird, M. Morgan, and S. Weinreb, "New tunnel diode for zero-bias direct detection for millimeter-wave imagers," *SPIE Intl. Symp. on Aerospace/Defense Sensing, Simulation, and Controls*, Orlando, FL, 2001.
[5] J. Schulman, S. Thomas, D. Chow, E. Croke, H. Dunlap, K. Holabird, W. Clark, and M. Morgan, "High-frequency performance of Sb-heterostructure millimeter-wave diodes: Sb-heterostructure diodes for high-frequency radiometric applications," *14th Indium Phosphide and Related Materials Conference*, Stockholm, 2002.
[6] J. Schulman, J. Zinck, S. Skeith, S. Thomas, D. Chow, E. Croke, H. Dunlap, K. Holabird, M. Morgan, and S. Weinreb, "Physics of Sb-heterostructure quantum tunneling millimeter-wave diodes," *44th Electron Materials Conference*, Santa Barbara, CA, 2002.
[7] A. Mellberg, N. Wadefalk, N. Rorsman, E. Choumas, J. Stenarson, I. Angelov, P. Starski, E. Kollberg, J. Grahn, and H. Zirath, "InP HEMT-based, cryogenic, wideband LNAs for 4-8 GHz operating at very low DC-power," *14th Indium Phosphide and Related Materials Conference*, Stockholm, 2002.
[8] Arecibo Observatory Home Page, www.naic.edu
[9] NRAO Very Large Array Home Page, www.aoc.nrao.edu/vla/html/VLAhome.shtml
[10] The Atacama Large Millimeter Array Web Site, www.mma.nrao.edu
[11] SETI Institute, www.seti-inst.edu/Welcome.html
[12] ASTRON Homepage, www.astron.nl/skai
[13] Deep Space Network Homepage, deepspace.jpl.nasa.gov/dsn
[14] S. Weinreb, "Study of an array of small antennas for space communication applications," JPL presentation, April 16, 2001.
[15] S. Weinreb, "Technology and applications of large microwave arrays, " Caltech presentation, May 13, 2002.
[16] M. Morgan and S. Weinreb, "A full waveguide band MMIC tripler for 75-110 GHz," *IEEE MTT-S Intl. Microwave Symp. Digest*, pp. 103-106, Phoenix, AZ, 2001.
[17] P. Penfield and R. Rafuse, *Varactor Applications*, Cambridge, MA: MIT Press. 1962.
[18] S. Maas, *Nonlinear Microwave Circuits*, New York, NY: IEEE Press, 1997.
[19] S. Chen, T. Ho, F. Phelleps, J. Singer, K. Pande, P. Rice, J. Adair, and M. Ghahremani, "A high-performance 94-GHz MMIC doubler," *IEEE Microwave Guided Wave Lett.*, vol. 3, pp. 167-169, June 1993.
[20] J. Papapolymerou, F. Bauchler, J. East, and L. Katehi, "W-band Finite Ground Coplanar monolithic multipliers," *IEEE Trans. Microwave Theory and Tech.*, vol. MTT-47, pp. 614-619, May 1999.
[21] "Fullband Frequency Triplers," Product data sheet, REV00 C 051199, Millitech Corporation, Technology and Manufacturing Center, South Deerfield, MA.
[22] "Frequency Multipliers," Product data sheet, Pacific Millimeter Products, Golden, CO.
[23] M. Cohn, R. Freitag, H. Henry, J. Degenford, and D. Blackwell, "A 94 GHz MMIC tripler using anti-parallel diode arrays for idler separation," *IEEE MTT-S Intl. Microwave Symp. Digest*, pp. 763-766, San Diego, CA, 1994.
[24] A. Rahal, R. Bososio, C. Rogers, J. Ovey, M. Sawan, and M. Missous, "A W-band medium power multi-stack quantum barrier varactor tripler," *IEEE Microwave Guided Wave Lett.*, vol. 5, pp. 368-370, November 1995.

[25] Y. Campos-Roca, L. Verweyen, M. Fernandez-Barciela, E. Sanchez, M.C. Curras-Francos, W. Bronner, A. Hulsmann, and M. Schlechtweg, "An optimized 25.5-76.5 GHz PHEMT-based coplanar frequency tripler," *IEEE Microwave Guided Wave Lett.*, vol. 10, pp. 242-244, June 2000.
[26] H. Fudem, and E. Niehenke, "Novel millimeter-wave active MMIC triplers," *IEEE MTT-S Intl. Microwave Symp. Digest*, pp. 387-390, Baltimore, MD, 1998.
[27] A. Raisanen, "Frequency multipliers for millimeter and submillimeter wavelengths," *Proc. IEEE*, vol. 80, pp. 1842-1852, November 1992.
[28] K. Lin, H. Wang, M. Morgan, T. Gaier, and S. Weinreb, "A W-band GCPW MMIC diode tripler," *32nd European Microwave Conference*, Milan, 2002.
[29] V. Radisic, M. Micovic, M. Hu, P. Janke, C. Ngo, L. Nguyen, L. Samoska, and M. Morgan, "164-GHz MMIC HEMT doubler," *IEEE Microwave and Wireless Components Letters*, vol. 11, pp. 241-243, June 2001.
[30] M. Morgan and S. Weinreb, "A monolithic HEMT diode balanced mixer for 100-140 GHz," *IEEE MTT-S Intl. Microwave Symp. Digest*, pp. 99-102, Phoenix, AZ, 2001.
[31] S. Maas, *Microwave Mixers*, 2nd ed. Boston, MA: Artech House, 1993.
[32] Y. L. Kok, H. Wang, M. Barsky, R. Lai, M. Sholley, and B. Allen, "A 180-GHz monolithic sub-harmonic InP-based HEMT diode mixer," *IEEE Microwave Guided Wave Lett.*, vol. 9, pp. 529-531, December 1999.
[33] K. Chang, H. Wang, K. Tan, S. Bui, T. Chen, G. Dow, J. Berenz, T. Ton, D. Garske, T. Lin, and L. Liu, "A W-band monolithic downconverter," *IEEE Trans. Microwave Theory and Tech.*, vol. 39, pp. 1972-1979, December 1991.
[34] Y. Kok, P. Huang, H. Wang, B. Allen, R. Lai, M. Sholley, T. Gaier, and I. Mehdi, "120 and 60 GHz monolithic InP-based HEMT diode sub-harmonic mixer," *IEEE MTT-S Intl. Microwave Symp. Digest*, pp. 1723-1726, Baltimore, MD, 1998.
[35] W. Menzel, "A 140-GHz balanced mixer for finline integrated-circuits," *Microwaves & RF*, p. 34, 1983.
[36] R. Tahim, K. Chang, and K. Hummer, "Wideband microstrip balanced mixer," *Electronics Letters*, vol. 23, pp. 767-768, July 1987.
[37] Y. C. Leong and S. Weinreb, "Synthesis of broadband TEM coupled line phase shifters," submitted.
[38] Y. C. Leong and S. Weinreb, "Novel technique of phase velocity equalization for microstrip coupled-line phase shifters," *IEEE MTT-S Intl. Microwave Symp. Digest*, pp. 1453-1456, Boston, MA, 2000.
[39] R. Lai, M. Barsky, T. Huang, M. Sholley, H. Wang, Y. Kok, D. Streit, T. Block, P. Liu, T. Gaier, and L. Samoska, "An InP HEMT MMIC LNA with 7.2-dB gain at 190 GHz," *IEEE Microwave Guided Wave Lett.*, vol. 8, pp. 393-395, Nov. 1998.
[40] Environmental Monitoring page, http://www.trexenterprises.com/environ.html
[41] A. Anastassiou and M. Strutt, "Effect of source lead inductance on the noise figure of GaAs FET," *Proc. IEEE*, vol. 62, pp. 406-408, March 1974 (corr. S. Iversen, *Proc. IEEE*, vol. 63, pp. 983-984, June 1975).
[42] J. Lange, "Noise characterization of linear twoports in terms of invariant parameters," *IEEE Journal of Solid State Circuits*, vol. 2, pp. 37-40, June 1967.
[43] M. Pospieszalski, "Modeling of noise parameters of MESFET's and MODFET's and their frequency and temperature dependence," *IEEE Trans. Microwave Theory and Tech.*, vol. 37, pp. 1340-1350, September 1989.
[44] S. Cripps, *RF Power Amplifiers for Wireless Communications*, Norwood, MA: 1999.
[45] S. Kee, I. Aoki, A. Hajimiri, and D. Rutledge, "The class E/F family of ZVS switching amplifiers," *IEEE Trans. Microwave Theory and Tech.*, vol. 51, May 2003.
[46] L. Samoska and Y. Leong, "65-145 GHz InP HEMT medium power amplifiers," *IEEE MTT-S Intl. Microwave Symp. Dig.*, pp. 1805-1808, Phoenix, AZ, 2001.
[47] M. Morgan and S. Weinreb, "A W-band monolithic medium power amplifier," *IEEE MTT-S Intl. Microwave Symp.*, Philadelphia, PA, 2003.
[48] D. Ingram, Y. Chen, J. Kraus, B. Brunner, B. Allen, H. Yen, and K. Lau, "A 427 mW, 20% compact W-band InP HEMT MMIC power amplifier," *IEEE RFIC Symp. Dig.*, pp. 95-98, June 1999.

[49] M. Matloubian, P. Petre, L. Hamilton, R. Bowen, M. Lui, H. Sun, C. Ngo, P. Janke, D. Baker, R. Robertson, "W-band InP HEMT MMICs using finite-ground coplanar waveguide (FGCPW) design," *IEEE Journal of Solid-State Circuits*, vol. 34, pp. 1212-1218, September 1999.
[50] S. Ortiz, J. Hubert, L. Mirth, E. Schlecht, A. Mortazawi, "A high-power Ka-band quasi-optical amplifier array," *IEEE Trans. Microwave Theory and Tech.*, vol. 50, pp.487-494, February 2002.
[51] G. Gonzalez, *Microwave Transistor Amplifier: Analysis and Design*, 2nd ed., Upper Saddle River, NJ: Prentice Hall, 1997.
[52] J. Rollett, "Stability and power-gain invariants of linear twoports," *IRE Trans. Circuit Theory*, vol. 9, pp. 29-32, March 1962.
[53] R. Meys, "Review and discussion of stability criteria for linear 2-ports," *IEEE Trans. Circuits and Systems*, vol. 37, pp. 1450-1452, November 1990.
[54] G. Lombardi and B. Neri, "Criteria for the evaluation of unconditional stability of microwave linear two-ports: a critical review and new proof," *IEEE Trans. Microwave Theory and Tech.*, vol. 47, pp. 746-751, June 1999.
[55] L. Samoska, K. Lin, H. Wang, Y. Chung, M. Aust, S. Weinreb, and D. Dawson, "On the stability of millimeter-wave power amplifiers," *IEEE MTT-S Intl. Microwave Symp. Digest*, pp. 429-432, Seattle, WA, 2002.
[56] M. Morgan and S. Weinreb, "A millimeter-wave perpendicular coax-to-microstrip transition," *IEEE MTT-S Intl Microwave Symp. Digest*, pp. 817-820, Seattle, WA, 2002.
[57] E. England, "A coaxial to microstrip transition," *IEEE Trans. Microwave Theory and Tech.*, vol. MTT-24, pp. 47-48, January 1976.
[58] R. Eisenhart, "Electrical coupler," U.S. Patent: 4,280,112, July 1981.
[59] R. Neidert, "Waveguide-to-coax-to-microstrip transitions for millimeter-wave monolithic circuits," *Microwave Journal*, vol. 26, June 1983.
[60] J. Chenkin, "DC to 40 GHz coaxial-to-microstrip transition for 100 μm thick GaAs substrates," *IEEE Trans. Microwave Theory and Tech.*, vol. 37, July 1989.
[61] J. Browne, "Coax test fixture checks microstrip circuits to 60 GHz," *Microwave & RF*, vol. 28, pp. 136-137, December 1989.
[62] B. Oldfield, "Connector and termination construction above 50 GHz," *Applied Microwave & Wireless*, pp. 56-66, April 2001.
[63] "Precision RF and Microwave Components," catalog, 2001 edition, Anritsu Corporation.
[64] Y. C Leong and S. Weinreb, "Full band waveguide-to-microstrip probe transitions," *IEEE MTT-S Intl. Microwave Symp. Digest*, pp. 1435-1438, Anaheim, CA, 1999.
[65] S. Weinreb, T. Gaier, R. Lai, M. Barsky, Y. C. Leong, and L. Samoska, "High-gain 150-215-GHz MMIC amplifier with integral waveguide transitions," *IEEE Microwave Guided Wave Lett.*, vol. 9, pp. 282-284, July 1999.
[66] UltraSource Inc. - The Thin Film Source, www.ultra-source.com
[67] ATP: Home, www.thinfilm.com
[68] American Technical Ceramics - Welcome, www.atceramics.com/index.html
[69] M. Morgan and S. Weinreb, "Octave-bandwidth high-directivity microstrip codirectional couplers," *IEEE MTT-S Intl. Microwave Symp.*, Philadelphia, PA, 2003.
[70] S. Uysal, *Nonuniform Line Microstrip Directional Couplers and Filters*, Norwood, MA: Artech House, 1993.
[71] P. Ikalainen and G. Matthei, "Wideband forward-coupling microstrip hybrids with high-directivity," *IEEE Trans. Microwave Theory and Tech.*, vol. 35, pp. 719-725, August 1987.
[72] M. Morgan, S. Weinreb, N. Wadefalk, and L. Samoska, "A MMIC-based 75-110 GHz signal source," *IEEE MTT-S Intl. Microwave Symp. Digest*, pp. 1859-1862, Seattle, WA, 2002.
[73] "Series AMC active multiplier chain," product data sheet rev01 C 021801, Millitech, Northampton, MA.
[74] "Agilent 83557A/83558A 50 to 75 GHz/75 to 110 GHz mm-wave source modules," product data sheet, Agilent Technologies, Test and Measurement
[75] *Reference Data for Radio Engineers*, Indianapolis, IN: Howard W. Sams & Co., 1981.
[76] G. Matthaei, L. Young, and E. Jones, *Microwave Filters, Impedance-Matching Networks, and Coupling Structures*, Dedham, MA: Artech House, 1980.

[77] N. Erickson, "High performance dual directional couplers for near-mm wavelengths," *IEEE Microwave and Wireless Component Lett.*, vol. 11, pp. 205-207, May 2001.